Trinity College Dublin

Doctoral Thesis

Broadband Surface Wave Tomography of Ireland, Britain, and Other Regions

---

Author:
Raffaele Bonadio

Supervisors:
Dr. Sergei Lebedev (DIAS)
Dr. David Chew (TCD)

A thesis submitted in fulfillment of the requirements
for the degree of Doctor of Philosophy

in the

Trinity College Dublin
Coláiste na Tríonóide, Baile Átha Cliath
The University of Dublin

Department of Geology
School of Natural Sciences
Faculty of Engineering, Mathematics and Science

November 22, 2019

Declaration of Authorship

I, Raffaele BONADIO, declare that this thesis titled, “Broadband Surface Wave Tomography of Ireland, Britain, and Other Regions” has not been submitted as an exercise for a degree at this or any other university and it is entirely my own work.

I agree to deposit this thesis in the University’s open access institutional repository or allow the library to do so on my behalf, subject to Irish Copyright Legislation and Trinity College Library conditions of use and acknowledgement.

I consent to the examiner retaining a copy of the thesis beyond the examining period, should they so wish (EU GDPR May 2018).

Signed:

Date:

TRINITY COLLEGE DUBLIN

Abstract

Faculty of Engineering, Mathematics and Science
Department of Geology

Doctor of Philosophy

Broadband Surface Wave Tomography of Ireland, Britain, and Other Regions

by Raffaele BONADIO

Over the last decades, seismic surface-wave studies have produced increasingly detailed images of the Earth's structure at a regional scale. In this study, we have tuned well-established techniques and–when required–implemented new ones in order to investigate regions in which important debates are still ongoing, regarding the structure and the evolution of the Earth beneath them.

Several studies suggested that the Paleogene uplift of parts of Britain and Ireland was caused by a lateral branch of the Iceland mantle plume, which played a fundamental role in the evolution of the North Atlantic Ocean over the past 60 M.y. Alternatively, among competing hypothesis, it was suggested that the uplift could be due to the far-field stress associated with the Alpine and Pyrenees Orogenies, with reactivation of old Variscan and Caledonian faults across Ireland and Britain. A major part of this study is aimed at gaining new insights into the seismic structure of the British Isles, which can help us answer these open questions. Teleseismic earthquakes and ambient noise, recorded at densely spaced seismic stations in the region, were used to determine the surface-wave dispersion across the British Isles and construct detailed images of the seismic structure beneath the area. The measurements, obtained using independent surface-wave analysis techniques (cross-correlation of teleseismic surface waves, multimode waveform fitting, and ambient noise interferometry), were applied to produce the first 3D shear-velocity model of the lithosphere and the asthenosphere of the entire region including Ireland, Britain, and the Irish Sea. The application of different methodologies yielded complementary frequency bands of the measurements, sensitive to different depths, from the shallow crust to the deep upper mantle.

Abundant, newly available data was used to image the region with higher resolution than previously. The highly uneven station coverage resulted in a considerably irregular distribution of the measurements in the area; this, and the effects of errors on the measurements, required the development of a new, multi-resolution tomographic scheme. This scheme allows us to maximize the information extracted from the data and reach an optimal target resolution of the model at each knot, minimizing the effects of uneven data sampling and of the propagation of systematic errors.

The multi-resolution phase-velocity maps, obtained at densely spaced periods, were inverted, point by point, for shear-velocity structure in order to produce a 3D, shear-velocity model of the lithosphere and asthenosphere. The optimal resolution tomography offers important new insights into the structure and evolution of the British Isles. A robust, low-velocity anomaly beneath the Irish Sea and its surroundings persists in the models from ~60 to at least 140 km depth, indicating an anomalously thin lithosphere. The area that exhibits the low velocity anomaly corresponds to where uplift and volcanism are evidenced by geological data. Our results also show a striking correlation with proposed underplating thickness and denudation, gravity, and thermochronological measurements, and rule out the once common assumption of a constant lithospheric thickness across Britain and Ireland.

At lithospheric depths, a clear contrast in seismic velocities between Ireland and Britain could possibly explain why the seismicity is nearly absent in Ireland, while modest but clearly higher in Britain. The higher velocities beneath most of Ireland indicate thicker lithosphere and colder geotherms, likely resulting in a higher-strength lithosphere, resisting deformation. In the lithospheric mantle, the model displays an elongated high-velocity anomaly stretching W-E approximately along the Iapetus Suture Zone in Ireland, which may be the expression of a remnant of the Caledonian Iapetus slab beneath the suture or, alternatively, fragments of thick continental lithosphere incorporated into the Irish landmass in the course of the Caledonian Orogeny.

Another part of this study was on using surface-wave analysis to investigate the lithosphere-asthenosphere system beneath the Tristan da Cunha Hotspot, with the goal of understanding the enigmatic intraplate volcanism in the region. Surface-wave analysis was applied in a challenging setting, as this work involved the use of data recorded by ocean-bottom seismometers, which required data-processing and measurement approaches substantially different from those tuned for land-based arrays of stations. We constrained a region-average, shear-velocity structure, using two-station, cross-correlation measurements across the area, and inferred the temperature of the lithosphere and asthenosphere beneath the area by means of petrological modeling. Seismic inversion and petrological modeling show a lithospheric thickness of only 65–70 km, confirming the previous estimates obtained from receiver functions. Our observations are consistent with a hot plume from the deep mantle, but the excess temperature estimated is much smaller than that reported for some other major hotspots, in particular, Hawaii.

Statement of co-authorship

Chapter 4 is a peer-reviewed paper published with Wolfram H. Geissler, Sergei Lebedev (my supervisor at Dublin Institute for Advanced Studies), Javier Fullea, Matteo Ravenna, Nicolas L. Celli, Wilfried Jokat, Marion Jegen, Christoph Sens-Schönfelder, and Kiyoshi Baba (Bonadio et al., 2018). I processed the data, performed the analysis, generated the models, and made the interpretation. Petrological analysis and Bayesian inversion have been generated in collaboration with, respectively, Javier and Matteo. I wrote the manuscript with suggestions from Wolfram and Sergei.

Chapters 2 and 3 are manuscripts in preparation for submission in peer-reviewed journals. I obtained and processed the data, wrote part of the software and adapted existing ones, performed the analysis, generated the models, and made the interpretations. I wrote the manuscripts with suggestions from Sergei.

In addition I am second author of two peer-reviewed papers published as:

> Lebedev, S., **Bonadio, R.** et al. Education and public engagement using an active research project: lessons and recipes from the SEA-SEIS North Atlantic Expedition's programme for Irish schools (Lebedev et al., 2019). I have managed the production of digital content for outreach and public engagement, and I have contributed to the organization and scientific planning of the SEA-SEIS Expedition, as well as the logistics.
>
> Carvalho, J., **Bonadio, R.** et al. Evidence for high temperature in the upper mantle beneath Cape Verde archipelago from Rayleigh-wave phase-velocity measurements (Carvalho et al., 2019). I have contributed to the data processing, software implementation, generation and interpretation of the models, analysis, and editing of the manuscript.

I am also co-author of a peer-reviewed published paper:

> Moretti, M., Pondrelli, S., Margheriti, L., . . . , **Bonadio, R.**, . . . , and Mazza, S. SISMIKO: emergency network deployment and data sharing for the 2016 central Italy seismic sequence. INGV - Annals of Geophysics, 59, Fast Track 5. https://doi.org/10.4401/ag-7212 (Moretti et al., 2016). I have contributed to the testing of part of the seismic stations and their

deployment, and the logistics in Central Italy after the August 2016 Central Italy earthquake.

Publications

Some of the work presented in this thesis has been presented to the scientific community during the course of this Ph.D. as follows (note only main contributions are listed):

Peer-reviewed papers

Bonadio, R. et al. Hot upper mantle beneath the Tristan da Cunha hotspot from probabilistic Rayleigh-wave inversion and petrological modeling. Geochemistry, Geophysics, Geosystems, 19, 1412–1428. https://doi.org/10.1002/2017GC007347 (Bonadio et al., 2018).

Lebedev, S., **Bonadio, R.** et al. Education and public engagement using an active research project: lessons and recipes from the SEA-SEIS North Atlantic Expedition's programme for Irish schools (Lebedev et al., 2019).

Carvalho, J., **Bonadio, R.** et al. Evidence for high temperature in the upper mantle beneath Cape Verde archipelago from Rayleigh-wave phase-velocity measurements (Carvalho et al., 2019).

Moretti, M., Pondrelli, S., Margheriti, L., ..., **Bonadio, R.**, ..., and Mazza, S. SISMIKO: emergency network deployment and data sharing for the 2016 central Italy seismic sequence. INGV - Annals of Geophysics, 59, Fast Track 5. https://doi.org/10.4401/ag-7212 (Moretti et al., 2016).

Oral and poster presentations

Bonadio, R., et al. Surface-Wave Tomography of Ireland and Surroundings. European Geosciences Union General Assembly. Vienna, 2019 April.

Bonadio, R., et al. Hot Upper Mantle Beneath the Tristan da Cunha Hotspot From Probabilistic Rayleigh-Wave Inversion and Petrological Modeling. Tristan da Cunha Workshop. Hamburg, 2018 June 5-6.

Bonadio, R., et al. Hot upper mantle beneath the Tristan da Cunha Hotspot, from probabilistic Rayleigh-wave inversion and petrological modeling. European Geosciences Union General Assembly. Vienna, 2018 Apr 09-13.

Bonadio, R., et al. Surface-wave tomography of Ireland and Surroundings. Atlantic Margins Conference. Dublin, 2018 Apr 26-27.

Bonadio, R., et al. Asthenospheric Temperature and Lithospheric Thickness Beneath the Tristan da Cunha Hotspot From Probabilistic Inversion of Surface-Wave Dispersion Data and Petrological Modeling. America eophysical Union (AGU) fall meeting. New Orelans, 2017 December.

Bonadio, R., et al. Structure of the lithosphere-astenosphere system in the vicinity of the Tristan da Cunha hotspot as seen by surface waves. Irish Geological Research Meeting (IGRM). Cork, 2017 March 03-05.

Bonadio, R. et al. Surface-wave imaging of Ireland's crust and lithospere. Geology Post Graduate day, Trinity College Dublin. Dublin, 2016 November 07.

Bonadio, R. et al. Surface-wave tomography of Ireland and surroundings. Irish Geological Research Meeting (IGRM). Galway, 2016 November 01.

Bonadio, R. et al. Surface wave imaging of Ireland's crust and lithosphere. SFI mid-term confirmation report, Dublin Instutute for Advanced Studies. Dublin, 2016 October 05.

Bonadio, R. et al. Surface-wave tomography of Ireland and surroundings using ambient noise and teleseismic data. European Geosciences Union General Assembly. Vienna, 2016 April 17-22.

Bonadio, R. et al. Surface-wave tomography of Ireland and surroundings. Irish Geological Research Meeting (IGRM). Galway, 2016 February 19-21.

Bonadio, R. et al. Integrated surface-wave imaging of Ireland's lithosphere. Geology Post Graduate day, Trinity College Dublin. Dublin, 2015 November 15.

Bonadio, R. et al. Structure and seismicity of Ireland's crust. Atlantic Ireland Conference. Dublin, 2015 October 27.

Preface

This thesis is based on a collection of one published journal article (Chapter 4 and Appendix C) and two manuscripts in preparation for submission in peer-reviewed journals (Chapters 2 and 3).

The content of the published article was unaltered to conform with Journal copyrights (Bonadio et al., 2018), except for correction of a few typographical errors (indicated by footnotes).

The results presented were generated using programs written mostly in Unix Shell, C, C++, Fortran, and Python, as well as Matlab. All programs were compiled and run on Ubuntu Linux distributions.

The figures were produced using Generic Mapping Tools (Wessel et al., 2013).

Acknowledgements

I am grateful to my supervisor at Dublin Institute for Advance Studies, Dr. Sergei Lebedev for giving me the opportunity to work with him and entrusting me with this research. I would not be here without his guidance, advices, and support.

I would like to thank Dr. David Chew for agreeing to be my supervisor at Trinity College Dublin, and for giving me the chance to participate in wonderful discussions about Geology.

I would like to express my gratitude to Prof. Nicholas Rawlinson and Dr. Juan Diego Rodriguez-Blanco for insightful comments and suggestions that helped me improve this work.

I also would like to thank Wolfram H. Geissler for the great possibility to collaborate with him and the Alfred Wegener Institute in Bremerhaven, Thomas Meier for the software code and all his useful suggestions, Graça Silveira for her collaboration, and Brian Baptie for inviting me to join the deployment campaign after the August 2016 Central Italy earthquake.

This study was supported by the Science Foundation Ireland (SFI) (grant 13/CDA/2192).

Thanks to Brian O'Reilly, Nicola Piana Agostinetti, Javier Fullea, Matteo Ravenna, Andrea Licciardi, Florian Le Pape, Clara Gómez García, Nicolas L. Celli, Joana Carvalho, and Andrew Schaeffer for all the interesting discussions.

I would like to give special thanks to Pierre Arroucau and Manel Prada.

Last but not least, I would like to thank my family for the support, and Kata for all the patience.

Contents

List of Figures

List of Tables

Dedicated to Teodoro

“Mintha szivemből folyt volna tova,
zavaros, bölcs és nagy volt a Duna.
(As if it flowed from my own heart in spate,
Wise was the Danube, turbulent and great.) ”

József Attila, A Dunánál (József, 1936)

Chapter 1

Introduction

1.1 Overview

Through the use of passive seismology, we aim to gain information on the structure of the Earth's interior and on the relationships between tectonic and magmatic processes and the deep dynamics of the lithosphere. We do this by recording and interpreting natural seismic wave fields, as opposed to active seismic techniques, which involve, instead, the study of artificially-generated elastic waves in the subsurface (a seismic man-made wave or pulse is generated at the surface by an active seismic source as a vibration, a mechanical impact, or an explosion). Natural seismic wave fields include the waves propagating from earthquakes and volcanic tremors, as well as the so-called ambient noise, which is generated by wind, ocean waves, and anthropogenic activity.

When an earthquake occurs, seismic waves radiate away from the hypocentre in all directions. Through the use of permanent seismological observatories, land temporary seismic stations and ocean bottom seismometers deployed around the globe, the vibrations of the Earth produced by earthquakes and other sources are recorded and used to obtain models of the Earth's internal structure. The two main types of seismic waves are body waves, which can propagate deep inside the Earth and, when recorded at long distances from the source, provide information about deep structures and surface waves which, instead, travel within the Earth's outer layers (Fig. 1.1).

Surface waves are commonly used to produce tomographic images of the Earth's interior. They allow us to constrain the structure of the Earth's lithosphere and sublithospheric mantle at high resolution. Surface waves can be retrieved by measuring the propagation between the source and seismic stations, or between two or more seismic stations. The different nature of propagation and speed of seismic waves results in distinct seismic phases arriving at different times at a seismic station: the P (primary) body wave is recorded first, followed by S (secondary) and, then, surface waves. The

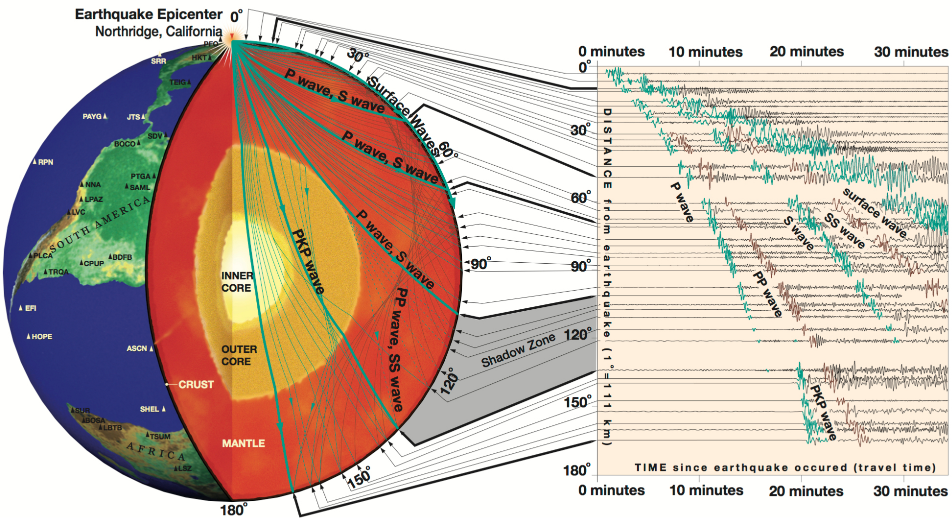

FIGURE 1.1: Wave propagation (after Braile et al. (2003)). Body waves propagate deep inside the Earth and, when recorded at long distances from the source, provide information about deep structures. Surface waves, instead, travel within the Earth's outer layers and are commonly used to produce tomographic images of the Earth's lithosphere and sublithospheric mantle.

surface waves, which are usually the most energetic arrivals in the seismogram and are responsible for the destructive motion of the ground, travel within the Earth according to two different polarization. Love waves depend on the horizontally polarised shear wave propagation (with particle motion perpendicular to the great-circle plane), whereas Rayleigh waves depend on the vertically polarised shear wave and P wave propagation (with particle motion parallel to the great-circle plane) (Fig. 1.2). Surface waves, which are the main tool of investigation utilized in this work to probe the structure of the Earth's crust and upper mantle, are dispersive. This means that the waves travel at different velocities for different frequencies (Fig. 1.3). This frequency-depth dependence of the propagation of the waves makes it possible to infer the shear velocity as a function of depth, thus it gives us the possibility to infer the structure of the sub-surface (e.g., Aki and Richards, 2002; Dahlen and Tromp, 1998; Thorne and Wallace, 1995; Shearer, 1999; Udías and Buforn, 2017). In the period range from ~1 to 500 s, surface waves are sensitive to the structure of the crust, mantle lithosphere and asthenosphere (e.g., Figs. 1.4 and 1.6).

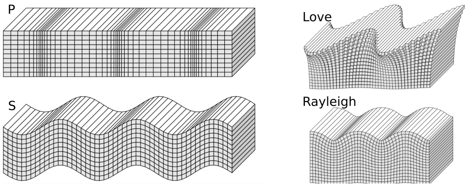

FIGURE 1.2: Left panel: illustration for the displacements occurring from a P wave (primary) and S wave (secondary) traveling horizontally across the page. Right panel: illustration for fundamental mode Love surface wave (purely transverse motion) and Rayleigh surface wave (both vertical and radial motion) displacements for horizontal propagation across the page (figure adapted from Shearer (1999)).

1.2 Methodology

We use the two-station method (e.g. Sato, 1955; Meier et al., 2004; Endrun et al., 2008; Deschamps et al., 2008; Yao et al., 2006; Soomro et al., 2016; Bonadio et al., 2018) to retrieve Rayleigh- and Love-wave fundamental-mode dispersion from teleseismic earthquakes and seismic ambient noise. Broadband phase velocities between pairs of stations are obtained using three complementary independent approaches: cross-correlation of teleseismic earthquakes (Section 1.2.1), waveform inversion (Section 1.2.2), and ambient noise interferometry (Section 1.2.3).

Typically the phase velocity measurements retrieved using the interstation teleseismic cross-correlation (TSCC) method (e.g., Meier et al., 2004; Lebedev et al., 2006; Agius and Lebedev, 2013) span a broader period range than those used in global tomography (e.g., Lebedev and van der Hilst, 2008; Schaeffer and Lebedev, 2013). The advantage of using automated waveform inversion (AMI) for interstation measurements and combining them with those obtained by teleseismic cross-correlation is that the method produces phase velocities for long-period surface waves where the cross-correlation, instead, often fails because of strong interference between body and surface waves. In addition to these, ambient noise cross-correlation (ANCC) yields higher frequency measurements compared to those obtained by TSCC and AMI. Therefore, utilizing these three independent surface wave methodologies, we obtain measurements in a very broad period range (e.g., Fig. 3.5), and are thus able to map the Earth's structure from the shallow crust to the deep upper mantle.

1.2.1 Teleseismic two-station cross-correlation

Surface-wave tomography has suffered a lack of measurements at high frequency for a long time. Source-receiver surface wave dispersion

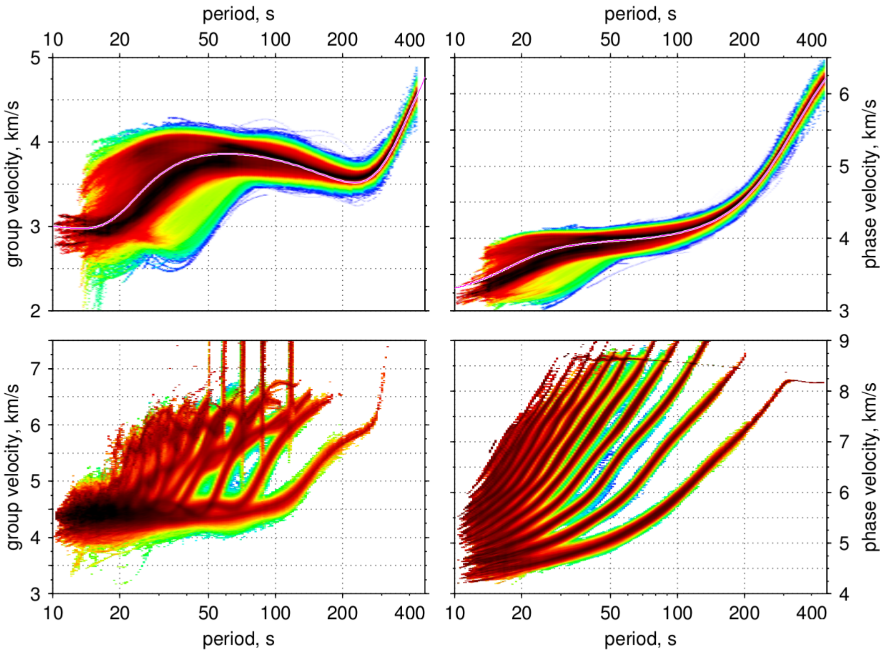

FIGURE 1.3: Empirical distribution of the group (left panel) and phase velocities (right panel) of the fundamental (top) and higher modes (bottom) for Rayleigh waves, plotted logarithmically as a function of period. Surface waves are dispersive; this means that the waves travel at different velocities for different frequencies (figure after Schaeffer (2014)).

measurements are limited at high frequency (frequencies sensitive to shallow structure of the lithosphere) because of scattering of the short-period waves, long-path coverage, uneven distribution of receivers and sources, lack of information on the characteristics of the source. The inter-station cross-correlation allows us to overcome some of these limitations. The measurements are obtained from wave phase differences between the stations, so the phase shifts due to the source mechanism and due to the propagation of the fundamental modes from the source to the stations are eliminated. It is therefore possible to use distant earthquakes to study, at a regional scale, the Earth's structure between the two considered stations.

The classical two-station method was implemented recently (Meier et al., 2004; Soomro et al., 2016) to yield measurements at regional distances (10s to 100s of km) in broader period ranges than previously possible: down to 5 s and shorter periods instead of down to 15–20 s only in previous implementations. Over the last decades, the interstation phase-velocity measurements have been widely used for regional studies (e.g., Meier et al., 2004; Endrun et al., 2008; Lebedev et al., 2006; Darbyshire and Lebedev, 2009; Adam and Lebedev, 2012;

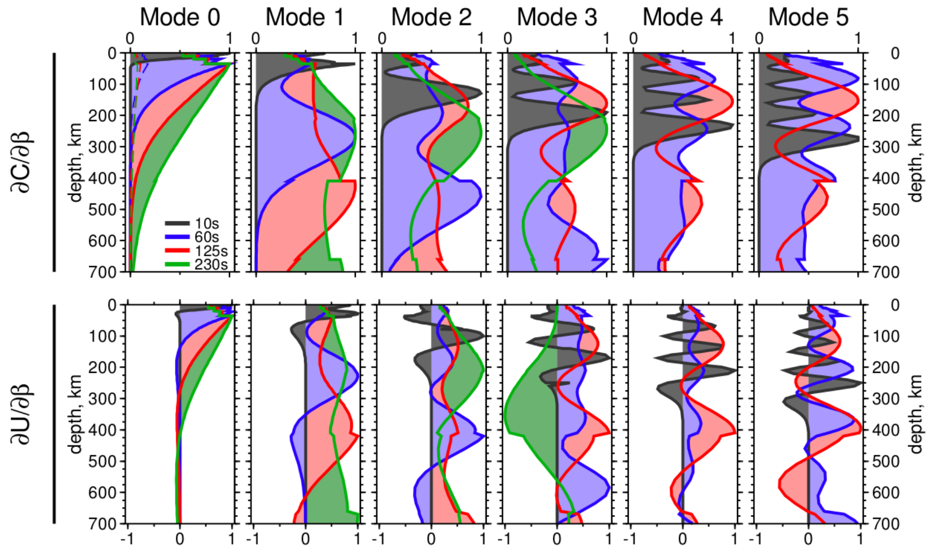

FIGURE 1.4: Depth sensitivity kernels (after Schaeffer (2014)) of Love-wave phase velocities to changes in compressional (α, top panel) and shear (β, bottom panel) velocities for the fundamental and higher modes, computed for AK135 (Kennett et al., 1995).

Agius and Lebedev, 2013; Soomro et al., 2016; Bonadio et al., 2018). The TSCC method can provide phase-velocity measurements in a very broad frequency band, and this band overlaps the measurements obtained by AMI (e.g., Lebedev et al., 2006) and ambient noise interferometry in the intermediate periods band.

Inter-station phase velocities, in the recent implementation of the two-station method (Meier et al., 2004), are computed by analyzing the phase difference of teleseismic surface waves recorded at two different stations, aligned on the great circle path of the considered event. The phase difference is computed using the cross-correlation of the two signals, after elaborate filtering in frequency and time. The frequency is discretized with increasing-length increments (the length of the increments depends on the frequency) (Lebedev et al., 2009), and for each frequency the cross-correlogram is filtered around that specific frequency. The resulting filtered signal is windowed in the time-domain using a Gaussian window centered around the time of the maximum amplitude of the signal itself. The phase measurement is computed in the frequency domain as the arctangent of the ratio of the imaginary to real part of the cross-correlation function (e.g., Udías, 1999; Meier et al., 2004).

This scheme allows to reduce the strong, high-frequency effects of noise and interference between the fundamental mode and higher modes, and other

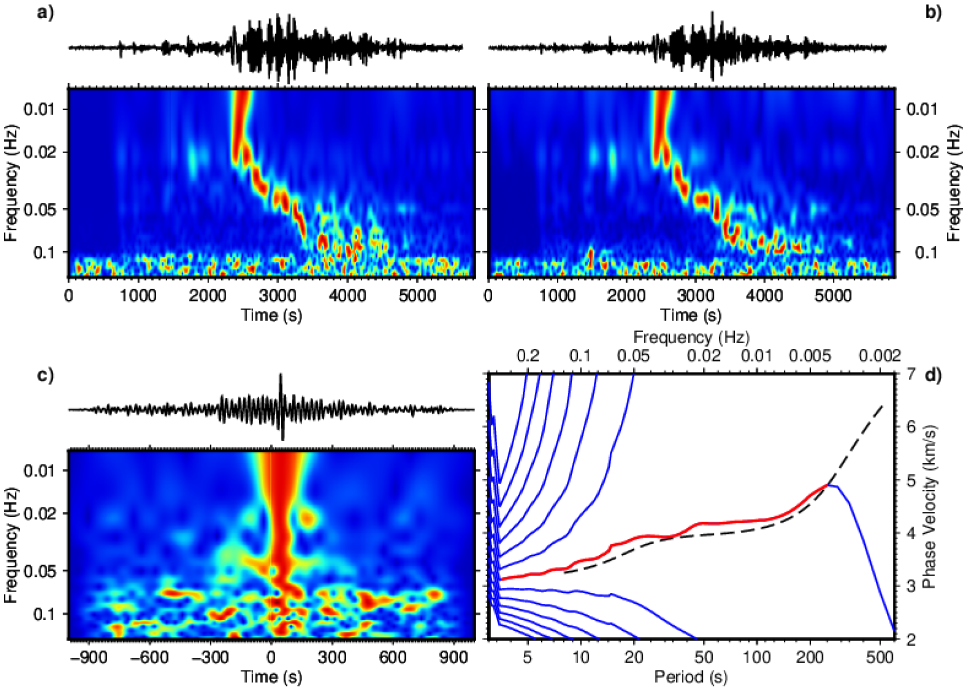

FIGURE 1.5: Phase velocity dispersion can be computed analyzing the phase difference of teleseismic surface waves recorded at two different stations, aligned on the great circle path of the considered event. The figure shows an example of an interstation, Rayleigh-wave, phase-velocity measurement for one station pair. (a and b) The recorded seismograms and the time-frequency representations of their waveforms. (c) The cross-correlation function and its time-frequency representation. (d) Phase-velocity curves (in blue) plotted together with a reference curve (dashed black line) and the accepted segment (in red).

scattered waves. The phase velocity dispersion computed between the two stations can be written as (this formula is valid under the approximation of a spherically symmetric isotropic Earth model (e.g., Snieder and Nolet, 1987; Tromp and Dahlen, 1992)):

$$c(\omega) = \frac{\omega(\Delta_1 - \Delta_2)}{arctan[Im(\phi(\omega))/Re(\phi(\omega))] + 2n\pi} \tag{1.1}$$

where Δ_1 and Δ_2 are the distances between each station and the source, ω is the frequency, ϕ the phase, and c the phase velocity (e.g., Meier et al., 2004). The method is valid for both Love- and Rayleigh-wave dispersion, but for Love measurements the transverse components of the signals have to be used rather than the vertical ones. Fig. 1.5 shows an example of an interstation, Rayleigh-wave, phase velocity measurement for the pair formed by the Irish National Seismic Network (INSN) station IGLA and the Ireland

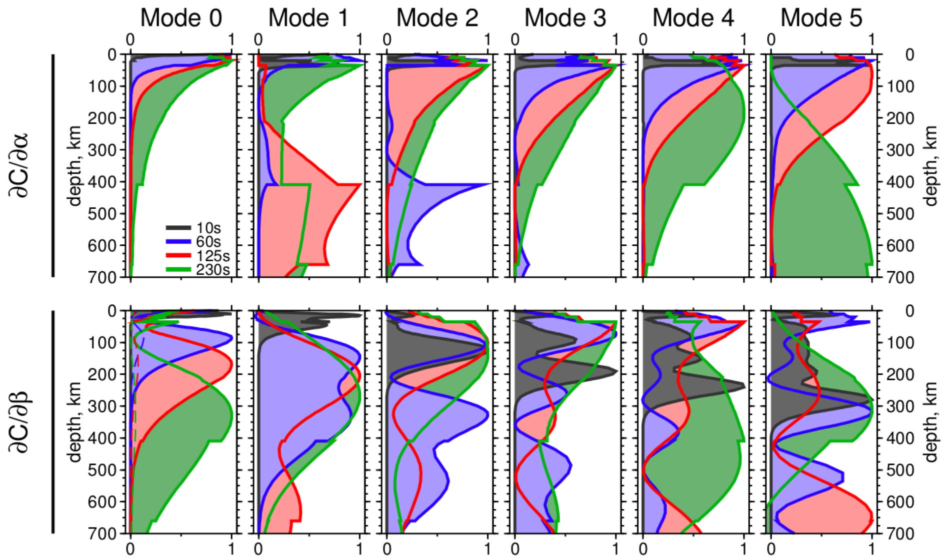

FIGURE 1.6: Depth sensitivity kernels (after Schaeffer (2014)) of Rayleigh-wave phase velocities to changes in compressional (α, top panel) and shear (β, bottom panel) velocities for the fundamental and higher modes, computed for AK135 (Kennett et al., 1995).

Array station IAVAL; both stations are in Ireland, ~174 km away from each other, and recorded a magnitude 7.3 earthquake that occurred on March 9, 2011 at 2.45 a.m., ~100 km east of the coast of Japan, at ~14 km depth. The recorded seismograms and the time-frequency representations of their waveforms are in panels (a) and (b). Panel (c) represents the cross-correlogram and its time-frequency representation. The phase velocity curves extracted from the cross-correlation signal are in panel (d) plotted in blue. To resolve the 2π ambiguity, a reference model needs to be used–in the figure the global model AK135 (Kennett et al., 1995) recomputed at 50 s is drawn (dashed black line). The accepted segment relative to this teleseismic event recorded at the two stations is shown in red. Details on the methodology are given in Sections 2.3.1 and 4.2.2 (see also Figs. 2.4 and 4.3).

The advantage of this method is that measurements are often successful even when the waveforms recorded at each station appear complex. Unfortunately, at longer periods, due to interference between surface and body waves (this is particularly true for Love waves), the TSCC methods often fails to retrieve good quality measurements.

1.2.2 Waveform Inversion

Where the teleseismic cross-correlation method could potentially fail (at long periods), the measurements can also be retrieved using the Automated Multimode Inversion (AMI) (Lebedev et al., 2005). These measurements contribute to the intermediate and long period range and are essential for mapping the deeper lithospheric and asthenospheric structures. AMI is a waveform fitting technique that extracts structural information from S, multiple S, and surface waves. Using synthetic seismograms generated by mode summation in seismogram-dependent time-frequency windows, it also measures phase velocities within the frequency bands constrained by the accurate waveform fits.

Using waveform inversion, it is therefore possible to extract the fundamental mode phase velocity for each source-receiver pair and use a pair of stations to compute the interstation phase velocity, using the relation

$$c_{12} = \frac{\Delta_2 - \Delta_1}{\Delta_2 / c_2 - \Delta_1 / c_1}, \tag{1.2}$$

where c_{12} is the interstation phase velocity, $c_{i=1,2}$ and $\Delta_{i=1,2}$ represents the phase velocity and the distance between the source and each of the two stations, respectively (e.g., Lebedev et al., 2006; Agius and Lebedev, 2014). An example of AMI measurement is in Fig. 1.7.

1.2.3 Ambient noise

Surface wave measurements using teleseismic earthquakes (using TSCC and AMI) allow us to map in detail the seismic structure of both the crust and the mantle (e.g., Meier et al., 2004; Lebedev et al., 2006). The period range of the measurements, however, can be expanded even further, at its short-period end. Recently, a new methodology has been developed and became widely used. It allows us to estimate the surface-wave empirical Green's function between two stations using long-time cross-correlation of ambient seismic noise (e.g., Shapiro et al., 2005; Bensen et al., 2007; Yao et al., 2006; Lin et al., 2007; Lin et al., 2008; Arroucau et al., 2010; Rawlinson et al., 2014; Shapiro and Campillo, 2004; Snieder, 1972; Villaseñor et al., 2007; Tsai, 2009; Tsai, 2010).

Ambient seismic noise is naturally occurring, generated by wind, ocean waves, anthropogenic activities, and scattering caused by the Earth's heterogeneity. Normally, it would be discarded from traditional methods of seismic tomography, and considered unusable due to its non-impulsive nature. However, the ambient noise signal contains, in fact, information on the medium through which the seismic waves that contribute to it propagate;

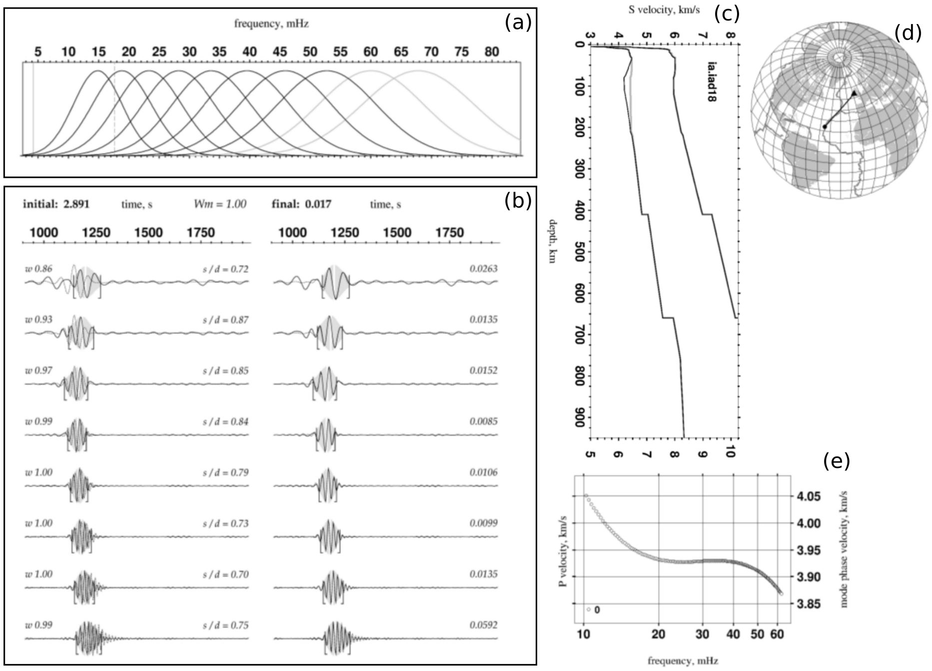

FIGURE 1.7: Example of automated multimode inversion (AMI) (Lebedev et al., 2005) for an earthquake recorded at the Ireland Array station IAD18 in Ireland. Panel (d): Station and event locations and their corresponding great circle path (GCP). Panel (a): Gaussian filters used for filtering of the seismogram. Panel (b): Initial and final fits of filtered waveforms (solid lines) with synthetics (dashed lines) computed from the 1D model in panel (c). The time-frequency windows are indicated by half-brackets and by gray shading of the signal envelope. White vertical lines represent the maxima of the envelope for the fundamental mode wave packets. Panel (e): final phase velocity dispersion curve for the fundamental mode extracted from the solution.

this information can be extracted in order to make inferences on the seismic properties of a region. The surface wave dispersion between station pairs is estimated by cross-correlating long time-sequences of ambient noise recorded simultaneously at the considered pairs of stations (e.g., Fig. 1.8).

Both group and phase velocities provide structural information. We use phase velocity measurements, which are preferred over group velocity for a variety of reasons (picking of phase velocity is more precise than the group velocity; phase velocity can image structure over a wider and deeper depth range than group velocity, and it is less likely to be affected by interference of other phases) (e.g., Boschi et al., 2013). Ambient noise interferometry contributes to the high and intermediate frequencies, making it possible to image the very shallow crust.

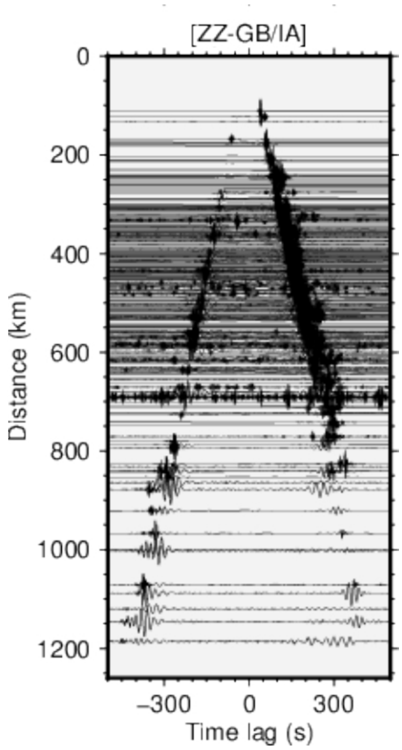

FIGURE 1.8: An example of the emergence of the Green's function from the cross correlation of vertical components of signals recorded at stations in Ireland and Britain.

1.3 Outline

In this thesis, the three methods described above are used to investigate the seismic structure of Ireland and Britain, as well as the Tristan da Cunha hotspot in the South Atlantic. Both areas present important, first-order questions, relating, in particular, to the existence of a mantle plume as the cause of intraplate volcanism at present (for the Tristan da Cunha Hotspot) and to the mechanisms of the uplift and intraplate volcanism in the past (for the British Isles region). The two regions presented some important challenges: for the Tristan da Cunha Hotspot, the noisy ocean-bottom seismometers data (if compared to land-based stations) required us to intensively test and finely tune the data-processing and measurement methods. For the tomography of the British Isle region it was necessary to develop a new, multi-resolution tomographic scheme, to extract the maximum information from the very large new dataset, in the presence of uneven data sampling and errors in the data.

In Chapters 2 and 3 we present seismic tomography of Ireland's and Britain's crust and upper mantle, using a large, new, surface-wave data set, from cross-correlation of teleseismic surface waves, waveform fitting, and ambient noise. The three independent techniques yield complementary frequency bands of the measurements, with sensitivities to different depths. The abundant, combined measurements and the use of finely tuned, automated techniques provided unprecedentedly dense coverage of the region, making it possible to improve substantially the resolution of the lithosphere of Ireland and its surroundings, compared to previous models. In order to address the unevenness of the coverage and the effects of errors on the final model, we developed a new, multi-resolution tomographic scheme in which the final model is built with an optimal resolution at each knot of the model grid, minimizing the effects of uneven data sampling and of the propagation of systematic errors, which are resistant to data redundancy and can cause tomographic models to be dominated by noise if the target resolution is too high.

In Chapter 4 we investigate the seismic structure of the lithosphere and asthenosphere beneath the Tristan da Cunha region in the South Atlantic Ocean. We used measured phase-velocity curves of Rayleigh waves using cross-correlation of teleseismic seismograms from an array of ocean-bottom seismometers deployed around the hotspot, to determine the shear-velocity structure beneath the area. Shear velocities are the best available constraints on a variety of geodynamic parameters, including temperature, composition, and melt fraction. We used our results to infer the temperature of the lithosphere and asthenosphere beneath Tristan. The temperature is anomalously high, and this is consistent with a hot mantle plume reaching Tristan from below and causing the unusual, long-lived volcanism at this location. The ocean-bottom data set presented some challenges, which required data-processing and measurement approaches different from those tuned for land-based arrays of stations.

Appendices A to C are appendices to Chapters 2 to 4, respectively. They contain some additional supporting material for the main chapters.

Appendix D contains a collection of co-authored works (see also "Statement of co-authorship" on page iv for details).

Appendix D.1 is a published peer-reviewed paper in which I am second author. It is about an education and public engagement project that followed the SEA-SEIS North Atlantic Expedition (Lebedev et al., 2019). I have managed the production of digital content for outreach and public engagement, and I have contributed to the organization and scientific planning of the SEA-SEIS Expedition, as well as the logistics.

Appendix D.2 is a published peer-reviewed paper in which I am second author (Carvalho et al., 2019). I have contributed to the data processing, software implementation, generation and interpretation of the models, analysis, and editing of the manuscript.

Appendix D.3 is a published peer-reviewed paper (Moretti et al., 2016) in which I am a co-author. I have contributed to the testing of part of the seismic stations and their deployment, and taken care of the logistics in Central Italy after the August 2016 Central Italy earthquake.

Chapter 2

Optimal resolution tomography with error tracking: Lithospheric thinning beneath the British Tertiary Igneous Province and other new observations

2.1 Summary

We present an optimal resolution seismic tomography of Ireland's and Britain's crust and upper mantle, using a large, new, surface-wave data set. Fundamental mode Rayleigh phase velocities, measured from a large number of broadband, land seismic stations across the region (Fig. 2.1), were used to constrain the seismic structure and produce the first 3D shear-velocity model of the lithosphere and the asthenosphere of the area. The use of abundant, recently collected new data and the use of finely tuned, automated techniques provided unprecedentedly dense coverage of the region (Fig. 2.2) making it possible to improve substantially the resolution of the lithosphere of Ireland and its surroundings, compared to previous models (e.g., Polat et al., 2012) (Fig. 2.35). We applied two independent surface-wave analysis techniques, cross-correlation of teleseismic surface waves, and multimode waveform fitting, yielding complementary frequency bands of the measurements, with sensitivities to different depths. The combined two-station dispersion measurements, measured over a broad period range (from ~4 to 500 s), were inverted for phase-velocity maps at different periods using multi-resolution tomography. The maps were then inverted, point by point, for shear-velocity (V_S) structure to produce a state-of-the-art, 3D, seismic model of the lithosphere and asthenosphere beneath the region.

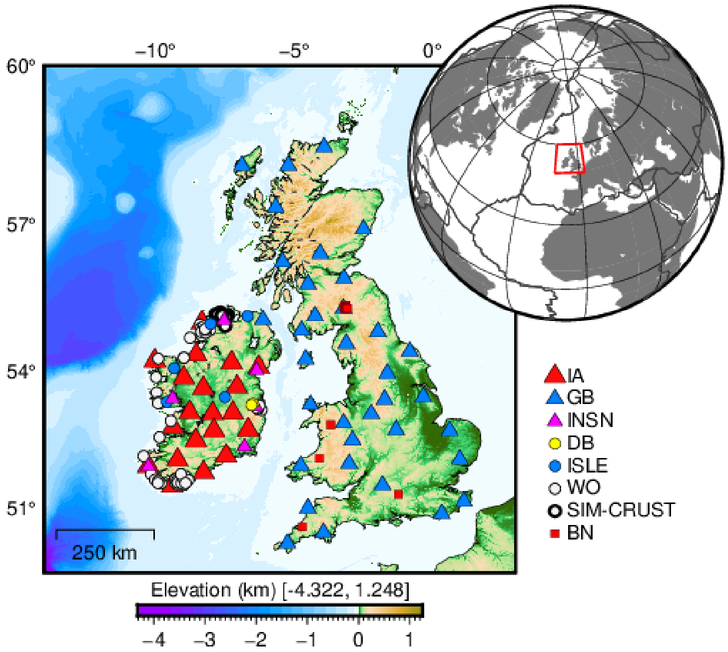

FIGURE 2.1: The investigated region comprises Ireland, Britain and the Irish Sea. The area presents considerable geophysical interest, especially because of a hypothetical interaction between the Proto-Iceland mantle plume and the lithosphere of the area during the Tertiary opening (~60 M.a.) of the North Atlantic which has been long discussed with diverging conclusions (e.g., Al-Kindi et al., 2003; Landes et al., 2007; Jones et al., 2002; Arrowsmith et al., 2005; Rickers et al., 2013; Cogné et al., 2016; Tiley et al., 2004; Davis et al., 2012). The seismic stations used in this study are shown in the legend on the bottom right. *IA*: Ireland Array network (Lebedev et al., 2012); *INSN*: permanent stations of the Irish National Seismic Network; *BGS*, *BN*: permanent and temporary stations of the British Geological Survey; *WO*: temporary stations belonging to the University College Dublin WaveOBS network; *ISLE*: temporary deployments from ISUME and ISLE projects (O'Donnell et al., 2011; Polat et al., 2012; Landes et al., 2004; Landes et al., 2007; Wawerzinek et al., 2008). Topography and bathymetry are from the GEBCO dataset (IOC et al., 2003).

The highly uneven station coverage in the Ireland-Britain region results in a substantially irregular distribution of the measurements in the area (Fig. 2.2). The uneven sampling and the presence of both random and systematic errors in the data results in imaging artifacts if the target resolution of the imaging is too high for the parts of the region that have insufficient data sampling or are particularly affected by errors. In order to address the unevenness of the coverage and the effects of errors on the final model, we developed a new, multi-resolution tomographic scheme. The target resolution at each knot of the model grid is determined so that the errors of the phase-velocity curve,

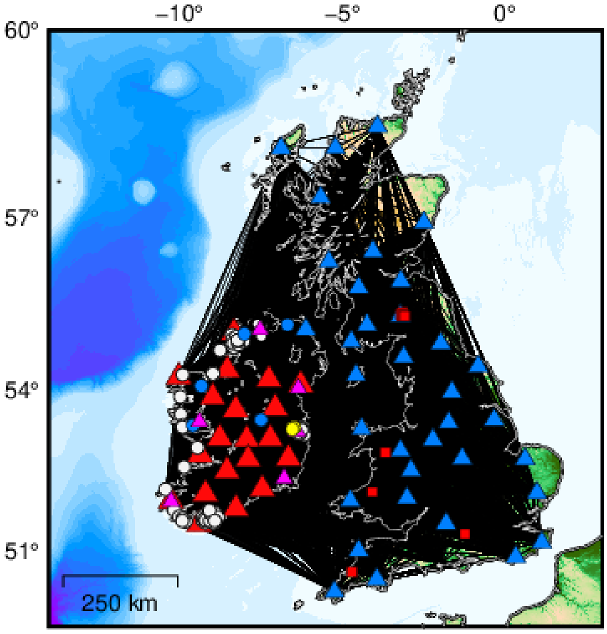

FIGURE 2.2: Station locations (as in the legend in Fig. 2.1) and interstation path coverage (black lines) yielded by our measurements. The coverage in Ireland is higher than Britain, due to data availability.

extracted from phase-velocity maps at this point, do not exceed an empirical threshold.

This scheme minimizes the effects of uneven data sampling and of the propagation of systematic errors, which are resistant to data redundancy and can cause tomographic models to be dominated by noise if the target resolution is too high.

We first measure inter-station phase-velocities at simultaneously recording station pairs (Section 2.3) and compute phase-velocity maps at densely, logarithmically spaced periods (Section 2.4). Unlike in the classical approach, multiple versions of the maps with varying smoothness constraints are computed, so that the maps range from very rough to very smooth. Phase-velocity curves extracted from the maps at every point can then be inverted for shear-velocity (V_S) profiles. Very smooth V_S models computed from very smooth phase-velocity maps will be the most robust, but at a cost of a loss of most structural information. At the other extreme, models that are too rough will be dominated by noise. We define the optimal resolution at a point such that the error of the local phase-velocity curve is below an empirical threshold. The error is estimated by isolating the roughness of the phase-velocity curve that cannot be explained by any Earth structure. A 3D V_S model is then computed by the inversion of the phase-velocity maps with the optimal resolution at every point (e.g., Figs. 2.14 and 2.15).

2.2 Introduction

The problem of unevenness of the data coverage, due to limited and irregular geographical distribution of sources and receivers, is a well known issue often encountered in global and regional tomography (Rawlinson et al., 2010; Sambridge and Rawlinson, 2005). Several methods have been implemented in tomographic studies in order to address this issue, since the pioneering works of Chou and Booker (1979) and Tarantola and Nercessian (1984). Most of these methods include the use of irregular parameterizations, aiming to place the nodes of the grid only where they are required by the data, and of adaptive regularization, where the inversion process adapts the parameters of the inversion itself to the constraints supplied by the data (e.g., Debayle and Sambridge, 2004; Fukao et al., 1992; Sambridge et al., 1995; van der Hilst et al., 1997; Bijwaard et al., 1998; Bijwaard and Spakman, 2000; Kárason and van der Hilst, 2001; Zhao, 2004; Michelini, 1995; Asencio et al., 1997; Sambridge and Faletič, 2003). The advantage of an irregular parameterization over a uniform one is that the information extracted from the data can be maximized without introducing artifacts or smoothing-out potential details. The study region can be parameterized using higher resolution grids in particular areas of the model (with nested cells where the sampling is greater) or denser regular grid embedded into a sparser global grid. The optimal grid density is thus chosen according to the resolving power of data at different areas. More recently, statistical approaches in Bayesian frameworks have been developed, which use dynamic parameterization and do not require explicit regularization (e.g., Bodin and Sambridge, 2009; Bodin et al., 2012; Galetti et al., 2016; Piana Agostinetti and Malinverno, 2010; Piana Agostinetti et al., 2015; Hawkins et al., 2019).

However, the maximum achievable resolution of a tomographic model varies spatially and depends not only on the azimuthal data coverage but also on the errors in the data. Adaptive parameterization schemes proposed previously can match the spatial variations in data sampling but do not address the effects of the errors. Here, we propose a surface-wave tomography method (Section 2.4) that finds optimal lateral resolution at every point by means of error tracking. We achieve the optimal target resolution at a point by finding an optimal regularization of phase-velocity tomography at the point, expressed primarily in terms of smoothing, at each knot of the model grid.

Improved knowledge of the seismic structure of the lithosphere and asthenosphere beneath the British Isles is required to understand the structure and evolution of the area and the mechanisms of its enigmatic Paleogene intraplate volcanism. Our present understanding of the seismic structure of the crust below the British Isles is mostly from active source seismic refraction and reflection experiments and related works (e.g., Bamford et al., 1978; Barton, 1992; Edwards and Blundell, 1984; Maguire et al., 2011; Bott et al., 1985; Jacob et al., 1985; Kelly et al., 2007; Jacob et al., 1985; Lowe and Jacob, 1989; Landes et al., 2000; Masson et al., 1998; Hodgson, 2001; Freeman et al., 1988; Snyder and Flack, 1990; Klemperer and Hobbs, 1991; Klemperer et al., 1991; O'Reilly et al., 1996; O'Reilly et al., 2010; O'Reilly et al., 2012). The results from the many active-source experiments have been compiled to obtain Moho maps, often combining results from active- and passive-source seismology (e.g., Licciardi et al., 2014; Chadwick and Pharaoh, 1998; Landes et al., 2005; Kelly et al., 2007; Davis et al., 2012; Di Leo et al., 2009; Asencio et al., 2003). More recently, the crust and mantle beneath the British Isles have been investigated using passive-source seismology, including teleseismic body wave tomography (e.g., Arrowsmith et al., 2005), local earthquake tomography (e.g., Hardwick, 2008), teleseismic receiver functions (e.g., Tomlinson et al., 2006; Davis et al., 2012), travel-time analysis (e.g., Masson et al., 1999), shear wave splitting measurements (e.g., Do et al., 2006; Bastow et al., 2007), surface-wave tomography (e.g., Polat et al., 2012), receiver functions (e.g., Landes et al., 2007; Davis et al., 2012; Shaw Champion et al., 2006; Licciardi et al., 2014), as well as magnetotellurics, gravity, and petrophysical approaches (e.g., Fullea et al., 2014; Jones et al., 2013; Rao et al., 2007; Readman et al., 1997; Brown and Whelan, 1955; Mather et al., 2018; Mather and Fullea, 2019; Baykiev et al., 2018).

Only a few studies used surface wave tomography to image the British Isles (e.g., Polat et al., 2012; Nicolson et al., 2012; Nicolson et al., 2014; Galetti et al., 2016), all of them focussing only on smaller subregions. Furthermore, the British Isles, located at the western extremity of the Eurasian Plate, are often not included in continent-scale tomographic models or, when included, are at the edge of the model, imaged with relatively low resolution (e.g., Marquering and Snieder, 1996; Fry et al., 2008; Schivardi and Morelli, 2009; Soomro et al., 2016). This is particularly true for Ireland, featuring poor broadband-station coverage until recently.

2.3 Data and Measurements

In this work we have used abundant, newly available data and obtained phase velocity measurements in a very broad frequency range (~4 to 500 s), so that we can image the entire region at a new level of detail. We use phase velocity measurements, which are more accurate than group-velocity ones (e.g., Nicolson et al., 2012; Boschi et al., 2013; Galetti et al., 2016) and can be expected to yield more accurate maps (e.g., Dahlen and Zhou, 2006). The phase velocity dispersion curves were obtained for ~11230 two-station paths across the area using a recent implementation of the two-station method and data from teleseismic earthquakes.

We use the two-station method (e.g., Meier et al., 2004; Soomro et al., 2016) to investigate the fundamental mode, Rayleigh-wave dispersion by cross-correlation of seismograms recorded at pairs of stations. These measurements are complemented with phase velocities computed for station pairs by waveform inversion (AMI, Automated Multimode Inversion) (Lebedev et al., 2005), which simultaneously fits S, multiple S and surface waves, using synthetic seismograms generated by mode summation (Fig. 2.3). The interstation dispersion measurements retrieved with the two methods (Fig. 2.3) are combined together to constrain the regional 2-D variations in phase velocity across the study region, performing an inversion for anisotropic phase-velocity maps (Figs. 2.14 and 2.15). Anisotropy in the area also contributes to better understanding the seismic structure of the sub-surface (e.g., Polat et al., 2012), and would provide insights for crustal accretion and evolution of the area within the Caledonian Orogeny. In this work we interpret the isotropic and anisotropic components of the maps (Figs. 2.23 to 2.25).

The waveform data used in this work come from permanent and temporary arrays in Ireland and Britain, with data covering a period of time from 1981 to 2018: the Ireland Array network (*IA*) (Lebedev et al. (2012)), permanent stations of the Irish National Seismic Network (*INSN*) and the British Geological Survey (*BGS*), temporary stations belonging to the University College Dublin WaveOBS network (*WO*) and the BGS (*BN*), and additional stations from ISUME project (O'Donnell et al., 2011; Polat et al., 2012) and ISLE experiment (*ISLE*) (Landes et al., 2004; Landes et al., 2007; Wawerzinek et al., 2008). We included all available broadband stations, which results in unprecedented data coverage of the region (Fig. 2.2).

The data went through automated quality checks and preprocessing (the integrity of the data was assured by removing all the data that were incomplete, clipped, had gaps and/or incorrect timing). The seismograms are converted to displacement after removal of the instrument response, rotated, and down-sampled to 1 Hz.

2.3.1 Teleseismic two-station cross-correlation

For each available station pair, we searched the Global Centroid Moment Tensor catalogue (Dziewonski et al., 1981; Ekström et al., 2012) for teleseismic

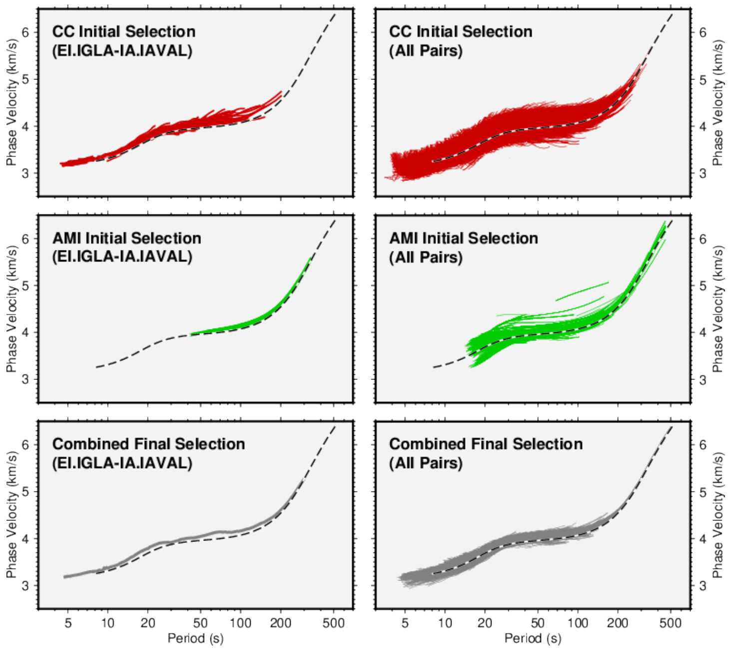

FIGURE 2.3: In this work two independent, complementary surface-wave analysis techniques are applied–cross-correlation (CC) of teleseismic surface waves (in the top panel), and multimode waveform fitting (AMI) (central panel). They provide a very large number of broadband measurements of Rayleigh surface-wave fundamental mode phase velocities. The two methods yield to complementary frequency bands of the measurements, with sensitivities to different depths. The figure shows successfully selected one-event two-station dispersion measurements from cross-correlation of teleseismic earthquakes for all analyzed station pairs on the right and for the pair EI.IGLA–IA.IAVAL on the left. Middle panel: one-event dispersion measurements from waveform inversion (AMI) of teleseismic earthquakes. Bottom panel: combined final selection of average phase velocity measurements from cross-correlation and waveform inversion. Only the measurements that passed the severe selection criteria (e.g., Soomro et al., 2016) are used for the successive tomographic inversion.

events within the operating time period of the two stations and with a chosen back-azimuth range of ±5° from the station-station great circle path (GCP). Events with a moment magnitude greater than 4.9 were chosen, using a distance-dependent magnitude threshold as described in Schaeffer and Lebedev (2013). Only Rayleigh wave data from the vertical component are used for the measurements in this work; Love wave measurements will be incorporated in a future work.

The use of the two-station method (as introduced by Sato (1955)) in surface wave analysis allows us to compute phase velocity dispersion of the surface waves which travel, ideally, along the GCP between a given pair of stations. It is possible to make a regional investigation using far-field teleseismic earthquakes, since the phase effects of the source (earthquake) and the common path between the source and the receivers (stations) are cancelled out (e.g., Meier et al., 2004; Soomro et al., 2016). In practise, the incoming energy for a certain given earthquake does not lie exactly on the GCP, so we need to allow a certain tolerance for the alignment between the earthquake and the pair of stations. This tolerance is often determined by the availability and quality of the data (in this paper a tolerance of $\pm 5^\circ$ is chosen, due to high availability of recordings and relatively high signal-to-noise; such a selective choice of data is allowed by the enormous quantity of available waveforms, as opposed to other works in which the tolerance has to be bigger, due to a smaller quantity of available data and lower signal-to-noise recordings (e.g., Bonadio et al., 2018)). Although the tolerance around the ideal GCP of the station-station/event alignment is very small, one may argue that the misalignment may have a non-negligible effect on the accuracy of the calculated phase velocity; however, the imperfect alignment of the two stations and the event has no immediate effect on the measurement accuracy because the phase velocities are computed from the phase of the cross-correlation function and the difference between the distances from the event to each of the stations, rather than the interstation distance between the two-stations (e.g., Soomro et al., 2016).

In this work we use an implementation of the two-station method by Meier et al. (2004). The automated selection is adapted for our particular dataset from Soomro et al. (2016). For each teleseismic event the vertical components of the seismographs recorded at the two stations are cross-correlated; the cross-correlation signal is then filtered using a frequency-dependent Gaussian band-pass filter, to minimize the effect of noise and interferences on the fundamental mode. The resulting signal is then weighted in the time domain to reduce the effects of scattering or higher modes. The phase velocity is computed from the resulting signal in the Fourier domain as the arctangent of the ratio of the imaginary to real part of the Fourier spectrum. This approach works best if the fundamental mode is preeminent compared to any other type of signal/noise. The roughness of the resulting curve is determined by the amplitude of the fundamental mode content, the signal-to-noise ratio, diffraction, and the interferences of Rayleigh and Love waves, and higher modes. The smaller the contribution of the diffraction and the interferences with regard to the fundamental mode are, the smoothest the dispersion curve is. To minimize the effect of the irregularities in the curves on the final average measurements we only accept smooth portions of phase-velocity curves. The approach used within the automatic selection framework allows us to select only smooth dispersion curves, excluding the outlier measurements, and only accepting curves not unreasonably, unrealistically far from a previously calculated reference dispersion curve (how the reference curves used in this work are retrieved is discussed in Section 2.3.3). The length of the selected segments (we avoid very short segments) and the minimum number of measurements for each frequency (at least 10 measurements for each frequency) were also criteria used to select the optimal dispersion curves. Both these criteria are frequency-dependent. Measurements have been also carefully analyzed for systematic inconsistency between measurements from events at opposite directions from the station pair. We needed to be definitely sure of not introducing this inconsistency in the data, as this effect could indicate instrumental errors (station timing or instrument response) or strong diffraction effects.

We only used interstation distances greater than 1 km, in the area delimited as in Fig. 2.1. For each station pair we computed an average over a very large number of one-event measurements, made using recordings of earthquakes in different source regions, with different directions from the station pair. Doing so we reduce the effect of wave diffraction and interferences between fundamental and higher modes, obtaining robust measurements in very broad period ranges. The automatic selection just described applies to measurements obtained from two-station cross-correlation (CC) and automated multimode inversion (AMI) (see Section 2.3.2).

2.3.2 Integrating measurements from waveform inversion

We use Automated Multimode Inversion of surface and S-wave forms (e.g., Lebedev et al., 2005; Schaeffer and Lebedev, 2013) to complement our phase velocity measurements for intermediate and long periods. The AMI method simultaneously fits S, multiple S and surface waves for each teleseismic event, using synthetic seismograms generated by mode summation in seismogram-dependent time-frequency windows. As a by-product of waveform inversion, it measures phase velocities within the frequency bands constrained by this particular waveform fit. For each source-receiver pair we extracted the fundamental-mode phase velocity and used pairs of stations to calculate the interstation phase velocity (as for the two-station cross-correlation, we accepted a ±5° tolerance for source-station/source-station azimuth difference) using the relation

$$c_{12} = \frac{\Delta_2 - \Delta_1}{\Delta_2/c_2 - \Delta_1/c_1}, \tag{2.1}$$

where $c_{i=1,2}$ and $\Delta_{i=1,2}$ represents the phase velocity and the distance between the source and each of the two stations, respectively, and c_{12} is the interstation phase velocity (e.g., Lebedev et al., 2006; Agius and Lebedev, 2014).

The advantage of using AMI for interstation measurements and combining them with those obtained by cross-correlation is that the method produces phase velocities of long-period surface waves where the cross-correlation often fails because of strong interference between surface and body waves.

We computed, with these methods, a large number of phase-velocity, inter-station curves in a period range of ~4 – 500 s (Fig. 2.3). The measurements generated by independent techniques, with cross-correlation of teleseismic events contributing for a broad short/intermediate period range and waveform inversion for intermediate/long periods, show consistency where they overlap. The curves from cross-correlation (CC) and AMI, independently computed, are then averaged all together as described in Section 2.3.1. The final results, used for generating the velocity maps (see Section 2.4 for details), are illustrated in Fig. 2.3.

2.3.3 Choice of the Reference Model

A $\pm 2\pi$ ambiguity arises when phase velocities are computed from the cross-correlation function (e.g., Meier et al., 2004; Soomro et al., 2016; Bonadio et al., 2018). We need a reference model to discriminate the curves that represent the true Earth structure from the ones that are a result of a trigonometric ambiguity.

For longer periods, identifying the correct dispersion curve is normally straightforward. For example, in Fig. 2.4 it would not be difficult to discriminate the correct curve (drawn in red in panel (d)) at around 100 s, from the other ones (drawn in blue) which are clearly unreasonable to describe any Earth structure at that depth, according to the phase-velocity sensitivity functions (e.g., Schaeffer and Lebedev, 2013). The ambiguity occurs, instead, at higher frequencies where the choice of the correct curve is not trivial, with the curves close to each other. Depending on the distance between the stations, the parameters used for the frequency/time filters, the signal-to-noise ratio, the continuity of the curve, and other factors, the detection of the correct curve can become an issue.

Using an a priori reference model is thus important for the measurement of the phase velocity curve, and the reference model must be close to the actual surface-wave dispersion in the investigated area. It would not be a correct approach, e.g., to use a global reference model (e.g., AK135 (Kennett et al., 1995) or PREM (Dziewonski and Anderson, 1981)) if the investigated area presents substantially different phase dispersion than these models.

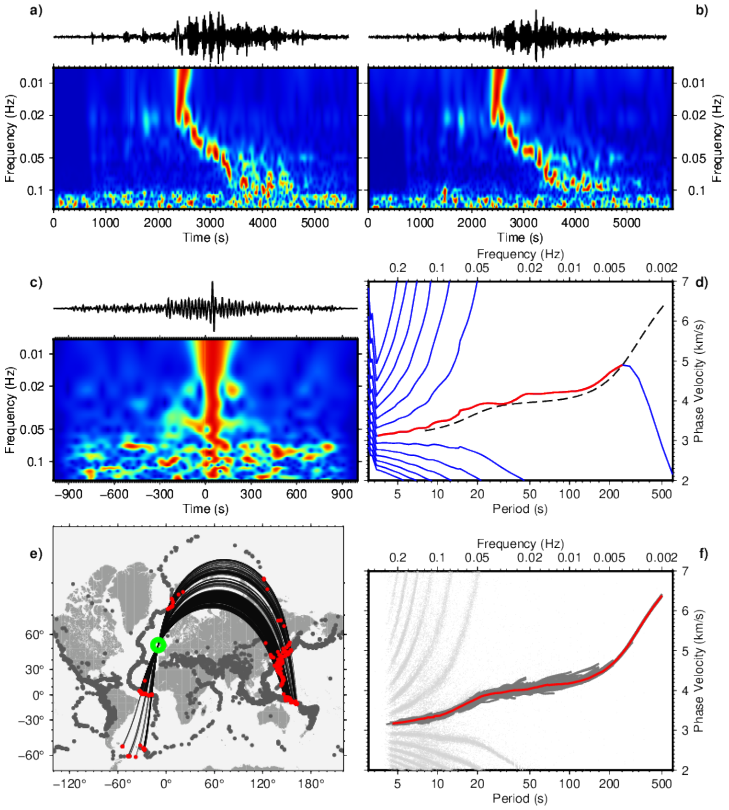

FIGURE 2.4: Example of an interstation, Rayleigh-wave, phase velocity measurement for the station pair EI.IGLA–IA.IAVAL (both stations are in Ireland) (see Section 2.3). Panels (a) and (b) show the recorded seismograms and the time-frequency representations of their waveforms. Panel (c) represents the cross-correlation signal and its time-frequency representation. In panel (d) we find the phase velocity curves extracted from the arctangent of the ratio of the imaginary to real part of the Fourier spectrum of the cross-correlation signal Section 2.3.1. In blue are drawn all the alternative curves resulting from the 2π ambiguity, plotted together with the global model AK135 (Kennett et al., 1995) recomputed at 50 s (dashed black line). The accepted segment is shown in red. Panel (e) shows the distribution of all events used in this work (in gray), the ones used for this pair of stations (in red) and the GCP between these and the pair of station (locations of the two stations are within the green circle). In panel (f) we plot the set of accepted measurements for the current pair (shown in dark gray) and the final average measurement (in red) for the actual pair, produced from teleseismic two-station cross-correlation and waveform inversion. The pale gray dots illustrate the 2π ambiguity (see Section 2.3.1). Station EI.IGLA has coordinates 53.420N, 9.380W, is 84.923° distant from the event, with back azimuth 21.558°. Station IA.IAVAL has coordinates 51.939N,10.244W, is 86.493° distant from the event, with back azimuth 20.865°. The event (magnitude 7.323) is located at 38.560N, 142.780E, at a depth of 14.1 km. The interstation distance, computed as the difference between the source-receiver distances, is 174.631 km.

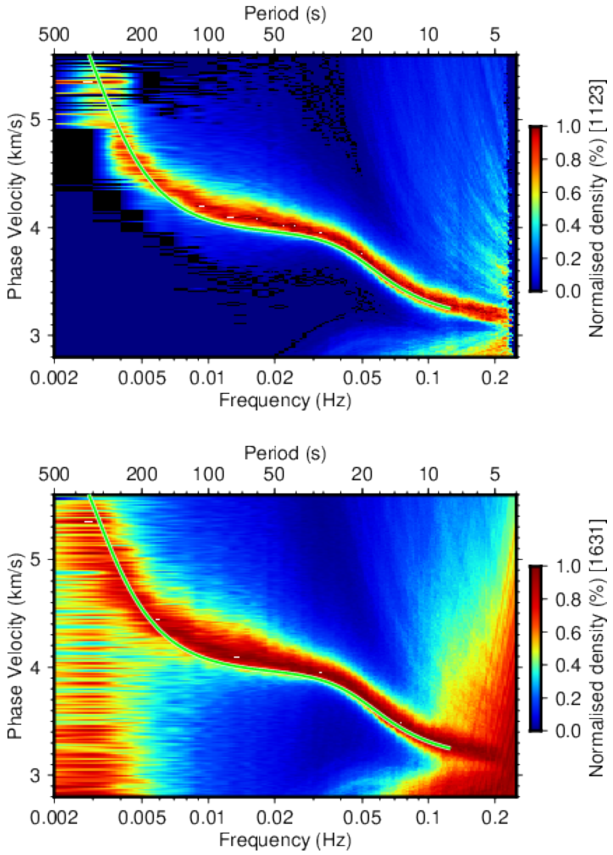

FIGURE 2.5: The density plot for the stack of all possible measurements in the region (bottom panel), normalized to the maximum at each frequency, shows a clear region average dispersion (see Section 2.3.3). The stack is computed using all branches of possible phase velocity curves, including those affected by the 2π ambiguity, for all pairs of stations. The branches that do not represent the real sub-surface structure are canceled out by the stacking procedure. The regional distribution of measurements is substantially different from the global reference model AK135 (Kennett et al., 1995), plotted in green. Top panel: density plot for the stack of selected measurements in the region, normalized to the maximum at each frequency. The stack, obtained from a loose selection of preliminary measurements (as explained in Section 2.3.3), shows a consistent improvement compared to the stack obtained from all measurements (bottom panel), and it represents a more suitable reference model for the one-by-one phase dispersion measurement selection.

We have computed a reference model using the method of Bonadio et al. (2018), which provides a fully data-based initial reference curve for the area. Stacking together all possible phase velocity curves derived from cross-correlations for the entire set of station pairs, without any selection applied, we produce a density plot as in the bottom panel in Fig. 2.5. Applying a loose selection on the data (such that for each measurement we only plot the curve closest to AK135 model in a certain frequency range, 0.02 – 0.05 Hz for this work) we can improve substantially the density plot (e.g., top panel in Fig. 2.5) and obtain an average phase velocity curve for the region that can be used as reference for the final, more precise one-by-one event measurements. The reference curve is obtained from the maximum values of the density distribution and then smoothed by means of a very weakly regularized inversion for a shear-velocity profile (the inversion for shear velocity is discussed in Section 2.5.2, which provides details on the non-linear Levenberg-Marquardt gradient search inversion algorithm used). The density plot of stacked measurements for the entire area (Fig. 2.5) displays clearly the basic properties of the phase-velocity curve, which in this case appears to be not too different from that computed for AK135 (Kennett et al., 1995) (plotted in green in the figure).

Provided that a large number of measurements is contributing to the stack, one could analyze parts of the data for different sub-areas, which could provide different reference curves if the investigation area presents strong heterogeneity. In this work we have used five sub-areas, which provided averages relatively similar to each other (the relatively small heterogeneity in the area could be observed in Fig. 2.6, or with more detail in the velocity maps in Figs. 2.14 and 2.15). The average obtained from this stacking procedure is, importantly, not to be trusted as the curve representing the real Earth structure, because also diffraction, scattered waves and interference between fundamental and higher modes, and high frequency noise are contributing to the stack. Errors in the curve due to these effects are reduced by our strict measurement selection, described in Section 2.3.1.

We have obtained density distribution plots of stacked phase velocity measurements for the 5 different sub-areas, but the difference between the stacked references did not justify the use of different reference models for the investigated area (ideally one must use different reference curves if the investigated area comprises tectonic settings very different from each other, such that the stacked phase velocity dispersion density plot shows strong heterogeneity, especially true for higher frequencies).

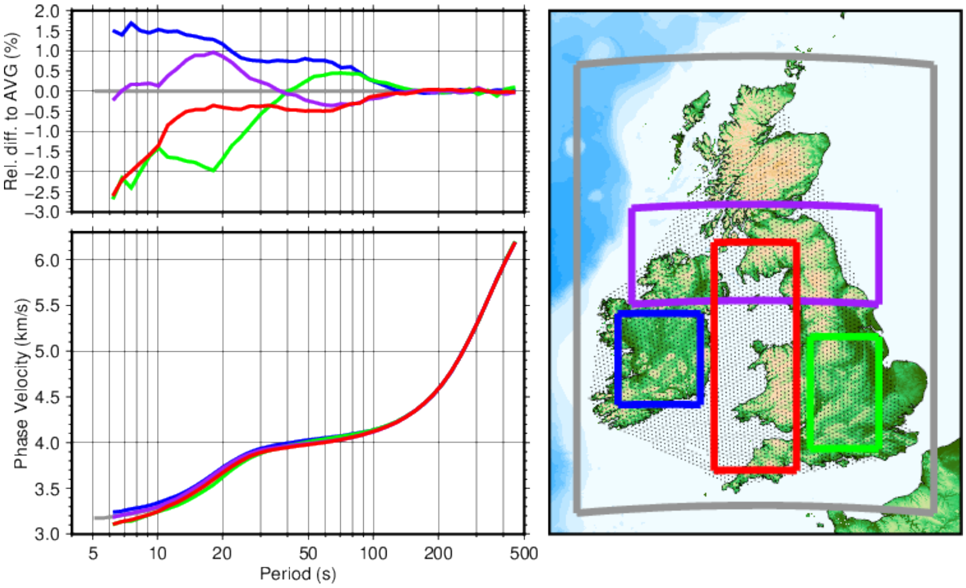

FIGURE 2.6: The investigated area shows a considerable heterogeneity in the lithosphere, which vanishes smoothly in the asthenosphere. The figure shows a comparison of average phase velocity curves for different sub-regions (gray for the entire area; red, green, blue, and purple for sub-regions of the investigation areas, as drawn). Most noticeable are the high velocity anomaly of the blue area (Ireland), and the persistent low velocity anomaly in the red area (representing mostly the Irish Sea). Bottom left panel: average phase velocity curves of the regions represented with different colors , as indicated in the right panel. The gray curve represents the average of all obtained measurements. The black dots on the map represent the knots of the grid. Top left panel: relative difference in percentage of the average phase velocities for each sub-area, expressed with respect to the average of the entire area (drawn in gray).

2.4 Optimal resolution surface wave Rayleigh tomography with error tracking

2.4.1 Irregular data sampling and systematic errors distribution

In a tomographic problem, resolution relates to data sampling, but this relation is strongly complicated by noise. If the dataset is dominated by systematic errors, for example, then increasing the number of measurements or using a finer grid would not lead, in general, to better results. Our challenge is to identify errors and target the highest possible resolution while making sure the model is not significantly affected by noise. The tomographic scheme we develop here allows us to obtain an optimal target resolution of the model at each knot, maximizing the information extracted from the data, without over-or down-fitting parts of the model due to irregular distribution of information or systematic errors. The target resolution is defined by the strength of the lateral smoothing over knots of a quasi-uniform triangular grid. As we show, the resolution of the model is not always higher where data sampling is higher. It also depends on the noise.

2.4.2 Description of the approach

We invert phase-velocity curves from all interstation pairs for phase-velocity maps using a least-squares technique (LSQR) with smoothing and slight norm damping (e.g., Paige and Saunders, 1987; Lebedev and van der Hilst, 2008; Darbyshire and Lebedev, 2009; Lebedev and Van Der Hilst, 2008; Deschamps et al., 2008). The maps are parameterized using a triangular grid with a 10 km spacing. The five parameters at each grid knot include the isotropic-average anomaly and four anisotropic coefficients, two for π-periodic and two for $\pi/2$-periodic variations with azimuth (e.g., Smith and Dahlen, 1973; Deschamps et al., 2008). The inversion solves the system of equations yielded by all the path measurements at each period, simultaneously for isotropic and anisotropic terms. Regularization is by means of norm damping, Laplacian smoothing, and gradient damping (see Lebedev and van der Hilst (2008) for a detailed description), applied independently to the isotropic and anisotropic components of the model. Through regularization, we discourage unrealistic rough models and constrain the inversion parameters to avoid over-fitting. Conversely, we do not want excessively smoothed models with obvious loss of information.

In the final tomographic maps (Figs. 2.14 and 2.15) each of the 4328 grid knots has its own level of regularization, which is chosen in order to have an optimal local resolution. First, a series of 2D inversions for phase velocity maps is performed at each period, with the smoothing coefficients incremented at small steps from very low to very high. The gradual change in smoothing (S) for the velocity maps (Fig. 2.7) is obtained with the Laplacian smoothing coefficient three times the gradient damping coefficient, norm damping as small as possible and the regularization coefficients for the anisotropic terms 1.5 times those for the isotropic term. After an initial inversion, each phase-velocity map is recomputed with 25% of the "outlier" measurements discarded at each frequency (Lebedev and van der Hilst, 2008). The outliers are defined here as the measurements fit the worst by the model; the procedure effectively selects the most mutually consistent measurements and removes the least mutually consistent ones, likely to contain the largest errors in the dataset.

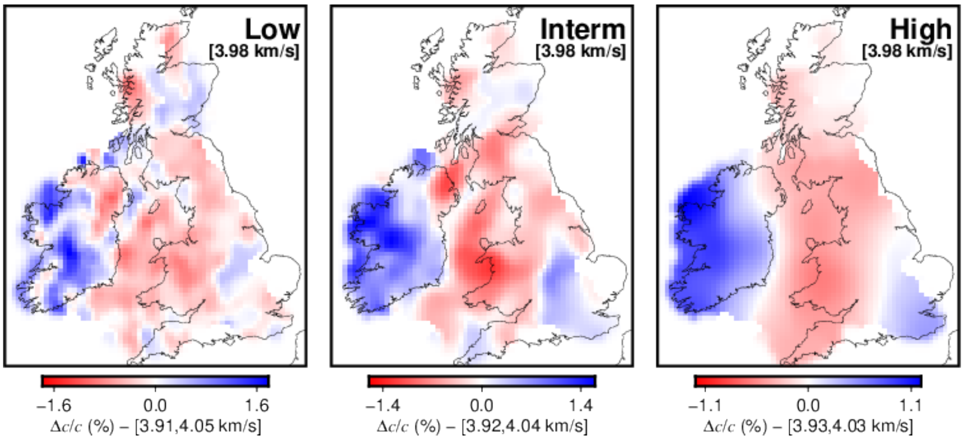

FIGURE 2.7: An inversion that is not smooth enough (e.g., left panel), could potentially fit noise and introduce artifacts in the final model. Conversely, extremely smooth inversions (e.g., right panel), are the most robust but at the cost of lower resolution. The figure shows an example of phase velocity map with different smoothing at 43.66 s. *Low* and *High* are under- and over-smoothed inversions; *Interm* is an intermediately smoothed map which may look correctly regularized, but at a closer inspection presents non-optimal regularization (instead achieved, e.g., in Fig. 2.14, as explained in Section 2.4).

Once the 2D tomographic maps are produced at each period (47 logarithmically spaced periods from 5.1 s to 454.09 s) and for each smoothing level $S_{i=0,1,2,...,38}$, we extract a phase-velocity curve at each of the 4328 knots of the grid (a total of 168792 dispersion curves). In the top panels of Fig. 2.8, we plot, as examples, the dispersion curves extracted at two knots of the grid, one in Wales (left) and one in Ireland (right).

2.4.3 Criteria for identification of the optimal S at each knot

As we show below, a local phase-velocity curve at a point–extracted from a set of phase-velocity maps at different periods–generally has errors that scale with the roughness of the maps: the smoother the maps (the smaller the roughness), the smaller the errors. This offers us a straightforward way of identifying the optimal resolution at a point. We can increase the target resolution of the phase-velocity maps (that is, reduce their smoothness) until the estimated error of the phase-velocity curve at the point reaches a threshold. The problem is now reduced to finding the smallest level of smoothing of the maps such that the errors of the local dispersion curve are below the threshold. The procedure is repeated for each point, with the optimal resolution varying from one point to another.

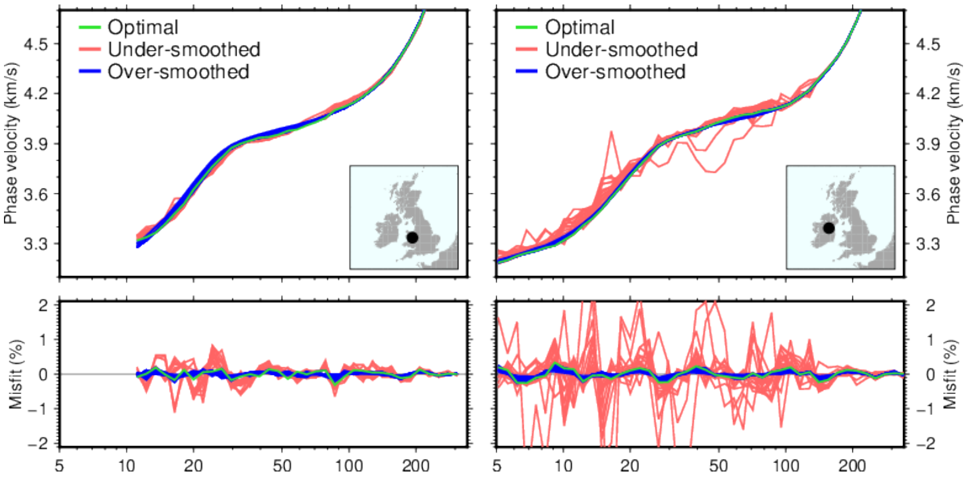

FIGURE 2.8: We use weakly regularized inversions to isolate the roughness of the phase velocity curves (top panels). The bottom panels show the relative misfit between the measured data and synthetic models, obtained after weakly regularized inversion for 1D shear velocity. We show two examples for two points, in Wales (left panel) and in Ireland (right panel), extracted from the velocity maps. In red the curves obtained from rough maps, in blue the ones obtained from smooth maps. The curve (and relative misfit) drawn in green is the one chosen as optimal (Section 2.4.3). Even though the knot in Ireland presents higher data coverage (see also Fig. 2.12) than the one in Wales, the inversions show noisier results.

To identify the optimal S_i for each knot of the model, we use the following strategy. For every local dispersion curve–for each S_i and at each knot–we estimate its errors by isolating its roughness. Due to the surface-wave sensitivity kernels' broad depth range and smooth variations with period, any realistic phase velocity curve is smooth. This is true even for dispersion curves computed for unrealistic Earth models with highly oscillatory depth dependence of seismic velocities. The rough (not smooth) variations of phase velocities with period are, therefore, entirely due to errors. The frequency-dependent roughness of a phase-velocity curve can thus yield an estimate of its frequency-dependent errors (Ravenna et al., 2018).

The roughness of a phase-velocity curve can be isolated by means of a very weakly-regularized inversion of it for a 1D Earth model. The smooth component of the curve can be matched closely by a synthetic curve computed for a best-fitting 1D Earth model (which is not required to be realistic in this inversion). The rough component is then given by the remaining misfit–varying rapidly with period–between the curve and its synthetic counterpart. This rough component cannot be fit by any Earth structure and is due to the errors of the dispersion curve. An estimate of the frequency-dependent error can now be obtained from the misfit or its envelope (Ravenna et al., 2018). This error estimate is conservative in the sense that the weakly regularized inversion fits the dispersion curve as closely as possible, even if this requires an unrealistic, oscillatory 1D model. This may be offset, to some extent, by the fact that this approach will miss errors that do not vary with period (or vary with period slowly) and, thus, do not manifest themselves in the dispersion-curve roughness.

Our weakly regularized inversion for a 1D shear velocity profile is a non-linear, Levenberg-Marquardt gradient search (e.g., Meier et al., 2004; Lebedev et al., 2006; Endrun et al., 2008; Erduran et al., 2008; Agius and Lebedev, 2013; Agius and Lebedev, 2014) (see Section 2.5 for details on the inversion algorithm). The misfit is computed as the relative difference of the synthetic data with regard to the "measured" data. Provided that all the 1D inversions are performed using the same weak regularization, the relative data–synthetic misfit is smaller for curves extracted from maps with higher S_{i}, and higher for curves extracted from maps with lower S_{i} (as illustrated by Fig. 2.8). These inversions are not meaningful in terms of real Earth structure; we use this strategy to isolate the roughness of the curves, which, we postulate, is entirely due to errors.

Extremely smooth phase-velocity maps are the most robust but at the cost of lower resolution: they display large-scale structural trends but fail to show structure at a high level of detail. Conversely, phase-velocity maps that are not smooth enough will fit noise and may be dominated by artifacts.

In Figs. 2.9 to 2.11 and A.11 we can observe that the error of the phase-velocity curves, estimated by the roughness-isolating 1D inversions, decreases with increasing smoothing of the 2D velocity map. Fig. 2.11 shows the root mean square (RMS) misfit (panels (e) and (f)) computed for every inversion at two different sets of knots, in Ireland (top panel) and in Britain (bottom panel), as indicated by the black dots in the maps. Panels (a) and (b) show the phase velocity curves extracted from the 2D tomographic maps, for three different level of smoothing (S), as indicated by the colors (red, green, and blue, respectively low, intermediate and high S). The relative misfit is shown in panels (c) and (d). It appears clear from this figure that the smoother the 2D phase velocity map, the smaller the misfit in the 1D inversion for shear velocity. We also note that the error increases nearly monotonically with the decrease of smoothing factor. (This also confirms that the models converge consistently, and the convergence is not affected by local minima or random behaviour.)

The same behaviour is observed in Fig. 2.9, where the portion of phase velocity curves with estimated errors less than 0.15%, rather than the RMS

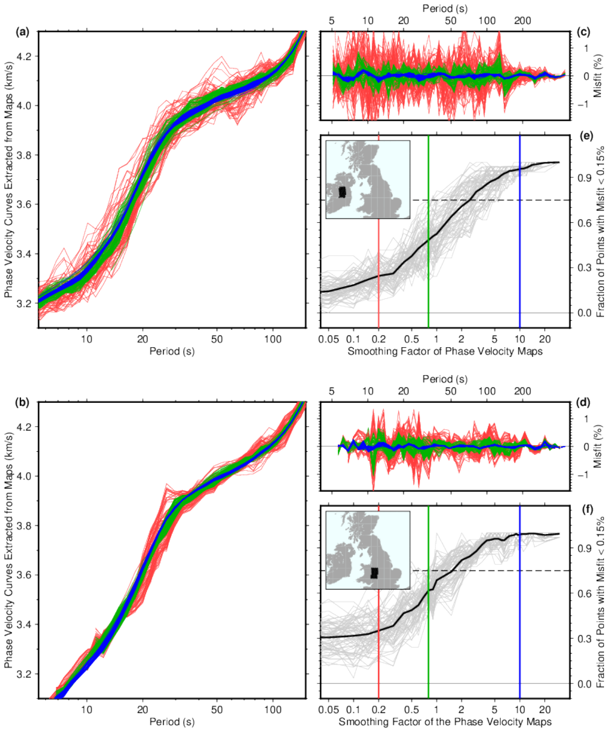

FIGURE 2.9: Weakly regularized inversions used to isolate the phase velocity curve roughness. The roughness of the phase-velocity curves is indicative of frequency dependent errors and can be isolated by means of weakly regularized 1D inversions. Thus estimated errors of phase-velocity curves at a point decrease with increasing smoothness of the phase-velocity maps that they are derived from. Panels (a) and (b) show phase velocity curves extracted from the phase velocity maps at 3 different smoothing levels (indicated in red, green, blue), for a set of knots in Ireland as drawn with black dots in the maps. In panels (c) and (d) we show the misfit of the weakly regularized 1D inversions. Panels (e) and (f) show in gray the fraction of points with misfit lower than 0.15%, for the whole range of smoothing levels applied (the black line represents the average).

misfit, is plotted as a function of S. We can then affirm that to reduce the error (as expressed in the misfit after weakly regularized inversion for shear velocity at each knot of the grid) we need smoother 2D phase velocity maps. This is the basis of the strategy we use to track the noise.

The data sampling given by our large phase-velocity dataset is so redundant that random noise cancels out, but not the systematic error (possibly due to geographical variations, non-resolved heterogeneities, wave propagation effects). This is apparent from the fact that the error of the local phase-velocity curve does not scale with data sampling (e.g., in Fig. 2.12).

We now define an empirical criterion to identify the optimal S_i for each

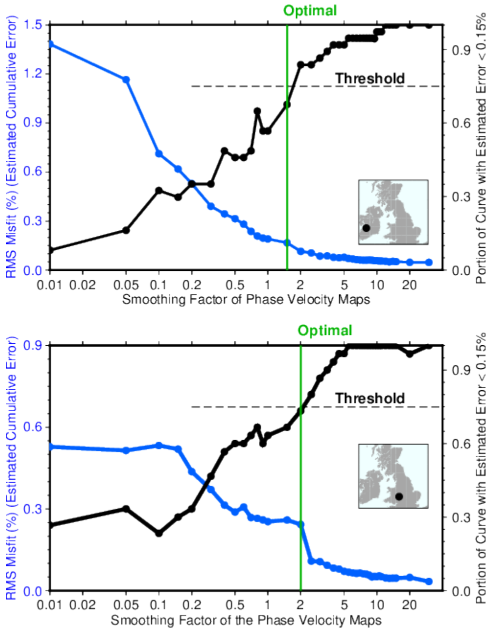

FIGURE 2.10: The cumulative error, as well as the portion of curve with estimated error less than 0.15% (which is our criterion for selecting the optimal regularization (see Section 2.4.3)), are monotonically changing with S. Two grid-knots, in Ireland and in Wales, are shown as examples.

knot of the model. We set a threshold of 0.15% for the relative misfit and we accept only those phase velocity curves that produce misfit within this threshold at least for 75% of the frequencies. This way, curves too rough (low S_i) are discarded, and we keep the remaining curves, those from reasonably smooth to very smooth. We choose the roughest one of the remaining curves as the optimal one (we assume that the roughest curve over the set of smoothest ones is the curve which provides the most detailed image of the sub-surface without over-fitting the error contributions).

The criteria for choosing the optimal resolution has been chosen empirically after intensive testing. In Fig. 2.13 the choice of the optimal selection is plotted (columns (c)) together with two looser and two stricter selections (columns (a), (b) and (d), (e) respectively), for three different periods. This data-based empirical approach allows us to suppress the error and maximize resolution, evaluating noise (or how the noise limits the resolution of our image) at every step and finding the highest possible resolution at every knot. The empirical criteria are, to an extent, subjective but applied consistently and are data-driven. In Fig. 2.10 we show that the cumulative error, as well as the portion of curve with estimated error less than 0.15%, are monotonically changing with S. Parts of the maps where the coverage is extremely low have been removed from the analysis, based

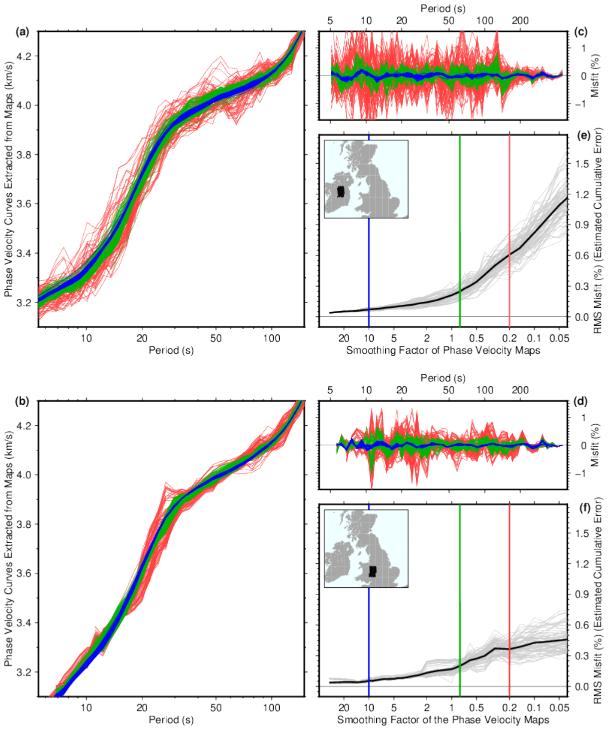

FIGURE 2.11: See also Fig. 2.9. Panels (a) and (b) show phase velocity curves extracted from the phase velocity maps at 3 different smoothing levels (indicated in red, green, blue), for a bunch of knots in Ireland as drawn with black dots in the maps. In panels (c) and (d) we show the misfit of the weakly regularized 1D inversions. Panels (e) and (f) show in gray the RMS misfit (the black line represents the average).

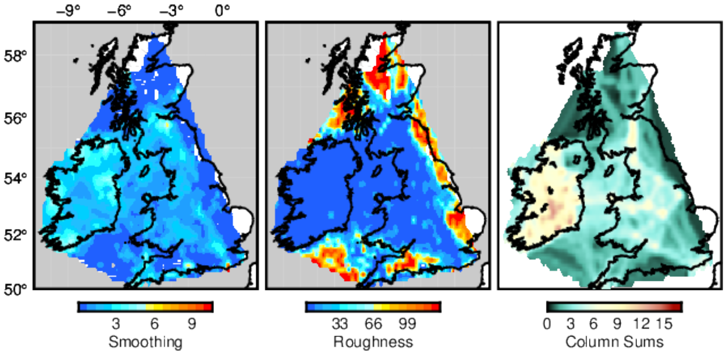

FIGURE 2.12: The optimal smoothing level applied at each knot (left panel) does not scale with the density of data coverage. The roughness and density of data coverage are plotted for period 115.84 s.

on sensitivity-matrix column sums–accepting only knots with value over a certain threshold–for example, at the edges of the region, where the coverage deteriorates and the data sampling is insufficient to constrain the structure.

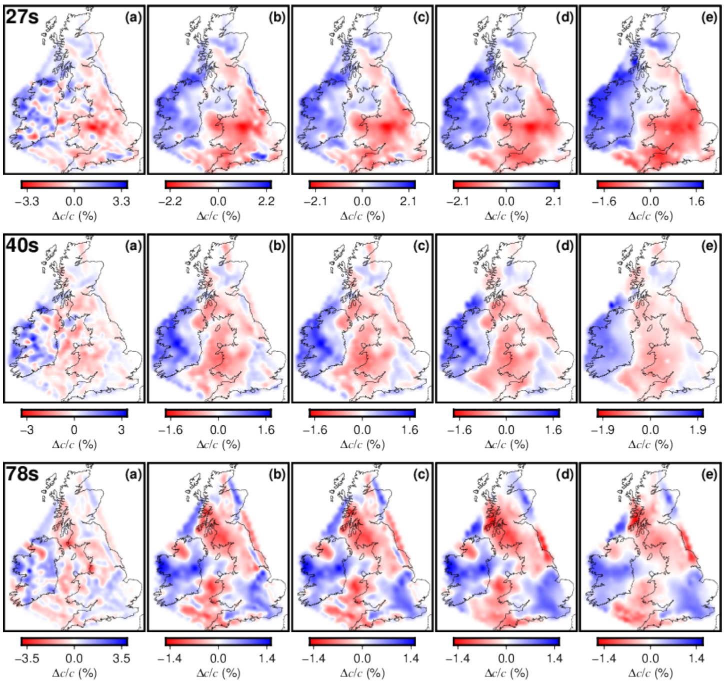

FIGURE 2.13: Optimal resolution phase velocity maps can be reconstructed at each point of the grid, by means of isolating the roughness of weakly regularized inversions for shear velocity of the phase velocity curves extracted at differently smoothed phase velocity maps. In panel (c) we show the velocity maps with optimal resolution reconstructed at each knot. The maps in (a), (b) and (d), (e) correspond to looser and stricter criteria of selection (see Section 2.4.3 for details). The maps shown are for the periods 26.8, 39.6, and 78.4 s, approximated in the figure for clarity.

The chosen values of S_i for each knot are shown in Fig. 2.12, together with the density of the data coverage (column sums) and the map of the roughness (at an example period of 115.84 s). The optimal-resolution phase velocity maps, for a selection of periods, are shown in Figs. 2.14 and 2.15. The optimal target resolution is reached by isolating the roughness of the phase velocity curve, which we postulate is due to systematic errors in the data. It would not be possible to identify the noise, but with this approach we manage to track it, and see how it propagates. The estimated optimal resolution shows smooth lateral variations, confirming the robustness of the procedure.

2.5 Shear Velocity Structure

We now invert the optimal-resolution phase velocity maps at each knot of the model grid for shear velocity profiles, in order to obtain a 3D model of the crust and upper mantle.

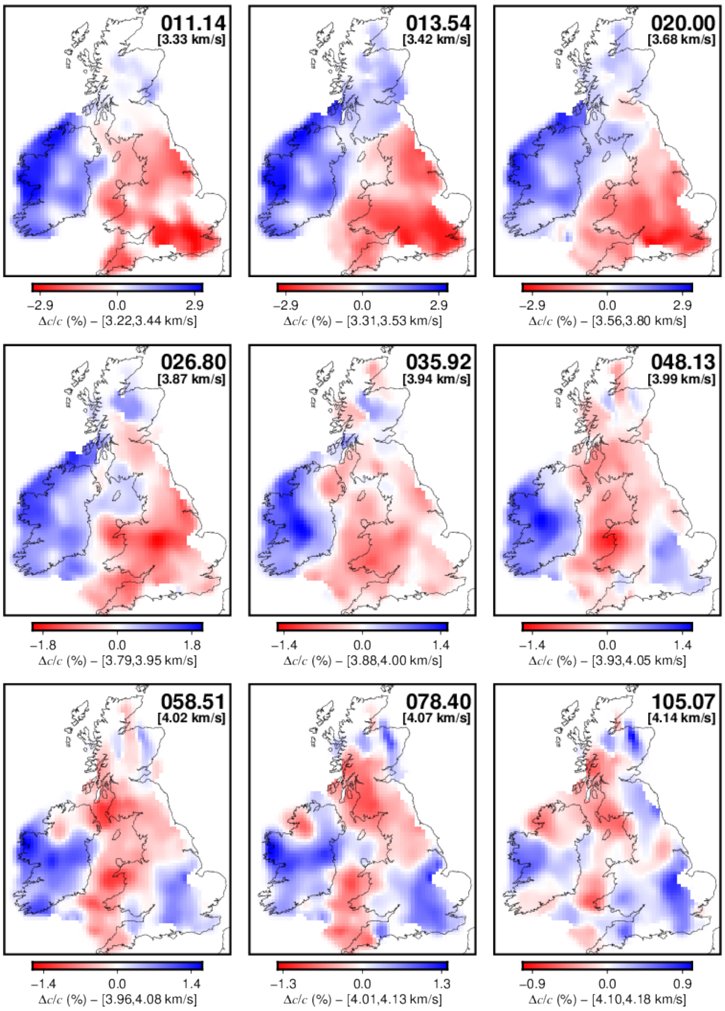

FIGURE 2.14: Optimal resolution phase velocity maps for Ireland, Britain, and the Irish Sea (see Section 2.4).

2.5.1 Tail removal

Before proceeding with the 1D inversion of the phase velocity curves for shear velocity structure, we have applied additional quality checks to the dispersion curves. Even though the 2D tomographic maps generate smooth results, one could find that the knot-specific (local) dispersion curve presents, occasionally, noisy "tails"–the highest-frequency portion of the curve with more noise than the rest of it. An example of this is shown in the top panel in Fig. 2.16 (central panel shows a selection of measurements and bottom panel shows the whole set of measurements, for clarity). The selection of the noisy tales has been applied on the extremities (the first 8 points and the last 3) of the each relative misfit curve (relative to the weakly regularized inversion of each phase velocity curve): if any of the tail points deviates from the average more than 1.6 times the standard deviation of the velocity curve, then the entire tail

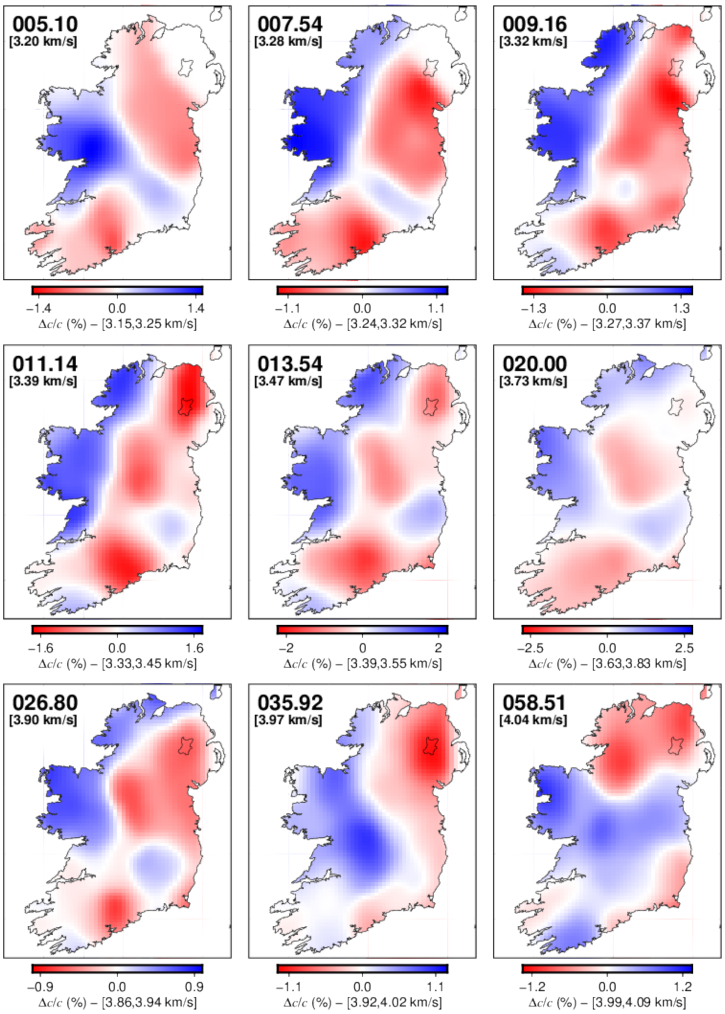

FIGURE 2.15: Optimal resolution phase velocity maps for Ireland (see Section 2.4).

is removed and thus will not contribute to the final inversions.

2.5.2 Levenberg-Marquardt gradient search inversion algorithm

Ravenna and Lebedev (2018) showed that a well-tuned, non-linear, gradient-search inversion of phase-velocity curves yields robust 1D Earth models nearly equivalent to the median model given by a Bayesian McMC inversion scheme. While a Bayesian approach still has advantages in providing a posteriori model uncertainties, we opted for a fully non-linear gradient-based technique, as the dataset size would have made probabilistic inversions prohibitively expensive. We do, however, perform a series of gradient inversions in each case, using variable regularization to approximately map the model uncertainty at different depths.

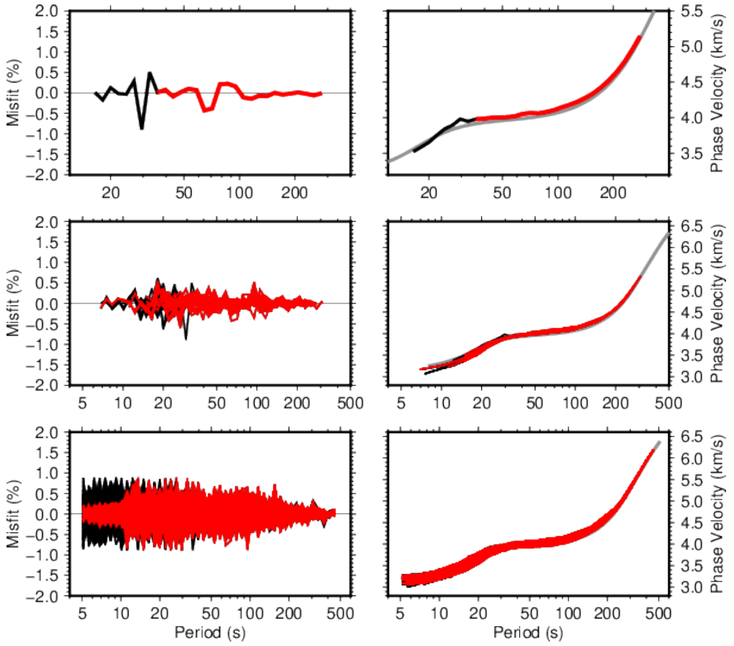

FIGURE 2.16: The tomographic maps generate smooth results but dispersion curves extracted at each knot presents occasionally noisy tails, which cannot be explained by any realistic subsurface structure (see Section 2.5.1). These parts of the curves are removed from the consecutive analysis. Top panel shows an example of noisy tail removal, prior of 1D inversion for shear velocity structure. In black the original curve, in red the curve after removal. Middle panel shows a bunch of curves, lower panel the whole dataset.

We use the same non-linear, Levenberg-Marquardt gradient search inversion algorithm that we used to isolate the noise in Section 2.4, with the difference that the inversions are not regularized too weakly. We choose reasonable regularization (e.g., which penalizes oscillatory V_S models) to produce appropriate representation of the V_S structure of the area (e.g., in Fig. 2.17, the V_S profiles in the right column are most likely to represent a "true" structure rather than the profiles in the left column).

The algorithm computes synthetic phase velocities at each iteration from V_S, compressional velocity (V_P), density, and attenuation using the forward solver MINEOS (Masters et al., 2007). The ratio between V_S and V_P is kept fixed during the inversion, according to the values of the initial reference model (see below). Density and compressional and shear attenuation factors are fixed at the reference values, taken from PREM and AK135, respectively. The perturbations in the model, from the surface to the shallow lower mantle (~1300km), are controlled using basis functions, 13 triangular-shaped ones in the mantle and 3 boxcar-shaped in the crust (e.g., Bartzsch et al., 2011; Agius and Lebedev, 2013). The triangular basis functions are defined by linear

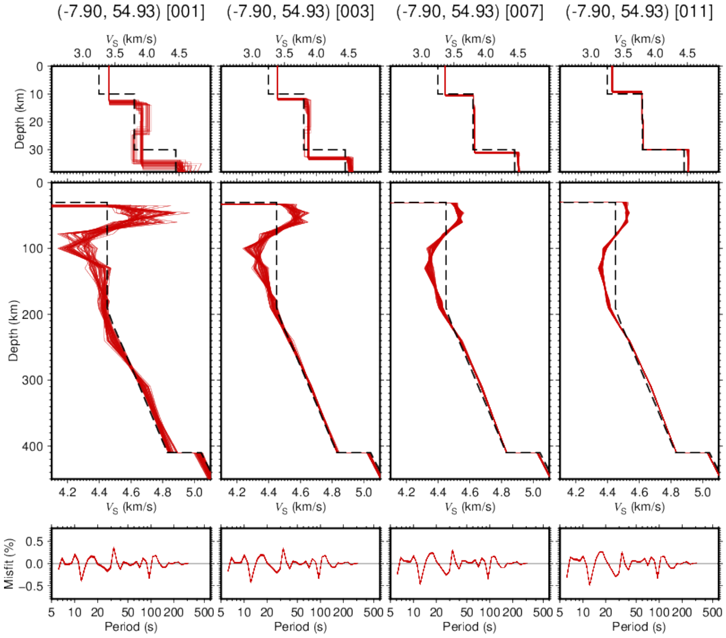

FIGURE 2.17: Sets of differently damped V_S inversions for one grid-knot, with increasing damping from left to right. The reference model is plotted with a dashed black line. Top panel shows a zoom on the crust, central panel the profile from 0 to 450 km, bottom panel the misfit between the models and the data. The models obtained after inversions (each of which is independent) are non-unique but the robust features in the V_S profile are evident (see Section 2.5).

interpolation between neighbouring depth knots; the boxcar ones represent constant-velocity layers. The depth of the Moho and two intra-crustal discontinuities are additional inversion parameters.

2.5.3 Reference model

As a reference crustal model, we used a three-layered crustal model of the region based on a priori information from CRUST 2.0 (e.g., Bassin et al., 2000) and previous works carried out in the area (e.g., Landes et al., 2000; Davis et al., 2012; Licciardi et al., 2014; Tomlinson et al., 2006), with Moho depth of 30 km. The reference model for the mantle is a modified version of AK135 (Kennett et al., 1995), recomputed at 50 s, and characterized by constant shear velocities (4.45 km/s) from the Moho down to 190 km depth and linearly increasing shear velocities below. The density for the reference model has been taken from PREM (Dziewonski and Anderson, 1981), as AK135 presents an unlikely-to-be-true sharp increase with radius in the uppermost mantle. We have performed extensive tests, however, and established that this modification does not substantially change our results. The reference model is

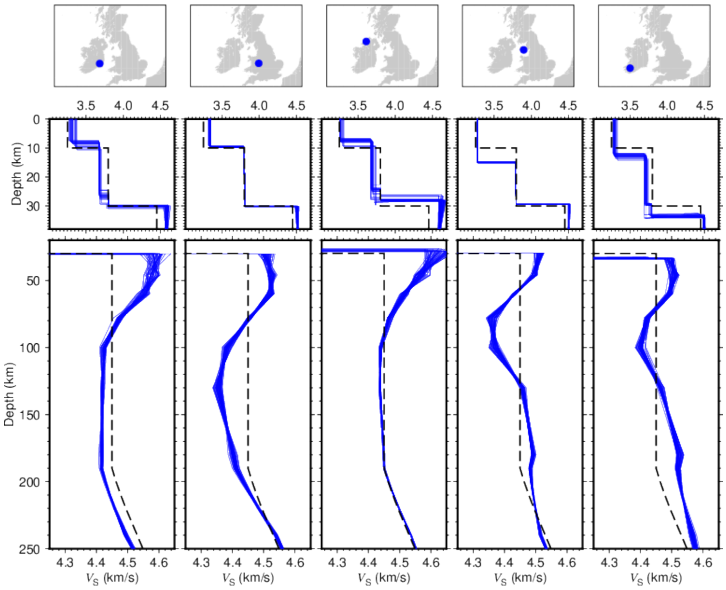

FIGURE 2.18: Final V_S inversions at 5 different locations in Ireland, Britain, and the Irish Sea.

plotted, e.g., in Figs. 2.17 and 2.18 with a dashed black line. Due to noise in the data and the non-uniqueness of the models, we use norm damping in order to avoid physically unrealistic models.

2.5.4 Inversion tests for optimal damping

A number of tests have been performed to estimate the optimal regularization (this time, the regularization is kept equal at all the grid-knots for each test). Rather than choosing a preferred model, and also to reduce the effect of noise, we perform a series of inversions to produce a bundle of possible models which fit the data (for all the models and all the differently damped sets, the misfits are well within ±0.5%). The relative damping for each basis function is allowed to vary randomly within a range of values. This produces a set of 50 models for each knot at each damping level ($d_{j=0,1,2,...,49}$) as, for example, in each of the panels in the middle row in Fig. 2.17. A global damping factor (constant for all basis function at each inversion) then multiplies the relative factors in each inversion ($D \times d_{j=0,1,2,...,49}$). The relative damping d_j, which is randomly changed at different depths (each basis function has a different value of d_j), is used to avoid the bias possibly introduced by a subjective choice of regularization; the overall damping factor (D) is instead introduced in order to obtain differently regularized sets of reasonable models, and verify a posteriori which is the optimal model.

In Fig. 2.17, we observe, from left to right, 4 differently damped (D) sets of models, with each set including 50 models with randomly varying relative damping (d_j). We generated, in order to cover a wide range of reasonable regularization, 18 differently damped models which produced $4328 \times 50 \times 18$ independent, non-linear, gradient-search inversions.

2.5.5 V_S map construction

In Fig. 2.18 we show, for a defined choice of damping factor D, 5 different sets of inversions at 5 different locations. The optimal damping factor is chosen according to the following criteria. We do not need to introduce complexity in our model, if a simpler model fit the data equally well (according to the general principle of parsimony, also known as Ockham's razor (e.g., Bodin et al., 2016)). We discourage deviations from the reference model, and stop right before the misfit deteriorates. If there is no deterioration in the misfit, then we could penalize the deviations more.

The accepted V_S profiles are then resampled at a 0.1 km step, and the final V_S maps are constructed, for each damping level, at different depths averaging for each knot over the obtained 50 inverted models. Examples of final maps are plotted in figure Figs. 2.19, 2.20 and 2.23 to 2.25. Vertical cross sections of the 3D model, with different orientations, are shown in Figs. 2.26 to 2.29. A comparison of velocity maps retrieved with different damping levels is in figure Fig. 2.22 (the maps are shown for depth 80, 100, and 130 km); in this figure we show how, for a reasonable choice of damping, the maps show similar features (although the amplitudes are not preserved). It can be observed that smoother 3D map views are produced by more damped 1D inversions. This further validates our regularization.

2.6 Discussion

We have developed a tomographic scheme which allows us to maximize the information extracted from the data and obtain an optimal target resolution of the model at each knot, achieved through tracking of systematic errors in the data. Using this approach we evaluate the systematic errors (which are limiting the resolution of the model) at every knot of the model grid, for a wide and densely spaced range of differently smoothed models, and we choose the optimal resolution as the highest achievable, after isolation of the error. We show that the cumulative error, estimated from the relative misfit obtained after weakly regularized inversions for shear velocity, decreases monotonically with the smoothing of the 2D tomographic maps. This allows us to track the systematic errors and isolate them. Importantly, optimal

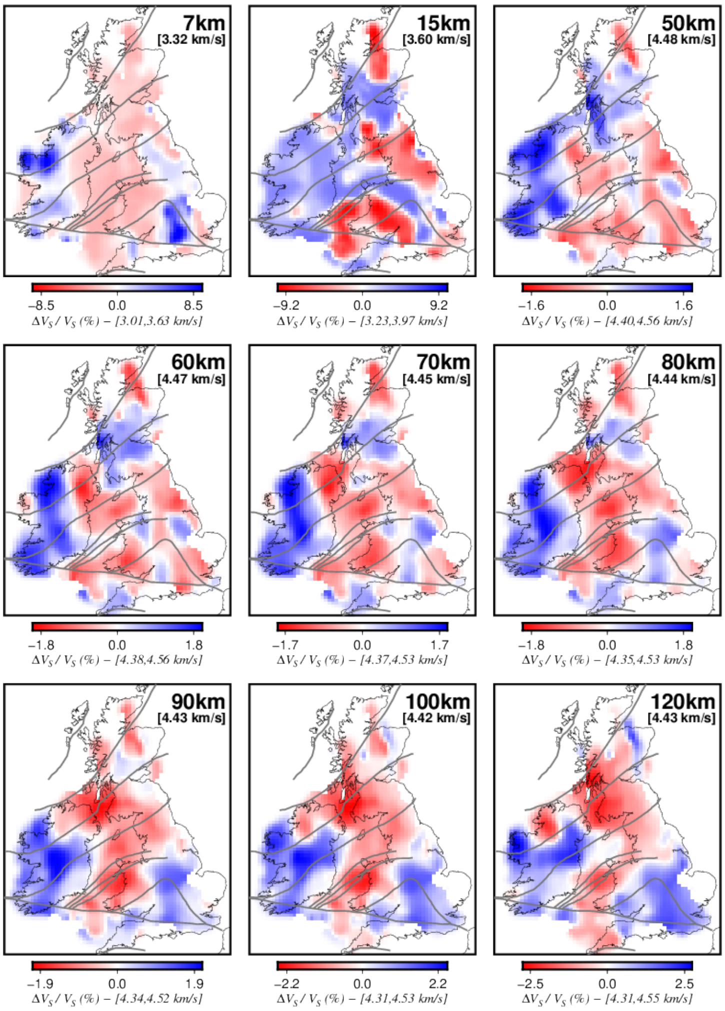

FIGURE 2.19: Shear velocity maps (see also Figs. 2.20 and 2.21) show new insights of the seismic structure of the area. The anomaly is plotted with respect to the average at each depth. The gray lines represents the major geological terranes of the area (after Tomlinson et al. (2006)). At depths from ~50 to 140 km the maps show evidence of a consistent pronounced low-velocity anomaly centered at the Irish Sea and including northern Ireland, Wales, and Western Scotland. This anomaly is consistent with a relatively thin lithosphere beneath the area. The area of the lithospheric thinning coincides roughly with where uplift and magmatism occurred at 50-60 Ma, previously attributed (e.g., Al-Kindi et al., 2003) to the Iceland Hotspot activity at the onset of the opening of the Atlantic Ocean. At shallower depth the maps show consistent clear boundaries between well consolidated blocks beneath Ireland and Scotland and sediments in the rest of the region. An elongated high-velocity anomaly stretched W-E approximately along the Iapetus Suture Zone may indicate the remnant of the Caledonian Iapetus slab beneath the suture (e.g., Chew and Stillman, 2009). Our shear-velocity model is parameterized on a 10 km spaced triangular grid of 4328 knots.

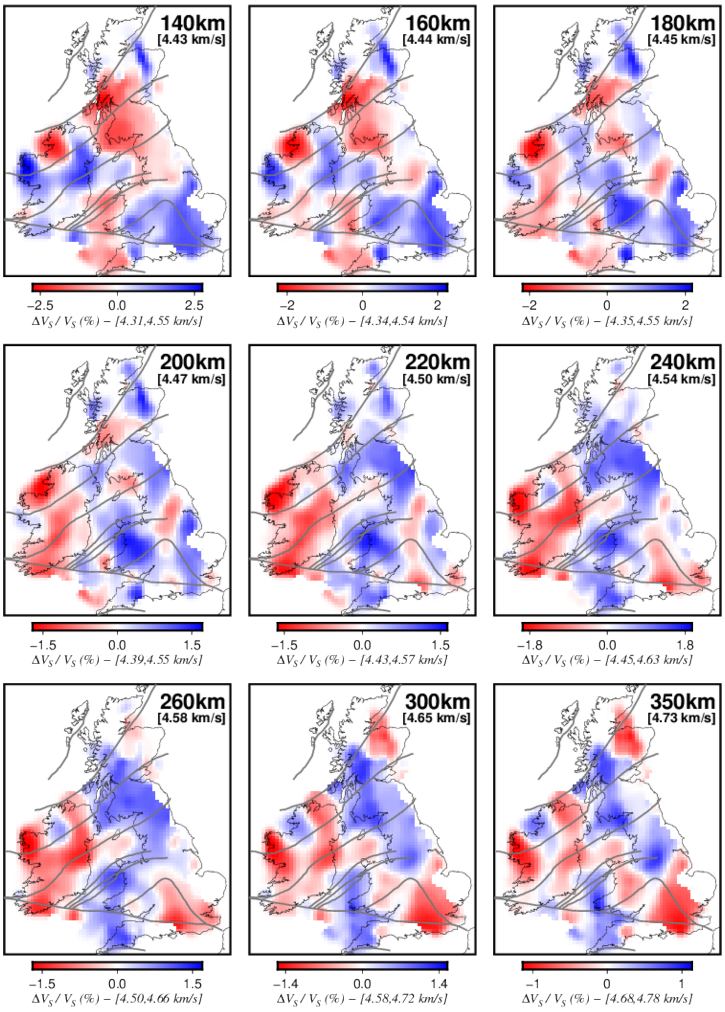

FIGURE 2.20: Shear velocity maps (see also Figs. 2.19 and 2.21) at greater depths.

resolution does not scale with the density of the data coverage: due to systematic data errors some of the best-sampled locations require relatively low lateral resolution. After the construction of the optimal phase velocity maps, characterized by the best realistically achievable resolution (allowed, fundamentally, by data sampling and noise distribution), we have produced a 3D V_S model of the area by inverting the dispersion curves at each knot of the model grid. This new scheme is applied to a very large number of broadband measurements of Rayleigh surface-wave phase velocities, obtained by teleseismic cross-correlation and waveform inversion, in order to constrain the seismic structure of the British Isles.

Our tomography reveals substantial heterogeneity in the area, offering exciting new insights into the structure and evolution of the British Isles. The optimal resolution obtained for the images allows us to resolve in detail,

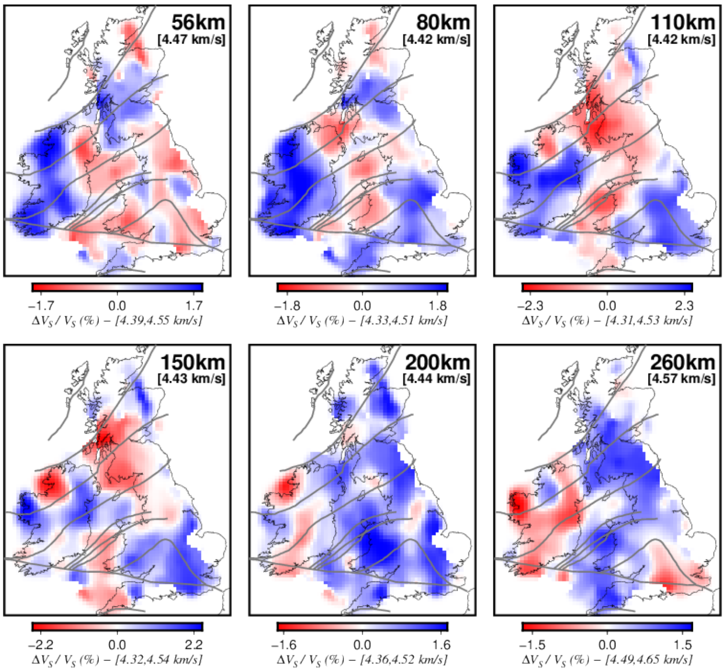

FIGURE 2.21: Shear velocity maps (see also Figs. 2.19 and 2.20) plotted with respect to values of velocity used as reference in the global model SL2013sv (Schaeffer and Lebedev (2013)). While Figs. 2.19 and 2.20 show the anomaly with respect to the average V_S at each depth, we use here a global model reference.

laterally and vertically, structures such as sedimentary basins and volcanic areas.

One of the striking features of the model is a robust low-velocity anomaly indicating anomalously thin lithosphere beneath the Irish Sea and its surroundings (including Wales, Western Scotland, Northern England and Northern Ireland). The Cenozoic uplift and exhumation history of the British Isles is still a controversial topic. The British Isles, with the exception of southeast Britain and a few Cenozoic outcrops exposed in northern Ireland (Antrim Lava Group) and western Scotland (e.g., Fig. 2.40), do not present evidence of onshore, post-Cretaceous sediments, as the area is mostly dominated by Palaeozoic and older rocks. Thus direct observation of the exhumation is not possible, and only indirect methods are available to assess the amount of Cenozoic uplift.

Several studies, during the last decades, suggested that uplift of parts of Britain and Ireland was caused by a lateral branch of the proto-Iceland mantle plume, which played a fundamental role in the evolution of the North Atlantic Ocean over the past 60 M.y. (White and Lovell, 1997; Jones et al., 2002; Al-Kindi et al., 2003; Jones and White, 2003; Arrowsmith et al., 2005; Tomlinson et al., 2006; Davis et al., 2012; Schoonman et al., 2017; Luszczak

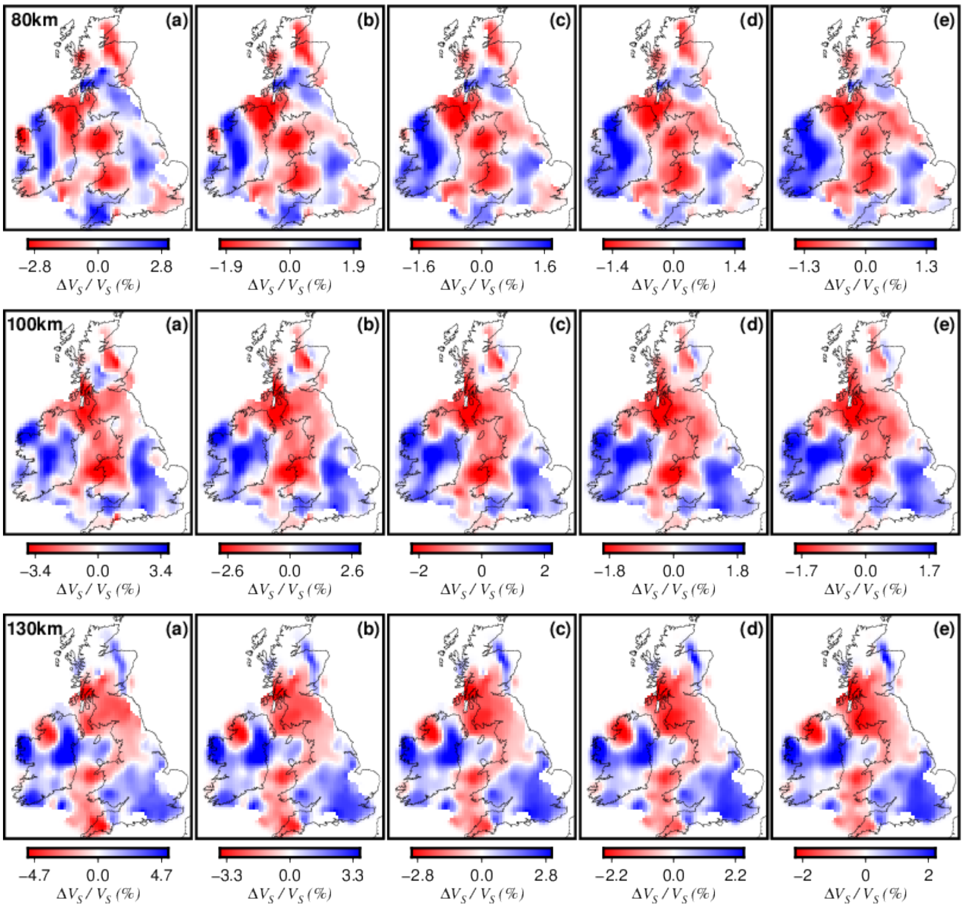

FIGURE 2.22: Shear velocity maps reconstructed at each knot, for 5 different damping levels (increasing from (a) to (e)), at three different depths (as indicated at the top left corner of each map). The maps (at each different depth) show similar features, except the very low damped inversion (panels (a)) that shows some irregularities. The amplitudes are not preserved, as different damping penalizes differently the variations from the reference model.

et al., 2018; Tiley et al., 2004, e.g.,). Alternatively, some authors suggested that the uplift could be associated with far-field stress between the North Atlantic and the Alpine orogenic belt, with reactivation of old Variscan and Caledonian faults across Ireland and Britain (Holford et al., 2009; Hillis and Holford, 2008, e.g.,).

Recent thermochronological studies provided new evidence of probable Paleogene uplift in the area (Cogné et al., 2016; Döpke, 2017). Our results (Figs. 2.19 and 2.20) exhibit a strong velocity anomaly (particularly evident from 50 to at least 140 km) centered in the Irish Sea, approximately below the area which it has been suggested has been influenced by the lateral branch of the Iceland plume. This low velocity anomaly, which can be observed in

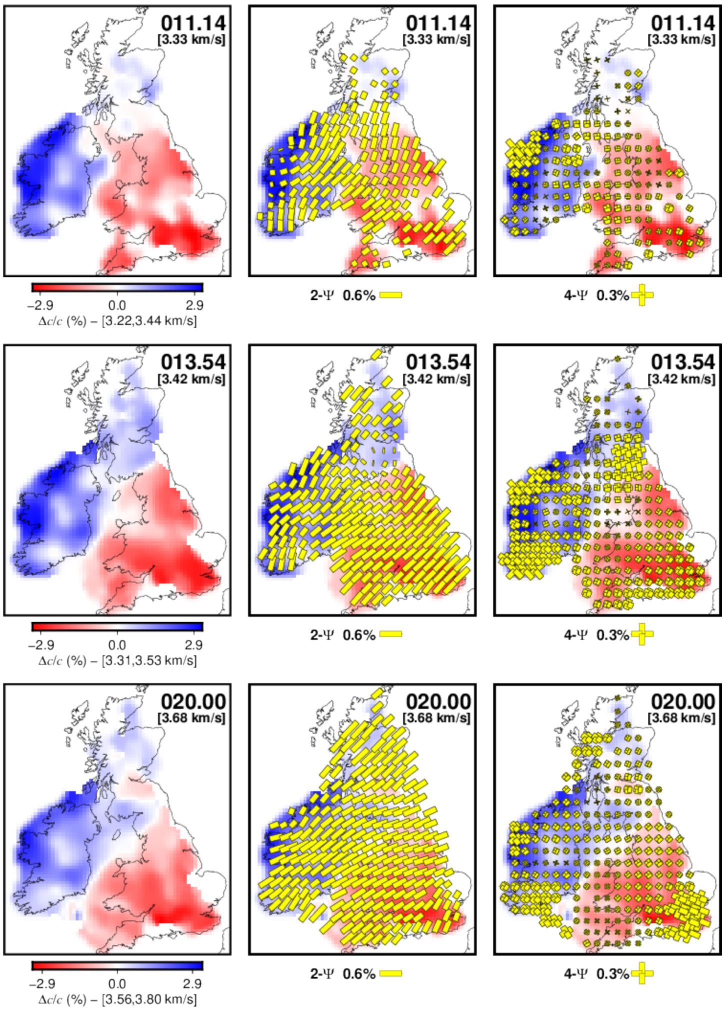

FIGURE 2.23: Seismic anisotropy provides complementary information regarding the past and present deformation in the crust, lithosphere and asthenosphere (see also Figs. 2.24 and 2.25). The fast-propagation direction is orientated parallel to the prominent Caledonian SW–NE structural fabrics observed at the surface (e.g., Chew and Stillman, 2009), and persist throughout the entire crust.

the shear velocity slices in Figs. 2.19 to 2.21 (from below ~50 km), and it is evident also in the velocity maps in 2.14 (at intermediate and long periods), is consistent with a relatively thin lithosphere beneath the area.

Our results suggest that it may have been the dramatic thinning of the lithosphere in this area – possibly triggered by thermal erosion by the hot asthenosphere arriving from the hotspot – that has caused the uplift and volcanism, with the lithosphere remaining relatively thin to this day.

We show that the assumption of a constant lithospheric thickness across Britain and Ireland, used in the past, is not valid. Our results show a striking correlation with proposed underplate thickness (up to ~7 km according to

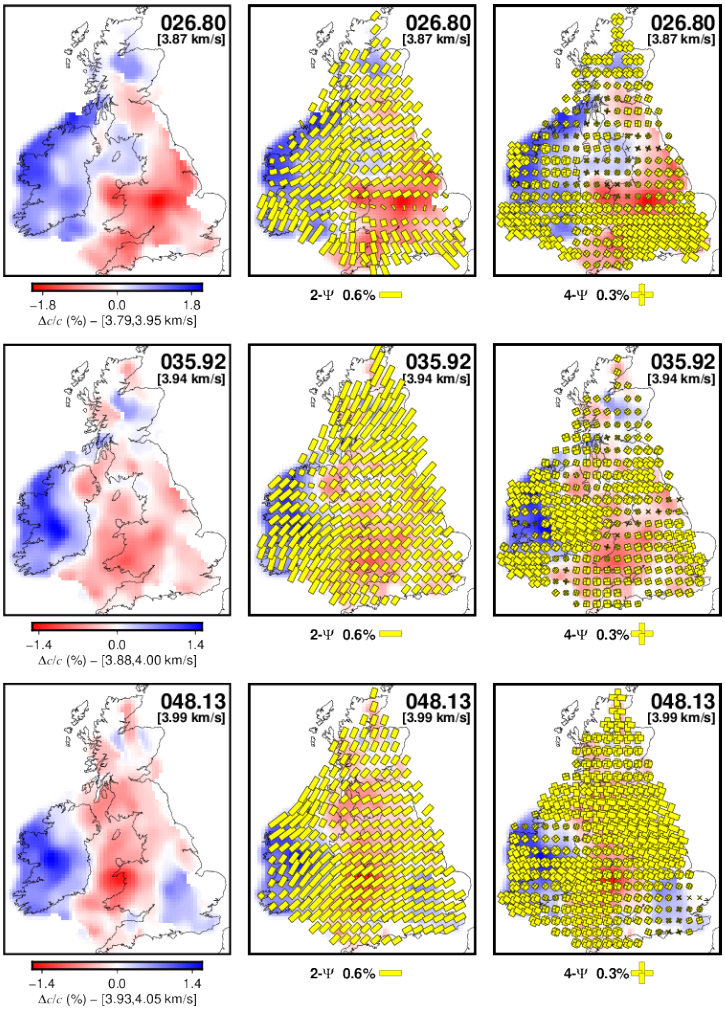

FIGURE 2.24: Seismic anisotropy provides complementary information regarding the past and present deformation in the crust, lithosphere and asthenosphere (see also Figs. 2.23 and 2.25).

Tomlinson et al. (2006)) and denudation, gravity, and thermochronological measurements. To facilitate the comparison between the low velocity anomaly in our results and other geophysical observable previously measured, we show figures from Tomlinson et al. (2006), Rickers et al. (2013), Al-Kindi et al. (2003), Arrowsmith et al. (2005), Davis et al. (2012), Jones et al. (2002), Cogné et al. (2016), and Döpke (2017) in Fig. 2.45, Fig. 2.38, Fig. 2.39, Fig. 2.50, Fig. 2.40, Fig. 2.41, Fig. 2.42, Fig. 2.43, respectively. The anomaly can also be observed in the V_S profiles in Fig. 2.18. Shear velocity profiles for two locations in the Irish Sea and NW Ireland have also been compared with profiles of shear velocity obtained for Hawaii (Laske et al., 2011) and Tristan da Cunha (Bonadio et al., 2018), to verify the extent of the present anomaly in the area (Fig. 2.32). The anomalies in our V_S profiles look moderate if compared with

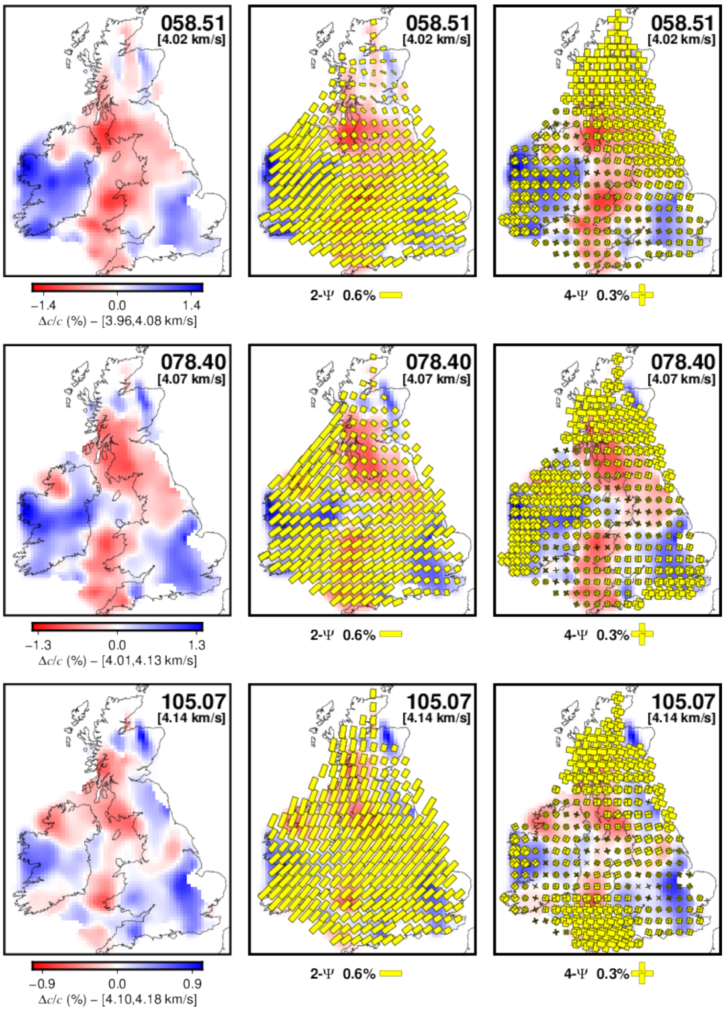

FIGURE 2.25: Seismic anisotropy provides complementary information regarding the past and present deformation in the crust, lithosphere and asthenosphere (see also Figs. 2.23 and 2.24).

Hawaii and TdC hotspots, consistent with the absence of volcanism for the last 50 m.y.

At shallowest depths, Ireland and Scotland show similar velocities (there are clear boundaries between well consolidated blocks beneath Ireland and Scotland and sediments on the rest of the area), as one would expect from the continuity of the surface terranes (this is also evident, e.g., in the velocity maps at 13.54 s in Fig. 2.14). In the deeper crust and lithospheric mantle, most of Ireland is surprisingly different from Scotland, showing substantially higher velocities. The shear velocity maps also exhibit (especially at 90 and 100 km in Fig. 2.19) an elongated high-velocity anomaly stretching W-E approximately along the Iapetus Suture Zone in Ireland; this may indicate the remnant of the Caledonian Iapetus slab beneath the suture or, alternatively, fragments

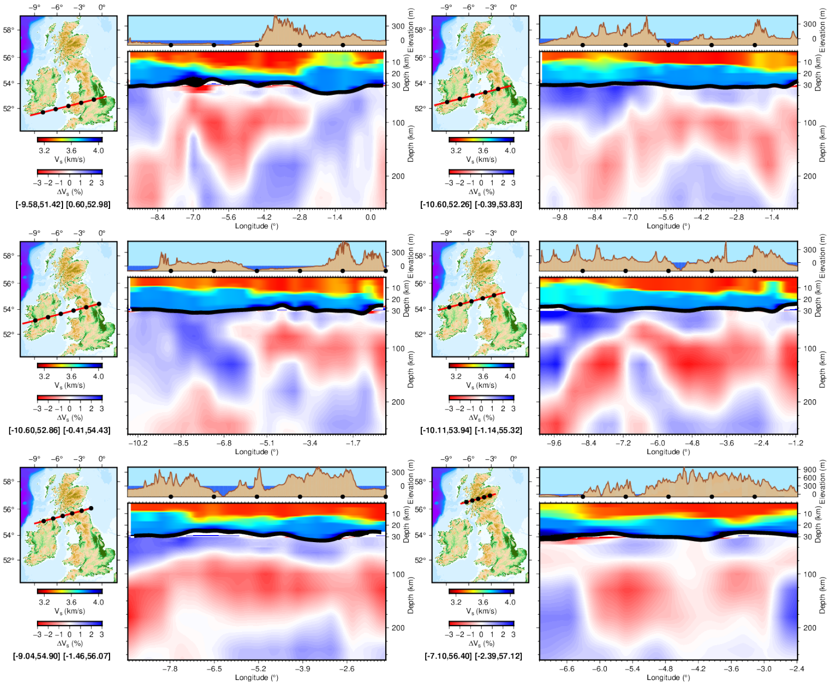

FIGURE 2.26: V_S vertical cross sections of the model (W–E).

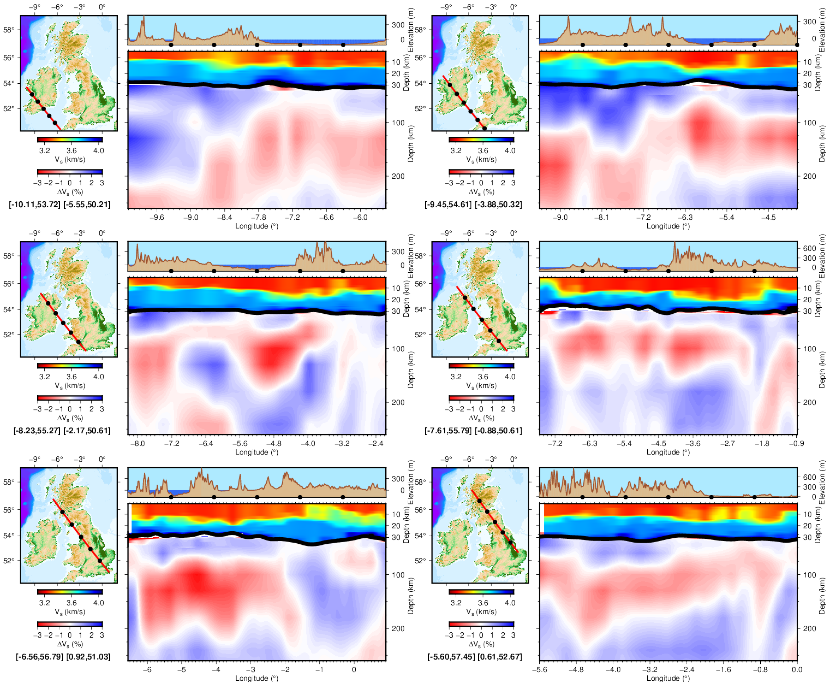

FIGURE 2.27: V_S vertical cross sections of the model (NW–SE).

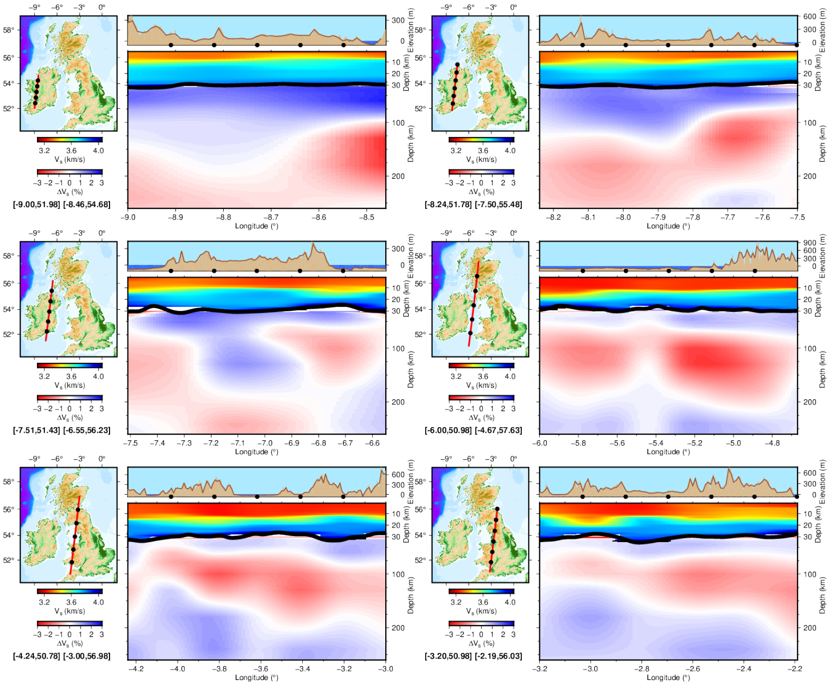

FIGURE 2.28: V_S vertical cross sections of the model (S–N).

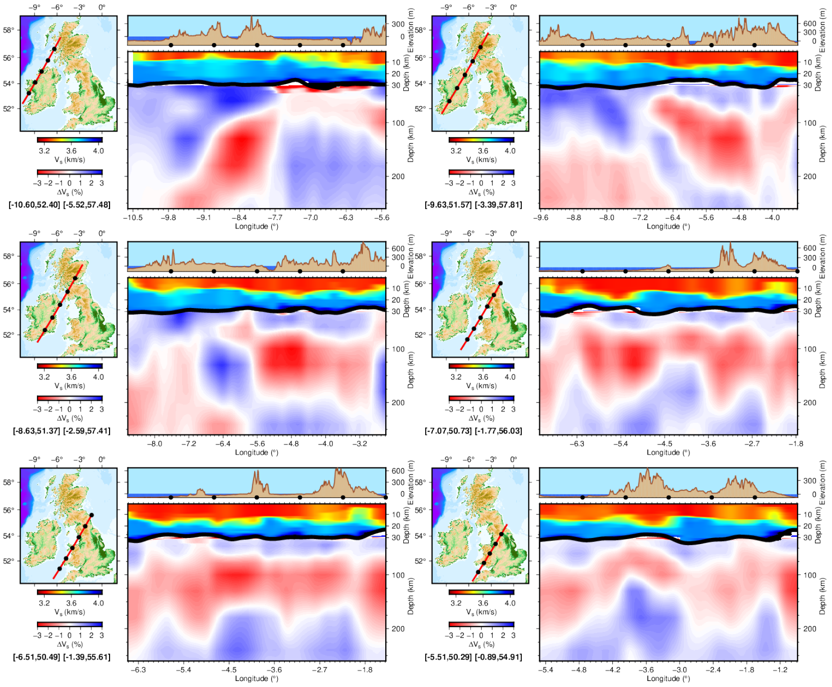

FIGURE 2.29: V_S vertical cross sections of the model (SW–NE).

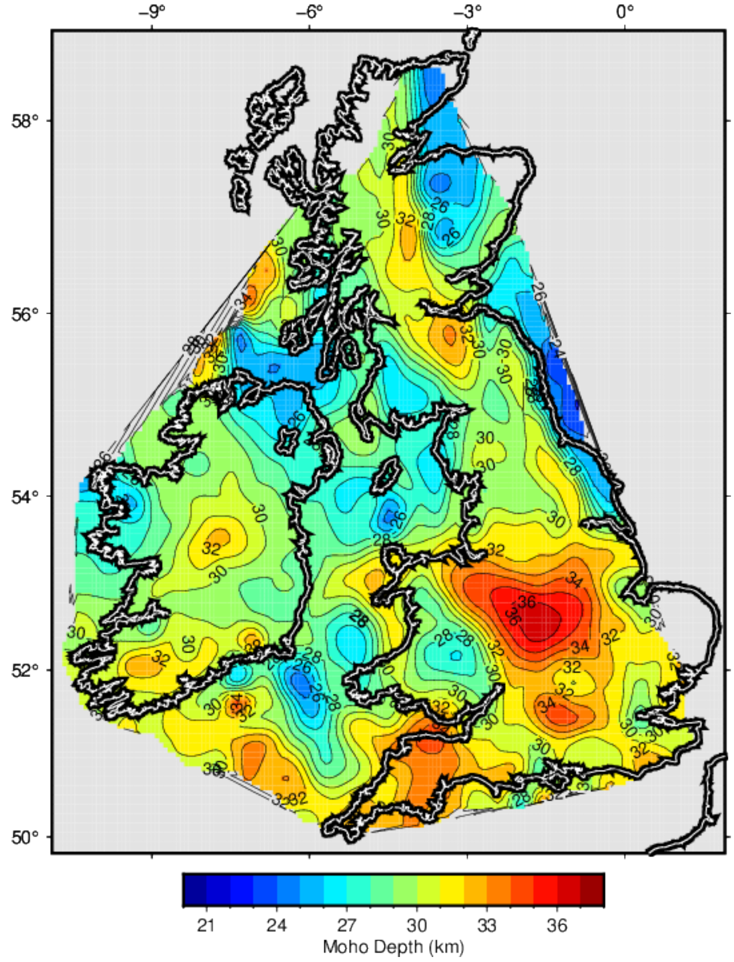

FIGURE 2.30: Reconstructed Moho map of the British Isles obtained by surface wave analysis. The map presents very good agreement with previous results on the Moho depth of Ireland and Britain obtained with methods more suitable to detect sharp discontinuities (e.g., receiver functions, (e.g., Licciardi et al., 2014; Davis et al., 2012; Tomlinson et al., 2006)). See also Fig. 2.31.

of thick continental lithosphere amalgamated into the Irish landmass in the course of the Caledonian Orogeny (e.g., Chew and Stillman, 2009) (Fig. 2.46). The lithospehere in Ireland appears to be thick beneath the Iapetus Suture Zone, even though not oriented along it, as mapped from surface geology. The heterogeneity in the area fades out at greater depths (Fig. 2.6).

The Moho map obtained in this work, in Fig. 2.30, shows general agreement with previous results obtained with data types more sensitive to sharp discontinuities (e.g., Licciardi et al., 2014; Landes et al., 2007; Davis et al., 2012; Kelly et al., 2007). In Fig. 2.31 we compare our results on the Moho depth with the ones obtained by Licciardi et al. (2014) using teleseismic P-wave receiver functions. The maps agree with the general thinning of the

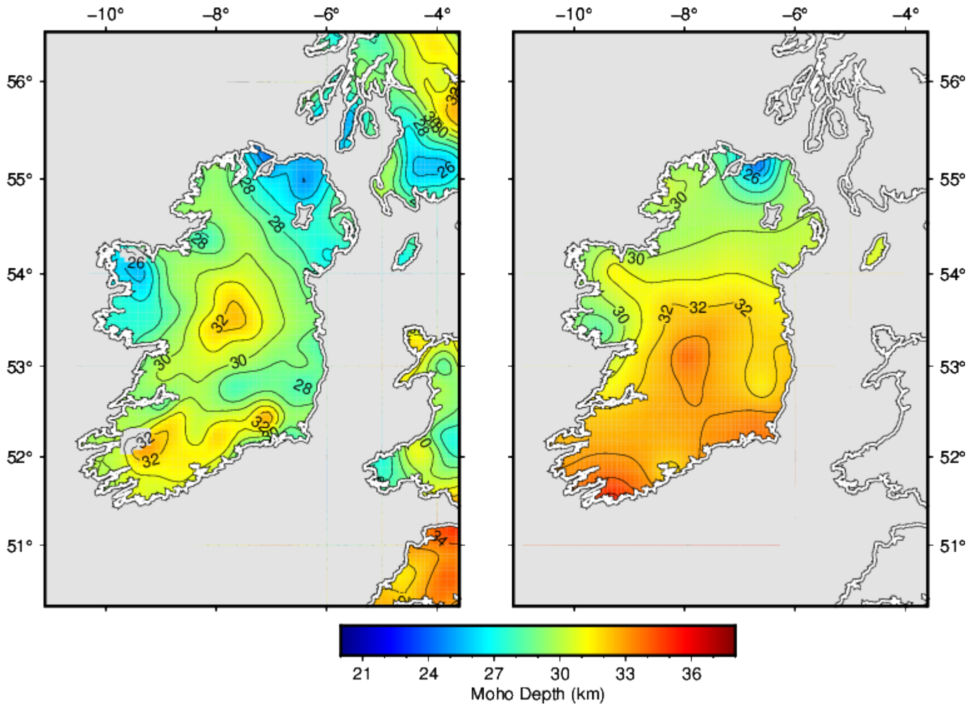

FIGURE 2.31: Moho maps obtained from surface wave analysis (left) and receiver functions by Licciardi et al. (2014) (right) show general agreement. Particularly interesting is the agreement on the south to north thinning of the crust.

crust from SW to NE in Ireland, but present some differences (in particular, our Moho map is constrained by more data and is thus less smooth than the map from Licciardi et al. (2014)). A Moho map for the British Isles obtained within a probabilistic approach utilizing data from a compilation of refraction, reflections profiles, and P-wave receiver functions is also plotted in Fig. 2.34.

The topography of the Moho computed in this work is reasonably accurate, at least comparing it with other previous works (see below for details), which confirms that the V_S distributions in our models are not affected by trade-offs with the crustal thickness. There is not full agreement, e.g., between Davis et al. (2012) (the authors estimated Moho map for several profiles within the British Isles using receiver functions), Landes et al. (2005) (which used data from 11 seismic refraction profiles onshore and offshore to investigate the crustal velocity structure of Ireland and surrounding seas), Kelly et al. (2007) (which compiled a regional model for crustal seismic P-wave velocities for NW Europe, from wide-angle reflection and refraction profiles), Tomlinson et al. (2006) (which computed the crustal thickness from teleseismic receiver functions analysis). Note, for example, that results from Tomlinson et al. (2006) on the Moho estimation correlate reasonably well with results from seismic reflection and refraction profiles (according to the authors, ±2 km),

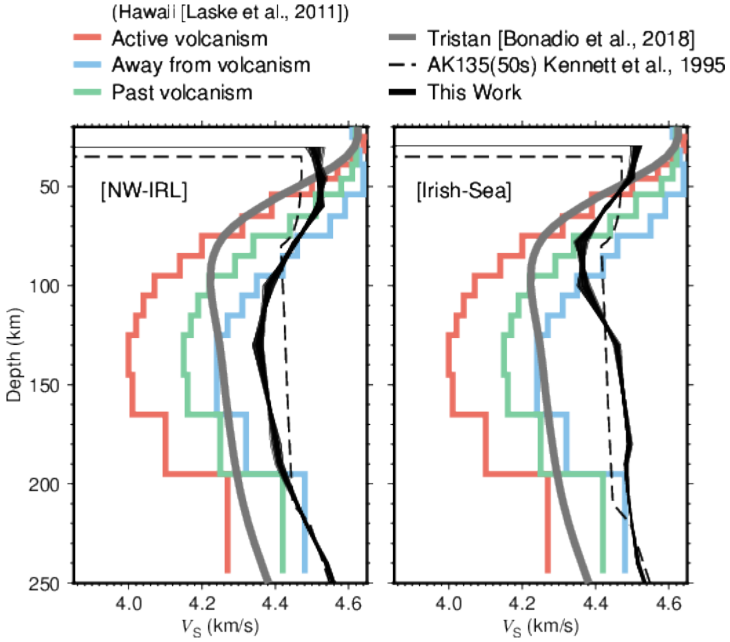

FIGURE 2.32: The shear-velocity anomaly profiles from our model (in black), for two locations in NW Ireland and in the Irish Sea, are compared with shear velocity profiles obtained in proximity of the Hawaii (Laske et al., 2011) and the Tristan da Cunha hotspots (Bonadio et al., 2018).

but receiver functions measurements from the stations close to the Iapetus Suture Zone (ISZ) show a difference up to 5 km. The main features of the area are, however, generally consistent across different maps. The British Isles generally present thicker crust in Avalonia (32–35 km), which thins north of the ISZ from ~35 to 26 km in northwest Scotland and Ireland. For comparison, the Moho maps after Landes et al. (2005), Kelly et al. (2007), Davis et al. (2012), and Tomlinson et al. (2006) are plotted in Figs. 2.36, 2.37, 2.47 and 2.48, respectively. One noteworthy feature is the inconsistency between the crustal thickness retrieved in Wales, between our results and, e.g., Tomlinson et al. (2006), Davis et al. (2012), and Maguire et al. (2011) (the Moho appears to be shallower according to our results). There is, however, an evident relationship between our results and the Curie depth (the Curie depth is often interpreted as the depth to the 580°C isotherm, and it is used to constrain the geothermal heat flow), with regards to a contrast between Wales and the neighbouring areas (e.g., Mather et al., 2018; Baykiev et al., 2018; Mather and Fullea, 2019) (e.g., Figs. 2.49 and 3.17).

Our results reveal important, previously unknown heterogeneity in the structure of the lithospheric plate beneath Ireland and Britain. The thinning of the lithosphere beneath the circum-Irish Sea region matches the area of the Paleogene uplift and volcanism and offers important evidence on their

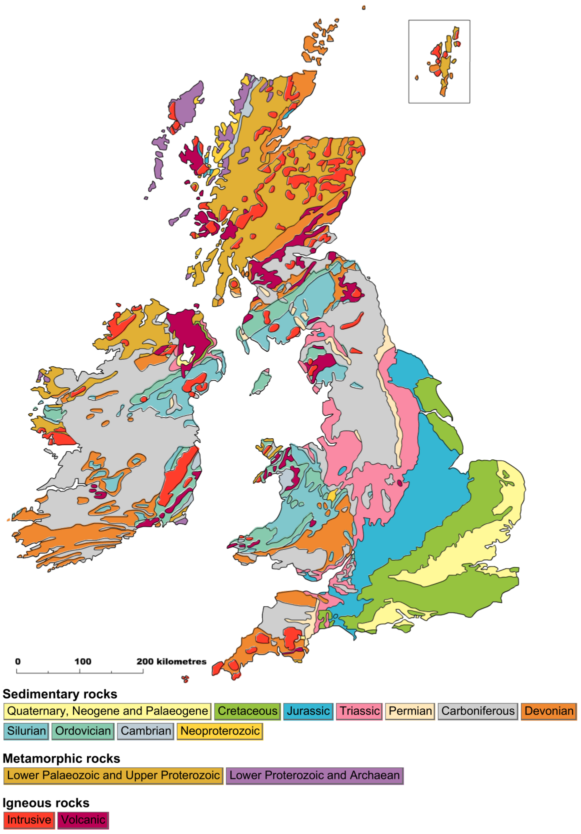

FIGURE 2.33: Simplified geological map adapted from British Geological Survey (*Make-a-map*).

mechanisms. The high velocity anomaly (which can be associated with a surprisingly thick lithosphere) in west-central and east-central Ireland may indicate the incorporation of previously unknown Precambrian continental blocks into the Irish landmass during the Caledonian Orogeny. This interpretation is consistent with the observations of Precambrian rocks in the west of Ireland (Figs. 2.33, 3.15 and 3.16).

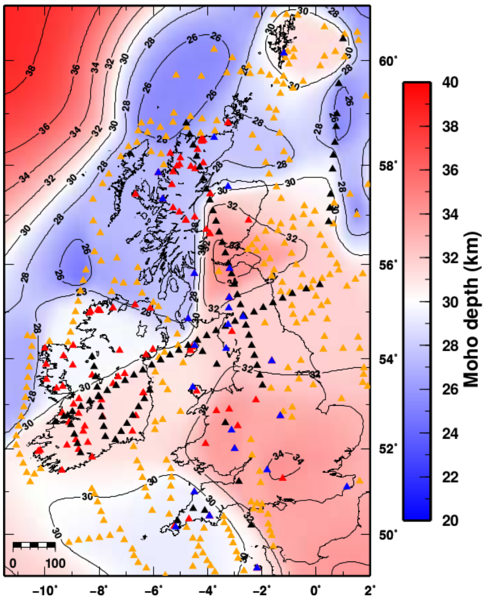

FIGURE 2.34: The Moho depth of the British Isles from a probabilistic perspective, courtesy of Licciardi A., England R., Piana Agostinetti N., and Gallagher K.

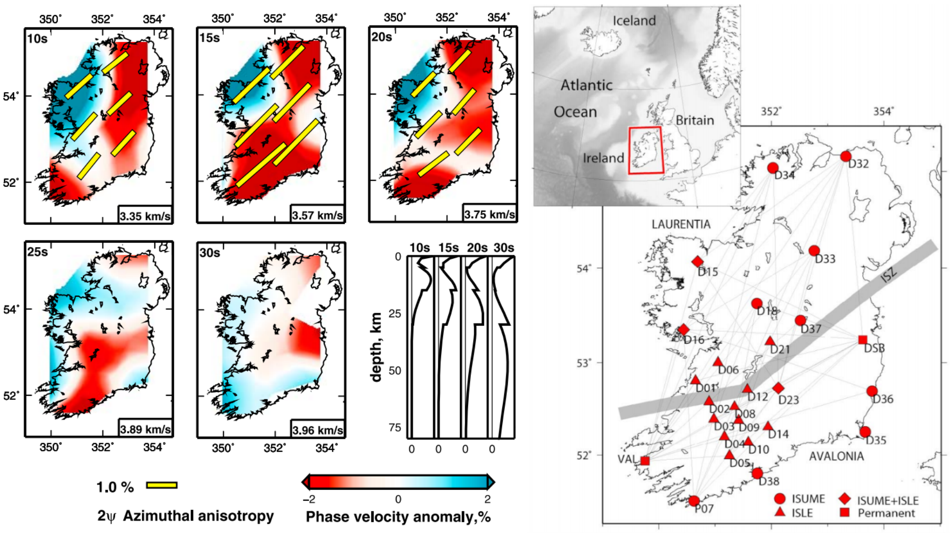

FIGURE 2.35: Tomographic maps of Rayleigh-wave phase velocities obtained by Polat et al. (2012). Yellow sticks show the fast-propagation directions and strength of azimuthal anisotropy. The data coverage of this work is significantly lower than the one used in our work (see Chapter 2).

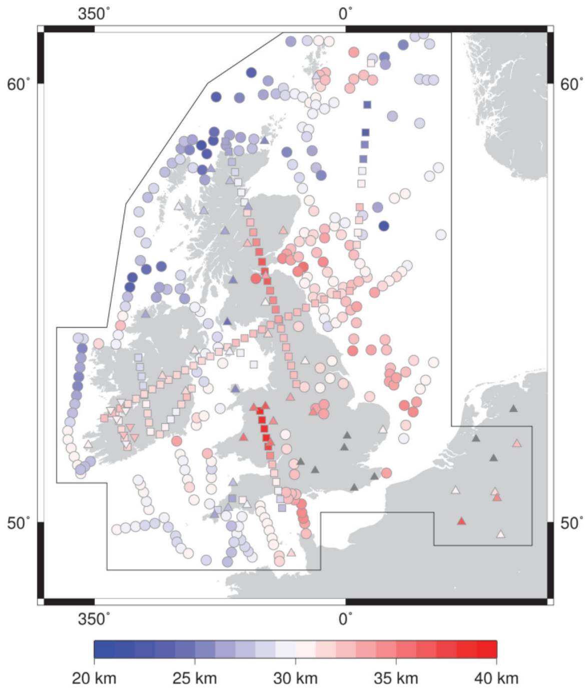

FIGURE 2.36: Estimated Moho depth for profiles within the British Isles, using receiver functions, after Davis et al. (2012).

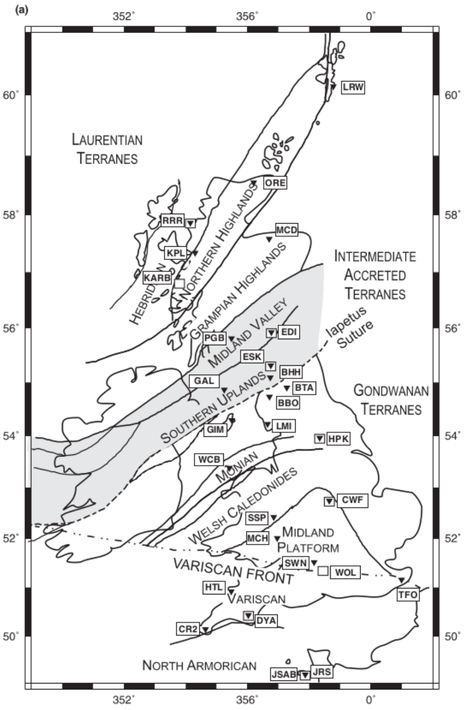

FIGURE 2.37: A geological terrane map of the British Isles after Tomlinson et al. (2006).

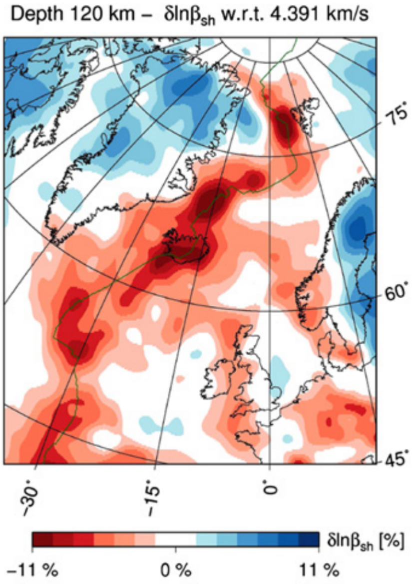

FIGURE 2.38: Slice at 80 km of the S-velocity model of the North Atlantic region obtained by Rickers et al. (2013), using full-waveform tomography. This slice shows a strong correlation between low velocity anomalies and the hypothesized branch of the Icelandic mantle plumes (e.g., Al-Kindi et al., 2003).

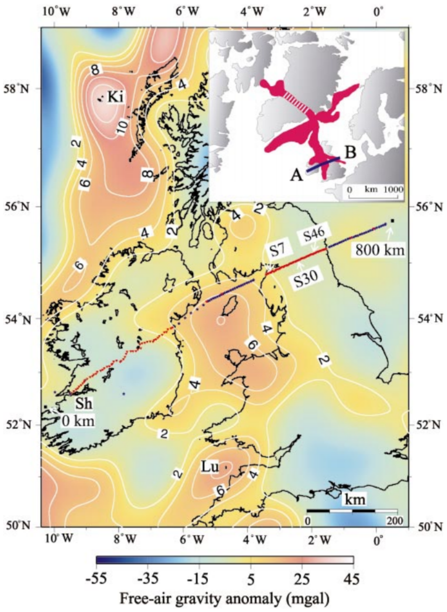

FIGURE 2.39: Free-air gravity map and reconstruction of the hypothesized hot convective plume fingers in the North Atlantic region from Al-Kindi et al. (2003). A positive gravity anomaly is centered in the Irish Sea, and correlates well with our tomographic images (e.g., in Chapter 2). The white contours show the predicted thickness of magmatic underplating determined by the authors using gravity and seismic data.

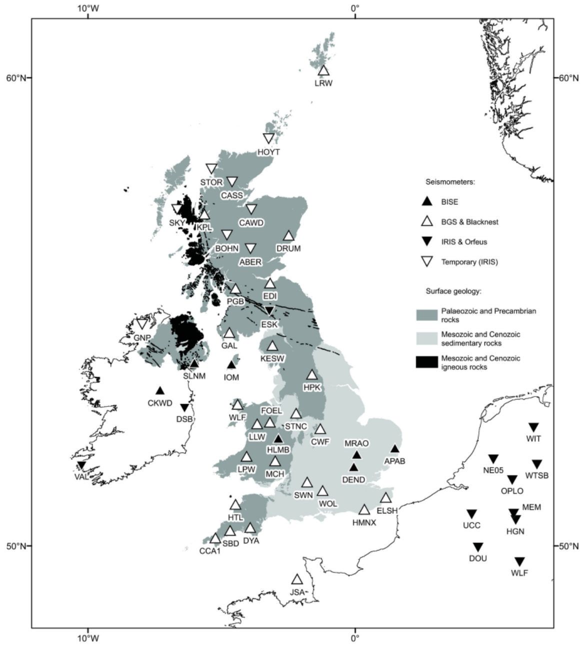

FIGURE 2.40: Simplified geological map of British Isles from Davis et al. (2012), shows the location of igneous rocks and dike swarms locations in the British Isles.

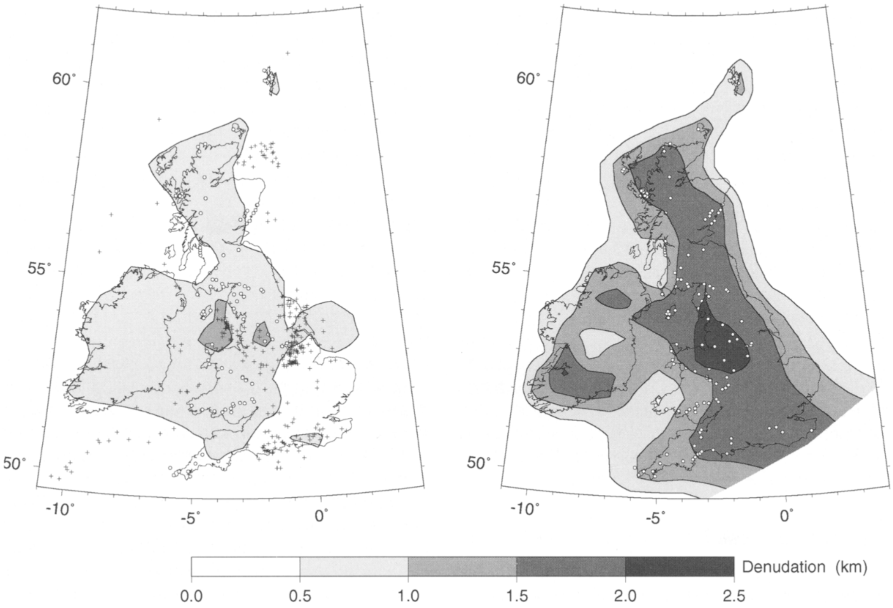

FIGURE 2.41: Jones et al. (2002) estimated minimum and maximum Cenozoic denutation in the British Isles due to dynamic uplift associated with the proto-Iceland plume. The influence of the proto-Iceland plume is manifesting itself strongly by long-wavelength free-air gravity anomalies, according to Jones et al. (2002).

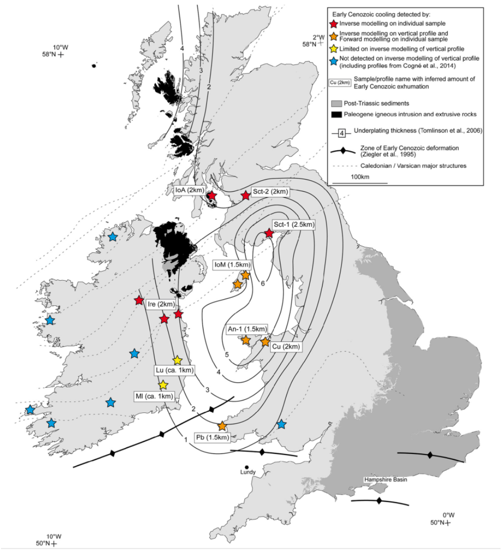

FIGURE 2.42: Map of Britain and Ireland after Cogné et al. (2016), showing the estimations of Early Cenozoic exhumation made by the authors, from low-temperature thermochronological measurements. Black lines represent the region of magmatic underplating postulated by Tomlinson et al. (2006).

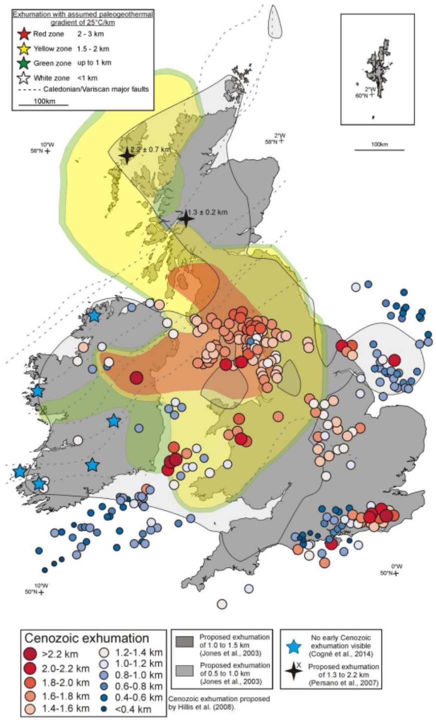

FIGURE 2.43: Early Cenozoic exhumation proposed by Döpke (2017), from low-temperature thermochronological measurements.

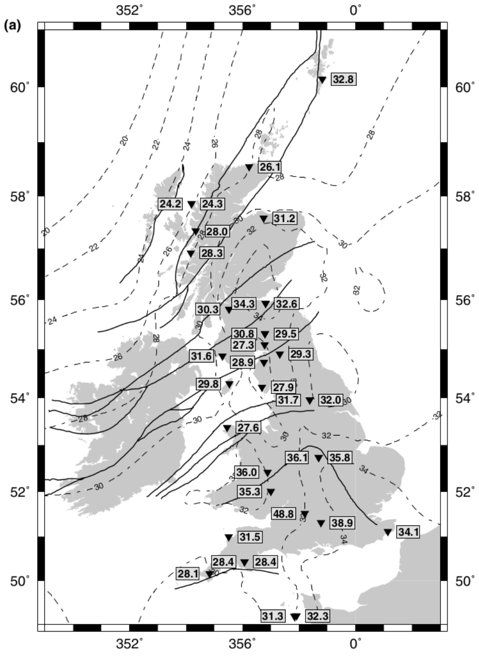

FIGURE 2.44: Map of crustal thicknesses after Tomlinson et al. (2006), inferred by the authors using teleseismic receiver functions analysis.

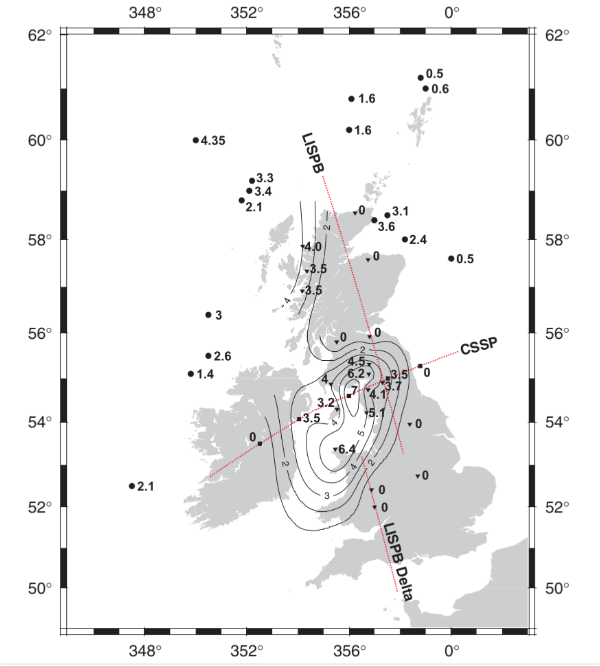

FIGURE 2.45: Map of underplate thickness beneath the British Isles proposed by Tomlinson et al. (2006), using results from receiver functions modelling (triangles) and seismic refraction velocity model from (Al-Kindi et al., 2003) (squares). The anomalously thick underplate layer beneath the Irish Sea and its surrounding areas correlates well with the low shear-velocity anomaly present in our model.

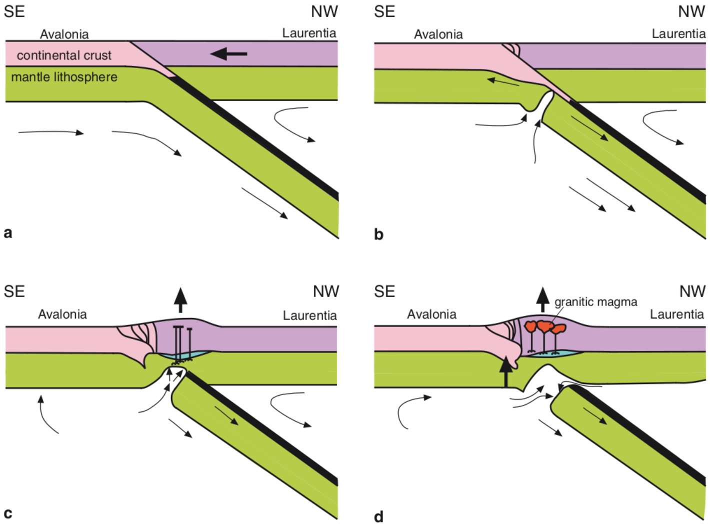

FIGURE 2.46: The cartoons represent the sequence of events induced by the slab break-off that followed the collision of Avalonia with Laurentia; figure after Chew and Stillman (2009).

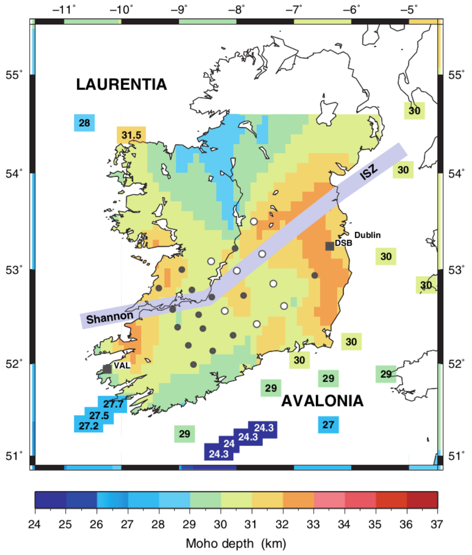

FIGURE 2.47: Map of Moho depth from Landes et al. (2005). The authors used data from seismic refraction profiles to investigate the crustal velocity structure of Ireland and surrounding seas.

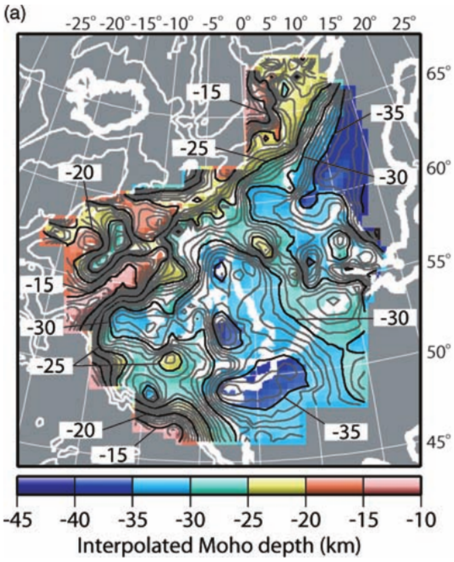

FIGURE 2.48: Moho topography map and its uncertainty after Kelly et al. (2007). The authors compiled a regional model for crustal seismic P-wave velocity structure, from a compilation of wide-angle reflection and refraction profiles.

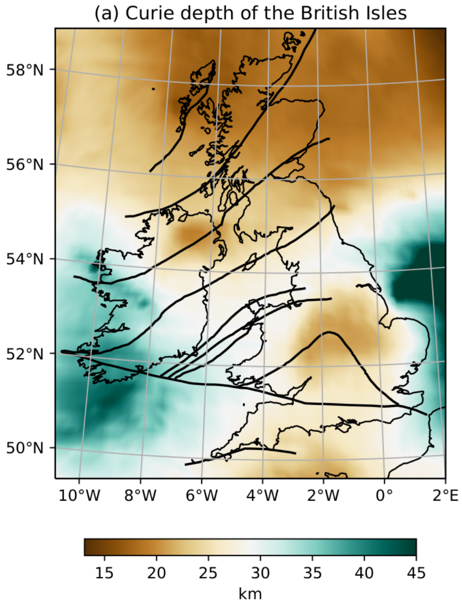

FIGURE 2.49: Estimated Curie depth topography in the British Isles after Mather and Fullea (2019), estimated in a Bayesian framework from magnetic data and associated surface heat flow (see also Fig. 3.17).

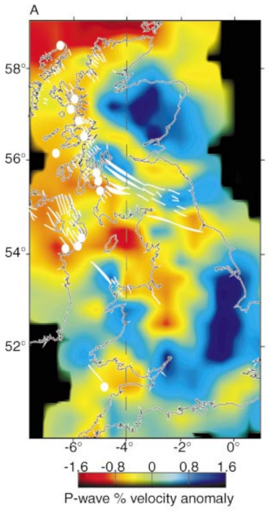

FIGURE 2.50: A horizontal slice, for a depth of 100 km, of P-wave velocity model from Arrowsmith et al. (2005). The circles and lines drawn in white show locations of Paleogene igneous centers and dike swarms, respectively. A very good correlation exists between the P-wave anomaly in this figure and the shear velocity anomaly in, e.g., Fig. 2.19, even though in Fig. 2.19 the anomaly extends even more southward in the Irish Sea.

Chapter 3

Rayleigh and Love surface wave tomography of the British Isles from ambient seismic noise

3.1 Introduction

In an attempt to better understand the lithospheric structure and tectonic evolution of the British Isles, several active and passive seismic studies have been carried out in the region. Our present understanding of the seismic structure of the crust below the region is mostly from active source experiments, including refraction and reflection seismics, and related works in which previously obtained active source results are used to infer information on the structure of the area (e.g., Bamford et al., 1978; Barton, 1992; Edwards and Blundell, 1984; Maguire et al., 2011; Bott et al., 1985; Jacob et al., 1985; Kelly et al., 2007; Lowe and Jacob, 1989; Landes et al., 2000; Masson et al., 1998; Hodgson, 2001; Freeman et al., 1988; Snyder and Flack, 1990; Klemperer and Hobbs, 1991; Klemperer et al., 1991; O'Reilly et al., 1996; O'Reilly et al., 2010; O'Reilly et al., 2012; Chadwick and Pharaoh, 1998; Hauser et al., 2008; Hodgson, 2001; Landes et al., 2005; Lowe and Jacob, 1989; Masson et al., 1998; Davis et al., 2012; Di Leo et al., 2009; Abramovitz et al., 1999; Freeman et al., 1988; Shaw Champion et al., 2006). In order to estimate the topography of the Moho beneath the area, and to investigate the crustal seismic properties, many authors combined results from active- and passive-source seismology (including receiver functions) (e.g., Licciardi et al., 2014; Asencio et al., 2003; Chadwick and Pharaoh, 1998; Landes et al., 2005; Kelly et al., 2007; Davis et al., 2012; Di Leo et al., 2009; Tomlinson et al., 2006). The crustal structure of the region has been also investigated using magnetotelluric, gravity, and petrological methods (e.g., Jones et al., 2013; Fullea et al., 2014; Rao et al., 2007; Readman et al., 1997; Brown and Whelan, 1955; Mather et al., 2018; Mather and Fullea, 2019; Baykiev et al., 2018). Surface-wave imaging of the lithosphere

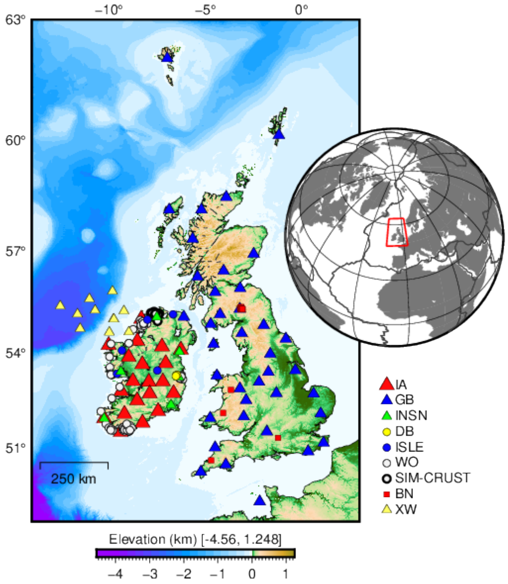

FIGURE 3.1: Topographic map of the investigated region. The seismic stations used in this study are shown in the legend on the bottom right. Topography and bathymetry are from the GEBCO dataset (IOC et al., 2003).

has been carried out in the past by Polat et al. (e.g., 2012) for Ireland (with relatively sparse and uneven data coverage achievable at the time, Fig. 2.35) and by Nicolson et al. (2012), Nicolson et al. (2014), and Galetti et al. (2016) for Britain and the Irish Sea, using group velocities (Figs. 3.18 and 3.19).

In this study, we use surface wave ambient noise tomography to derive detailed images of Rayleigh and Love wave phase velocities, in order to image the crustal structure beneath Ireland and its surroundings (Fig. 3.1). There are significant nearby sources of noise from the North Atlantic Ocean (e.g., Craig et al., 2016), and we can expect it to be very suitable for this type of measurements. All the available waveform data recorded at permanent and temporary arrays across the region, from more than 190 stations and collected between 1981 and 2018, were used to produce ~18000 vertical and ~8500 horizontal cross-correlation stacks. The networks and arrays include the Ireland Array (*IA*) (Lebedev et al., 2012), permanent stations of the Irish National Seismic Network (*INSN*) and the British Geological Survey (*BGS*), temporary stations deployed by the University College Dublin WaveOBS network (*WO*) and the BGS (*BN*), ocean bottom seismometers deployed offshore NW Ireland (Le Pape et al., 2016) (*XW*), and additional stations from the ISUME project (O'Donnell et al., 2011; Polat et al., 2012) and ISLE experiment (*ISLE*) (Landes et al., 2004; Landes et al., 2006; Wawerzinek et al., 2008). The combined station distribution yields an unprecedented geographical coverage of the region (Fig. 3.2) and makes possible detailed

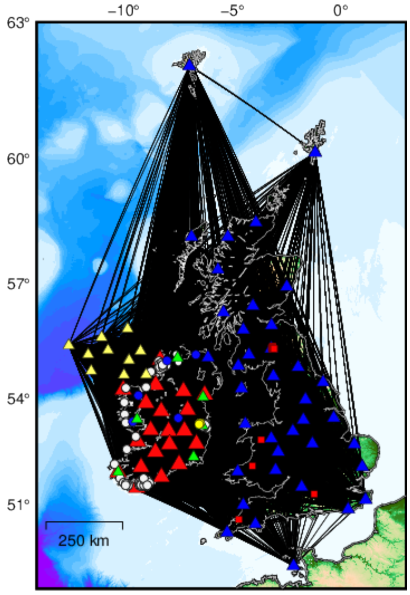

FIGURE 3.2: Station locations (as in the legend in Fig. 3.1) and interstation path coverage (black lines) yielded by our Rayleigh measurements.

tomographic mapping of the area.

3.2 Method

Over the last 15 years, ambient noise interferometry has revolutionized passive crustal seismology and has become an established technique for seismic imaging (e.g., Shapiro et al., 2005; Bensen et al., 2007; Yao et al., 2006; Lin et al., 2007; Lin et al., 2008; Arroucau et al., 2010; Rawlinson et al., 2014; Shapiro and Campillo, 2004; Snieder, 1972; Villaseñor et al., 2007; Tsai, 2009; Tsai, 2010). The ambient noise signal, which normally would be removed in traditional methods of seismic tomography, contains, in fact, information on the medium through which the seismic waves that contribute to it propagate. The signal is generated by wind, ocean waves, anthropogenic activities, and scattering caused by the Earth's heterogeneity and contains valuable structural information that can be extracted in order to make inferences on the seismic properties of a region. The information is extracted from the long-term cross-correlation of waveforms recorded at pairs of stations. The cross-correlation yields the Green's function between the two stations (in a virtual setting in which one of the station is the receiver, and the other station is an impulsive source), under the assumption that the ambient noise wavefields are random and uniformly distributed.

In this work we used 190 stations, some of which are from dense temporary arrays around local areas of special interest and others from networks distributed across Ireland and Britain. This results in a dense coverage for the entire region, with diverse path lengths (from ~2 to 1327 km). For the data processing, we developed our own workflow with a number of advantages over standard approaches (Bensen et al., 2007). We compute the ambient noise cross-correlation (ANCC) using the 3 (vertical and two horizontal) components for all simultaneously recording station pairs, with signals resampled at 10 Hz. The cross-correlation is performed on traces of 1 hour, for each possible station pair and each combination of components. No additional pre-processing is applied to the data, with no normalization or filtering, in particular (e.g., Saygin and Kennett, 2009; Arroucau et al., 2010). We only remove the trace from the dataset if it contains a recording gap. After stacking all the cross-correlograms for each station-station pair we take the so-called symmetric component, obtained by averaging the acausal and causal parts of the cross-correlograms (Fig. 3.3). The resulting waveforms can be interpreted, after the rotation of the horizontal components to the radial and transverse orientations, as the Rayleigh and Love wave components of the empirical Green's function, depending on which component of the cross-correlation tensor is considered (e.g., Lin et al., 2008; Udías, 1999). In this study, we used the ZZ and RR components for the retrieval of Rayleigh dispersion and the TT component for the retrieval of Love dispersion. Due to the varying availability of the data, the final stacked cross-correlograms are computed on sets from a minimum of 214 days (4914 hourly cross-correlations) to a maximum of 1365 days (32766 hourly cross-correlations). We verified that for all the azimuths across the area coherent wave signals exist in the empirical Green's functions (e.g., Fig. 3.3). This implies that the ambient noise computed within our frequency band of investigation (periods from ~0.2 to 37 s) is distributed sufficiently isotropically with azimuth and is likely to yield to unbiased dispersion measurements.

The extraction of the phase velocity dispersion of the fundamental Rayleigh and Love modes for each stacked cross-correlogram is obtained after using the multiple-filter technique to filter and window it (Dziewonski and Hales, 1972). Every stacked cross-correlation is filtered with a frequency-dependent Gaussian bandpass filter; in order to enhance the signal-to-noise ratio and reduce the effects of scattering, noise, correlations between fundamental mode and other parts of the waveform, the resulting signal is then windowed in the time domain with a frequency-dependent Gaussian window centered around the maximum amplitude of the frequency-filtered cross-correlation signal (Fig. 3.4). The phase velocity is then

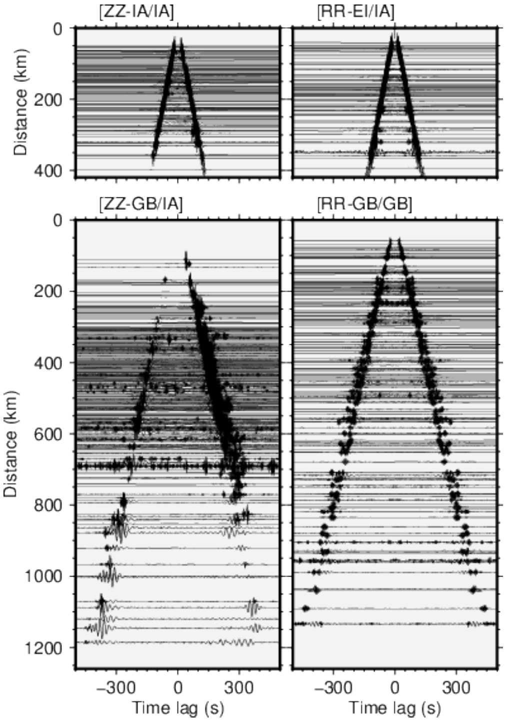

FIGURE 3.3: Unfiltered stacked cross-correlograms for some stations in Ireland (IA, EI) and in Britain (GB) show coherent signal. Cross-correlation functions are ordered by interstation distance. Left panel shows examples for ZZ component of the cross-correlation tensor; right panel shows the RR symmetric component, obtained by averaging the causal and acausal parts of the cross-correlograms. The coherent signal can be interpreted as the Rayleigh wave component of the Green's function, and be used to extract the phase velocity dispersion at each station-station pair.

computed from the resulting signal in the Fourier domain as the arctangent of the ratio of the imaginary to real part of the cross-correlation function (e.g., Meier et al., 2004). The difference between the two-station method used for teleseismic earthquakes (e.g., Meier et al., 2004; Soomro et al., 2016) and for ambient noise consists in applying a correction ($\pi/4$) to the phase, which is due to the far-field approximation (e.g., Boschi et al., 2013; Yao et al., 2006; Tsai, 2009; Tsai, 2010).

Accepted frequency bands for the phase velocities for each of the ~27000 cross-correlograms are selected automatically. Due to the $\pm 2\pi$ ambiguity generated when retrieving the phase velocity from the cross-correlation function (e.g., Boschi et al., 2013; Meier et al., 2004; Soomro et al., 2016; Bonadio et al., 2018), we needed to implement a criterion for the selection of the correct phase velocity curve (Figs. 3.4 and 3.5). Within the frequency range 0.1 – 0.5 Hz, we select the curve closest to a reference one. In this study, this

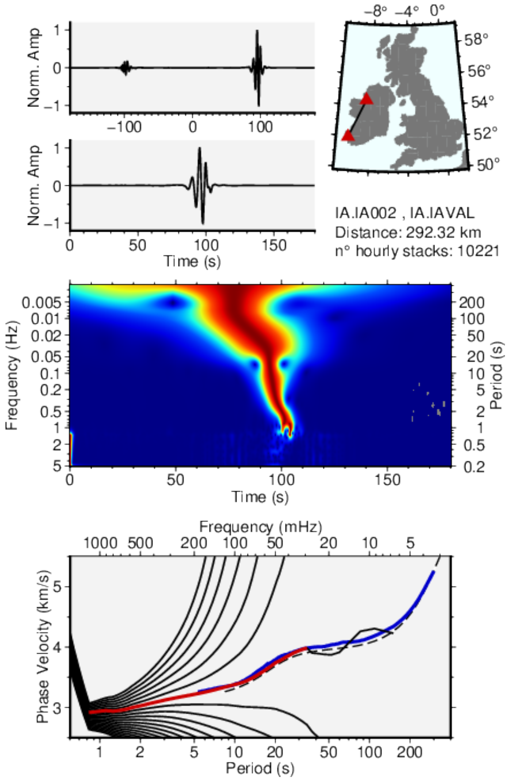

FIGURE 3.4: An example of phase velocity dispersion extracted from a ZZ cross-correlogram recorded at two stations in Ireland; the cross-correlation signal is filtered using a frequency-dependent Gaussian band-pass filter, to minimize the effect of noise and interferences on the fundamental mode. The resulting signal is then weighted in the time domain to reduce the effects of scattering or higher modes. The phase velocity is computed from the resulting signal in the Fourier domain as the arctangent of the ratio of the imaginary to real part of the Fourier spectrum. Black lines represents the phase velocity dispersion, including the curves resulting from the 2π ambiguity. The dashed black line represents the global model AK135 (Kennett et al., 1995) recomputed at 50 s (e.g., Lebedev and van der Hilst, 2008). The blue line is the average dispersion curve obtained by teleseismic cross-correlation (Chapter 2). The red line is the current selected dispersion curve for the considered interstation pair.

is the average phase velocity curve obtained by teleseismic cross-correlation (TSCC) at this particular station pair. If the TSCC measurement for a pair is unavailable, an average for the region is used as reference (Chapter 2). Only the smooth part of the curve, without roughness or bumps (e.g., Bonadio et al., 2018), is accepted as the final measurement. The automatic procedure, applied to all the stacks at each possible pair of stations, produces phase velocity dispersion measurements between ~0.2 and 37 s. The selection of measurements is then checked for outliers, removing measurements that are

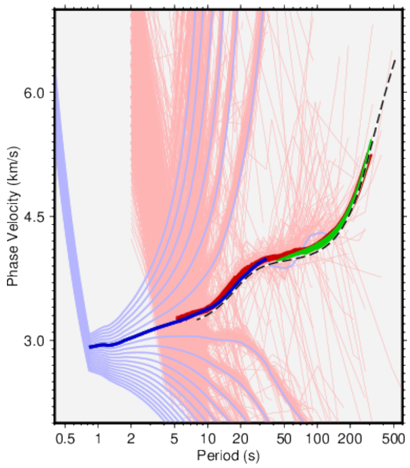

FIGURE 3.5: Different surface-wave analysis techniques contribute to complementary frequency bands of measurements, for stations pairs IA.IA002–IA.IAVAL (both stations in Ireland, see also Fig. 3.4). Dark blue, dark red, and green represents measurements from ambient noise, teleseismic cross-correlation, and waveform inversion (see also Chapter 2), respectively. Pale blue and pale red lines represent the curves affected by the 2π ambiguity for ANCC and TSCC. The match between different techniques decreases at the edge of the characteristic frequency band for each method. The dashed black line represents the global model AK135 (Kennett et al., 1995) recomputed at 50 s.

too far from the average. The final set of measurements is shown in Fig. 3.6. A sufficient number of measurements (3520) is obtained to produce tomographic dispersion maps (Deschamps et al., 2008; Lebedev and van der Hilst, 2008), as discussed in Section 3.3.

3.2.1 Comparison of ambient noise and teleseismic cross-correlation measurements

The ANCC allows us to obtain measurements at frequencies considerably higher than what we can obtain with TSCC (e.g., Fig. 3.7). The measurements produced using ANCC and TSCC overlap for a certain frequency band. The overlap range depends, for each station pair, on the signal-to-noise ratio, the interstation distance, and other factors. This offers us the possibility to compare the measurements obtained using the two different methodologies and cross-validate our results (Figs. 3.8 and 3.9). TSCC and ANCC measurements show an encouraging overall consistency (Fig. 3.10). There is, however, a relatively small but systematic inconsistency, increasing with periods and independent of the interstation distance or azimuth (Fig. 3.11).

The inconsistency between TSCC and ANCC at longer periods has been

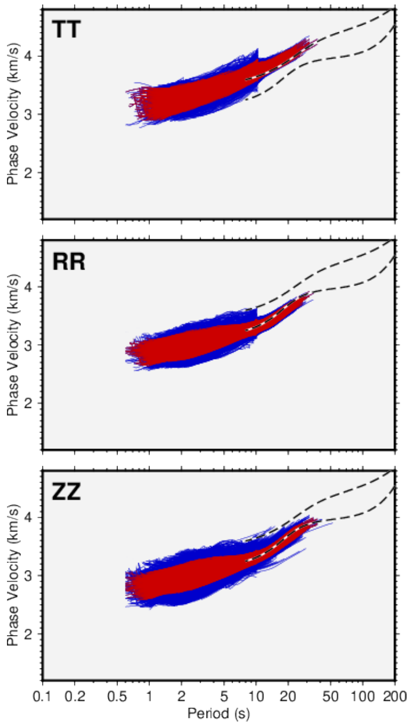

FIGURE 3.6: Final phase velocity measurements (in red) for ZZ, RR, and TT cross-correlograms, selected from the initial selections (in blue), used to produce the tomographic maps (see Figs. 3.12 to 3.14). Dashed black lines represent the global model AK135 (Kennett et al., 1995) recomputed at 50 s, for Rayleigh and Love surface waves.

attributed to the fact that the sensitivity kernels for earthquake data are more sensitive to off-path heterogeneity, and that wavefront perturbations may lead to a positive bias (e.g., Boschi et al., 2013; Weemstra et al., 2015; Kästle et al., 2016). However, the bias could also be due to a systematic processing artifact, as the signal-to-noise-ratio for ambient noise is usually decreasing with period whereas for earthquake data it is increasing. In spite of this small systematic discrepancy, our phase velocity maps (Figs. 3.12 to 3.14) at different periods are mutually consistent and agree well with geological and tectonic features and, more importantly, there is strong consistency in the patterns of lateral heterogeneity between the maps produced by TSCC and ANCC (e.g., Fig. 3.10). The velocity maps computed at all periods are shown in Appendix B.

3.3 Discussion

The interstation phase velocity curves for ZZ, RR, and TT components have been inverted for Rayleigh and Love phase-velocity maps (e.g., Deschamps

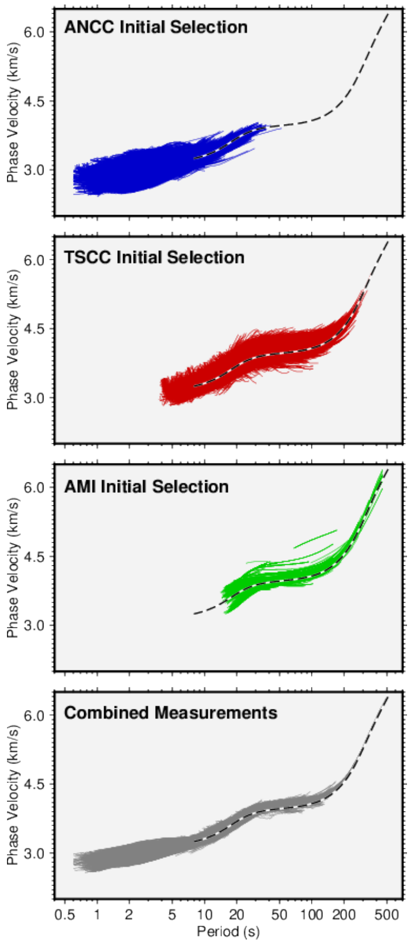

FIGURE 3.7: Different surface-wave analysis techniques contribute to complementary frequency bands of measurements. Ambient noise cross-correlation (ANCC) contributes for short/intermediate periods, two-station cross-correlation of teleseismic earthquakes (TSCC) produces measurements for intermediate periods, waveform inversion (AMI) contributes for longer period measurements. Combining the complementary measurements provide a large period range of measurements, which allows to map the subsurface from the crust to the asthenosphere.

et al., 2008; Lebedev and van der Hilst, 2008). The maps show interesting lateral variation in phase velocity (Figs. 3.12 to 3.14). Unfortunately, due to data availability and data quality, some areas in Britain are poorly covered at certain periods (especially the south-east England area). We can interpret the phase velocity maps in terms of shear velocity according to the sensitivity of Rayleigh- and Love-wave phase velocities as a function of depth (e.g., Schaeffer and Lebedev, 2013).

Our new tomographic results offer new insights into the structure of the crust of Ireland and surroundings. The maps are sensitive to velocities

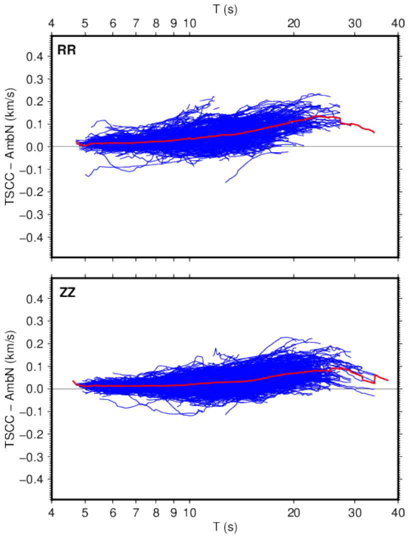

FIGURE 3.8: The differences between measurements produced with ANCC and TSCC, for ZZ and RR component, show a systematic inconsistency, greater at longer periods. Blue lines represents the difference for each measurement (for the overlapping band), red curve is the average of the entire dataset.

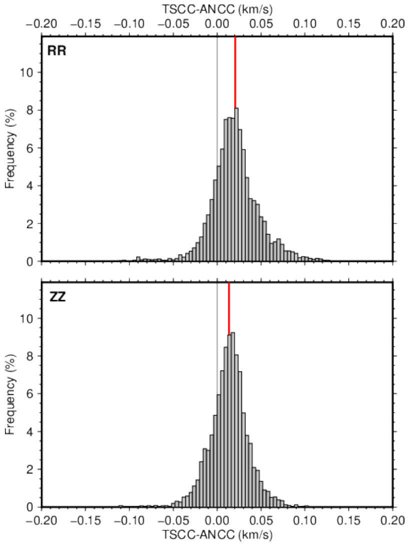

FIGURE 3.9: Histograms showing the differences between measurements produced with ANCC and TSCC, for ZZ and RR component, between 5 and 9 s. Red lines represents the mean.

throughout the shallow and middle-lower crust. At a broad look at the surface geology (Figs. 3.15 and 3.16) we see good agreement between the major geological features and the variations in phase speed; the contrast between the sedimentary cover, which shows pronounced low velocity anomalies, and

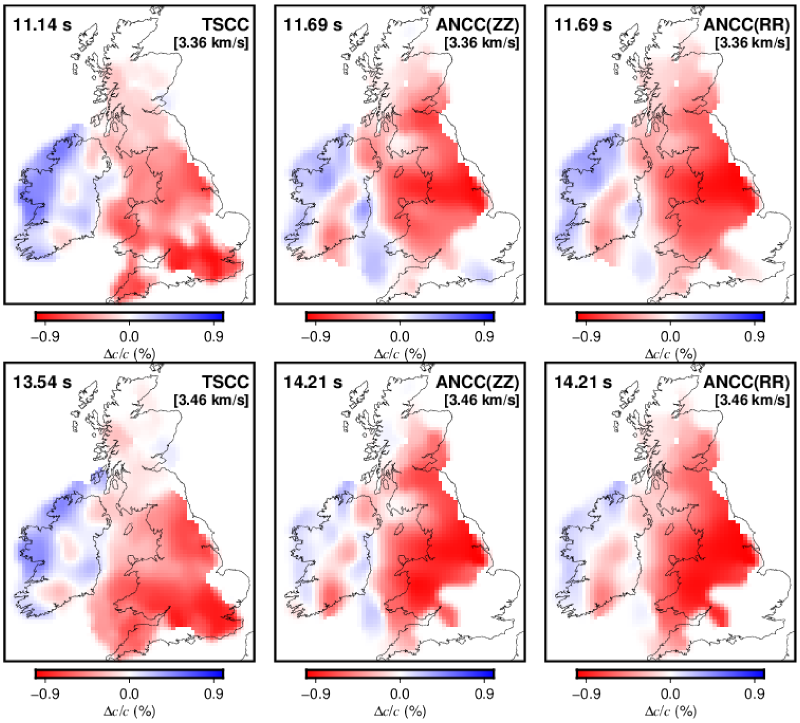

FIGURE 3.10: The comparison between phase velocity maps computed by TSCC and ANCC (for the vertical components), at periods ~11.5 and 14 s, show an encouraging overall consistency. Note that, due to different sampling, the maps are shown for slightly different periods.

the crystalline rocks beneath Ireland is evident (e.g., Figs. 2.33, 3.15 and 3.16) (e.g., Chew and Stillman, 2009; Chew and van Staal, 2014; Yardley et al., 1982; Dewey, 1982; Todd et al., 1991; Soper et al., 1992; Vaughan and Johnston, 1992). Ireland is surprisingly different from Scotland, showing much higher velocities, except for Northern Ireland.

A persistent feature in the phase velocity maps at very short periods is an elongated higher velocity region in Ireland, from west to east. At longer periods, this high velocity region fades out, but a clear boundary between west and east Ireland is still present. There is no correlation between the phase velocity maps and the major Caledonian and Variscan structures depicted (the gray lines in the maps). Generally, variations in the composition and temperature will affect seismic velocities at depth, which will be reflected in phase-velocity variations (e.g., Fullea et al., 2014; Mather et al., 2018; Mather and Fullea, 2019; Noller et al., 2015) (Fig. 3.17). The lack of correlations with the surface geology is even more evident at longer periods, given that the maps have stronger sensitivity to deeper structures. A clear correlation is observable, however, between marked low velocity anomalies and igneous intrusions, e.g., in north-eastern Ireland and western Scotland (Isle of Skye, Isle

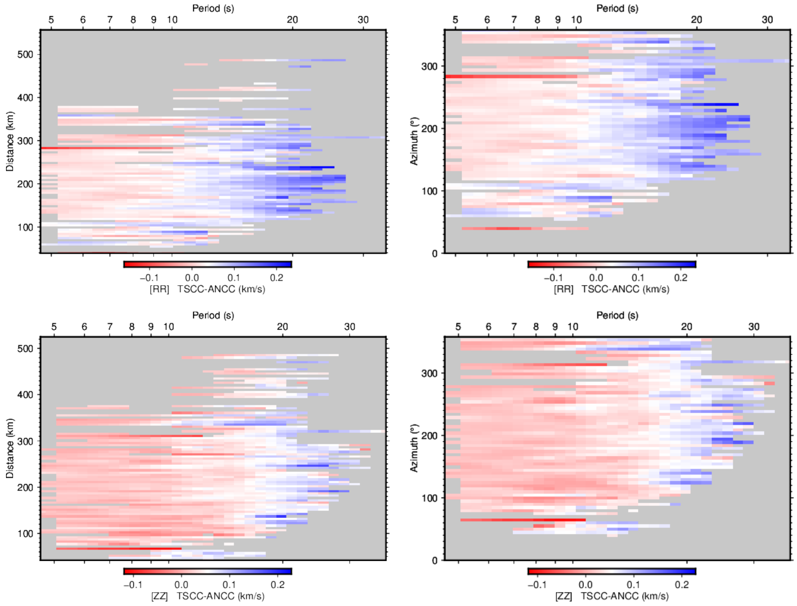

FIGURE 3.11: There is a relatively small but systematic inconsistency between TSCC and ANCC measurements, increasing with periods and independent of the interstation distance or azimuth. (Left panel: TSCC/ANCC difference VS frequency VS distance; right panel: TSCC/ANCC difference VS frequency VS azimuth.)

of Mull, Isle of Arran in Scotland and Antrim in Ireland are locations in which igneous outcrops dated in the Paleogene are found (e.g., Holford et al., 2009; Ganerød et al., 2010; Davis et al., 2012; Wilkinson et al., 2016)). A pronounced low-velocity anomaly is always manifest in the Irish Sea extending from North to South.

The velocity maps obtained with ANCC and TSCC (see Chapter 2) exhibit similar features at overlapping periods (Fig. 3.10). We note, however, that the shallow crustal structure is better constrained by ambient noise measurements.

A noticeable feature is the consistent difference between Britain and Ireland, at all periods. The higher velocity anomaly in western Ireland, in contrast to lower velocity anomalies in the rest of the area (including Britain and the Irish Sea) could be, potentially, an explanation for the lack of seismicity in Ireland, compared with the modest but clearly higher seismicity in Britain (Fig. 3.18) (e.g., Galetti et al., 2016). We show figures from previous group velocity tomography of the British Isles from Galetti et al. (2016) and Nicolson et al. (2014) for further comparison (Figs. 3.18 and 3.19).

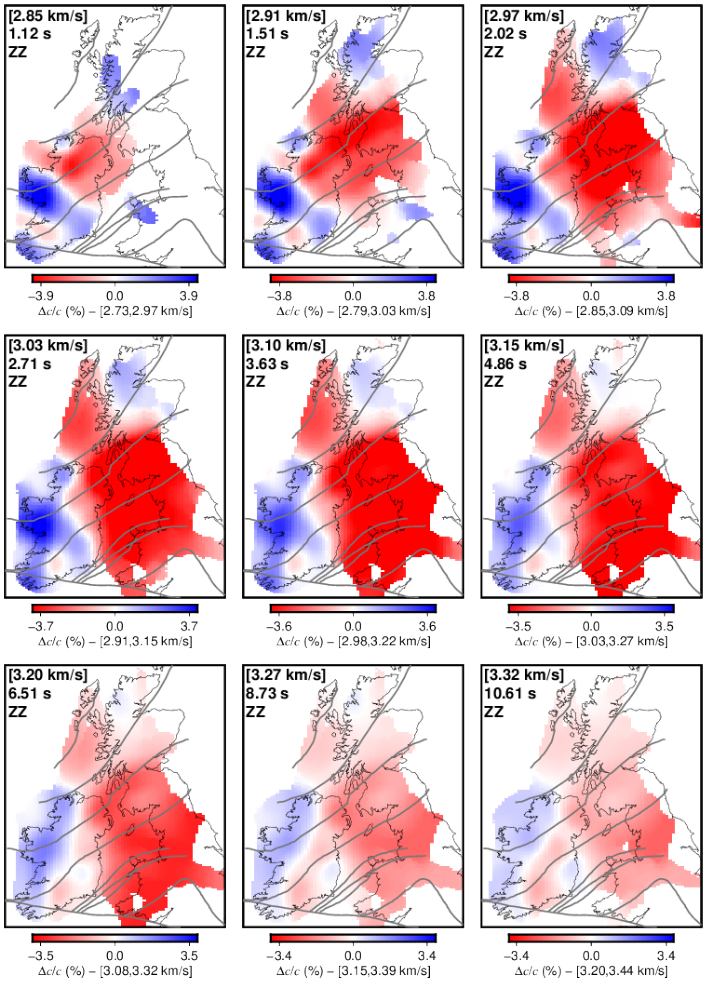

FIGURE 3.12: Phase velocity maps, for ZZ component. We show the reference phase velocity, the period of which the maps is computed, and the component on the top left corner of each map. The images have been cropped where coverage is extremely low. Color scale is relative to each map. We superimpose in gray lines the boundaries of the major surface geological features. We refer to Section 3.3 for discussion on the tomographic images.

3.4 Conclusions

We have presented surface wave phase velocity tomography from ambient noise measurements for Ireland and its surroundings. Rayleigh and Love phase velocity maps, obtained from more than 27000 cross-correlograms for 190 stations spread around the area, offer new insights into the structure of the crust of the investigated area.

We have further analyzed our data and compared the results with previously obtained phase velocity measurements from cross-correlation of teleseismic earthquakes. In spite of a systematic bias between the

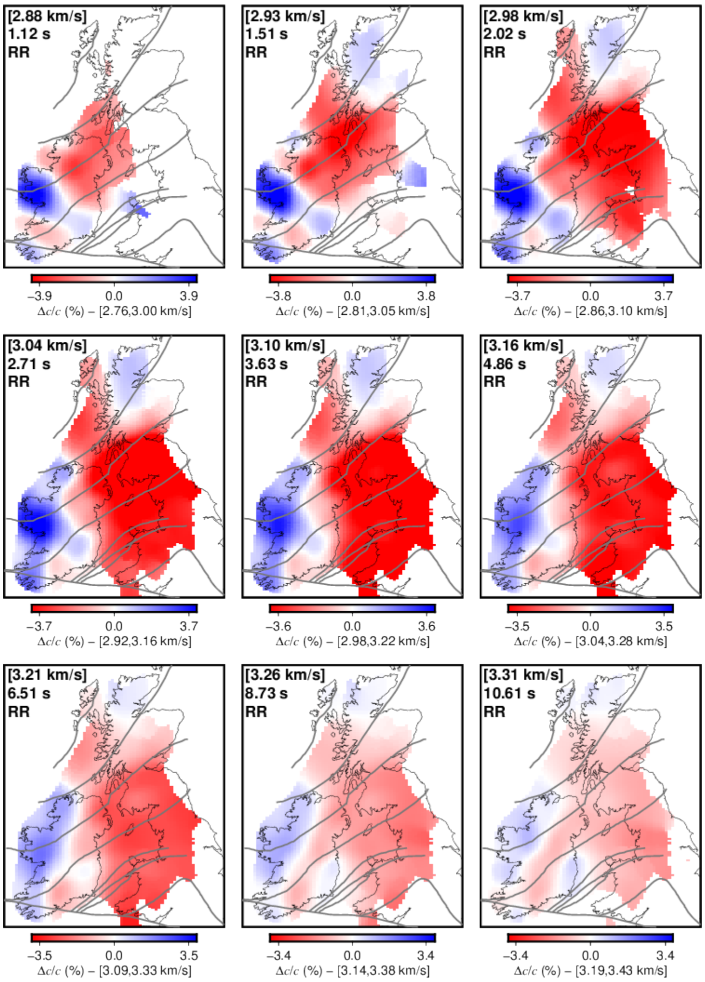

FIGURE 3.13: Phase velocity maps, for RR component. We show the reference phase velocity, the period of which the maps is computed, and the component on the top left corner of each map. The images have been cropped where coverage is extremely low. Color scale is relative to each map. We superimpose in gray lines the boundaries of the major surface geological features. We refer to Section 3.3 for discussion on the tomographic images.

two methods, previously attributed to different sensitivity to off-path heterogeneity for the two methodologies, the phase velocities show similar features for overlapping periods and show an overall encouraging consistency.

The phase velocity maps, sensitive to crustal structure, display a clear contrast between well consolidated blocks beneath Ireland and Scotland (high velocities) and sediments on the rest of the area (lower velocities). The strong velocity contrast between Ireland and Britain could be one of the answers to the long-standing mystery of the near absence of seismicity of Ireland, as opposed to the modest seismicity in Britain. The higher seismic velocities in the lithospheric mantle beneath Ireland (Chapter 2) indicate thicker, colder

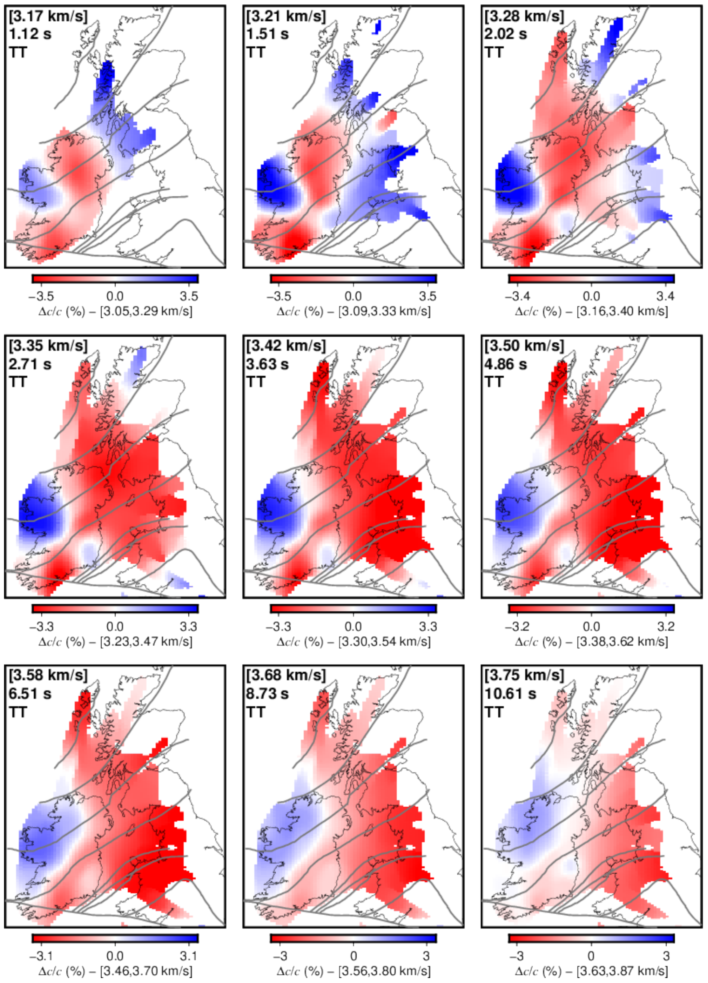

FIGURE 3.14: Phase velocity maps, for TT component. We show the reference phase velocity, the period of which the maps is computed, and the component on the top left corner of each map. The images have been cropped where coverage is extremely low. Color scale is relative to each map. We superimpose in gray lines the boundaries of the major surface geological features. We refer to Section 3.3 for discussion on the tomographic images.

and stronger mantle lithosphere. In the crust, the higher seismic velocities can be explained by either a colder geotherm or a combination of thermal and compositional differences.

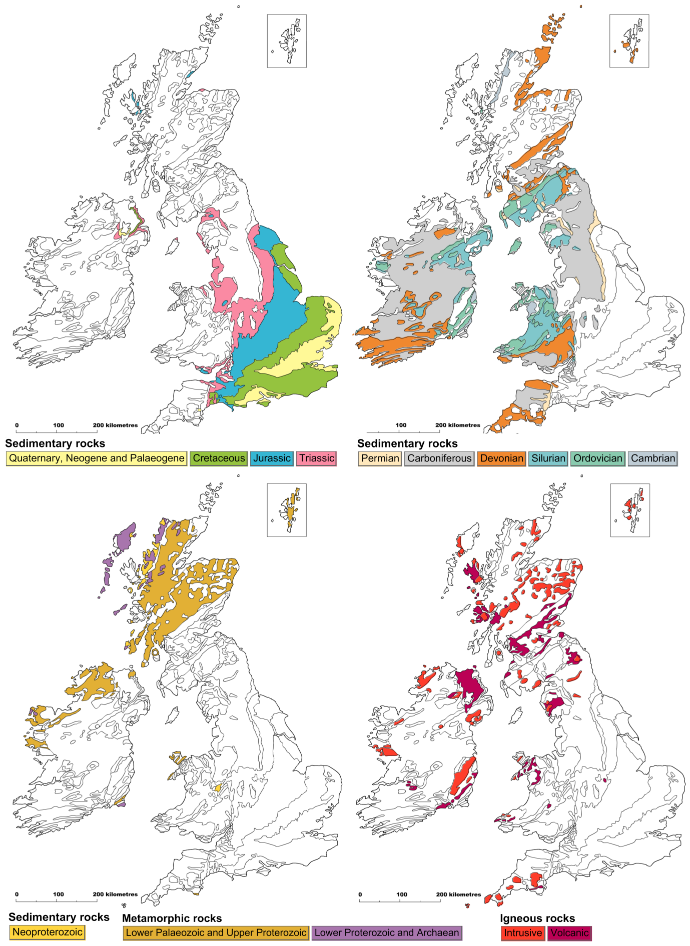

FIGURE 3.15: Simplified geological maps adapted from British Geological Survey (*Make-a-map*). Same features as in Fig. 2.33 are plotted, but in separated panels (top left panel: Cenozoic and Mesozoic rocks; top right panel: Paleozoic rocks; bottom panels: Upper Proterozoic rocks), to facilitate comparison with velocity maps (Figs. 3.12 to 3.14).

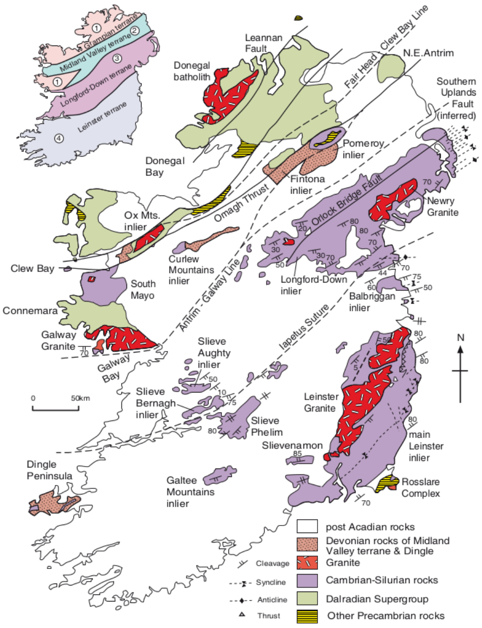

FIGURE 3.16: Map of Ireland showing location Late Caledonian tectonic features, from Chew and Stillman (2009). The inset figure on the top left shows the main tectonic terranes.

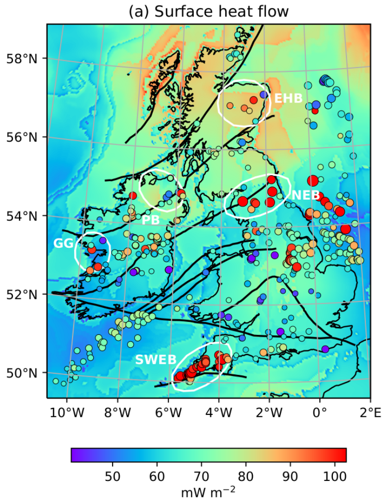

FIGURE 3.17: Surface heat flow in the British Isles obtained from Mather and Fullea (2019). Different surface heat flow, together with other factors, may be one of the explanation for the clear contrast between we find in Ireland in the velocity maps obtained, e.g., in Chapter 3.

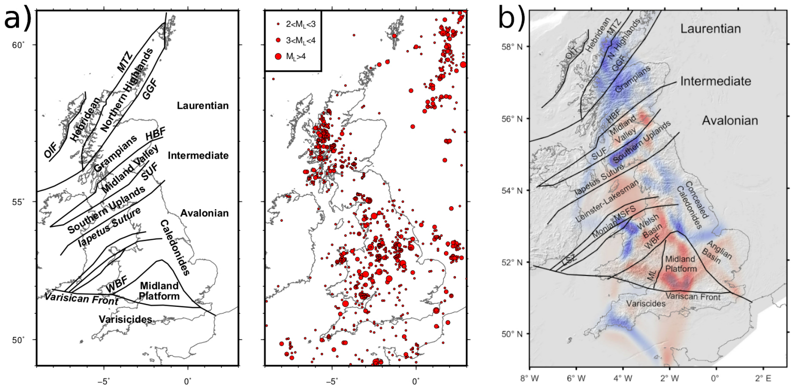

FIGURE 3.18: Panel (a): terrane boundaries (left) and seismicity (right) in the British Isles between 1970 and 2014 after Galetti et al. (2016) (Outer Isles Thrust (OIT); Moine Thrust (MTZ); Great Glen Fault (GGF); Highland Boundary Fault (HBF); Southern Uplands Fault (SUF); Welsh Borderland Fault System (WBF)). A strong contrast in seismicity between Ireland (where the seismicity is almost absent) and the rest of the area is evident. Panel (b): group velocity slice of the British Isles at 5 s obtained by Nicolson et al. (2014), using Rayleigh wave group velocity maps from ambient seismic noise.

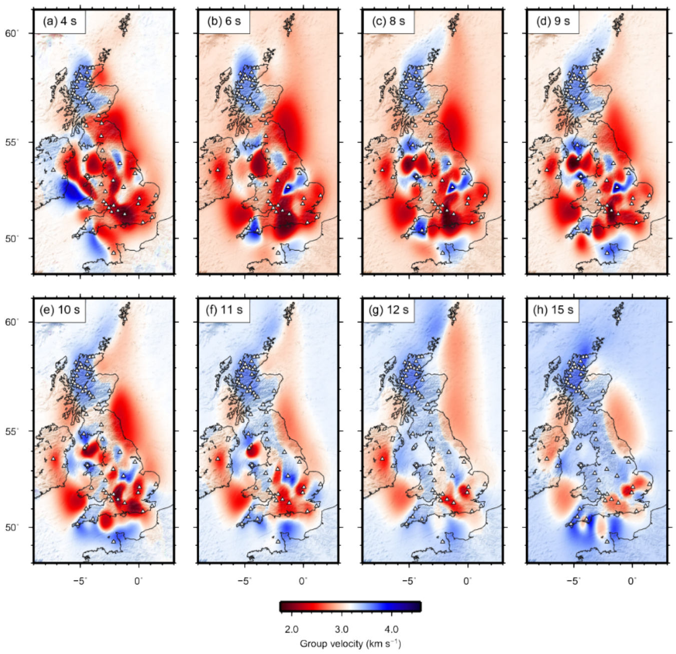

FIGURE 3.19: Love-wave Group velocity of the British Isles obtained with transdimensional tomography by Galetti et al. (2016).

Chapter 4

Hot upper mantle beneath the Tristan da Cunha Hotspot, from probabilistic Rayleigh-wave inversion and petrological modeling

[1] **Abstract** Understanding the enigmatic intraplate volcanism in the Tristan da Cunha region requires knowledge of the temperature of the lithosphere and asthenosphere beneath it. We measured phase-velocity curves of Rayleigh waves using cross-correlation of teleseismic seismograms from an array of ocean-bottom seismometers around Tristan, constrained a region-average, shear-velocity structure, and inferred the temperature of the lithosphere and asthenosphere beneath the hotspot. The ocean-bottom data set presented some challenges, which required data-processing and measurement approaches different from those tuned for land-based arrays of stations. Having derived a robust, phase-velocity curve for the Tristan area, we inverted it for a shear wave velocity profile using a probabilistic (Markov chain Monte Carlo) approach. The model shows a pronounced low-velocity anomaly from 70 to at least 120 km depth. V_S in the low velocity zone is 4.1–4.2 km/s, not as low as reported for Hawaii (~4.0 km/s), which probably indicates a less pronounced thermal anomaly and, possibly, less partial melting. Petrological modeling shows that the seismic and bathymetry data are consistent with a moderately hot mantle (mantle potential temperature of 1410–1430°C, an excess of about 50–120°C compared to the global average) and a melt fraction smaller than 1%. Both purely seismic inversions and petrological modeling

---

[1] This chapter has been published as: Bonadio et al., 2018. Hot upper mantle beneath the Tristan da Cunha hotspot from probabilistic Rayleigh-wave inversion and petrological modeling. Geochemistry, Geophysics, Geosystems, 19, 1412âĂŞ1428. https://doi.org/10.1002/2017GC007347.

indicate a lithospheric thickness of 65–70 km, consistent with recent estimates from receiver functions. The presence of warmer-than-average asthenosphere beneath Tristan is consistent with a hot upwelling (plume) from the deep mantle. However, the excess temperature we determine is smaller than that reported for some other major hotspots, in particular Hawaii.

Plain Language Summary The chains of volcanic ocean islands such as Hawaii are created when oceanic tectonic plates move over anomalously hot regions (hotspots) in the underlying mantle. The origin of hotspots has been attributed to mantle plumes, spectacular hot upwellings from the Earth's core-mantle boundary (2,800 km depth). The existence of the plumes and their occurrence beneath particular locations of volcanism are a matter of a heated debate. One way to find out whether a hot upwelling may be present is to determine the temperature in the mantle at depths just beneath the tectonic plate in the location of a hotspot. These depths are around 100 km, however, and temperature there cannot be measured directly. In this study, we used new seismic data from an array of ocean-bottom seismometers deployed around Tristan da Cunha, a prominent hotspot in the South Atlantic Ocean, and determined seismic velocities beneath it. Seismic velocities depend on the temperature of the mantle rock. We were able to use this dependence to infer the temperature within and below the tectonic plate around Tristan. The temperature is anomalously high. This is consistent with a hot mantle plume reaching Tristan from below and causing the unusual, long-lived volcanism at this location.

Key Points

- Lithosphere beneath Tristan is 65–70 km thick; the low-velocity zone below shows V_S of 4.1–4.2 km/s
- Mantle potential temperature that fits surface-wave and other data is 1410–1430°C
- The high mantle temperature is consistent with a plume origin of volcanism, but it is lower than beneath Hawaii

4.1 Introduction

Tristan da Cunha (TdC) is a hotspot in the South Atlantic Ocean, located ~450 km east of the Mid Atlantic Ridge (MAR) (Fig. 4.1 panel (a)). The intraplate volcanoes and seamounts that form the TdC archipelago are connected to the Cretaceous (~132 Ma) Etendeka continental flood basalt province in Namibia via the aseismic Walvis Ridge. The ridge is built-up by seamounts and submarine volcanic plateaus that show a clear age progression and extend from the Namibian continental margin (north-east) to the volcanic islands of TdC and Gough (south-west), surrounded by 10–30 m.y. old lithosphere. Age-progressive distribution of volcanic rock samples collected from the Walvis Ridge and the Rio Grande Rise west of the Mid-Atlantic Ridge provide evidence for the volcanism at TdC and the formation of the flood basalts in Namibia and Brazil to be due to a common hotspot source, with the Walvis Ridge and the Rio Grande Rise being the hotspot tracks (e.g., O'Connor and Duncan, 1990).

The origin of the TdC hotspot volcanism is debated, with competing hypothesis suggested. The TdC-Walvis Ridge system is one of the few examples of a complete hotspot track, and thus the TdC is believed by many workers to be a surface expression of an underlying mantle plume (e.g., Morgan, 1971; Morgan, 1997). The hypothesis of a deep mantle plume origin of the hotspot volcanism at the TdC archipelago is supported by anomalous geochemical data and geochronological constraints (REE inversions, ^{40}Ar/^{39}Ar geochronology and geochemistry of alkaline igneous rocks, chemical zonation, petrological and geochemical variations along the hotspot track) (e.g., Humphris et al., 1985; Gibson et al., 2006; Rohde et al., 2013b; Rohde et al., 2013a) and global tomography; Courtillot et al. (2003) defines TdC plume as "primary", French and Romanowicz (2015) classify TdC as "clearly resolved" plume.

Alternative explanations for the hotspot volcanism at and around TdC include convective processes in the shallow mantle, possibly a consequence of the South Atlantic opening, and faulting and fracturing of the oceanic lithosphere (e.g., Foulger and Natland, 2003; Fairhead and Wilson, 2005; Anderson, 2005). Other models (e.g., O'Connor et al., 2012; O'Connor and Jokat, 2015), while adopting the idea of a deep-sourced mantle plume, emphasize the relative motion between the African plate and the Tristan-Gough mantle plume since the opening of the South Atlantic. It has also been suggested that the origin of TdC could be controlled by the interaction between the African superplume and surrounding depleted mantle (Rohde et al., 2013a), or by the interaction of a plume with the MAR (e.g., Gassmöller et al., 2016).

Until recently, the seismic-station coverage of the South Atlantic, including the TdC region, was very sparse. Regional shear wave velocity (V_S) models derived from global observations of surface and shear waves (Fig. 4.1 panel (b)) show an anomalous region with low upper mantle velocities close to TdC (e.g., Zhang and Tanimoto, 1993; Schaeffer and Lebedev, 2013; Celli

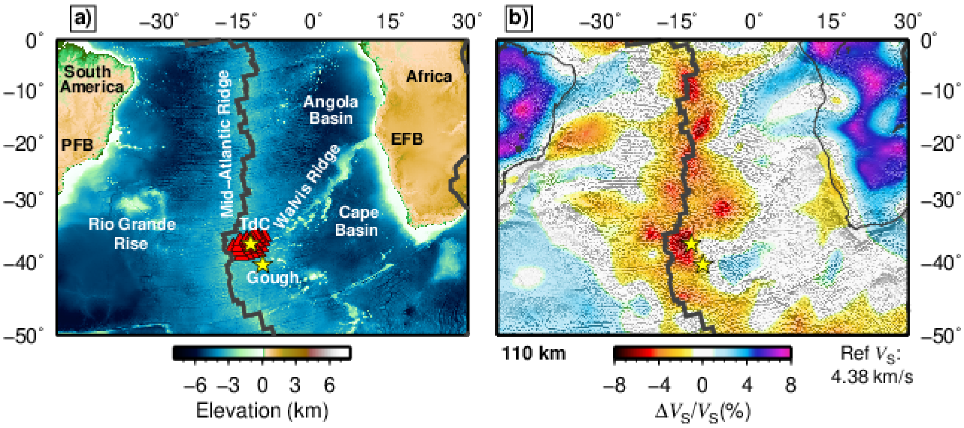

FIGURE 4.1: a) Topographic map of the South Atlantic region. The seismic stations deployed in the vicinity of the Tristan da Cunha (TdC) Hotspot are shown with red triangles. The TdC Hotspot (the yellow star over the triangles) is located ~450 km east of the MAR, at the southwestern extremity of the Walvis Ridge. b) Shear wave speed anomalies at 110 km depth beneath the South Atlantic region, according to waveform tomography of Celli et al. (2016). The two stars indicate the position of the TdC and Gough hotspots. A strong low V_S anomaly is located between TdC and the MAR. Topography and bathymetry are from the GINA (Lindquist et al., 2004) and ETOPO2 (NOAA, 2006) data sets.

et al., 2016), generally consistent with the hotspot volcanism there being due to anomalously hot asthenosphere, brought about by a mantle plume. However, the large-scale models are characterized by strong lateral averaging in the region and cannot be used to determine the thermal structure of the lithosphere and asthenosphere beneath TdC and its immediate surroundings.

In 2012–2013, an amphibious seismological and electromagnetic experiment was carried out in the vicinity of the archipelago (Section 4.2.1), with the goal of recording regional data that could provide insights into the regional-scale structure of the upper mantle beneath the area. The new data have already been used in a number of studies, including receiver-function analysis (Geissler et al., 2016), petrological analysis (Weit et al., 2016), magnetotelluric imaging (Baba et al., 2017), P-wave tomography (Schlömer et al., 2017) and ambient noise tomography (Ryberg et al., 2017). Intriguingly, the inferences from these studies differed. Schlömer et al. (2017) reported evidence for an underlying plume, imaging a low P-wave velocity conduit within the upper mantle, which could be regarded as the top part of a weak mantle plume. Geissler et al. (2016) measured the thicknesses of the crust, lithosphere and mantle transition zone using receiver functions and found no clear indications for the presence of a plume. Weit et al. (2016)

investigated melt generation and magma transport and storage beneath TdC, using thermo-barometric measurements, and inferred a mantle potential temperature (T_P) of ~1360°C for the TdC hotspot; the models proposed were consistent with a hot upwelling column with its base at around 90 km and its top at around 60 km. Baba et al. (2017) investigated the electrical conductivity structure of the upper mantle beneath TdC and did not find evidence of a distinct plume-like conductor beneath the area.

Key outstanding questions thus remain: is the asthenosphere beneath TdC anomalously hot, which it should be if the intraplate volcanism is caused by a hot upwelling (plume) from the deep mantle? Is the asthenosphere as hot as beneath recognized major hotspots, such as Hawaii? Are the thermal structure and thickness of the lithosphere beneath TdC anomalous and how do they compare to those beneath other major hotspots?

More observational evidence on the structure of the lithosphere-asthenosphere system beneath TdC is required to answer these questions and, ultimately, establish the origin of the TdC hotspot. In this paper, we measure phase velocities of Rayleigh surface waves using the data recorded by the Ocean Bottom Seismometer (OBS) array (Section 4.2.2) and invert them for the V_S distribution with depth using a probabilistic approach (Section 4.3). The V_S structure is sensitive to temperature and composition and yields new constraints on the thickness of the oceanic lithosphere and temperature within the asthenosphere. To verify and quantify our results further, we use computational petrological modelling (Section 4.4) and derive estimates of the mantle potential temperature, melt content in the asthenosphere and the thickness of the lithosphere beneath TdC.

4.2 Data and Measurements

Cross-correlation of seismograms from pairs of stations can produce measurements of the fundamental-mode phase velocities in a very broad period range (e.g., Meier et al., 2004; Roux et al., 2011; Soomro et al., 2016), sufficient to constrain V_S structure in the entire lithosphere-asthenosphere depth range (e.g., Lebedev et al., 2006; Ravenna and Lebedev, 2018). Our ocean-bottom data set, however, presented a number of challenges: low signal to noise ratios, low data redundancy due to the short term of the deployment and its remoteness from areas of abundant seismicity, and the (nominal) 60 s period limit of the wide-band instruments. This required development of data-processing and measurement approaches different from those tuned for land-based arrays of stations. Applying these to our data, we assembled a

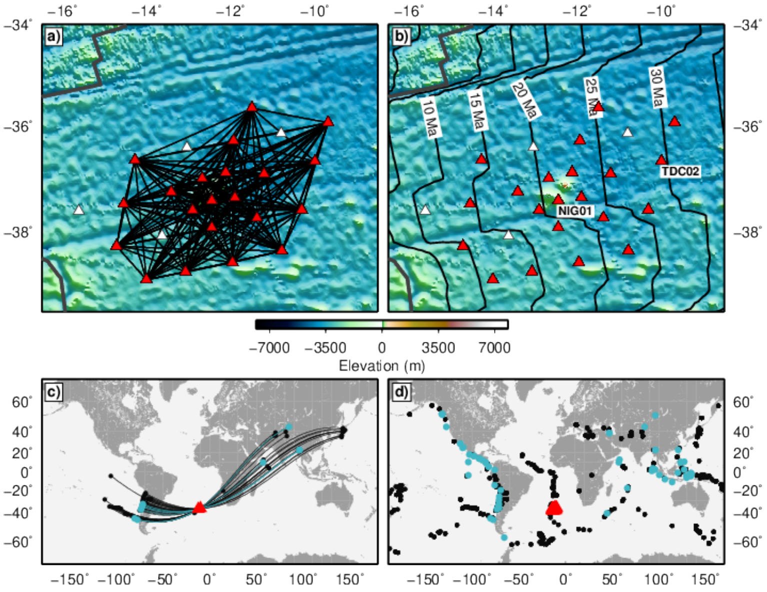

FIGURE 4.2: a) Station locations (triangles) and interstation path coverage (black lines) yielded by our measurements. White triangles are stations with no data available. b) Seismic stations and the seafloor age. The highlighted stations NIG01 and TDC02 are used in the following to illustrate the measurements (Figs. 4.3 and 4.4). c) Distribution of the events used to measure phase-velocity curves with the two-station method for the NIG01-TDC02 station pair; blue dots represent the events producing accepted measurements, out of all the events considered (blue and black). d) Distribution of the events used to measure phase-velocity curves with the two-station method for all the pairs; blue dots represent the events used for the final set of accepted measurements. Topography and bathymetry are from the GINA (Lindquist et al., 2004) and ETOPO2 (NOAA, 2006) data sets.

large number of carefully selected phase-velocity measurements, and derived a robust phase-velocity curve that averaged across the TdC area.

4.2.1 Data/Experiment

24 OBS from the German DEPAS pool (Deutscher Geräte-Pool für Amphibische Seismologie) and 26 ocean-bottom magneto-telluric stations from GEOMAR Kiel and the University of Tokyo were deployed around the archipelago of TdC (Geissler, 2014) (Fig. 4.2). The 24 OBS were equipped with Güralp CMG-40T broadband seismometers (60 s). The network also included two land stations (installed on Nightingale Island, southwest of the main island), each of which was equipped with a Guralp-3ESP seismometer (60 s). One of the stations (NIG01, Fig. 4.2 panel (b)), recorded earthquake data for the entire year, whereas the second station failed after a few days due to water

damage. Unfortunately, the permanent station TRIS also recorded very little data from early 2012 until the end of this experiment. Because the internal clocks of the OBS work independently for the duration of the experiment, the drifts of the clocks have to be measured by GPS synchronization before deployment and after recovery of the instruments. In two cases the second synchronization failed. We thus used the noise-correlation approach (Sens-Schönfelder, 2008) to estimate the clock drift for these two instruments. The data were then corrected for the 2012 leap second, quality-checked and response-corrected to displacement. Tilt and compliance corrections were not performed on the data, given that, ultimately, we used only vertical-component signal at intermediate periods.

4.2.2 Measurements

Phase velocities were measured using a powerful recent implementation of the interstation cross-correlation method (Meier et al., 2004; Soomro et al., 2016). For each pair of stations within the array, phase velocities of the fundamental Rayleigh mode were calculated by means of cross-correlation of the waveforms of teleseismic earthquake recordings.

In this implementation of the two-station method, the cross-correlation function is filtered with a frequency-dependent Gaussian bandpass filter, and then it is windowed in the time domain with a frequency-dependent Gaussian window centered on the maximum amplitude of the cross-correlation function. Parts of the cross-correlation signal likely to be due to noise or correlation between the fundamental mode and other parts of the waveform (body waves and surface-wave coda) are down-weighted (an example of phase velocity measurement is shown in Fig. 4.3). The resulting signal is transformed into the frequency domain and the phase is computed as the arctangent of the ratio of the imaginary to real part of the Fourier spectrum (Meier et al., 2004).

We performed our measurements using events from the Global Centroid Moment Tensor catalogue (Dziewonski et al., 1981; Ekström et al., 2012). We chose the events with back-azimuth within 20° from the station-station great circle path (GCP) and with a moment magnitude greater than 4.9, using a distance-dependent magnitude threshold as described in Schaeffer and Lebedev (2013). Phase velocities were computed from the phase of the cross-correlation function and the difference between the distances from the event to each of the stations (hence, the imperfect alignment of the two stations and the event had no immediate effect on the measurement accuracy).

The high noise level and the limited amount of usable ocean-bottom data necessitated careful, manual selection of acceptable phase-velocity

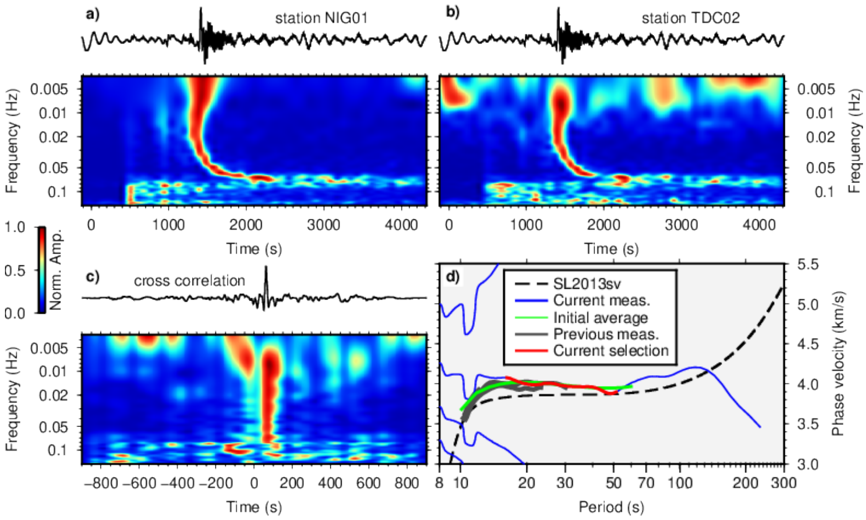

FIGURE 4.3: Example of an interstation, Rayleigh-wave, phase-velocity measurement for the station pair NIG01 (land) and TDC02 (ocean-bottom) (Fig. 4.2 panel (b)). a) and b): The recorded seismograms and the time-frequency representations of their waveforms. c) The cross-correlation function and its time-frequency representation. d) Phase-velocity curves (in blue, including alternative curves resulting from the 2π ambiguity) plotted together with the reference curve extracted from the global tomographic model SL2013sv (Schaeffer and Lebedev, 2013) (dashed black line). The current accepted segment is shown in red, previous measurements accepted for the current pair are shown in dark gray, initial average (computed from the distribution density plot, Fig. 4.5) used as the regional reference model is shown in green.

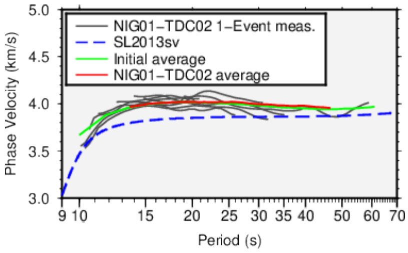

FIGURE 4.4: Results of the interactive, cross-correlation 1-event measurements of phase-velocity curves for the station pair NIG01-TDC02 (dark gray lines). Reference curves shown are SL2013sv (computed from Schaeffer and Lebedev (2013)) and the average regional curve extracted from the distribution density plot (Fig. 4.5).

measurements for each event. During the interactive measurement procedure, only smooth portions of phase-velocity curves were accepted. The criteria used for the selection were based on (1) the smoothness of the dispersion curve, (2) reasonable closeness to the reference model (exclusion of the

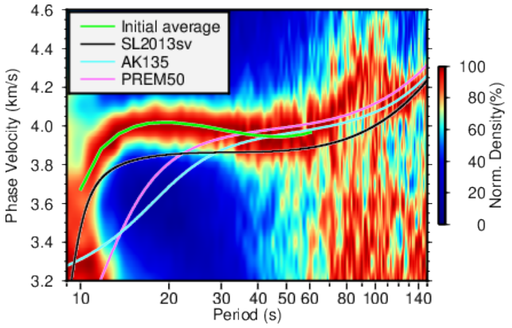

FIGURE 4.5: Density plot for the stack of automated preliminary measurements, normalized to the maximum at each period. The stack was computed using all branches of possible phase-velocity curves (including those affected by the 2π ambiguity), for all pairs of stations and for all automatically selected events. The average curve ("Initial average") determined from this distribution is shown in green. This regional reference is substantially different from those given by the global reference models AK135 (Kennett et al., 1995) and PREM50 (Dziewonski and Anderson, 1981) and from that extracted from the tomographic model SL2013sv (Schaeffer and Lebedev, 2013).

outlier measurements), (3) the length of the selected segments (very short segments were not accepted), (4) the difference between measurements from events at opposite directions from the station pair (a systematic inconsistency – not encountered with measurements with this data set – could indicate instrumental errors or strong diffraction effects), and (5) the minimum number of measurements for each frequency (2 measurements at least for each period) (Soomro et al., 2016). An example of the selection of dispersion curves for a pair of stations is shown in Fig. 4.4.

The phase velocity estimated from the cross-correlation function has to be compared with a reference model to eliminate the 2π ambiguity of the arctangent function and remove outlier measurements (Meier et al., 2004) (Fig. 4.3 panel (d) shows the array of possible phase velocity curves estimated from the cross-correlation function in blue). Initially, we tried out, as reference models, the Preliminary Reference Earth Model (PREM) (Dziewonski and Anderson, 1981), AK135 (Kennett et al., 1995), both models recomputed at a reference period of 50 s, and SL2013sv (Schaeffer and Lebedev, 2013) (as this is a 3-dimensional model, for each pair of stations five points of the model grid along the path are used in the average, the two end points and three equally spaced points along the GCP). Neither of these turned out to be suitable, however, and a more accurate regional reference was required.

An accurate, representative reference model is essential in order to resolve the 2π ambiguity, especially at shorter periods, in the course of interactive

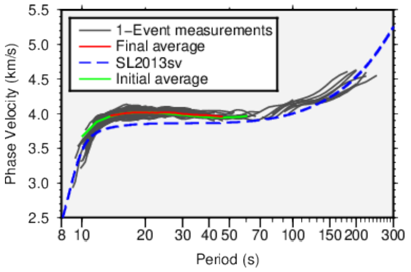

FIGURE 4.6: One-event dispersion measurements for all analyzed station pairs. The average phase velocity curve (red line) is used for the 1D inversion for V_S profile in depth. We limited the range of this curve to 13.6–46.5 s, where it is the smoothest, constrained by the most measurements and, therefore, the most accurate.

phase-velocity measurements. We found a way to extract such an average regional curve from the data quickly. We ran the automated phase-velocity measurement routine of Soomro et al. (2016) with loose selection criteria and marked all event-station pair combinations for which a measurement was successful for any curve segment. (This initial pre-selection is necessary to remove random "measurements" from seismograms dominated by noise.) For all the selected signals, we summed all branches of the entire families of possible phase velocity curves (with no attempt to resolve the 2π ambiguity) in the entire 8–250 s period range. This yielded a density distribution plot (Fig. 4.5) with a stack of all the measurements in the broad period range. With measurements from different interstation pairs stacked together, the region-average dispersion curve emerges clearly, with the curves affected by 2π ambiguity cancelling out. The stacking strategy for the extraction of a reference phase velocity dispersion curve is somewhat similar to that applied to ambient-noise data by Rawlinson et al. (2014). The maximum values of the distribution at each period have been used to extract a dispersion curve that was inverted using a nonlinear Levenberg-Marquardt gradient search algorithm (e.g., Meier et al., 2004; Lebedev et al., 2006; Erduran et al., 2008; Agius and Lebedev, 2013; Agius and Lebedev, 2014) for a V_S profile. The synthetic phase-velocity curve computed for this profile (green line in Fig. 4.5) represents an accurate regional reference model. The best-fitting synthetic is very similar to the simple stack but is smoother, as is appropriate for a reference model. Despite being computed using relatively noisy data, the density plot shown in Fig. 4.5 not only yields a useful reference for the subsequent case-by-case selection, but also shows that the measurements from the OBS data set naturally provide mutually consistent information.

We measured interstation phase velocities in a period range from ~8 to

~250 s, but since the instruments have a corner period of 60 s, only a small number of measurements (from the largest events) were successful at periods above 60 s. In order to constrain the lithosphere-asthenosphere structure beneath the area, we selected the most accurate measurements from all station pairs and computed a region-average dispersion curve (Fig. 4.6). Generally, all the single-measurement curves show similar features and almost all of them lie above the global reference curves and show phase velocities close to 4 km/s at periods above 12–15 s. The region-average curve was computed as a simple average of all the single-event measurements. It is the most robust and accurate in the period range 13.6–46.5 s. The curve in this range (Fig. 4.6) was inverted for the 1D V_S structure beneath the study area using a Markov chain Monte Carlo (McMC) algorithm (Section 4.3).

Our average dispersion curve (Fig. 4.6) shows a pronounced low-velocity anomaly at periods above 20 s. Comparing it to the Atlantic-average curves for 20-52 Ma lithospheric ages from James et al. (2014) (their Figure 5a), we observe that the curves show similar velocity values in the lithospheric range, while Tristan da Cunha average shows lower velocities at periods above 40 s (asthenospheric range). This indicates that the asthenosphere beneath Tristan is hotter than the Atlantic average for the Tristan-region lithospheric age. It is also useful to compare our phase velocities with those for the Indian Ocean from Godfrey et al. (2017); although the range of their overlap is narrow, we can see that the Indian Ocean dispersion curve for 20-52 Ma (green line in their Figure 3) and our average for Tristan da Cunha (e.g., Fig. 4.6) are similar. The 20-52 Ma dispersion curve in Godfrey et al. (2017) is probably representative mostly of the eastern part of the Indian Ocean, with the spreading along the Southwest Indian Ridge much slower than that along the Southeast Indian Ridge and, thus, with the area from which the curves are computed greater in the eastern part of the ocean. The phase-velocity average for the Indian Ocean thus reflects the rejuvenation of the lithosphere by the Kerguelen hotspot (Godfrey et al., 2017; Schaeffer and Lebedev, 2015). Our phase velocities at periods over 40 s, sampling the low velocity zone, are around 4.0 km/s, not as low as the 3.9 km/s reported for the active-volcanism part of Hawaii by Laske et al. (2011) (their Figure 4). By contrast, the Hawaii dispersion curve averaging along a path far from active volcanism (blue path in their Figure 4) shows velocities higher than in the Tristan da Cunha area.

We also inverted the interstation measurements from the various station pairs for phase-velocity maps (Lebedev and van der Hilst, 2008; Deschamps et al., 2008). The inversions showed that seismic-velocity heterogeneity in the area is relatively weak, which justified our use of a region-average profile to constrain the thermal structure of TdC. Because the lateral variations are relatively small and because the errors of the measurements are larger than in terrestrial studies using the same methods (e.g., Endrun et al., 2011; Polat et al., 2012; Pawlak et al., 2012), the variance reductions given by the tomographic inversions (Fig. C.1) are relatively low. The maps do show interesting lateral variation in phase velocity; maps for different periods and for stacked period ranges (computed to highlight the dominant anomalies and reduce artifacts) are shown, for completeness, in Appendix C (Fig. C.1 and Fig. C.2).

4.3 Probabilistic Inversion for an S-Velocity Profile

We inverted the average Rayleigh-wave, phase-velocity curve for the 1-D crustal and lithospheric V_{SV} (vertically polarized shear wave speed) structure using a Markov chain Monte Carlo (McMC) algorithm (Ravenna and Lebedev, 2018). The algorithm addresses the model non-uniqueness by directly sampling the parameter space in a Bayesian framework, providing a quantitative probabilistic measure of the solution space instead of a unique best-fitting model. The algorithm is also able to address the issue of data noise estimation by using a Hierarchical Bayesian approach (Bodin et al., 2012; Bodin et al., 2016), which allows the variance of data noise to be treated as an unknown in the inversion (Ravenna and Lebedev, 2018).

Both the crustal and mantle structure were inverted for. The a priori information on the model parameters was expressed in terms of Gaussian prior probability distributions (characterized by standard deviations of approximately 400 m/s for the shear-velocity parameters and 2 km for the Moho depth) centered at values from the reference model. As a reference crustal model, we used a 4-layered crustal model of the TdC region taken from CRUST 2.0 (Bassin et al., 2000), with a 3.4 km thick water layer and a Moho depth of 10.1 km. The reference model for the mantle is a modified version of AK135 (Kennett et al., 1995), characterized by constant shear velocities (4.45 km/s) until 220 km depth and linearly increasing shear velocities below 220 km depth. The sampled models were parameterized with ten control points in the mantle (until 410 km depth) that represented the knots of piecewise cubic Hermite spline polynomials.

The posterior distribution of the V_S profile and the models sampled in the McMC inversions are shown in Fig. 4.7 panels (a) and (b), respectively. The posterior distribution comprises an ensemble obtained by merging the models sampled by four chains of iterations running independently. The corresponding synthetic phase velocities and the relative misfit to the measured data are shown in Fig. 4.7 panels (c) and (d), respectively.

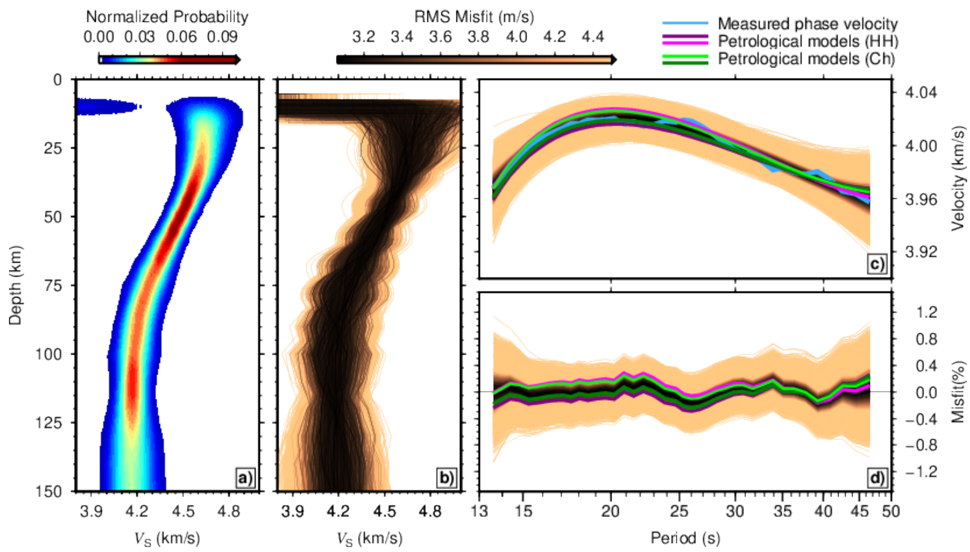

FIGURE 4.7: a) The posterior distribution of the V_S profile with depth. b) The models sampled in the McMC inversions. The posterior distribution comprises an ensemble obtained by merging the models sampled by four chains of iterations, each running independently. c) The corresponding synthetic phase velocities. d) The relative misfit relative to the measured data. All curves in b), c), and d) are colored according to the level of fit to the data. The light-blue line shows the measured phase velocities used in the inversions. The other curves show phase velocities computed for the petrological models described in Section 4.4.

Because of the limited period range of the data, we can expect it to constrain V_S structure down to somewhere in the shallow asthenosphere only. Fig. 4.7 panel (a) shows that the model is well constrained down to about 120 km depth and is uncertain below. [2]The profile displays a clear contrast between the high-velocity lithosphere, with V_S up to 4.6–4.65 km/s, and a low-velocity asthenosphere, with V_S down to 4.1–4.2 km/s. The depth of the lithosphere-asthenosphere boundary can be estimated at around 65–70 km.

4.4 Petrologically Derived Models

Our inversion of phase velocities yields a probabilistic V_S profile and shows a range of models that fit the surface-wave data. Only some of these models would be consistent with other available data, in particular the bathymetry in the region. We now take an alternative approach to the purely seismic inversion and use the integrated geophysical-petrological software LitMod

---

[2] The following text in Bonadio et al. (2018) presents a typographic mistake which has been corrected here.

(e.g., Afonso et al., 2008; Fullea et al., 2009) to estimate the thermal structure of the lithosphere-asthenosphere system consistent with both the seismic data and bathymetry. We compute a series of models of the lithosphere and the sublithospheric upper mantle and use them to estimate the range of values for the lithospheric thickness and the melt fraction and temperature of the asthenosphere beneath TdC.

The lithospheric geotherm is computed under the assumption of steady-state heat transfer in the lithospheric mantle, considering a P-T-dependent thermal conductivity in the mantle and prescribed thermal parameters in the crust. In the convecting sub-lithospheric mantle, the geotherm is given by an adiabatic temperature gradient. Between the lithosphere and the convecting sub-lithospheric mantle, we postulate a transitional buffer layer, characterized by a continuous linear super-adiabatic gradient (i.e., heat transfer is controlled by both conduction and convection, see Fullea et al. (2009) for details). This linear super-adiabatic gradient is controlled by the assumed temperature at the base of the lithosphere and sublithospheric mantle potential temperature. Stable mineral assemblages in the mantle are calculated using a Gibbs free energy minimization as described by Connolly (2005). Anharmonic seismic velocities are computed as a function of pressure, temperature and bulk composition in the mantle as described in Fullea et al. (2012). Melt fractions are computed based on a mantle-peridotitic dry solidus and liquidus (Katz et al. (2003) and references therein). The effects of melt on V_S and V_P are computed according to the two experimental models: (Hammond and Humphrey, 2000a; Hammond and Humphrey, 2000b) and Chantel et al. (2016) ("HH" and "Ch", respectively, in the legend in Fig. 4.8).

Introducing melting into our models leads to discontinuous V_S and V_P decreases at the onset of even small fractions of melt (<1%). In line with experimental results suggesting a progressive, V_S-decreasing effect of anelasticity below the solidus temperature (e.g., Yamauchi and Takei, 2016; Takei, 2017), we implement a linear parameterization to smooth the effect of melt on anharmonic seismic velocities over a temperature range in the vicinity of the solidus. We use a homologous temperature T_m defined as the temperature normalized to the solidus temperature (i.e., $T_m = 1$ at the solidus) and define a critical homologous temperature, T_{mc}, at which the anelasticity effects are introduced. Within the buffer range $T_{mc} <= T_m < 1$ the melt fraction varies linearly from zero at $T_m = T_{mc}$ to a threshold melt fraction at $T_m = 1$. (We emphasize that the gradient so defined does not represent actual melt but serves as a smoothing parameter, reflecting pre-melt effects on the rock aggregate anelastic behaviour.) Slight further smoothing of the V_S profiles is performed using a sliding boxcar window with a 20 km half-width.

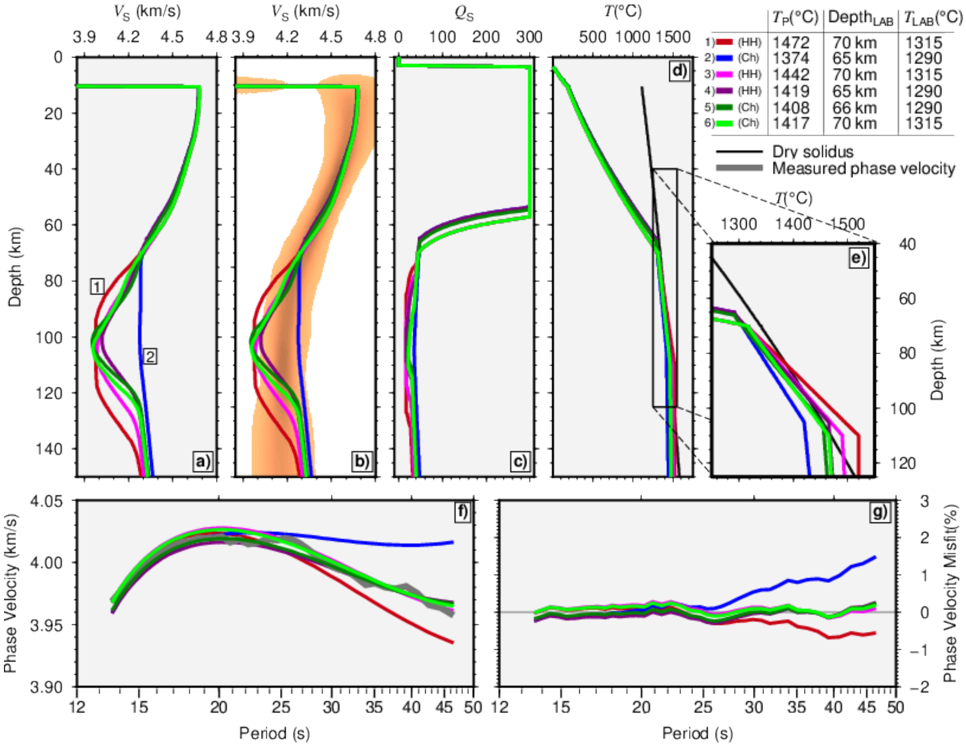

Figure 4.8: Six different petrological-geophysical models. Models 5 and 6 (dark and light green lines) and models 4 and 3 (dark and light purple lines) fit the data, whereas the other two models (1 and 2, red and blue lines, with the lowest and the highest V_S in the asthenosphere, respectively) do not. The key differences that set the models apart are the mantle potential temperature (T_P), LAB depth (Depth$_{LAB}$) and LAB temperature (T_{LAB}); the values for these parameters are listed in the legend, top right. a) and b) Shear velocity. The posterior distribution yielded by the purely seismic inversion is plotted in the background in Fig. 4.8 panel (b)). c) Anelastic attenuation factor. d) Temperature. e) A zoom on the geotherms in the depth range comprising the LAB and the transitional layer beneath it. f) Phase velocities. g) Phase-velocity misfits yielded by the models. ~1% melt is present in model 1 from ~85 to ~140 km, in model 3 from ~88 to ~130 km, in model 4 from ~95 to ~122 km; <~0.5% melt is present in model 5 from ~80 to ~117 km; melt is absent in models 2 and 6. "HH" and "Ch" indicate whether the model has been computed using, respectively, the parameterization by Hammond and Humphrey (2000a) and Hammond and Humphrey (2000b) or Chantel et al. (2016).

In all our models we correct for anelastic attenuation effects as in Fullea et al. (2012) but we also include melt related variations in the seismic quality factor (Q) based on the laboratory results by Chantel et al. (2016). Surface elevation is modeled according to the local isostasy at lithospheric scale as described in Fullea et al. (2009). The assumed lithospheric mantle composition corresponds to an average oceanic peridotite (Fullea et al., 2015). For an exhaustive technical description of the geotherm construction and model calculation, we refer the reader to Fullea et al. (2012).

Six selected models with varying degrees of fit to the seismic data are presented in Fig. 4.8, where we show the profiles of V_S, temperature and attenuation, as well as the observed and synthetic phase velocities and the phase-velocity misfit. Three key parameters of the models (given in the legend in the upper right corner) characterize the mantle geotherm: the mantle potential temperature T_P, the lithosphere-asthenosphere boundary (LAB) depth and the temperature at the LAB.

Four of the models (models 3, 4, 5, and 6 in Fig. 4.8), characterized by T_P in the 1410–1430°C range and the LAB depth of 65–70 km, fit the seismic data (Fig. 4.8 panels (f) and (g) and Fig. 4.7 panels (c) and (d)), while also fitting the observed bathymetry (in the ~3477–3521 m range, compared to 3452 ± 448 m the observed average across the region). The other two models (1 and 2, red and blue lines in Fig. 4.8 panels (f) and (g)) fit poorly and show that colder asthenosphere (lower T_P) (model 2, blue line) would result in synthetic phase velocities at the longer periods being much higher than the data; shallower or hotter LAB (model 1, red line) would result in phase velocities being lower than observed.

The well-fitting models are just four of the infinite number of similar models that would fit the data. The highly non-linear effects of partial melting contribute to the non-uniqueness of the model.

The purely seismic and petrologically derived models are, overall, remarkably similar (Fig. 4.8 panel (b)). In the lithosphere, the V_S profiles show a very close agreement. In the shallow asthenosphere, the petrological models that yield V_S profiles at the edges of the Monte Carlo-derived distribution do not fit the data, and only the petrological models with V_S profiles within the distribution band do. The close agreement of the results of the two types of inversion and modelling (seismic and petrological) is important and validates our results.

The main difference between the different models is in the smoothness of the profiles in the upper asthenosphere. While surface wave data constrain V_S tightly in sufficiently broad depth ranges in the lithosphere and asthenosphere, they are not sensitive to the sharpness of discontinuities or narrow gradients (e.g., Bartzsch et al., 2011; Lebedev et al., 2013). Thus, the rough and the smooth models seen in Fig. 4.8 panel (b) can fit the data equally well. Even though the fine-scale structure of the V_S profile in the models is non-unique, they do confirm our inferences on the lithospheric thickness from purely seismic inversion and provide useful estimates of the mantle

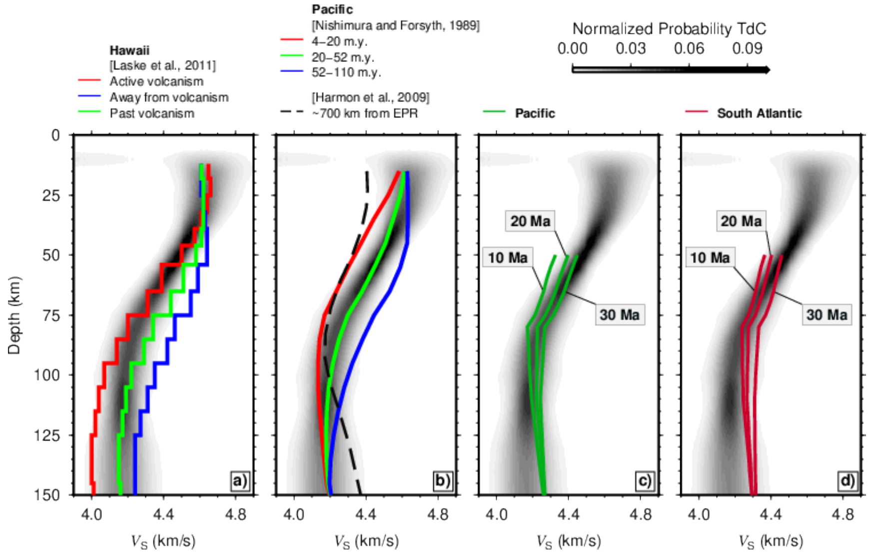

FIGURE 4.9: Comparison of our probabilistic shear velocity profile for the TdC region (gray color scale) with V_S profiles from published models. a) Hawaii ("Hawaii 1", "Hawaii 2", "Hawaii 3" from Laske et al. (2011)), b) Pacific lithosphere ("4–20 m.y.", "20–52 m.y.", "52–110 m.y." from Nishimura and Forsyth (1989) and "~700 km from EPR" from Harmon et al. (2009)). c) and d) Average V_S profiles for different seafloor ages in the Pacific and South Atlantic Oceans, respectively, according to global tomography (Celli et al., 2016).

temperature (lithospheric and sub-lithospheric), while also demonstrating that the models are consistent with the observed bathymetry and heat flow.

4.5 Discussion

4.5.1 Comparison With Published V_S Profiles

In Fig. 4.9 we compare our region-average V_S profile derived through McMC inversion with published V_S profiles for Hawaii (Laske et al., 2011), young Pacific lithosphere (Nishimura and Forsyth, 1989; Harmon et al., 2009) and the 10, 20, and 30 Ma profiles for the Pacific and South Atlantic Oceans from global waveform tomography (Celli et al., 2016).

The profiles of Laske et al. (2011) (Fig. 4.9 panel (a)) were obtained with similar data and methods to the ones used here, i.e. two-station dispersion measurements using data from an OBS array, with the interstation spacing in the two experiments comparable (the Hawaii OBS array, however, included more instruments, and they had a broader period range, including periods longer than 60 s). The Hawaii profiles of Laske et al. (2011) (Fig. 4.9 panel (a)) show clearly the rejuvenation of the old Pacific lithosphere by the Hawaii hotspot. The measure of the rejuvenation is the difference between the fastest profile (blue; Pacific lithosphere unaffected by the hotspot) and the slowest profile (red; Pacific lithosphere affected by the hotspot most recently). In the lithospheric depth range, shear wave velocities beneath TdC are remarkably similar to those in the rejuvenated lithosphere beneath Hawaii ("location 1" in Laske et al. (2011), red curve in Fig. 4.9 panel (a)). Below 80–90 km depth, however, velocities in the asthenosphere beneath Tristan (4.1–4.2 km/s) are not as low as the lowest velocities beneath Hawaii (4.0 km/s). This suggests that the asthenosphere beneath Hawaii is considerably hotter than beneath Tristan (and, possibly, has more partial melt). The similarity of V_S (and, by inference, temperature) in the lithosphere beneath Tristan and Hawaii is consistent with the Hawaiian asthenosphere being much hotter. Before the rejuvenation by the hotspot, the older Pacific lithosphere must have been colder and thicker. Thus, it had to be reheated by a substantially greater amount than the younger Atlantic lithosphere beneath Tristan, for the two to have similar lithospheric geotherms at present.

Our TdC V_S profile is similar to the profiles from Nishimura and Forsyth (1989) for young and intermediate-age (4–20 and 20–52 Ma, respectively) Pacific lithosphere (Fig. 4.9 panel (b)). In the shallow lithosphere, all the profiles, including ours and those from Laske et al. (2011) and Nishimura and Forsyth (1989), agree in that V_S reaches around 4.6 km/s. This similarity is because temperature in the shallow lithosphere, which is close to the surface and cools quickly after the plate is formed, should be similar for different lithospheric ages, even though the geotherms for the different ages diverge at greater depths, in the deep lithosphere-asthenosphere depth range. Because the profiles of Nishimura and Forsyth (1989) are for isotropic-average V_S, obtained from both Love and Rayleigh wave measurements, whereas our profile is for V_{SV}, obtained from Rayleigh waves only, we refrain from a quantitative comparison of the entire profiles, as radial anisotropy could bias any inferences. Interestingly, the model of Harmon et al. (2009) for a location around 700 km west from the East Pacific Rise (EPR), with the seafloor age of around 8 m.y., shows lower V_S in the uppermost mantle compared to the other profiles (Fig. 4.9 panel (b)). This suggests slow cooling of the Pacific lithosphere at this location. This can be attributed to the proximity of hotspots a little further west, with the profile located just between the hotspots and the ridge.

In Fig. 4.9 panels (c) and (d), we compare our Tristan profile with V_S profiles computed as averages for different lithospheric ages within the South Atlantic and Pacific Oceans, using a global tomographic model (Celli et al., 2016). The global tomography shows that V_{SV} in the asthenosphere beneath the South

Atlantic is higher than beneath the Pacific Ocean, on average. Shear velocity in the asthenosphere beneath the Tristan region, according to the profile obtained in this study, is lower than the South Atlantic average for the corresponding age range (10–30 m.y.), obtained from the tomography. This confirms that the asthenosphere beneath Tristan is anomalously warm.

4.5.2 Estimation of Temperature From V_S Profile

An alternative, independent quantitative estimate of the temperature anomaly beneath TdC can be obtained by using our V_S profile and published, petrologically derived V_S-T relationships (e.g., Goes et al., 2012). Converting seismic information to temperature is complicated by the large number of variables involved (temperature, pressure, composition, phase, melt content, water content, attenuation) and by uncertainties in the available thermodynamic databases. Goes et al. (2012) used three different published attenuation (Q) models specifically to relate the low velocity anomalies in the mantle below mid-ocean ridges to temperature anomalies. Taking into account anharmonic and anaelastic effects of temperature, pressure, composition, phase and water content, they computed V_S profiles for the different Q models, the first one a model from Behn et al. (2009) based on the results of Faul and Jackson (2005) and Jackson et al. (2002), the second one an empirical model from Goes et al. (2000) and van Wijk et al. (2008), and the third one a model proposed by Yang et al. (2007) (we refer to the models as Q_F, Q_g, and Q_Y, maintaining the notation from Goes et al. (2012) (e.g. their Figure 4)).

We estimated temperatures using V_S-T relationships from Goes et al. (2012) (e.g., their Figure 4). Assuming σ and 2σ uncertainties on the posterior V_S distribution yielded by our probabilistic inversion, we obtained the ranges of temperature at 50, 75, and 100 km shown in Table 4.1. The V_S-T relationships were recomputed at a reference period of 50 s (which is the reference period we use in our inversion). In order to obtain the estimates at 75 km, we interpolated logarithmically between 50 and 100 km. The resulting temperature values are also shown in Fig. 4.10, where we compare them with our petrological models and other models[3]. At 50 km, Q_F produces the highest temperature estimate and Q_Y the lowest; the opposite is true at 100 km. The 2σ error bars in Fig. 4.10 differ in width because of the different frequency dependence of the three models. At 50 km depth, all three estimates are close to temperatures in our petrologically-derived models (green and red lines in Fig. 4.10). At 75 and 100 km, our petrologically derived geotherms are in agreement with Q_g and Q_Y, but not Q_F. The two attenuation models that are consistent with

---

[3] Fig. 4.10 in Bonadio et al. (2018) presents a typographic mistake which has been corrected here.

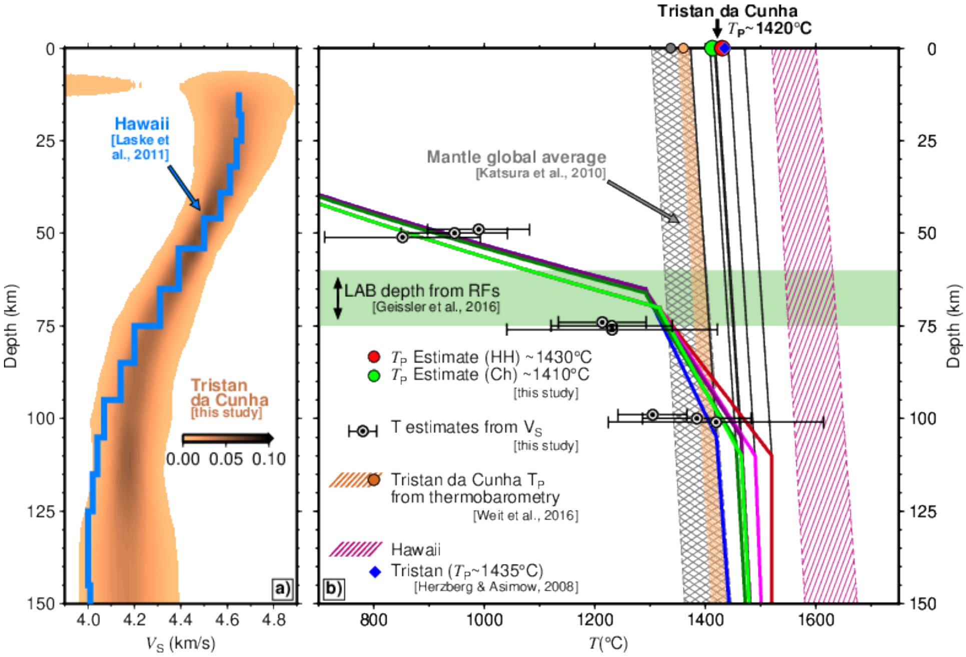

FIGURE 4.10: Synthesis of the key evidence on the thermal structure of the upper mantle beneath Tristan da Cunha. a) The lithosphere beneath TdC is underlain by a pronounced low-velocity zone, indicative of anomalously warm asthenosphere. However, V_S in the TdC asthenosphere is not as low as beneath Hawaii (Laske et al., 2011), which suggests that the thermal anomaly beneath TdC is not as high as that beneath Hawaii. b) The petrologically-derived models that are consistent with seismic and bathymetry data (dark/light green and dark/light purple lines – models 5, 6, 4, and 3 according to the legend at the top right corner in Fig. 4.8) have the LAB at a depth of 65–70 km, in agreement with the LAB depths computed from receiver functions (Geissler et al., 2016) (light green band). These models suggest a mantle potential temperature T_P beneath Tristan of 1410–1430°C, higher than the global average (~1337±35°C (Katsura et al., 2010)) but lower than at the Hawaii hotspot (~1520–1600°C, according to Herzberg and Asimow (2008)). Our estimated potential temperature for TdC is close to the value computed for Tristan by Herzberg and Asimow (2008) (~1435°C, blue diamond). The coldest and hottest petrological models (dark blue and dark red, respectively) are not consistent with seismic data. "HH" and "Ch" indicate if the model have been computed using the parameterization from Hammond and Humphrey (2000b) and Hammond and Humphrey (2000b) or Chantel et al. (2016), respectively (see also the legend in Fig. 4.8). We also plot the T_P recently inferred from thermobaromethry (Weit et al., 2016) (~1360°C; orange circle and band). The temperature estimates from our V_S and the V_S-T relationships of Goes et al. (2012) (Table 4.1) are plotted as circles with error bars. These temperature estimates are computed for three different attenuation models, all at the depths of 50, 75, and 100 km; they are plotted at slightly different depths (±1 km) for clarity. The (conservatively broad) geothermal gradient range used to relate T_P and the temperature in the asthenosphere is $[0.4, 0.5]$ K/km (Katsura et al., 2010).

TABLE 4.1: Estimation of temperature using our average V_S model and V_S-T relationships from Goes et al. (2012) at three different depths and for three different attenuation models, Q_F, Q_g, and Q_Y.

Depth (km)		T_σ(°C)	$T_{2\sigma}$(°C)
50	Q_F	1006 ± 41	989 ± 93
	Q_g	958 ± 47	946 ± 96
	Q_Y	866 ± 65	852 ± 141
75	Q_F	1223 ± 38	1213 ± 79
	Q_g	1239 ± 52	1230 ± 109
	Q_Y	1228 ± 95	1231 ± 190
100	Q_F	1310 ± 30	1304 ± 63
	Q_g	1391 ± 48	1384 ± 96
	Q_Y	1423 ± 93	1419 ± 195

the petrologically derived geotherms, Q_g and Q_Y, are both empirical, the first one designed to reconcile a wide range of observations and the second one to fit EPR attenuation (see Goes et al. (2012) for details). Q_F, in contrast, is a model based on laboratory results only. (We note that recent experimental updates from Jackson and Faul (2010) (following Faul and Jackson (2005)) would suggest higher predicted moduli (higher velocity and less attenuation) at a given temperature.)

4.5.3 Synthesis: thickness of the lithosphere and temperature of the asthenosphere

We summarize the evidence on the seismic and thermal structures of the lithosphere-asthenosphere system beneath TdC in Fig. 4.10. In Fig. 4.10 panel (a), TdC V_S probability distribution is compared to a recent V_S model for the rejuvenated lithosphere beneath Hawaii from Laske et al. (2011). Our model shows a pronounced low-velocity anomaly from ~70 to at least ~120 km depth with S-wave velocity in the low-velocity zone around 4.1–4.2 km/s, higher than beneath Hawaii (~4.0 km/s). The Pacific lithosphere beneath the eastern extremity of the Hawaii chain, where volcanism is now active, is 90–100 Ma, substantially older than the 10–30 My age of the lithosphere beneath the TdC region. The similarity of the lithospheric V_S profiles from the two locations thus indicates that the Hawaii hotspot has warmed and thinned the Pacific lithosphere by a much greater amount (seen in the comparison of the Hawaii-region profiles in Fig. 4.9 panel (a)) than the Tristan hotspot has the South Atlantic lithosphere. This is consistent with the asthenosphere beneath TdC being not nearly as hot as it is beneath Hawaii, as indicated by the higher V_S in the TdC asthenosphere.

Petrological modeling shows that the seismic and bathymetric data from the TdC region can be fit by models with a moderately hot mantle, a melt fraction smaller than 1% and a 65–70 km lithospheric thickness (in agreement with the purely seismic inversions). Fig. 4.10 panel (b) compares the well-fitting, petrologically derived geotherms with other estimates for TdC, with the global average, and with estimates for Hawaii. The mantle-adiabatic temperature gradient range used to relate the temperatures in the asthenosphere to the mantle potential temperature T_P is 0.4–0.5 K/km (taken from Katsura et al. (2010)). We also show the lithospheric thickness inferred from receiver functions (Geissler et al., 2016) and temperature estimates (Section 4.5.2) from V_S profile and V_S-T relationships (Goes et al., 2012).

Our results show that the TdC mantle is warmer than ambient mantle beneath normal ocean ridges: T_P of 1410–1430°C for Tristan versus 1280–1400°C (Katsura et al., 2010; Anderson, 2000; Chambers et al., 2005; Herzberg et al., 2007; Khan et al., 2013; Kuskov et al., 2014) for the ridges. Our potential temperature estimates are higher than the values calculated by Dalton et al. (2014) on the MAR for the closest locations to Tristan da Cunha (1349°C, 1367°C, 1393°C, and 1378°C at the values of latitude-longitude $[-40, -16]$, $[-38, -17]$, $[-36, -17]$, and $[-35, -15]$, respectively). This thermal anomaly is considerably smaller than anomalies beneath some of the other major hotspots (Hawaii, 1520–1600°C (Herzberg et al., 2007; Herzberg and Asimow, 2008; Taposeea et al., 2016); Samoa, ~1525°C; St. Helena, ~1520°C (Herzberg and Asimow, 2008)), but it is in the range of estimates reported for other hotspots (Iceland, 1435–1455°C; Azores, 1430–1465°C; Canaries, 1420–1480°C (Herzberg and Asimow, 2008)). (The overall higher values reported by Putirka (2005), Putirka et al. (2007), and Putirka (2008) also show Hawaii (1687–1722°C) to be hotter than Iceland (1583–1637°C).) Our estimated T_P for TdC is close to the value estimated for Tristan by Herzberg and Asimow (2008) (~1435°C). The temperature beneath Tristan, according to our models, is about 50–120°C higher than the global average value of 1337±35°C (Katsura et al., 2010).

4.6 Conclusions

Rayleigh-wave dispersion measurements from OBS data in the Tristan da Cunha region reveal a 65–70 km thick lithosphere and a pronounced low-velocity zone beneath 70 km depth, with V_S of 4.1–4.2 km/s within it. Both the probabilistic seismic inversion of the data and petrological modelling indicate the lithospheric thickness around 65–70 km, which agrees with independent estimates from receiver functions (Geissler et al., 2016). The temperature of the asthenosphere is around 50–120°C higher than global average, with a melt fraction smaller than 1%. The mantle potential temperature T_P is estimated at about 1410–1430°C.

Our observations are consistent with a hot upwelling from the deep mantle (a mantle plume) beneath the Tristan region, but the excess temperature we determine is smaller than that reported for some major hotspots such as Hawaii (100–180°C), although it is in the range of values reported for Iceland and some other hotspots. The upwelling beneath TdC may be not as hot as that beneath Hawaii or, alternatively, the present structure reflects a weaker upwelling (plume tail) than in the past, when the large igneous provinces onshore and the prominent hotspot tracks offshore were formed. It is also possible that the largest thermal anomaly is located at a distance from TdC, closer to the MAR (Fig. 4.1 panel (b)).

Acknowledgments We thank Pierre Arroucau for the numerous valuable discussions, Saskia Goes and Nicholas Harmon for sharing their data, and the Editor, Ulrich Faul, and an anonymous reviewer for insightful comments and suggestions that helped us to improve the manuscript. We thank Captain Ralf Schmidt, the crew of R/V Maria S. Merian and the Scientific Parties of cruise MSM20/2 and MSM24 as well as the people on Tristan da Cunha for the professional and friendly support. This work was supported by the Science Foundation Ireland (SFI) (grants 13/CDA/2192 and 16/ERCD/4303), European Space Agency (the project "3D Earth – A Dynamic Living Planet" funded through ESA-Support to Science Element) and the German Research Foundation (DFG) (grant GE 1783/4-1/2, as part of the Priority Program SPP1375). Additional support was provided by the Alfred Wegener Institute Bremerhaven. Instruments were provided by "Deutscher Geräte-Pool für Amphibische Seismologie (DEPAS)" at Alfred Wegener Institute Bremerhaven and Deutsches Geoforschungszentrum Potsdam. The authors wish to acknowledge the DJEI/DES/SFI/HEA Irish Centre for High-End Computing (ICHEC) for the provision of computational facilities and support. The waveform data used are listed in the references, tables and supporting information. All figures were produced using Generic Mapping Tools (Wessel et al., 2013).

Chapter 5

Conclusions and Future Work

5.1 Conclusions

The main goal of this thesis was to use surface-wave techniques to image, at regional scale, the lithosphere-asthenosphere systems beneath the British Isles and the Tristan da Cunha Hotspot in the South Atlantic. These regions presented important, open Earth-science questions, with both the evolution of the British Isles and the origin of the TdC Hotspot volcanism being matters of heated debate. The methodologies we applied to newly available data led to new insights into the seismic structure of the investigated areas. A number of challenges, however, needed to be overcome in order to arrive to the new understanding of the regions.

The making of a 3D shear-velocity model of the British Isles was facilitated by the availability of abundant, newly collected data, which led to unprecedentedly dense ray-path coverage of the area. In order to achieve the highest possible resolution of the imaging, it was necessary to deal with extreme lateral unevenness of the data sampling and with systematic errors in the data due to varying quality of the recorded data, geographical variations in coverage, non-resolved heterogeneities, and wave propagation effects, as well as possible instrumental errors. In order to achieve the best possible resolution of the final model, we have developed a tomographic scheme that allows us to obtain an optimal target resolution of the model at each knot, thus maximizing the information extracted from the data. The optimal resolution at each knot of the model grid is obtained after the isolation of the error of the local phase-velocity curve at the location of the knot. We show that, due to the systematic data errors and azimuthally uneven data coverage, the maximum achievable resolution does not scale with data sampling. Some of the best-sampled locations require relatively high smoothing, with the actual achievable resolution there not the highest. The optimal phase velocity maps, with best realistically achievable resolution, were inverted at each knot of the model grid to produce a 3D V_S model of the area.

The new tomographic results are corroborated by other surface geological and geophysical observations, including proposed underplate thickness and denudation, gravity, and thermochronological measurements. The most striking attribute of the model is a low-velocity anomaly beneath the Irish Sea and its surroundings (including Wales, Western Scotland, Northern England and Northern Ireland), which coincides with the area of the Paleogene uplift, exhumation and intraplate basaltic volcanism.

At shallow depths, Ireland and Scotland show similar seismic velocities, with clear boundaries between the high velocities beneath well consolidated blocks and the low velocities in sediment-covered areas. The shear velocity maps also exhibit, in Ireland, a particularly thick lithosphere beneath the Iapetus Suture Zone (ISZ), and display a pronounced elongated high-velocity anomaly stretching W-E approximately along it (especially at around 100-150 km). This may indicate a remnant of the Caledonian Iapetus slab beneath the ISZ or, alternatively, fragments of thick, Precambrian continental lithosphere incorporated into the Irish landmass in the course of the Caledonian Orogeny.

Investigating the Tristan da Cunha Hotspot lithosphere-asthenosphere system required re-tuning of previously established surface-wave techniques, due to the high level of noise that the data exhibited. The average Rayleigh-wave dispersion revealed a lithosphere-asthenosphere boundary at 65–70 km, which is in agreement with previous results obtained in the area by receiver-functions, a methodology more suited to detect discontinuities at depth. A pronounced low-velocity zone beneath 70 km depth is obtained using probabilistic inversion and petrological modelling, which provides an estimate of an excess temperature in the area of 50–120°C. These observations are consistent with a hot upwelling from the deep mantle (a mantle plume) beneath the Tristan region, although the anomaly is not as strong as found in other major hotspots (e.g., Hawaii).

5.2 Future work

Further developments of many aspects of this work are planned, and are currently being implemented.

The 3D shear velocity model, produced with the use of the new developed optimal-resolution tomography scheme, involved a 1D inversion at each knot of the model grid (Section 2.5.2). The inversion is a non-linear, Levenberg-Marquardt gradient search (e.g., Meier et al., 2004; Lebedev et al., 2006; Endrun et al., 2008; Erduran et al., 2008; Agius and Lebedev, 2013; Agius and Lebedev, 2014; Ravenna and Lebedev, 2018) that computes synthetic phase velocities at each iteration from shear velocity (V_S), compressional velocity (V_P), density, and attenuation using the forward solver MINEOS (Masters et al., 2007). The ratio between V_S and V_P is kept fixed during the inversion, and density and compressional and shear attenuation factors are fixed at the reference values, generally from a previously calculated reference global model (e.g., AK135 (Kennett et al., 1995) or PREM (Dziewonski and Anderson, 1981)). A new inversion scheme, based on this existing one, is now under development. In it, V_P, density, and compressional and shear attenuation factors will be not left fixed during the inversion but will be evaluated, at each iteration, from thermodynamic databases (e.g., Afonso et al., 2008; Fullea et al., 2009), according to the perturbation of V_S. The new inversion scheme will take into account thermodynamic information for different tectonic settings (e.g., Schaeffer, 2014) and will produce shear velocity profiles in which the effects of attenuation are not neglected. This, along with petrological modeling, will offer new insights on the structure of the British Isles lithosphere-asthenosphere system, particularly on the temperature, lithosphere-asthenosphere boundary topography, density and, possibly, composition.

On-going work is being done on the retrieval of Love wave measurements through teleseismic two-station cross-correlation. The Love measurements, together with the Rayleigh measurements, will provide the isotropic-average seismic velocities beneath the area, relatable to temperature and composition, and radial anisotropy, indicative of the past and present deformation in the lithosphere and asthenosphere.

I also aim to validate further the 3D shear-velocity model by means of resolution tests. I intend to make synthetic tests to investigate in more detail the behaviour of random and systematic noise in the phase velocity measurements and how they propagate after inversions for 2D tomographic maps and shear-velocity and to create lateral-resolution maps and vertical resolution estimates.

Furthermore, the ambient noise Love- and Rayleigh-wave phase velocity maps (Chapter 3) will also be used in a joint inversion to constrain the crustal structure of Ireland along with other geophysical observations, including magnetic, gravity, and receiver-functions measurements.

An exciting new development of this work is related to the connection identified between the shear-velocity model and thermochronological studies (Cogné et al., 2016; Döpke, 2017). The strong correlation between the V_S results and the estimates for the Cenozoic exhumation offers important inferences on the mechanisms of the uplift and volcanism, which must have been related to a pronounced thinning of the circum-Irish Sea region's lithosphere. This will be the focus of future investigations and should provide a newer, deeper understanding of the evolution of the British Isles.

Appendix A

Appendix to Chapter 2

A.1 Additional vertical cross sections of the 3D V_S model.

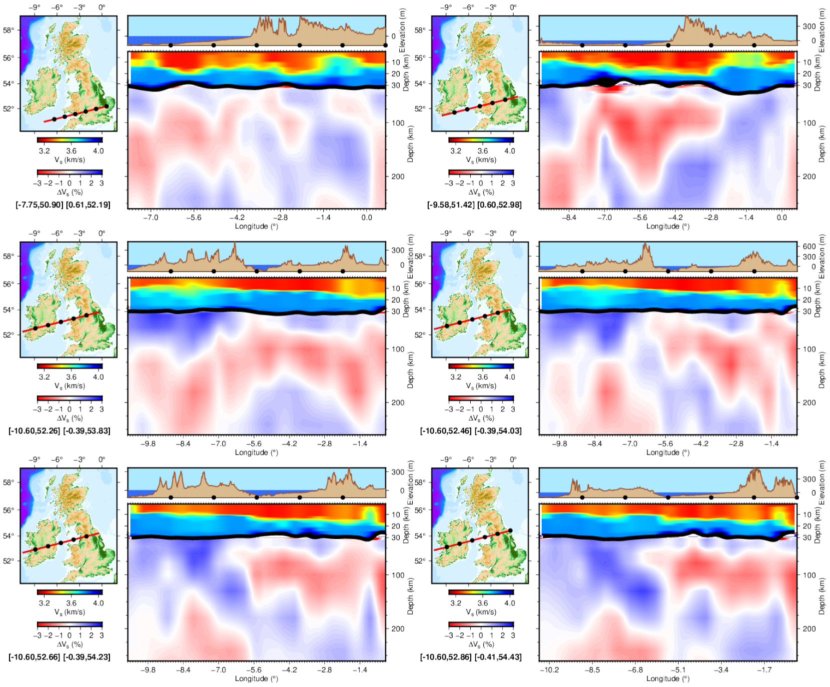

FIGURE A.1: V_S vertical cross sections of the model (W–E).

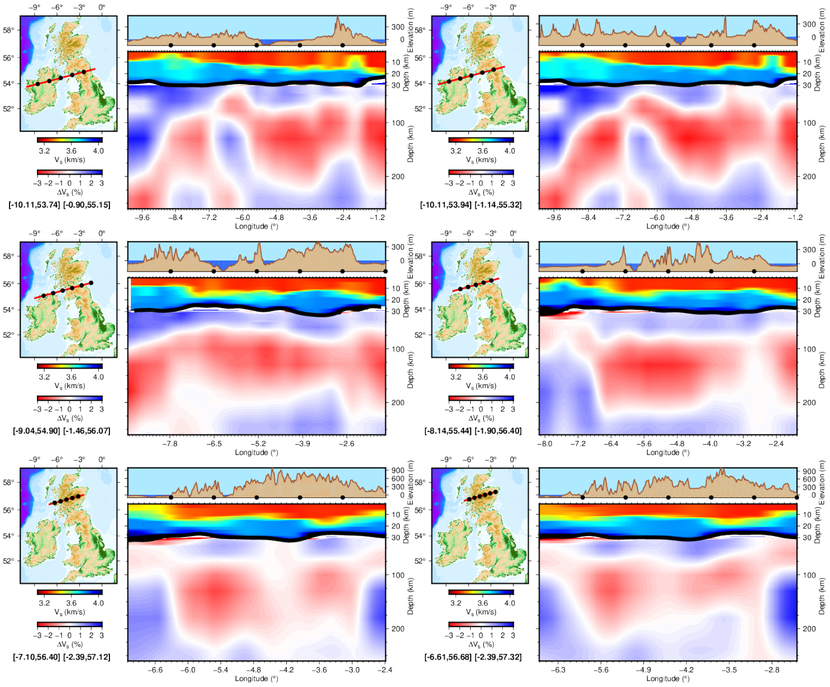

FIGURE A.2: V_S vertical cross sections of the model (W–E).

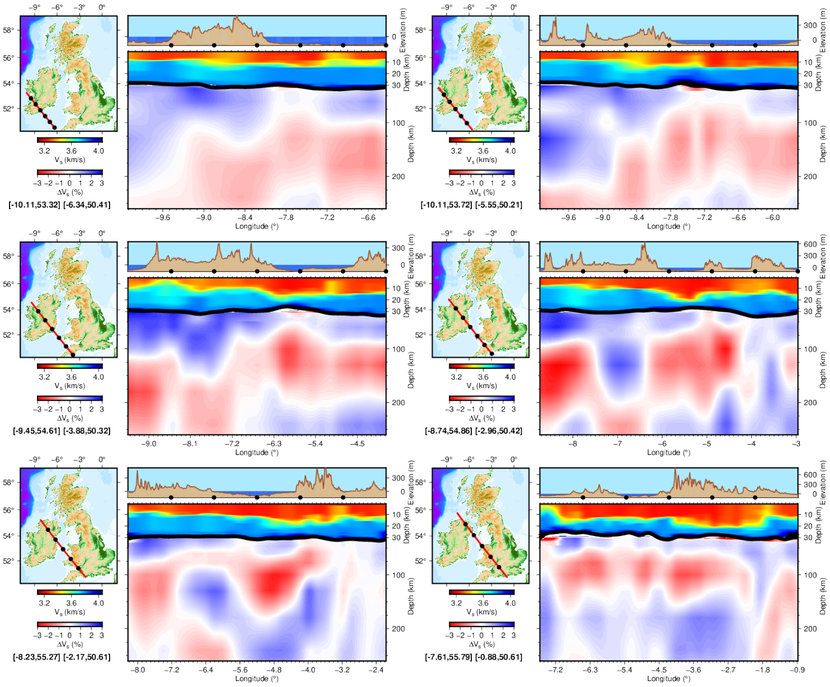

FIGURE A.3: V_S vertical cross sections of the model (NW–SE).

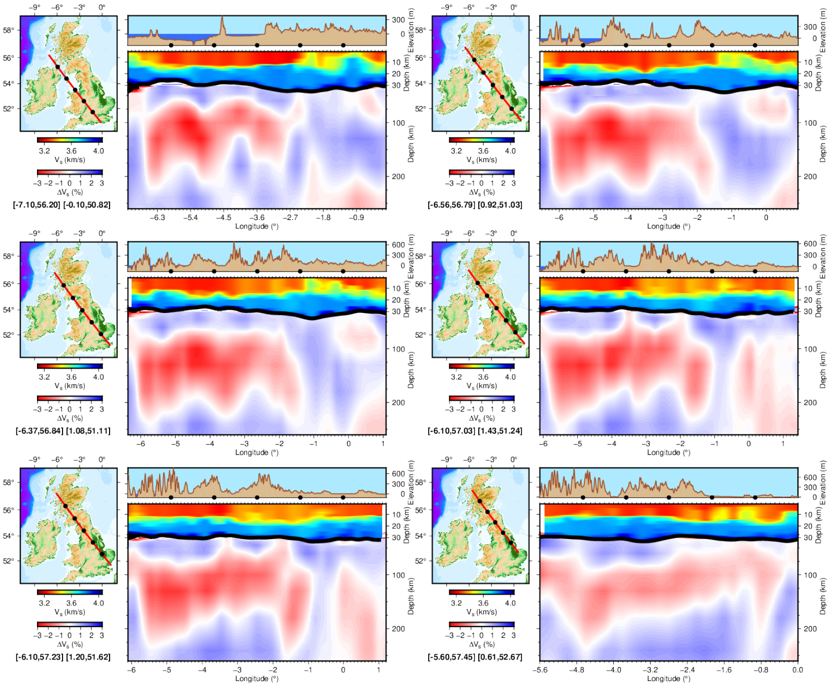

FIGURE A.4: V_S vertical cross sections of the model (NW–SE).

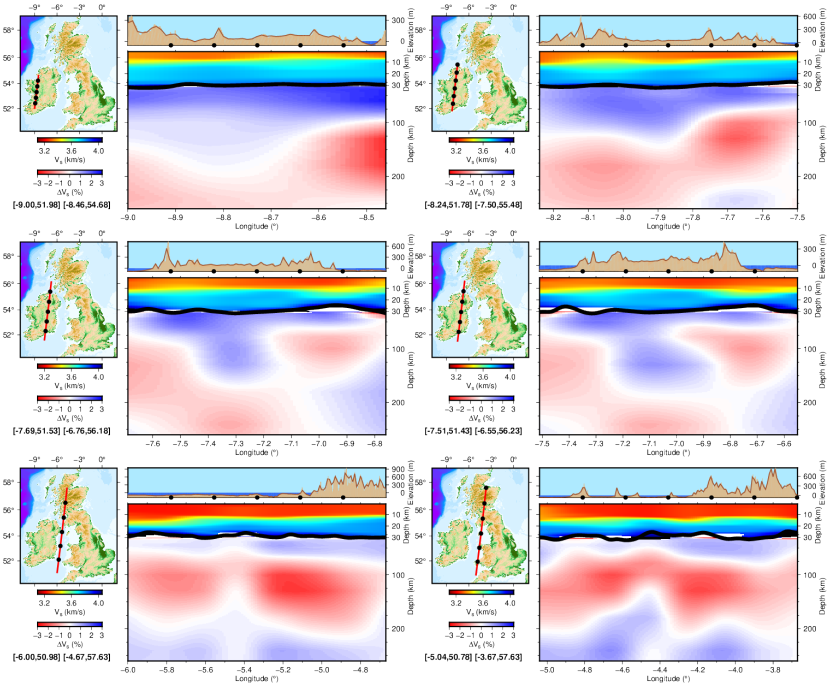

FIGURE A.5: V_S vertical cross sections of the model (S–N).

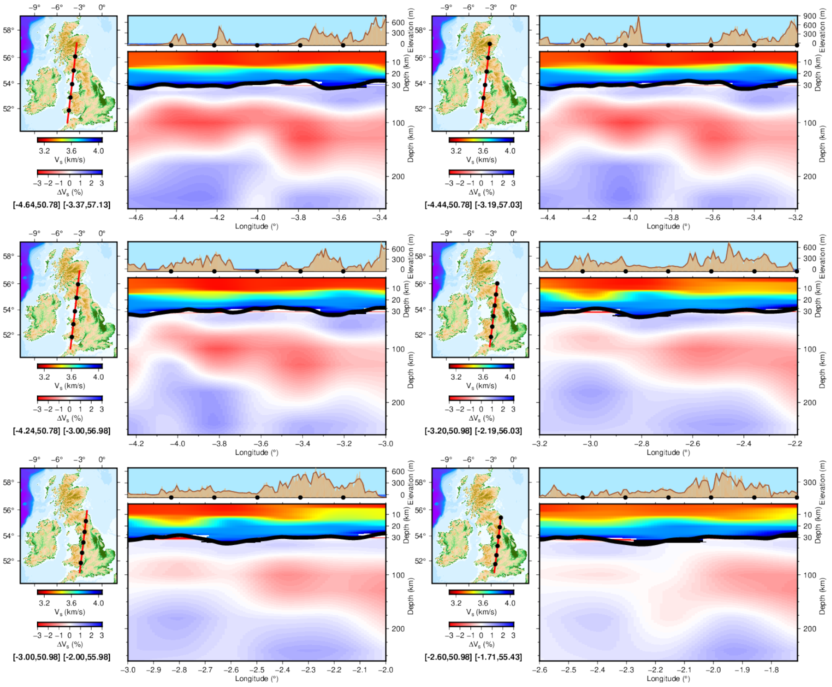

FIGURE A.6: V_S vertical cross sections of the model (S–N).

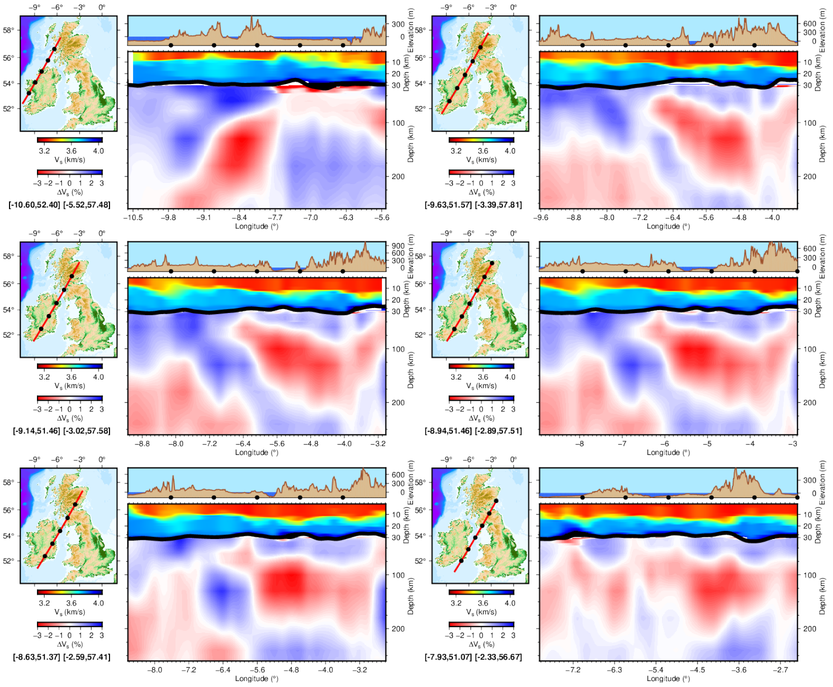

FIGURE A.7: V_S vertical cross sections of the model (SW–NE).

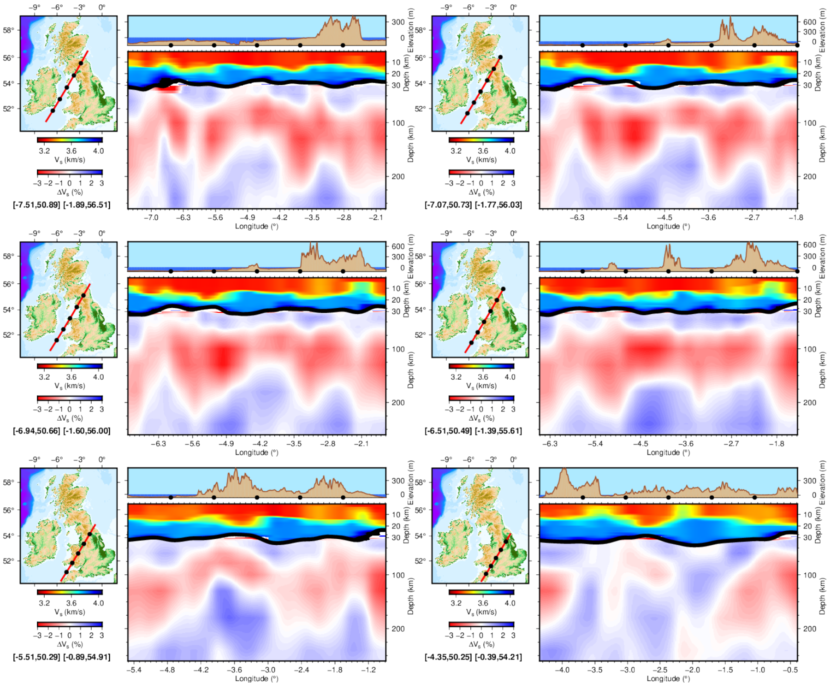

FIGURE A.8: V_S vertical cross sections of the model (SW–NE).

A.2 Additional material for Section 2.5.

Due to the random choice of the relative damping for the 1D shear-velocity inversion, often the resulting model is unreasonable (unnecessary complex structures are modeled, or noise is over-fitted) and consistently far from the rest of the generated models at each grid-knot, such that it can (and it needs to) be identified as an outlier and should not be used for the reconstruction of the final 3D model. In order to identify the outliers we have computed the RMS-misfit for each of the produced synthetics, and plot them together as in Fig. A.9 (only 5 examples over the 4328 knots are shown). Fig. A.9 shows that the inversions generally present similar values of RMS-misfit, depending on the damping level (stronger damping corresponding to bigger RMS-misfit), except for occasional inversions that show very high RMS-misfit and are easily identifiable as outliers (simply using a threshold, damping level dependent). In Fig. A.10, e.g., we show (left vertical panel) some inversions that have been identified as outliers (they are plot in gray) and will not contribute to the final results for the 3D V_S model.

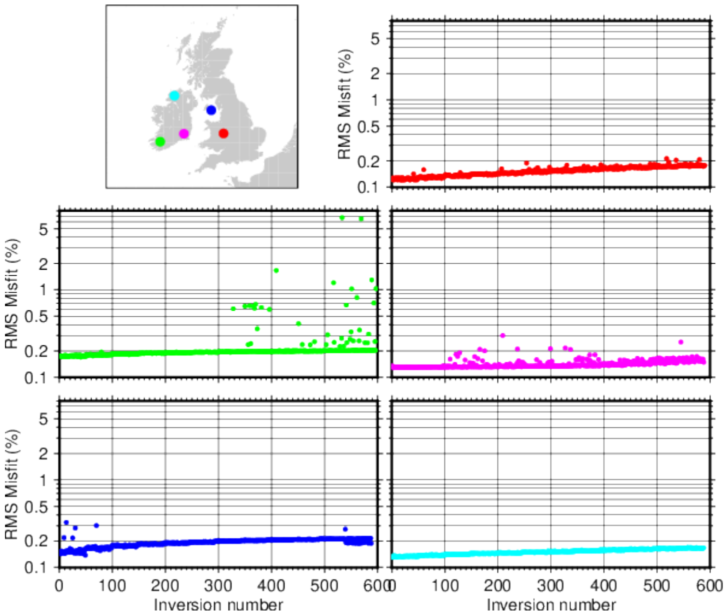

FIGURE A.9: RMS misfit computed at 5 different locations (as indicated in the map on the top-left), for the ~600 inversions (50 inversions for each damping applied). These plots were used to identify outliers inversion and remove them from the final models.

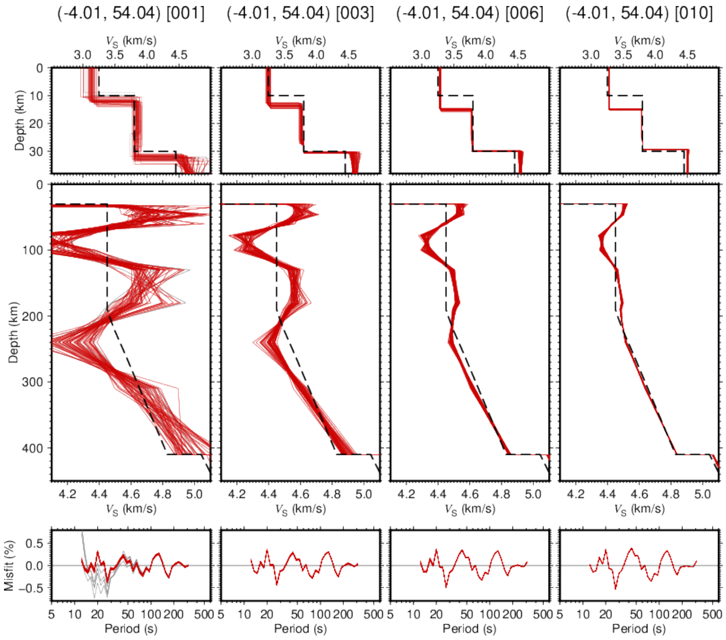

FIGURE A.10: Sets of differently damped V_S inversions, with increasing damping from left to right. The curves in gray are the ones removed from the final models, as they were classified as outliers due to RMS misfit too high (see also Fig. A.9).

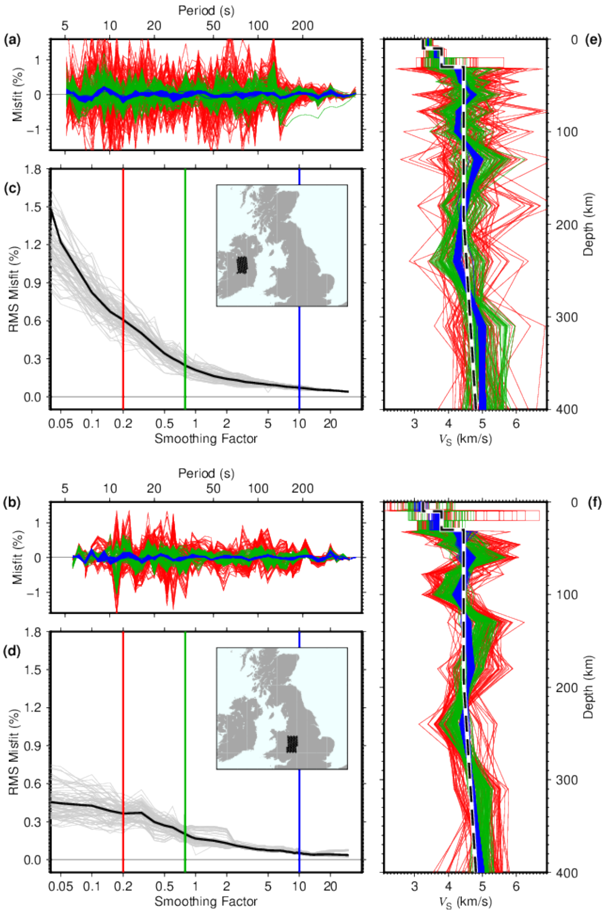

FIGURE A.11: Weakly regularized inversions to isolate curve roughness. These inversions do not aim to represent the real sub-surface, but are only used to isolate the curve roughness. The RMS Misfit (panels (c) and (d)) computed for the weakly reguralized inversions at two different sets of grid knots, in Ireland (top panel) and in Britain (bottom panel), as indicated by the black dots in the maps. For each grid knot 39 inversions (panels (e) and (f)), corresponding to 39 tomographic differently smoothed ($S_{i=0,1,2,\ldots,38}$) 2D maps, are shown. The RMS misfit relative to the data is shown in panels (a) and (b). The colors red, green, and blue indicate sets of inversions obtained from differently smoothed maps.

Appendix B

Appendix to Chapter 3

This appendix contains the phase velocity maps obtained from ambient noise cross correlation computed at each period.

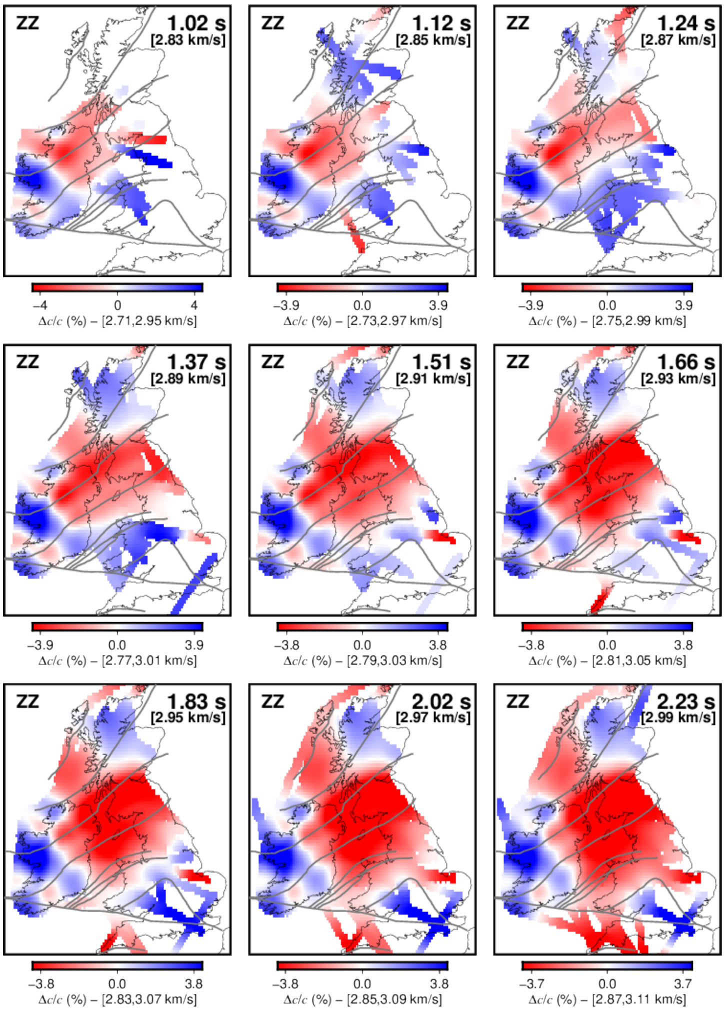

FIGURE B.1: Additional ambient noise ZZ phase velocity maps (see Chapter 3).

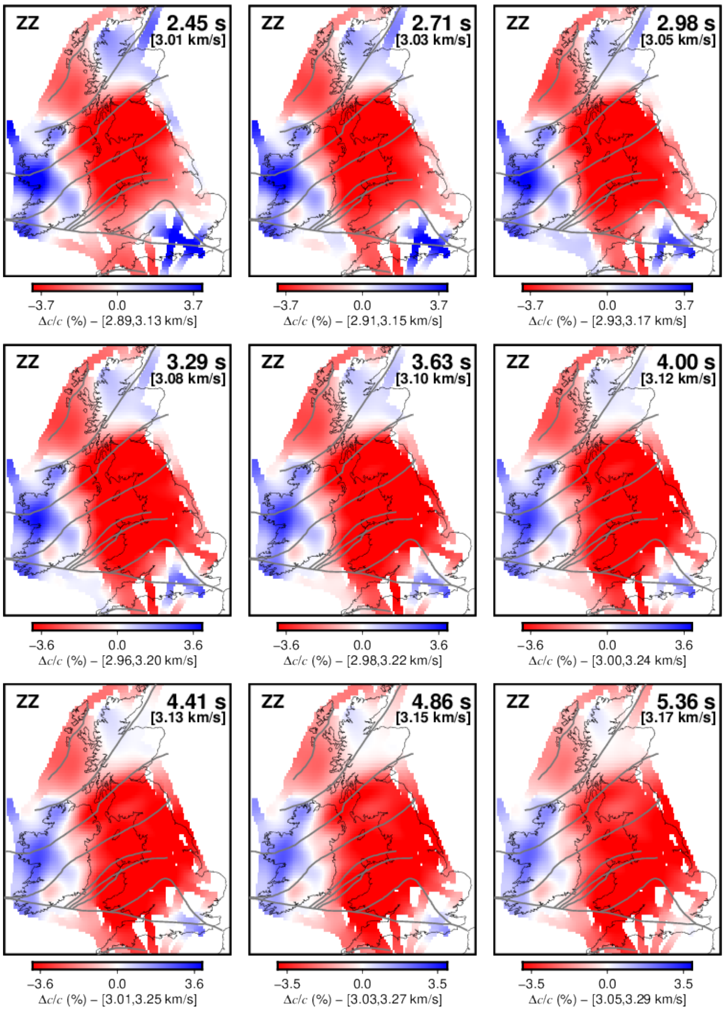

FIGURE B.2: Additional ambient noise ZZ phase velocity maps (see Chapter 3).

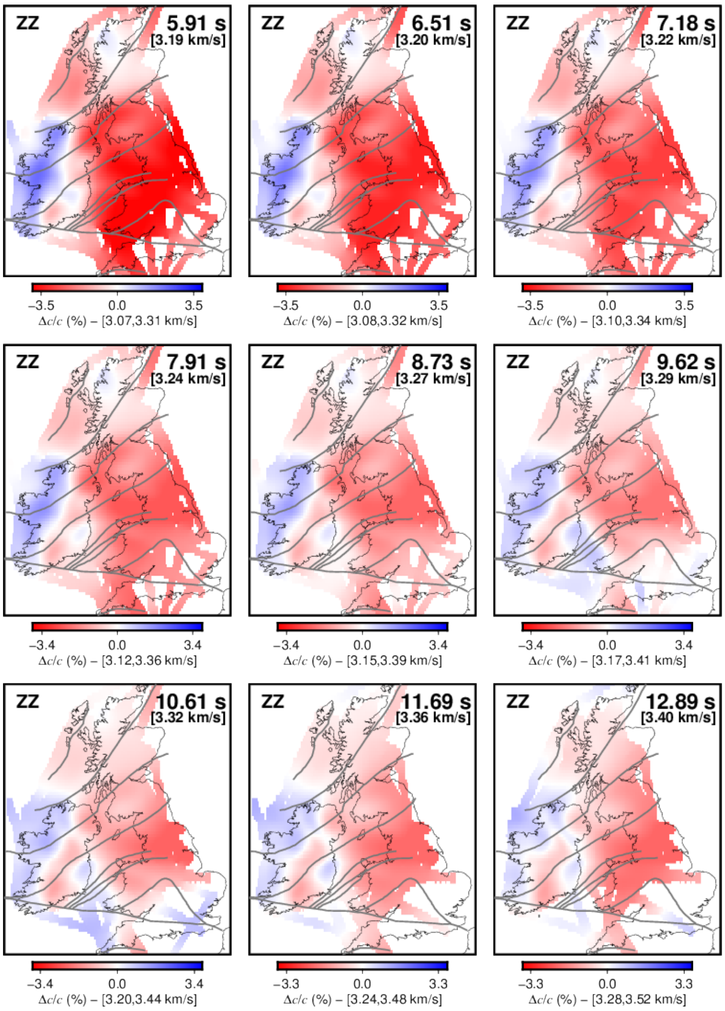

FIGURE B.3: Additional ambient noise ZZ phase velocity maps (see Chapter 3).

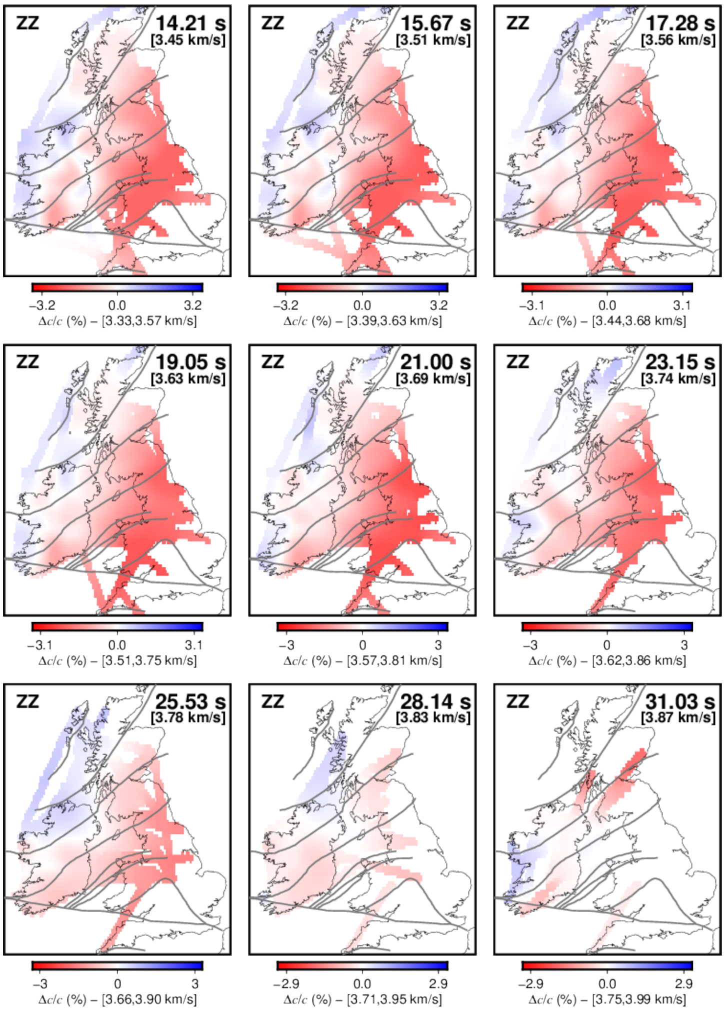

FIGURE B.4: Additional ambient noise ZZ phase velocity maps (see Chapter 3).

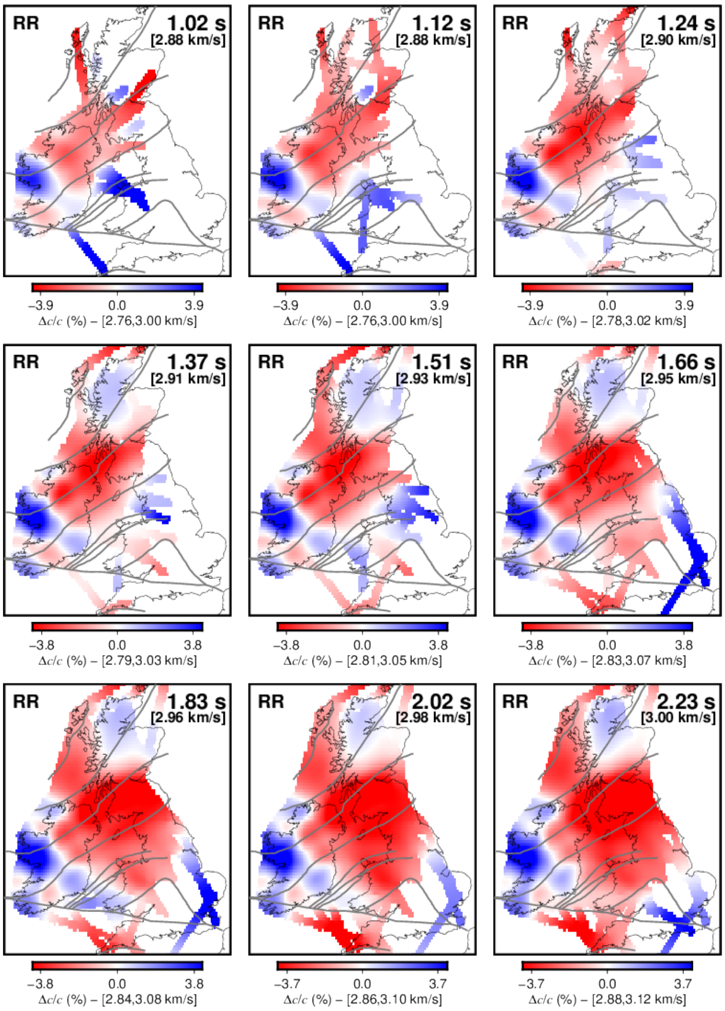

FIGURE B.5: Additional ambient noise RR phase velocity maps (see Chapter 3).

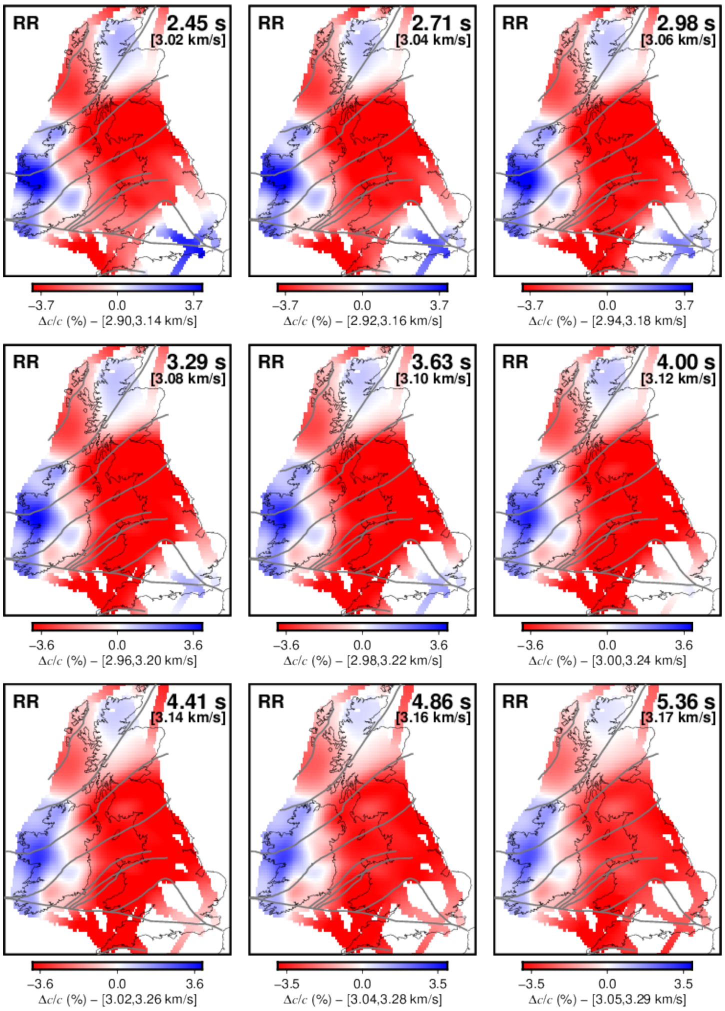

FIGURE B.6: Additional ambient noise RR phase velocity maps (see Chapter 3).

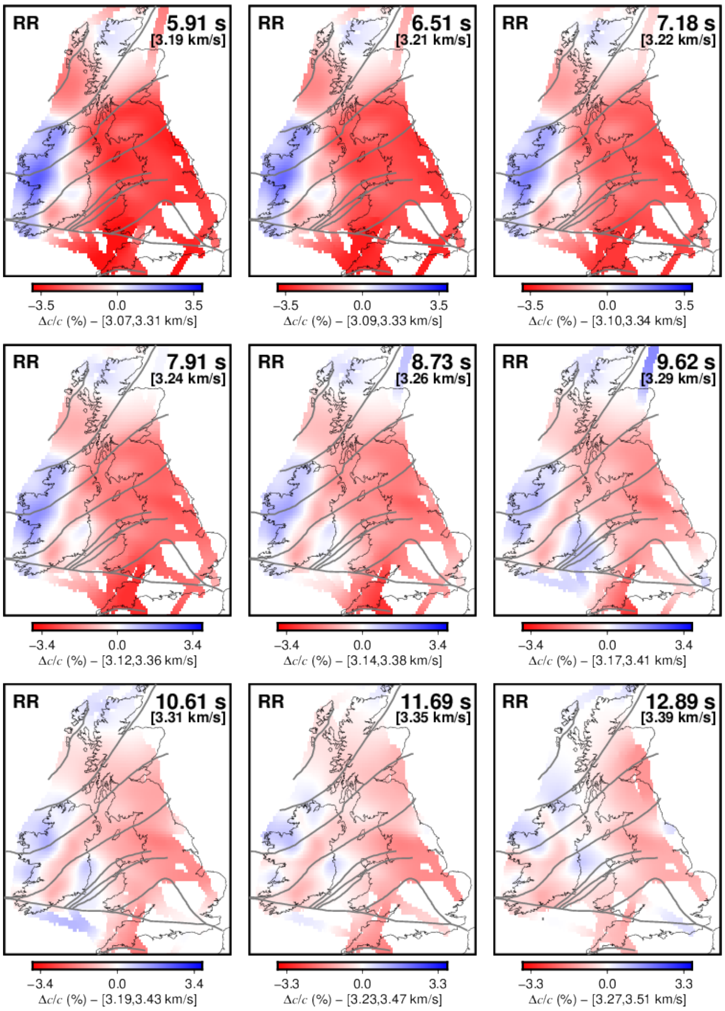

FIGURE B.7: Additional ambient noise RR phase velocity maps (see Chapter 3).

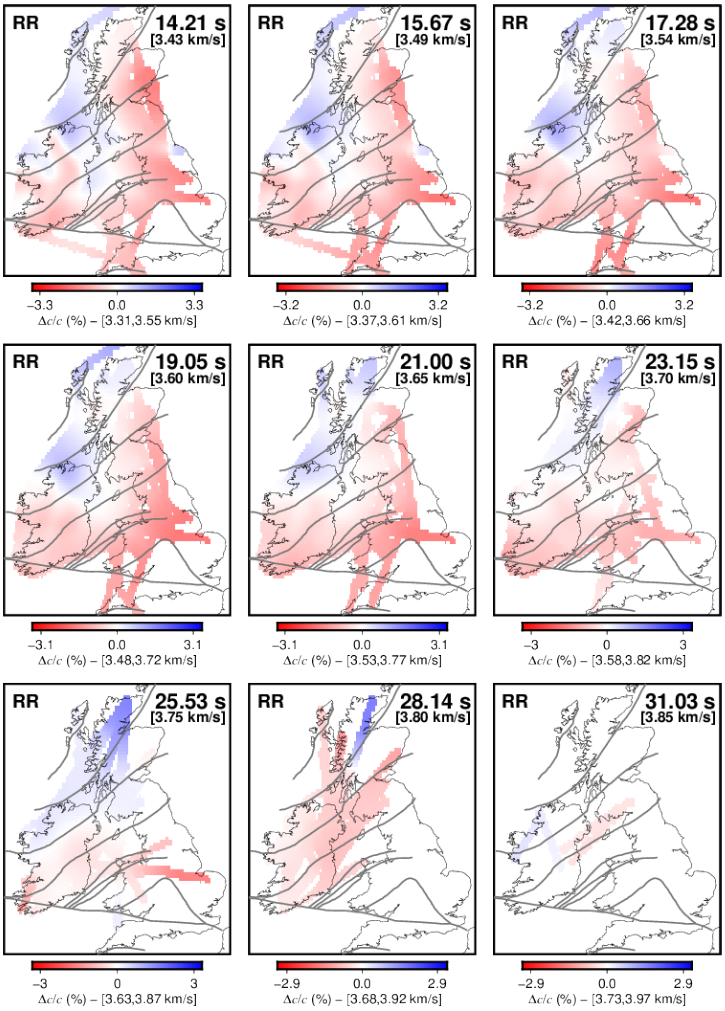

FIGURE B.8: Additional ambient noise RR phase velocity maps (see Chapter 3).

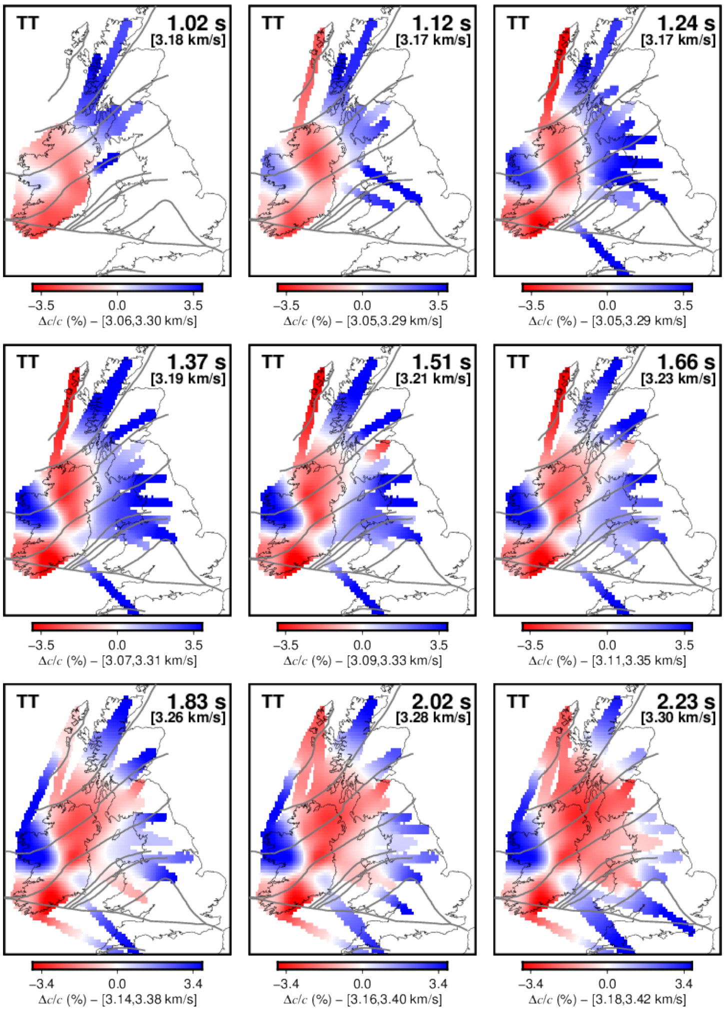

FIGURE B.9: Additional ambient noise TT phase velocity maps (see Chapter 3).

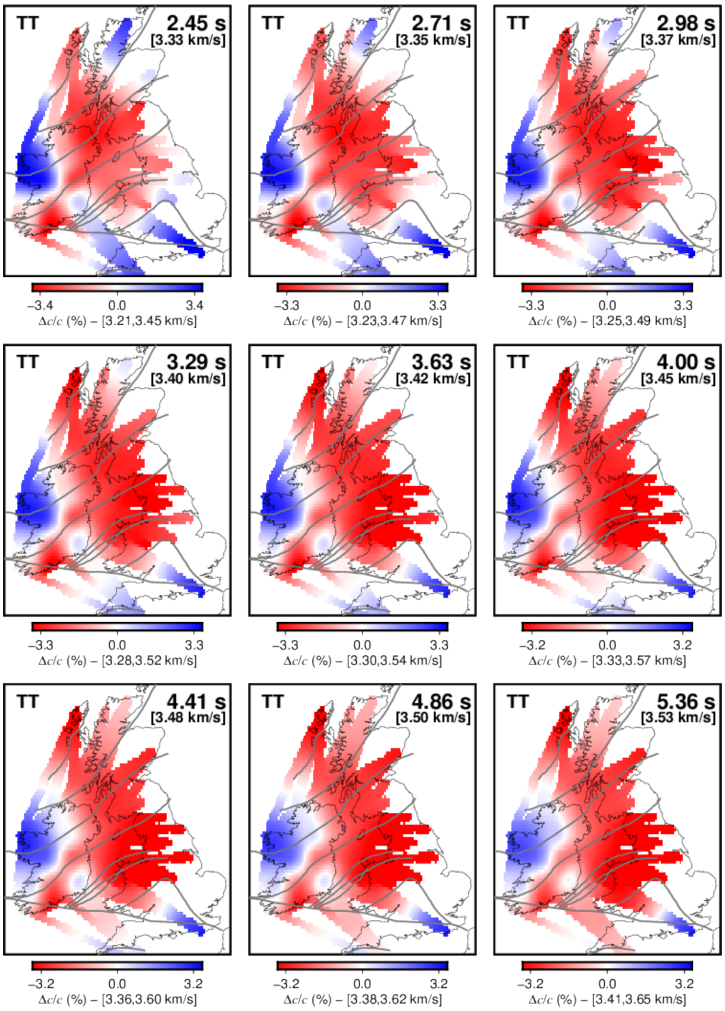

FIGURE B.10: Additional ambient noise TT phase velocity maps (see Chapter 3).

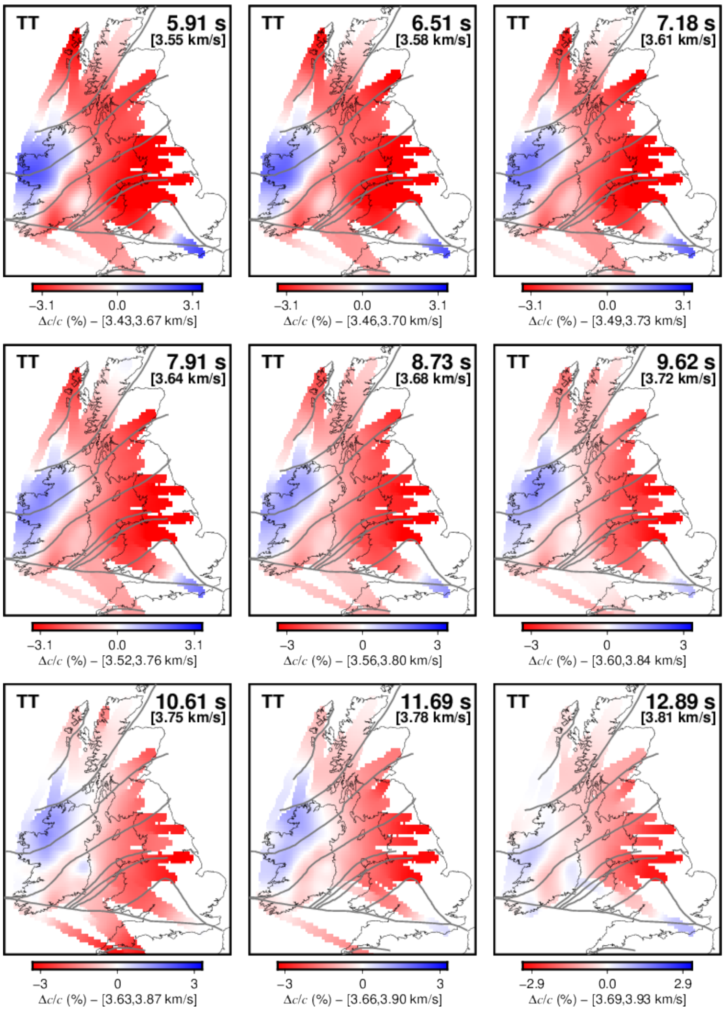

FIGURE B.11: Additional ambient noise TT phase velocity maps (see Chapter 3).

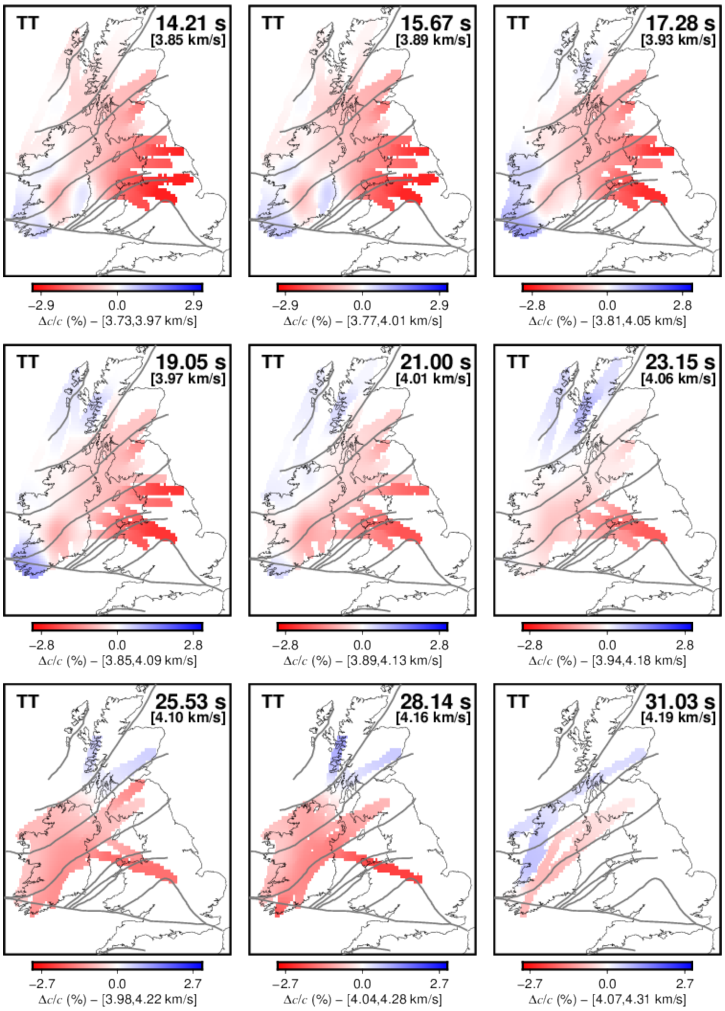

FIGURE B.12: Additional ambient noise TT phase velocity maps (see Chapter 3).

Appendix C

Supporting information for Chapter 4: Hot upper mantle beneath the Tristan da Cunha Hotspot, from probabilistic Rayleigh-wave inversion and petrological modeling

[1] In Fig. C.1 we show tomographic phase velocity maps at four periods[2]. The maps in each row are for the same periods, with the frames on the right showing the interstation path coverage at the period. Triangles show the seismic stations, the star indicates the Tristan da Cunha Island. The reference phase velocity at each period is given below the period value, top right of the frames on the left. The minimum and maximum deviations from the reference across the map are given at bottom left, in m/s and in per cent. The color scale used for all the maps is plotted at the bottom. The maps were computed with 15% of outlier interstation measurements removed, so as to constrain the models only with the most mutually consistent data (e.g., Deschamps et al., 2008; Endrun et al., 2011; Polat et al., 2012). Nevertheless, errors in the remaining data are still relatively large, whereas the lateral heterogeneity across the area is weak, as evidenced by the phase-velocity maps. Because of this, the inversions yield relatively low variance reductions (e.g., 28% at 13 s; 36% at 21 s; 26% at 30 s; 26% at 40 s). In order to reduce the effect of noise on interpretation, we try out an approach of "stacking" phase-velocity maps in

---

[1] The following text is part of the captions in the figures of *supporting information* in Bonadio et al. (2018).

[2] Fig. C.1 in Bonadio et al. (2018) presents a typographic mistake which has been corrected here.

ranges of periods (Figure S2).

Fig. C.2 presents "stacks" of phase-velocity maps. Phase-velocity maps were computed at a 1-s interval within the period ranges indicated and then averaged, so as to reduce random errors in the maps. The resulting "stacks" show the same large-scale features as original, period-specific[3] ones but with the small-scale noise removed, to a large extent. The maps at shorter periods (11–15 s) are sensitive to the oceanic crust and uppermost mantle. We observe a lower velocities in the NE compared to the SW part of the region. This can be attributed to the greater water depth in the NE (Figure 4a, 4b) (Rayleigh waves, especially at shorter periods, are influenced by the 3–4 km thick water layer). In contrast, low velocities in a ~1-km wide area beneath and around the active volcanic island are probably mostly due to the thicker crust there; relatively low seismic velocities in the crust and uppermost mantle may also play a role. At periods of 16–25 s, Rayleigh waves are mostly sensitive to the lithospheric mantle (~15–50 km depths). Relatively low velocities are now seen in the SW part of the region. This pattern, with the relatively low phase velocities to the south and southwest of Tristan da Cunha, persists at the longer periods as well. This suggests that the entire mantle lithosphere S-SW of TdC is warmer than N-NE from it. The phase-velocity contrast between the two domains is 1.0–1.5%, decreasing with period. The difference can probably be explained primarily by the lithosphere to the south and southwest of Tristan being younger than to the north and northwest of it (Figure 4b).

---

[3] This text in Bonadio et al. (2018) presents a typographic mistake which has been corrected here.

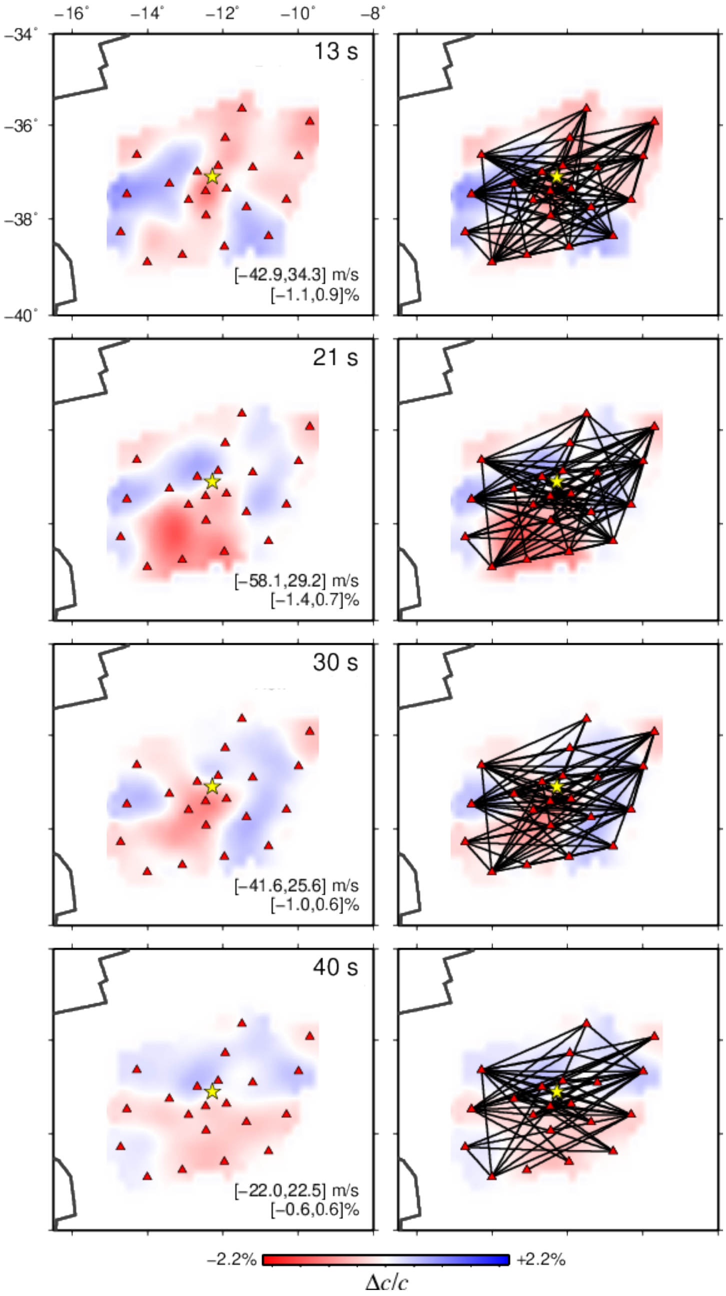

FIGURE C.1: Tomographic phase velocity maps at 13, 21, 30, and 40 s.

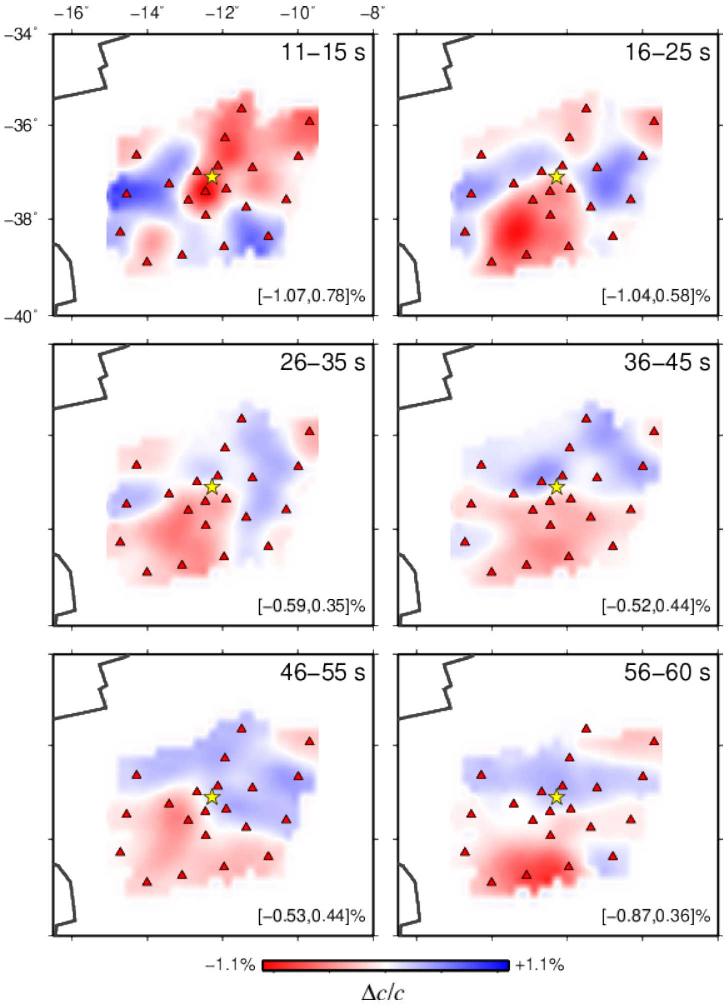

FIGURE C.2: "Stacks" of phase-velocity maps.

Bibliography

Abramovitz, T., M. Landes, H. Thybo, A.W.B. Jacob, and C. Prodehl (1999). “Crustal velocity structure across the Tornquist and Iapetus Suture Zones – a comparison based on MONA LISA and VARNET data”. In: *Tectonophysics* 314, pp. 69–82.

Adam, J. M.-C. and S. Lebedev (2012). “Azimuthal anisotropy beneath southern Africa from very broad-band surface-wave dispersion measurements”. In: *Geophys J. Int.* 191, pp. 155–174.

Afonso, J. C., M. Fernández, G. Ranalli, W. L. Griffin, and J. A. D. Connolly (2008). “Integrated geophysical-petrological modeling of the lithosphere and sublithospheric upper mantle: Methodology and applications”. In: *Geochemistry, Geophysics, Geosystems* 9 (5). DOI: `10.1029/2007GC001834`.

Agius, M. R. and S. Lebedev (2013). “Tibetan and Indian lithospheres in the upper mantle beneath Tibet: Evidence from broadband surface-wave dispersion”. In: *Geochemistry, Geophysics, Geosystems* 14 (10), pp. 4260–4281. DOI: `10.1002/ggge.20274`.

Agius, M.R. and S. Lebedev (2014). “Shear-velocity structure, radial anisotropy and dynamics of the Tibetan crust”. In: *Geophysical Journal International* 199, pp. 1395–1415.

Aki, K. and P.G. Richards (2002). *Quantitative Seismology*. University Science Books.

Al-Kindi, S., N. White, M. Sinha, R. England, and R. Tiley (2003). “Crustal trace of a hot convective sheet”. In: *Geology* 31.3, pp. 207–210.

Anderson, D. L. (2000). “The thermal state of the upper mantle; no role for mantle plumes”. In: *Geophysical Research Letters* 27 (22), pp. 3623–3626.

Anderson, D.L. (2005). “Scoring hotspots: the plume and plate paradigms”. In: *Geological Society of America Special Papers* 388, pp. 31–54.

Arroucau, P., N. Rawlinson, and Sambridge M. (2010). “New insight into Cainozoic sedimentary basins and Palaeozoic suture zones in southeast Australia from ambient noise surface-wave tomography”. In: *Geophys. Res. Lett.* 37.

Arrowsmith, Stephen J., Michael Kendall, Nicky White, John C. VanDecar, and David C. Booth (2005). “Seismic imaging of a hot upwelling beneath the British Isles”. In: *Geology* 33.5, pp. 345–348.

Asencio, E., J. H. Knapp, T. J. Owens, and G. Helffrich (1997). "Reconditioning inverse problems using the genetic algorithm and revised parameterization". In: *Geophysics* 62, pp. 1524–1532.

— (2003). "Mapping fine-scale heterogeneities within the continental mantle lithosphere beneath Scotland: Combining active- and passive-source seismology". In: *Geology* 31(6), pp. 477–480.

Baba, K., J. Chen, M. Sommer, H. Utada, W. H. Geissler, W. Jokat, and M Jegen (Oct. 2017). "Marine magnetotellurics imaged no distinct plume beneath the Tristan da Cunha hotspot in the southern Atlantic Ocean". In: *Tectonophysics* 716, pp. 52–63.

Bamford, D., K. Nunn, C. Prodehl, and B. Jacob (1978). "LISPB IV. Crustal structure of northern Britain". In: *Geophys. J. R. astr. Soc.* 54, pp. 43–60.

Barton, P. (1992). "LISPB revisited: a new look under the Caledonides of northern Britain". In: *Geophys. J. Int.* 110, pp. 371–391.

Bartzsch, S., S. Lebedev, and T. Meier (2011). "Resolving the lithosphere-asthenosphere boundary with seismic Rayleigh waves". In: *Geophysical Journal International* 186, pp. 1152–1164.

Bassin, C., G. Laske, and G. Masters (2000). "The current limits of resolution for surface-wave tomography in NorthAmerica". In: *Eos, Transactions, American Geophysical Union* 81.

Bastow, I. D., T. J. Owens, George Helffrich, and J. H. Knapp (2007). "Spatial and temporal constraints on sources of seismic anisotropy: Evidence from the Scottish highlands". In: *Geophysical Research Letters* 34.5. ISSN: 00948276. DOI: `10.1029/2006GL028911`.

Baykiev, Eldar, Mattia Guerri, and Javier Fullea (2018). "Integrating gravity and surface elevation with magnetic data: Mapping the curie temperature beneath the british isles and surrounding areas". In: *Frontiers in Earth Science* 6.October, pp. 1–19. ISSN: 22966463. DOI: `10.3389/feart.2018.00165`.

Behn, M. D., G. Hirth, and G. R. Elsenbeck II (2009). "Implications of grain size evolution on the seismic structure of the oceanic upper mantle". In: *Earth and Planetary Science Letters* 282, pp. 178–189.

Bensen, G.D., M.H. Ritzwoller, M.P. Barmin, A.L. Levshin, F. Lin, M.P. Moschetti, N.M. Shapiro, and Y. Yang (2007). "Processing seismic ambient noise data to obtain reliable broad-band surface-wave dispersion measurements". In: *Geophys J. Int.* 169, pp. 1239–1260.

Bijwaard, H. and W. Spakman (2000). "Non-linear global P-wave tomography by iterated linearized inversion". In: *Geophys. J. Int.* 141, pp. 71–82.

Bijwaard, H., W. Spakman, and E. R. Engdahl (1998). “Closing the gap between regional and global travel time tomography”. In: *Journal of Geophysical Research: Solid Earth* 103(B12), pp. 30055–30078. DOI: 10.1029/98jb02467.

Bodin, T. and M. Sambridge (2009). “Seismic tomography with the reversible jump algorithm”. In: *Geophysical Journal International* 178 (3), pp. 1411–1436. DOI: 10.1111/j.1365-246X.2009.04226.x.

Bodin, T., M. Sambridge, H. Tkalcic, P. Arroucau, K. Gallagher, and N. Rawlinson (2012). “Transdimensional inversion of receiver functions and surface-wave dispersion”. In: *Journal of Geophysical Research* 117.

Bodin, T., J. Leiva, B. Romanowicz, V. Maupin, and H. Yuan (2016). “Imaging Anisotropic Layering with Bayesian Inversion of Multiple Data Types”. In: *Geophysical Journal International*. DOI: 10.1093/gji/ggw124.

Bonadio, R., W. H. Geissler, S. Lebedev, J. Fullea, M. Ravenna, N. L. Celli, W. Jokat, M. Jegen, C. Sens-Schönfelder, and K. Baba (2018). “Hot upper mantle beneath the Tristan da Cunha hotspot from probabilistic Rayleigh-wave inversion and petrological modeling”. In: *Geochemistry, Geophysics, Geosystems* 19, pp. 1412–1428. DOI: https://doi.org/10.1002/2017GC007347.

Boschi, Lapo, Cornelis Weemstra, Julie Verbeke, Göran Ekström, Andrea Zunino, and Domenico Giardini (2013). “On measuring surface-wave phase velocity from station-station cross-correlation of ambient signal”. In: *Geophys J. Int.* 192, pp. 346–358.

Bott, M.H.P., R.E. Long, A.S.P. Green, A.H.J. Lewis, M.C. Sinha, and D.L. Stevenson (1985). “Crustal structure south of the Iapetus suture beneath northern England”. In: *Nature* 314, pp. 724–727. DOI: 1985.

Braile, L., M. K. Hall, J. J. Taber, and R. C. Aster (2003). “The IRIS education and outreach program”. In: *Seismological Research Letters* 74(5), pp. 1499–1518. DOI: 10.1785/gssrl.74.5.503. URL: https://www.iris.edu/hq/inclass/uploads/OnePager5.jpg.

British Geological Survey, Natural Environment Research Council. *Make-a-map*. https://www.bgs.ac.uk/discoveringGeology/geologyOfBritain/makeamap/map.html.

Brown, C. and J. P. Whelan (1955). “Terrane boundaries in Ireland inferred from the Irish Magnetotelluric Profile and other geophysical data”. In: *Journal of the Geological Society of London* 152, pp. 523–534.

Carvalho, J., R. Bonadio, G. Silveira, S. Lebedev, J. Mata, P. Arroucau, T. Meier, and N.L. Celli (2019). “Evidence for high temperature in the upper mantle beneath Cape Verde archipelago from Rayleigh-wave phase-velocity measurements”. In: *Tectonophysics*. DOI: 10.1016/j.tecto.2019.228225.

Celli, N. L., S. Lebedev, A. Schaeffer, and C. Gaina (2016). "Waveform Tomography of the South Atlantic Region". In: *American Geophysical Union (AGU) Fall Meeting, Conference Abstract*.

Chadwick, R. and T. Pharaoh (1998). "The seismic reflection Moho beneath the United Kingdom and adjacent areas". In: *Tectonophysics* 299, pp. 255–279.

Chambers, K., J. Woodhouse, and A. Deuss (2005). "Topography of the 410-km discontinuity from PP and SS precursors". In: *Earth and Planetary Science Letters* 235, pp. 610–622.

Chantel, J., G. Manthilake, D. Andrault, D. Novella, T. Yu, and Y. Wang (2016). "Experimental evidence supports mantle partial melting in the asthenosphere". In: *Science Advances* 2. DOI: `10.1126/sciadv.1600246`.

Chew, D. M. and C. J. Stillman (2009). *Late Caledonian orogeny and magmatism*. Dunedin Academic Press ltd.

Chew, D. M. and C. R. van Staal (2014). "The Ocean – Continent Transition Zones Along the Appalachian – Caledonian Margin of Laurentia: Examples of Large-Scale Hyperextension During the Opening of the Iapetus Ocean". In: *Geoscience Canada* 41. DOI: `10.12789/geocanj.2014.41.040`.

Chou, C.W. and J.R. Booker (1979). "A Backus–Gilbert approach to inversion of travel time data for three-dimensional velocity structure". In: *Geophys. J. Royal Astr. Soc.* 59, pp. 325–344.

Cogné, N., D. Doepke, D. Chew, F. M. Stuart, and C. Mark (2016). "Measuring plume-related exhumation of the British Isles in Early Cenozoic times". In: *Earth and Planetary Science Letters* 456, pp. 1–15. DOI: `dx.doi.org/10.1016/j.epsl.2016.09.053`.

Connolly, J. A. D. (2005). "Computation of phase equilibria by linear programming: A tool for geodynamic modeling and its application to subduction zone decarbonation". In: *Earth and Planetary Science Letters* 236, pp. 524–541. DOI: `10.1016/j.epsl.2005.04.033`.

Courtillot, V., J. Besse A. Davaille, and J. Stock (2003). "Three distinct types of hotspots in the Earth's mantle". In: *Earth and Planetary Science Letters* 205 (3–4), pp. 295–308. DOI: `http://dx.doi.org/10.1016/S0012-821X(02)01048-8.`.

Craig, D., C. J. Bean, I. Lokmer, and M. Möllhoff (2016). "Correlation of wavefield-separated ocean-generated microseisms with North Atlantic source regions". In: *Bulletin of the Seismological Society of America*.

Dahlen, F. A. and J. Tromp (1998). *Theoretical Global Seismology*. Princeton University Press.

Dahlen, F.A. and Y. Zhou (2006). "Surface-wave group-delay and attenuation kernels". In: *Geophysical Journal International* 165(2), pp. 545–554.

Dalton, C. A., C. H. Langmuir, and A. Gale (2014). "Geophysical and Geochemical Evidence for Deep Temperature Variations Beneath Mid-Ocean Ridges". In: *Science* 344 (80). DOI: `10.1126/science.1249466`.

Darbyshire, F. A. and S. Lebedev (2009). "Rayleigh wave phase-velocity heterogeneity and multilayered azimuthal anisotropy of the Superior Craton, Ontario". In: *Geophys. J. Int.* 176, pp. 215–234. DOI: `10.1111/j.1365-246X.2008.03982.x`.

Davis, M.W., N.J. White, K.F. Priestley, B.J. Baptie, and F.J. Tilmann (2012). "Crustal structure of the British Isles and its epeirogenic consequences". In: *Geophysical Journal International* 190, pp. 705–725.

Debayle, E. and M. Sambridge (2004). "Inversion of massive surface-wave data sets: Model construction and resolution assessment". In: *Journal of Geophysical Research* 109 (B02316). DOI: `10.1029/2003JB002652`.

Deschamps, F., S. Lebedev, T. Meier, and J. Trampert (2008). "Azimuthal anisotropy of Rayleigh-wave phase velocities in the east-central United States". In: *Geophysical Journal International* 173, pp. 827–843.

Dewey, J. F. (1982). "Plate tectonics and the evolution of the British Isles: Thirty-fifth William Smith Lecture". In: *Journal of the Geological Society* 139, pp. 371–412. DOI: `10.1144/gsjgs.139.4.0371`.

Di Leo, J., I. Bastow, and G. Helffrich (2009). "Nature of the Moho beneath the Scottish Highlands from a receiver function perspective". In: *Tectonophysics* 474, pp. 214–222.

Do, V.C., B.M. O'Reilly, M. Landes, and P.W. Readman (2006). "Shear-wave splitting observations across southwest Ireland". In: *Geophys. Res. Lett.* 33(L03309), pp. 1–23. DOI: `10.1029/2005GL024496`.

Döpke, D. (2017). "Modelling the thermal history of onshore Ireland, Britain and its offshore basins using low-temperature thermochronology". PhD thesis. Trinity College Dublin.

Dziewonski, A. M. and D. L. Anderson (1981). "Preliminary reference Earth model". In: *Physics of the Earth and Planetary Interiors* 25, pp. 297–356.

Dziewonski, A. M., T.-A. Chou, and J. H. Woodhouse (1981). "Determination of earthquake source parameters from waveform data for studies of global and regional seismicity". In: *Journal of Geophysical Research* 86, pp. 2825–2852. DOI: `10.1029/JB086iB04p02825`.

Dziewonski, A.M. and A.L. Hales (1972). "Numerical analysis of dispersed seismic waves, in Methods in Computational Physics". In: *Academic Press, New York, ed. Bolt, B.A.* 11.

Edwards, J.W.F. and D.J. Blundell (1984). "Summary of seismic refraction experiments in the English Channel, Celtic Sea and St. George's Channel". In: *British Geological Survey Marine Geophysics Report* 144.

Ekström, G., M. Nettles, and A.M. Dziewonski (2012). “The global CMT project 2004–2010: Centroid-moment tensors for 13017 earthquakes”. In: *Physics of the Earth and Planetary Interiors* 200–201, pp. 1–9.

Endrun, B., T. Meier, Lebedev, M. S. Bohnhoff, G. Stavrakakis, and H-P. Harjes (2008). “S velocity structure and radial anisotropy in the Aegean region from surface-wave dispersion”. In: *Geophys. J. Int.* 174, pp. 593–616.

Endrun, B., S. Lebedev, T. Meier, C. Tirel, and W. Friederich (2011). “Complex layered deformation within the Aegean crust and mantle revealed by seismic anisotropy”. In: *Nature Geoscience* 4, pp. 203–207.

Erduran, M., B. Endrun, and T. Meier (2008). “Continental vs. oceanic lithosphere beneath the eastern Mediterranean Sea – implications from Rayleigh wave dispersion measurements”. In: *Tectonophysics* 457, pp. 42–52.

Fairhead, J.D. and M. Wilson (2005). “Plate tectonic processes in the South Atlantic Ocean: Do we need deep mantle plumes?” In: *Geological Society of America Special Papers* 388, pp. 537–553.

Faul, U. H. and I. Jackson (2005). “The seismological signature of temperature and grain size variations in the upper mantle”. In: *Earth and Planetary Science Letters* 234, pp. 119–134.

Foulger, G. and J. H. Natland (2003). “Is "hotspot" volcanism a consequence of plate tectonics?” In: *Science* 300, pp. 921–922.

Freeman, B., S.L. Klemperer, and R.W. Hobbs (1988). “The deep structure of northern England and the Iapetus Suture zone from BIRPS deep seismic reflection profiles”. In: *J. geol. Soc. Lond.* 145, pp. 727–740.

French, S.W. and B. Romanowicz (2015). “Broad plumes rooted at the base of the Earth’s mantle beneath major hotspots”. In: *Nature* 525 (7567), pp. 95–99. DOI: `10.1038/nature14876`.

Fry, B., L. Boschi, G. Ekstrom, and D. Giardini (2008). “Europe-Mediterranean tomography: high correlation between new seismic data and independent geophysical observables”. In: *Geophys. Res. Lett.* 35(L04301). DOI: `doi:10.1029/2007GL031519`.

Fukao, Y., M. Obayashi, H. Inoue, and M. Nebai (1992). “Subducting slabs stagnant in the mantle”. In: *J. Geophys. Res.* 97, pp. 4809–4822.

Fullea, J., J. C. Afonso, J. A. D. Connolly, M. Fernandez, D. Garcia-Castellanos, and H. Zeyen (2009). “LitMod3D: An interactive 3-D software to model the thermal, compositional, density, seismological, and rheological structure of the lithosphere and sublithospheric upper mantle”. In: *Geochemistry, Geophysics, Geosystems* 10 (8). DOI: `10.1029/2009GC002391`.

Fullea, J., S. Lebedev, M. Agius, A. Jones, and J.C. Afonso (2012). “Lithospheric structure in the Baikal-central Mongolia region from integrated geophysical-petrological inversion of surface-wave data and topographic elevation". In: *Geochemistry, Geophysics, Geosystems* 13.

Fullea, J., M. R. Muller, A. G. Jones, and J. C. Afonso (2014). "The lithosphere-asthenosphere system beneath Ireland from integrated geophysical-petrological modeling II: 3D thermal and compositional structure". In: *Lithos* 189, pp. 49–64. ISSN: 00244937. DOI: 10.1016/j.lithos.2013.09.014. URL: http://dx.doi.org/10.1016/j.lithos.2013.09.014.

Fullea, J., A. G. Camacho, A. M. Negredo, and J. Fernández (2015). "The Canary Islands hot spot: New insights from 3D coupled geophysical–petrological modelling of the lithosphere and uppermost mantle". In: *Earth and Planetary Science Letters* 409, pp. 71–88.

Galetti, E., A. Curtis, B. Baptie, D. Jenkins, and H. Nicolson (2016). "Transdimensional Love-wave tomography of the British Isles and shear-velocity structure of the East Irish Sea Basin from ambient-noise interferometry". In: *Geophysical Journal International* 208 (1), pp. 36–58. DOI: 10.1093/gji/ggw286.

Ganerød, M., M. A. Smethurst, T. H. Torsvik, T. Prestvik, S. Rousse, C. McKenna, D. J.J. van Hinsbergen, and B. W.H. Hendriks (2010). "The North Atlantic Igneous Province reconstructed and its relation to the Plume Generation Zone: The Antrim Lava Group revisited". In: *Geophysical Journal International* 182.1, pp. 183–202. ISSN: 0956540X. DOI: 10.1111/j.1365-246X.2010.04620.x.

Gassmöller, R., E. Bredow J. Dannberg, B. Steinberger, and T. H. Torsvik (2016). "Major influence of plume-ridge interaction, lithosphere thickness variations, and global mantle flow on hotspot volcanism–The example of Tristan". In: *Geochemistry, Geophysics, Geosystems* 17 (4), pp. 1454–1479. DOI: 10.1002/2015GC006177.

Geissler, W. H., W. Jokat, M. Jegen, and K. Baba (2016). "Thickness of the oceanic crust, the lithosphere, and the mantle transition zone in the vicinity of the Tristan da Cunha hot spot estimated from ocean-bottom and ocean-island seismometer receiver functions". In: *Tectonophysics*. DOI: http://dx.doi.org/10.1016/j.tecto.2016.12.013.

Geissler, W.H. (2014). "Electromagnetic, gravimetric and seismic measurements to investigate the Tristan da Cunha hot spot and its role in the opening of the South Atlantic Ocean (MARKE) - Cruise No. MSM24 - December 27, 2012 - January 21, 2013 - Walvis Bay (Namibia) - Cape Town (South Africa), 1-56;" in: *MARIA S. MERIAN-Berichte; MSM24; 1-56; ISSN 2195-8483*. DOI: 10.2312/cr_msm24.

Gibson, S.A., R.N. Thompson, and J.A. Day (2006). "Timescales and mechanisms of plume-lithosphere interactions: ^{40}Ar/^{39}Ar geochronology and geochemistry of alkaline igneous rocks from the Paraná-Etendeka large igneous province". In: *Earth and Planetary Science Letters* 251 (1–2), pp. 1–17. DOI: `http://dx.doi.org/10.1016/j.epsl.2006.08.004`.

Godfrey, K. E., C. A. Dalton, and J. Ritsema (2017). "Seafloor age dependence of Rayleigh wave phase velocities in the Indian Ocean". In: *Geochemistry, Geophysics, Geosystems* 18, pp. 1926–1942. DOI: `10.1002/2017GC006824`.

Goes, S., R. Govers, and P. Vacher (2000). "Shallow mantle temperatures under Europe from P and S wave tomography". In: *Journal of Geophysical Research* 105 (B5), pp. 11153–11169.

Goes, S., J. Armitage, N. Harmon, H. Smith, and R. Huismans (2012). "Low seismic velocities below mid-ocean ridges: Attenuation versus melt retention". In: *Journal of Geophysical Research* 117 (B12403). DOI: `10.1029/2012JB009637`.

Hammond, W. C. and E. D. Humphrey (2000a). "Upper mantle seismic wave attenuation: Effects of realistic partial melt distribution". In: *Journal of Geophysical Research* 105 (B5), pp. 10987–10999.

— (2000b). "Upper mantle seismic wave velocity: Effects of realistic partial melt geometries". In: *Journal of Geophysical Research* 105 (B5), pp. 10975–10986.

Hardwick, A. (2008). "New insights into the crustal structure of the England, Wales and Irish Seas areas from local earthquake tomography and associated seismological studies". PhD thesis. University of Leicester.

Harmon, N., D. W. Forsyth, and D. S. Weeraratne (2009). "Thickening of young Pacific lithosphere from high-resolution Rayleigh wave tomography: A test of the conductive cooling model". In: *Earth and Planetary Science Letters* 278, pp. 96–106.

Hauser, J., M. Sambridge, and N. Rawlinson (2008). "Multiarrival wave-front tracking and its applications". In: *Geochem. Geophys. Geosyst.* 9. DOI: `10.1029/2008GC002069`.

Hawkins, R., T. Bodin, M. Sambridge, G. Choblet, and L. Husson (2019). "Trans-dimensional surface reconstruction with different classes of parameterization". In: *Geochemistry, Geophysics, Geosystems*. DOI: `10.1029/2018GC008022`.

Herzberg, C. and P. D. Asimow (2008). "Petrology of some oceanic island basalts: PRIMELT2.XLS software for primary magma calculation". In: *Geochemistry, Geophysics, Geosystems* 9 (9). DOI: `10.1029/2008GC002057`.

Herzberg, C., P.D. Asimow, N. Arndt, Y. Niu, C. Lesher, J. Fitton, M. Cheadle, and A. Saunders (2007). "Temperatures in ambient mantle and plumes:

Constraints from basalts, picrites, and komatiites". In: *Geochemistry, Geophysics, Geosystem* 8 Q02006. DOI: 10.1029/2006GC001390.

Hillis, R.R. and S.P. Holford (2008). "Cenozoic exhumation of the southern British Isles". In: *Geology* 36, pp. 371–374.

Hodgson, J. (2001). "A seismic and gravity study of the Leinster Granite: SE Ireland". PhD thesis. Dublin Institute for Advanced Studies, Dublin, Ireland.

Holford, Simon P., Paul F. Green, Richard R. Hillis, Jonathan P. Turner, and Carl T.E. Stevenson (2009). "Mesozoic-Cenozoic exhumation and volcanism in Northern Ireland constrained by AFTA and compaction data from the Larne No. 2 borehole". In: *Petroleum Geoscience* 15.3, pp. 239–257. ISSN: 13540793. DOI: 10.1144/1354-079309-840.

Humphris, S. E., G. Thompson, J.-G. Schilling, and R. H. Kingsley (1985). "Petrological and geochemical variations along the Mid-Atlantic Ridge between 46 S and 32 S: influence of the Tristan da Cunha mantle plume". In: *Geochimica et Cosmochimica Acta* 49 (6), pp. 1445–1464.

IOC, IHO, and BODC (2003). *Centenary Edition of the GEBCO Digital Atlas*. https://www.gebco.net.

Jackson, I. and U. H. Faul (2010). "Grainsize-sensitive viscoelastic relaxation in olivine: Towards a robust laboratory-based model for seismological application". In: *Physics of the Earth and Planetary Interiors* 183, pp. 151–163.

Jackson, I., J. D. Fitz Gerald, U. H. Faul, and B. H. Tan (2002). "Grain-size-sensitive seismic wave attenuation in polycrystalline olivine". In: *Journal of Geophysical Research* 107 (B12). DOI: 10.1029/2001JB001225.

Jacob, A.B.W., W. Kaminski, T. Murphy, W.E.A. Phillips, and C. Prodehl (1985). "A crustal model for a northeast-southwest profile through Ireland". In: *Tectonophysics* 113(1–2), pp. 75–103.

James, E. K., C. A. Dalton, and J. B. Gaherty (2014). "Rayleigh wave phase velocities in the Atlantic upper mantle". In: *Geochemistry, Geophysics, Geosystems* 15, pp. 4305–4324. DOI: 10.1002/2014GC005518.

Jones, A.G., J.C. Afonso, J. Fullea, M.R. Muller, and F. Salajegheh (2013). "The lithosphere–asthenosphere system beneath Ireland from integrated geophysical–petrological modeling – I: Observations, 1D and 2D modelling". In: *Lithos* 189.

Jones, S. M., N. White, B. J. Clarke, E. Rowley, and K. Gallagher (2002). "Present and past influence of the Iceland Plume on sedimentation". In: *Geological Society, London, Special Publications* 196, pp. 13–25. DOI: 10.1144/GSL.SP.2002.196.01.02.

Jones, S.M. and N.J. White (2003). "Shape and size of the starting Iceland Plume swell". In: *Earth planet. Sci. Lett.* 216, pp. 271–282.

József, A. (1936). *A Dunánál, in Szép Szó*. József, A.

Kárason, H. and R. D. van der Hilst (2001). “Whole mantle P-wave travel time tomography”. In: *Journal of Geophysical Research* 106 (B4), pp. 6569–6587. DOI: `10.1029/2000JB900380`.

Kästle, Emanuel D., Riaz Soomro, Cornelis Weemstra, Lapo Boschi, and Thomas Meier (2016). “Two-receiver measurements of phase velocity: Cross-validation of ambient-noise and earthquake-based observations”. In: *Geophysical Journal International* 207.3, pp. 1493–1512. ISSN: 1365246X. DOI: `10.1093/gji/ggw341`.

Katsura, T., A. Yoneda, D. Yamazaki, T. Yoshino, and E. Ito (2010). “Adiabatic temperature profile in the mantle”. In: *Physics of the Earth and Planetary Interiors* 183, pp. 212–218.

Katz, R.F., M. Spiegelman, and C. H. Langmuir (2003). “A new parameterization of hydrous mantle melting”. In: *Geochemistry, Geophysics, Geosystems* 4 (9). DOI: `10.1029/2002GC000433`.

Kelly, Annabel, Richard W. England, and Peter K.H. Maguire (2007). “A crustal seismic velocity model for the UK, Ireland and surrounding seas”. In: *Geophysical Journal International* 171.3, pp. 1172–1184. ISSN: 0956540X. DOI: `10.1111/j.1365-246X.2007.03569.x`.

Kennett, B.L.N., E.R. Engdahl, and R. Buland (1995). “Constraints on seismic velocities in the Earth from traveltimes”. In: *Geophysical Journal International* 122 (1), pp. 108–124.

Khan, A., A. Zunino, and F. Deschamps (2013). “Upper mantle compositional variations and discontinuity topography imaged beneath Australia from Bayesian inversion of surface-wave phase velocities and thermochemical modeling”. In: *Journal of Geophysical Research* 118. DOI: `10.1002/jgrb50304`.

Klemperer, S. and R. Hobbs (1991). “The BIRPS Atlas: Deep Seismic Reflection Profiles Around the British Isles”. In: *Cambridge Univ. Press.*

Klemperer, S.L., P.D. Ryan, and D.B. Snyder (1991). “A deep seismic reflection transect across the Irish Caledonides”. In: *J. Geol. Soc. Lond.* 148, pp. 149–164.

Kuskov, O., V. Kronrod, A. Prokofyev, and N. Pavlenkova (2014). “Thermo-chemical structure of the lithospheric mantle underneath the Siberian craton inferred from long-range seismic profiles”. In: *Tectonophysics* 615, pp. 154–166.

Landes, M., C. Prodehl, F. Hauser, A.W.B. Jacob, and N.J. Vermeulen (2000). “VARNET-96: influence of the Variscan and Caledonian orogenies on crustal structure in SW Ireland”. In: *Geophysical Journal International* 140 (3), pp. 660–676.

Landes, M., J.R.R. Ritter, V.C. Do, P.W. Readman, and B.M. O'Reilly (2004). "Passive teleseismic experiment explores the deep subsurface of southern Ireland". In: *Eos, Trans. - Am. Geophys. Union* 85(36), pp. 337–341. DOI: 10.1029/2018JB016555.

Landes, M., J.R.R. Ritter, P.W. Readman, and B.M. O'Reilly (2005). "A review of the Irish crustal structure and signatures from the Caledonian and Variscan orogenies". In: *Terra Nova* 17 (2), pp. 111–120.

Landes, M., J.R.R. Ritter, B.M. O'Reilly, P.W. Readman, and V.C. Do (2006). "A N–S receiver function profile across the Variscides and Caledonides in SW Ireland". In: *Geophys. J. Int.* 166, pp. 814–824. DOI: 10.1029/2018JB016555.

Landes, M., J.R.R. Ritter, and P.W. Readman (2007). "Proto-Iceland plume caused thinning of Irish lithosphere". In: *Earth and Planetary Science Letters* 255 (1), pp. 32–40. DOI: doi.

Laske, G., A. Markee, J. A. Orcutt, C. J. Wolfe, J. A. Collins, S. C. Solomon, R. S. Detrick, D. Bercovici, and E. H. Hauri (2011). "Asymmetric shallow mantle structure beneath the Hawaiian Swell–evidence from Rayleigh waves recorded by the PLUME network". In: *Geophysical Journal International* 187 (B12403), pp. 1725–1742. DOI: 10.1111/j.1365-246X.2011.05238.x.

Le Pape, F., D. Bean C.J. ans Craig, P. Jousset, C. Horan, C. Hogg, S. Donne, H. McCann, M. Mollhoff, H. Kirk, and A. Ploetz (2016). "New OBS network deployment offshore Ireland". In: *EGU General Assembly 2016 - Geophysical Research Abstracts* 18, pp. 1499–1518.

Lebedev, S. and R. D. van der Hilst (2008). "Global upper-mantle tomography with the automated multimode inversion of surface and S-wave forms". In: *Geophysical Journal International* 173, pp. 505–518.

Lebedev, S., G. Nolet, T. Meier, and R. D. van der Hilst (2005). "Automated multimode inversion of surface and S waveforms". In: *Geophys J. Int.* 162, pp. 951–964.

Lebedev, S., T. Meier, and R. D. van der Hilst (2006). "Asthenospheric flow and origin of volcanism in the Baikal Rift area". In: *Earth and Planetary Science Letters* 249, pp. 415–424.

Lebedev, S., J. Boonen, and J. Trampert (2009). "Seismic structure of Precambrian lithosphere: New constraints from broad-band surface-wave dispersion". In: *Lithos* 109, pp. 9–111.

Lebedev, S., C. Horan, P. W. Readman, A. J. Schaeffer, M. R. Agius, L. Collins, F. Hauser, B. M. O'Reilly, and T. Blake (2012). "Ireland Array: a new broadband seismic network targets the structure, evolution and seismicity of Ireland and surroundings". In: *Proceedings of EGU General Assembly*. URL: http://www.dias.ie/ireland_array/.

Lebedev, S., J. M.-C. Adam, and T. Meier (2013). “Mapping the Moho with seismic surface-waves: A review, resolution analysis, and recommended inversion strategies”. In: *Tectonophysics* 609, pp. 377–394.

Lebedev, S., R. Bonadio, C. Gómez-Garcia, J. de Laat, L. Bérdi, B. Chagas de Melo, D. Farrell, D. Stalling, C. Tirel, L. Collins, S. McCarthy, B. O’Donoghue, A. Schwenk, M. Smyth, C. J. Bean, and SEA-SEIS team (2019). “Education and public engagement using an active research project: lessons and recipes from the SEA-SEIS North Atlantic Expedition’s programme for Irish schools”. In: *Geoscience Communication*. DOI: `10.5194/gc-2019-13`.

Lebedev, Sergei and Rob D. Van Der Hilst (2008). “Global upper-mantle tomography with the automated multimode inversion of surface and S-wave forms”. In: *Geophysical Journal International* 173.2, pp. 505–518. ISSN: 0956540X. DOI: `10.1111/j.1365-246X.2008.03721.x`.

Licciardi, A, N. Piana Agostinetti, S. Lebedev, A. J. Schaeffer, P. W. Readman, and C. Horan (2014). “Moho depth and V_p/V_s in Ireland from teleseismic receiver functions analysis”. In: *Geophys. J. Int.* 199, pp. 561–579.

Lin, F.-C., M.H. Ritzwoller, J. Townend, S. Bannister, and M.K. Savage (2007). “Ambient noise Rayleigh wave tomography of New Zealand”. In: *Geophys J. Int.* 170, pp. 649–666.

Lin, F.-C., M.P. Moschetti, and M.H. Ritzwoller (2008). “Surface-wave tomography of the western United States from ambient seismic noise: Rayleigh and Love wave phase velocity maps”. In: *Geophys J. Int.* 173, pp. 281–298.

Lindquist, K. G., K. Engle, D. Stahlke, and E. Price (2004). “Global Topography and Bathymetry Grid Improves Research Efforts”. In: *Eos, Transactions, American Geophysical Union* 85 (19), p. 186.

Lowe, C. and A.W.B. Jacob (1989). “A north-south seismic profile across the Caledonian Suture zone in Ireland”. In: *Tectonophysics* 168, pp. 297–318.

Luszczak, K., C. Persano, and F. M. Stuart (2018). “Early Cenozoic denudation of central west Britain in response to transient and permanent uplift above a mantle plume”. In: *Tectonics*. DOI: `10.1002/2017TC004796`.

Maguire, Peter, Richard England, and Anthony Hardwick (2011). “LISPB DELTA, a lithospheric seismic profile in Britain: Analysis and interpretation of the Wales and southern England section”. In: *Journal of the Geological Society* 168.1, pp. 61–82. ISSN: 00167649. DOI: `10.1144/0016-76492010-030`.

Marquering, H. and R. Snieder (1996). “Surface-wave velocity structure beneath Europe, the northeastern Atlantic and western Asia from waveform inversion including surface wave mode coupling". In: *Geophys. J. Int.* 127, pp. 238–304.

Masson, F., A.W.B. Jacob, C. Prodehl, P.W. Readman, P.M. Shannon, A. Schulze, and U. Enderle (1998). "A wide-angle seismic traverse through the Variscan of southwest Ireland". In: *Geophys. J. Int* 134, pp. 689–705.

Masson, F., F. Hauser, and A. Jacob (1999). "The lithospheric trace of the Iapetus Suture in SW Ireland from teleseismic data". In: *Tectonophysics* 302, pp. 83–98.

Masters, G., M.P. Barmine, and S. Kientz (2007). "Mineos user's manual". In: *Computational Infrastructure for Geodynamics, California Institute of Technology, Pasadena, `http://geodynamics.org/cig/software/mineos`*.

Mather, B., T. Farrell, and J. Fullea (2018). "Probabilistic Surface Heat Flow Estimates Assimilating Paleoclimate History: New Implications for the Thermochemical Structure of Ireland". In: *Journal of Geophysical Research: Solid Earth*. DOI: `10.1029/2018JB016555`.

Mather, Ben and Javier Fullea (2019). "Constraining the geotherm beneath the British Isles from Bayesian inversion of Curie depth: Integrated modelling of magnetic, geothermal and seismic data". In: *Solid Earth Discussions* February, pp. 1–20. DOI: `10.5194/se-2019-9`.

Meier, T., K. Dietrich, B. Stockhert, and H.P. Harjes (2004). "One-dimensional models of shear wave velocity for the eastern Mediterranean obtained from the inversion of Rayleigh wave phase velocities and tectonic implications". In: *Geophysical Journal International* 156 (1), pp. 45–58. DOI: `10.1111/j.1365-246X.2004.02121.x`.

Michelini, A. (1995). "An adaptive-grid formalism for traveltime tomography". In: *Geophys. J. Int.* 121.

Moretti, M., S. Pondrelli, L. Margheriti, ..., R. Bonadio, ..., and S. Mazza (2016). "SISMIKO: emergency network deployment and data sharing for the 2016 central Italy seismic sequence". In: *INGV - Annals of Geophysics* 59 (Fast Track 5). DOI: `10.4401/ag-7212`.

Morgan, J. P. (1997). "The generation of a compositional lithosphere by mid-ocean ridge melting and its effect on the subsequent off-axis hotspot upwelling and melting". In: *Earth and Planetary Science Letters* 146, pp. 213–232.

Morgan, W. J. (1971). "Convection Plumes in the Lower Mantle". In: *Nature* 230 (5288), pp. 42–43.

Nicolson, H., A. Curtis, B. Baptie, and E. Galetti (2012). "Seismic interferometry and ambient noise tomography in the British Isles". In: *Proceedings of the Geologists' Association* 123 (1), pp. 74–86. DOI: `10.1093/gji/ggu071`.

Nicolson, H., A. Curtis, and B. Baptie (2014). "Rayleigh wave tomography of the British Isles from ambient seismic noise". In: *Geophysical Journal International* 198 (2), pp. 637–655. DOI: 10.1093/gji/ggu071.

Nishimura, C. E. and D. W. Forsyth (1989). "The anisotropic structure of the upper mantle in the Pacific". In: *Geophysical Journal* 96, pp. 203–229.

NOAA, National Geophysical Data Center (2006). *2-minute Gridded Global Relief Data (ETOPO2) v2*. DOI: 10.7289/V5J1012Q.

Noller, N. M. Willmot, J. S. Daly, and the IRETHERM team (2015). "The Contribution of Radiogenic Heat Production Studies to Hot Dry Rock Geothermal Resource Exploration in Ireland". In: *Proceedings World Geothermal Congress 2015*.

O'Connor, J. M. and R. A. Duncan (1990). "Evolution of the Walvis Ridge-Rio Grande Rise Hot Spot System: Implications for African and South American Plate motions over plumes". In: *Journal of Geophysical Research: Solid Earth* 95 (B11), pp. , 17475–17502. DOI: 10.1029/JB095iB11p17475.

O'Connor, J. M. and W. Jokat (2015). "Tracking the Tristan-Gough mantle plume using discrete chains of intraplate volcanic centers buried in the Walvis Ridge". In: *Geology*. DOI: 10.1130/G36767.1.

O'Connor, J. M., W. Jokat, A.P. le Roex, C. Class, J.R. Wijbrans, S. Keszling, K.F. Kuiper, and O. Nebel (2012). "Hotspot trails in the South Atlantic controlled by plume and plate tectonic processes". In: *Nature Geoscience* 5 (10), pp. 735–738.

O'Donnell, J. P., C. Daly E. Tiberi, I. D. Bastow, B. M. O'Reilly, P. W. Readman, and F. Hauser (2011). "Lithosphere–asthenosphere interaction beneath Ireland from joint inversion of teleseismic P-wave delay times and GRACE gravity". In: *Geophys. J. Int.* DOI: 10.1111/j.1365-246X.2011.04921.x.

O'Reilly, B. M., F. Hauser, and P. W. Readman (2010). "The fine-scale structure of upper continental lithosphere from seismic waveform methods: Insights into Phanerozoic crustal formation processes". In: *Geophysical Journal International* 180.1, pp. 101–124. ISSN: 0956540X. DOI: 10.1111/j.1365-246X.2009.04420.x.

— (2012). "The fine-scale seismic structure of the upper lithosphere within accreted Caledonian lithosphere: Implications for the origins of the 'Newer Granites'". In: *Journal of the Geological Society* 169.5, pp. 561–573. ISSN: 00167649. DOI: 10.1144/0016-76492011-128.

O'Reilly, B.M., F. Hauser, A.W.B. Jacob, and P.M. Shannon (1996). "The lithosphere below the Rockall Trough: wide-angle seismic evidence for extensive serpentinisation". In: *Tectonophysics* 255, pp. 1–23.

Paige, C. C. and M. A. Saunders (1987). "LSQR: An Algorithm for Sparse Linear Equations and Sparse Least Squares". In: *ACM Transactions on*

Mathematical Software (TOMS) 9 (1), pp. 43–71. DOI: 10.1145/355984.355989.

Pawlak, A., D. W. Eaton, F. Darbyshire, S. Lebedev, and I. D. Bastow (2012). “Crustal anisotropy beneath Hudson Bay from ambient noise tomography: Evidence for post-orogenic lower-crustal flow?” In: *Journal of Geophysical Research* 117, B08301. DOI: 10.1029/2011JB009066.

Piana Agostinetti, N. and A. Malinverno (2010). “Receiver function inversion by trans-dimensional Monte Carlo sampling”. In: *Geophysical Journal International* 181(2), pp. 858–872.

Piana Agostinetti, N., G. Giacomuzzi, and A. Malinverno (2015). “Local 3D earthquake tomography by trans-dimensional Monte Carlo sampling”. In: *Geophysical Journal International* 201(3), pp. 1598–1617.

Polat, G., S. Lebedev, P. W. Readman, B. M. O’Reilly, and F. Hauser (2012). “Anisotropic Rayleigh-wave tomography of Ireland’s crust: Implications for crustal accretion and evolution within the Caledonian Orogen”. In: *Geophysical Research Letters* 39 (L04302). DOI: 10.1029/2012GL051014.

Putirka, K. (2008). “Excess temperatures at ocean islands: Implications for mantle layering and convection”. In: *Geology* 36, pp. 283–286. DOI: 10.1130/G24615A.1.

Putirka, K. D. (2005). “Mantle potential temperatures at Hawaii, Iceland, and the mid-ocean ridge system, as inferred from olivine phenocrysts: Evidence for thermally driven mantle plumes”. In: *Geochemistry, Geophysics, Geosystems* 6 (5). DOI: 10.1029/2005GC000915.

Putirka, K. D., M. Perfit, F. J. Ryerson, and M. J. Jackson (2007). “Ambient and excess mantle temperatures, olivine thermometry, and active vs. passive upwelling”. In: *Chemical Geology* 241, pp. 177–206.

Rao, C., A.G. Jones, and M. Moorkamp (2007). “The geometry of the Iapetus Suture Zone in central Ireland deduced from a magnetotelluric study”. In: *Phys. Earth planet. Inter.* 161(1-2), pp. 134–141.

Ravenna, M. and S. Lebedev (2018). “Bayesian inversion of surface-wave data for radial and azimuthal shear-wave anisotropy, with applications to central Mongolia and west-central Italy”. In: *Geophysical Journal International* 213, pp. 278–300. DOI: 10.1093/gji/ggx497.

Ravenna, M., S. Lebedev, J. Fullea, and J. M.-C. Adam. (2018). “Shear-wave velocity structure of southern Africa’s lithosphere: Variations in the thickness and composition of cratons and their effect on topography”. In: *Geochem. Geophys. Geosyst.* 19, pp. 1499–1518. DOI: 10.1029/2017GC007399.

Rawlinson, N., S. Pozgay, and S. Fishwick (2010). “Seismic tomography: A window into deep Earth”. In: *Physics of the Earth and Planetary Interiors*. DOI: 10.1016/j.pepi.2009.10.002.

Rawlinson, N., P. Arroucau, R. Musgrave, R. Cayley, M. Young, and M. Salmon (2014). "Complex continental growth along the proto-Pacific margin of East Gondwana". In: *Geology* 42 (9), pp. 783–786. DOI: `10.1130/G35766.1`.

Readman, P.W., B.M. O'Reilly, and T. Murphy (1997). "Gravity gradients and upper-crustal tectonic fabrics, Ireland". In: *J. Geol. Soc. Lond.* 154, pp. 817–828.

Rickers, F., A. Fichtner, and J. Trampert (2013). "The Iceland–Jan Mayen plume system and its impact on mantle dynamics in the North Atlantic region: Evidence from full-waveform inversion". In: *Earth and Planetary Science Letters* 367, pp. 39–51. DOI: `dx.doi.org/10.1016/j.epsl.2013.02.022`.

Rohde, J. K., K. Hoernle, Hauff F., R. Werner, J. O'Connor, C. Class, D. Garbe-Schönberg, and W. Jokat (2013a). "70 Ma chemical zonation of the Tristan-Gough hotspot track". In: *Geology* 41, pp. 335–338. DOI: `10.1130/G33790.1`.

Rohde, J. K., P. van den Bogaard, K. Hoernle, F. Hauff, and R. Werner (2013b). "Evidence for an age progression along the Tristan-Gough volcanic track from new ^{40}Ar/^{39}Ar ages on phenocryst phases". In: *Tectonophysics* 604, pp. 60–71. DOI: `10.1016/j.tecto.2012.08.026`.

Roux, E., M. Moorkamp, A.G. Jones, M. Bischoff, B. Endrun, S. Lebedev, and T. Meier (2011). "Joint inversion of long-period magnetotelluric data and surface-wave dispersion curves for anisotropic structure: Application to data from Central Germany". In: *Geophysical Research Letters* 38 (L05304). DOI: `10.1029/2010GL046358`.

Ryberg, T., W.H. Geissler, W. Jokat, and S. Pandey (2017). "Uppermost mantle and crustal structure at Tristan da Cunha derived from ambient seismic noise". In: *Earth and Planetary Science Letters* 471, pp. 117–124.

Sambridge, M. and R. Faletič (2003). "Adaptive whole Earth tomography". In: *Geochemistry, Geophysics, Geosystems* 4 (3). DOI: `10.1029/2001GC000213`.

Sambridge, M. and N. Rawlinson (2005). "Seismic tomography with irregular meshes". In: *Levander, A., Nolet, G. (Eds.), Seismic Earth: Array Analysis of Broadband Seismograms, vol. 157. American Geophysical Union*, pp. 49–65.

Sambridge, M.S., J. Braun, and H. McQueen (1995). "Geophysical parametrization and interpolation of irregular data using natural neighbours". In: *Geophys. J. Int.* 122, pp. 837–857.

Sato, Y. (1955). "Analysis of Dispersed Surface Waves by means of Fourier Transform I." In: *Bulletin of the Earthquake Research Institute* 33, pp. 33–47.

Saygin, E. and B. Kennett (2009). "Ambient seismic noise tomography of Australian continent". In: *Tectonophysics*. DOI: `10.1016/j.tecto.2008.11.013`.

Schaeffer, A. (2014). “Imaging the structure and dynamics of the Earth’s upper mantle and crust using multimode waveform tomography”. PhD thesis. University College Dublin.

Schaeffer, A. J. and S. Lebedev (2013). “Global shear speed structure of the upper mantle and transition zone”. In: *Geophysical Journal International* 194, pp. 417–449.

— (2015). “Global heterogeneity of the lithosphere and underlying mantle: A seismological appraisal based on multimode surface-wave dispersion analysis, shear-velocity tomography, and tectonic regionalization”. In: *Invited Review in: The Earth’s Heterogeneous Mantle, A. Khan and F. Deschamps (eds.) - Springer Geophysics*, pp. 3–46. DOI: `10.1007/978-3-319-15627-9`.

Schivardi, R. and A. Morelli (2009). “Surface wave tomography in the European and Mediterranean region”. In: *Geophys. J. Int.* 177, pp. 1050–1066.

Schlömer, A., W. H. Geissler, W. Jokat, and M. Jegen (2017). “Hunting for the Tristan mantle plume - An upper mantle tomography around the volcanic island of Tristan da Cunha”. In: *Earth and Planetary Science Letters* 462, pp. 122–131.

Schoonman, C. M., Nicky White, and D. Pritchard (2017). “Radial viscous fingering of hot asthenosphere within the Icelandic plume beneath the North Atlantic Ocean”. In: *Earth and Planetary Science Letters* 468, pp. 51–61. ISSN: 0012821X. DOI: `10.1016/j.epsl.2017.03.036`. URL: `http://dx.doi.org/10.1016/j.epsl.2017.03.036`.

Sens-Schönfelder, Christoph (2008). “Synchronizing seismic networks with ambient noise”. In: *Geophysical Journal International* 174, pp. 966–970.

Shapiro, N. M. and M. Campillo (2004). “Emergence of broadband Rayleigh waves from correlations of the ambient seismic noise”. In: *Geophys. Res. Let.* 31.

Shapiro, N. M., M. Campillo, L. Stehly, and M. H. Ritzwoller (2005). “High resolution surface-wave tomography from ambient seismic noise”. In: *Science* 307, pp. 1615–1618.

Shaw Champion, M.E., N.J. White, S.M. Jones, and K.F. Priestley (2006). “Crustal velocity structure of the British Isles: a comparison of receiver”. In: *Geophys. J. Int.* 166, pp. 795–813.

Shearer, P. M. (1999). *Introduction to Seismology*. Cambridge University Press, New York.

Smith, M. L. and F. A. Dahlen (1973). “The azimuthal dependence of Love and Rayleigh wave propagation in a slightly anisotropic medium”. In: *Journal of Geophysical Research* 78 (17), pp. 3321–3333. DOI: `10.1029/JB078i017p03321`.

Snieder, R. (1972). “Extracting the Green’s function from the correlation of coda waves: a derivation based on stationary phase”. In: *Phys. Rev. E* 69. DOI: 10.1103/PhysRevE.69.046,610.

Snieder, R. and G. Nolet (1987). “Linearized scattering of surface waves on a spherical Earth”. In: *J. Geophys.* 61, pp. 55–63.

Snyder, D.B. and C.A. Flack (1990). “A Caledonian age for reflectors within the mantle lithosphere north and west of Scotland”. In: *Tectonics* 9, pp. 903–922.

Soomro, R.A., C. Weidle, L. Cristiano, S. Lebedev, and T. Meier. (2016). “Phase velocities of Rayleigh and Love waves in central and northern Europe from automated, broadband, inter-station measurements”. In: *Geophysical Journal International* 204 (1), pp. 517–534. DOI: 10.1093/gji/ggv462.

Soper, N.J., R.A. Strachan, R.E. Holdsworth, R.A. Gayer, and R.O. Greiling (1992). “Sinistral transpression and the Silurian closure of Iapetus”. In: *Journal of the Geological Society*. DOI: 10.1144/gsjgs.149.6.0871.

Takei, Y (2017). “Effects of Partial Melting on Seismic Velocity and Attenuation: A New Insight from Experiments”. In: *Annual Review of Earth and Planetary Sciences* 40, pp. 447–70. DOI: https://doi.org/10.1146/annurev-earth-063016-015820.

Taposeea, C. A., J. J. Armitage, and J. S. Collier (2016). “Asthenosphere and lithosphere structure controls on early onset oceanic crust production in the southern South Atlantic”. In: *Tectonophysics*. DOI: 10.1016/j.tecto.2016.06.026.

Tarantola, A. and A. Nercessian (1984). “Three-dimensional inversion without blocks”. In: *Geophys. J. Royal Astr. Soc.* 76, pp. 299–306.

Thorne, L. and T. C. Wallace (1995). *Modern Global Seismology*. Academic Press.

Tiley, Richard, Nicky White, and Suleiman Al-Kindi (2004). “Linking Paleogene denudation and magmatic underplating beneath the British Isles”. In: *Geological Magazine* 141.3, pp. 345–351. ISSN: 0016-7568. DOI: 10.1017/s0016756804009197.

Todd, S. P., F. C. Murphy, and P. S. Kennan (1991). “On the trace of the Iapetus Suture in Ireland and Britain”. In: *Journal of the Geological Society of London* 148, pp. 869–880.

Tomlinson, James P., P. Denton, P. K.H. Maguire, and D. C. Booth (2006). “Analysis of the crustal velocity structure of the British Isles using teleseismic receiver functions”. In: *Geophysical Journal International* 167.1, pp. 223–237. ISSN: 0956540X. DOI: 10.1111/j.1365-246X.2006.03044.x.

Tromp, J. and F.A. Dahlen (1992). “Variational principle for surface wave propagation on a laterally heterogeneous Earth–II. Frequency-domain JWKB theory”. In: *Geophys. J. Int.* 109, pp. 599–619.

Tsai, V.C. (2010). "The relationship between noise correlation and the Green's function in the presence of degeneracy and the absence of equipartition". In: *Geophysical Journal International* 182. DOI: `10.1111/j.1365-246X.2010.04693.x`.

Tsai, Victor C. (2009). "On establishing the accuracy of noise tomography travel-time measurements in a realistic medium". In: *Geophysical Journal International* 178.3, pp. 1555–1564. ISSN: 0956540X. DOI: `10.1111/j.1365-246X.2009.04239.x`.

Udías, A. (1999). *Principles of Seismology*. Cambridge University Press, Cambridge, UK.

Udías, A. and E. Buforn (2017). *Principles of Seismology*. Cambridge University Press. DOI: `10.1017/9781316481615`.

van der Hilst, R. D., S. Widiyantoro, and E. R. Engdahl (1997). "Evidence for deep mantle circulation from global tomography". In: *Nature* 386(6625), pp. 578–584. DOI: `10.1038/386578a0`.

van Wijk, J., J. van Hunen, and S. Goes (2008). "Small-scale convection during continental rifting: Evidence from the Rio Grande rift". In: *Geology* 36 (7), pp. 575–578. DOI: `10.1130/G24691A.1`.

Vaughan, A.P.M. and J.D. Johnston (1992). "Structural constraints on closure geometry across the Iapetus Suture in eastern Ireland". In: *Journal of the Geological Society of London* 149, pp. 65–74.

Villaseñor, A., Y. Yang, M. H. Ritzwoller, and J. Gallart (2007). "Ambient noise surface wave tomography of the Iberian Peninsula: Implications for shallow seismic structure". In: *Geophys. Res. Lett.* 34 (L11304). DOI: `10.1029/2007GL030164`.

Wawerzinek, B., J. R.R. Ritter, M. Jordan, and M. Landes (2008). "An upper-mantle upwelling underneath Ireland revealed from non-linear tomography". In: *Geophys. J. Int.* 175, pp. 253–268.

Weemstra, Cornelis, Roel Snieder, and Lapo Boschi (2015). "On the estimation of attenuation from the ambient seismic field: inferences from distributions of isotropic point scatterers". In: *Geophysical Journal International* 203.2, pp. 1054–1071. ISSN: 0956-540X. DOI: `10.1093/gji/ggv311`.

Weit, A., R.B. Trumbull, J.K. Keiding, W.H. Geissler, S.A. Gibson, and I.V. Veksler (2016). "The magmatic system beneath the Tristan da Cunha hotspot: insights from thermobarometry, melting models and geophysics." In: *Tectonophysics*. DOI: `10.1016/j.tecto.2016.08.010`.

Wessel, P., W. H. F. Smith, R. Scharroo, J. Luis, and Wobbe F. (2013). "Generic Mapping Tools: improved version released". In: *Eos, Transactions, American Geophysical Union* 94 (45), pp. 409–420.

White, Nicky and Bryan Lovell (1997). “Measuring the pulse of a plume with the sedimentary record”. In: *Nature* 387.6636, pp. 888–891. ISSN: 00280836. DOI: `10.1038/43151`.

Wilkinson, C., M. Ganerød, B.W.H. Hendriks, and E. A. Eide (2016). “Compilation and appraisal of geochronological data from the North Atlantic Igneous Province (NAIP)”. In: *Journal of the Geological Society of London* 447. DOI: `10.1144/SP447.10`.

Yamauchi, H. and Y. Takei (2016). “Polycrystal anelasticity at near-solidus temperatures”. In: *Journal of Geophysical Research: Solid Earth* 121, pp. 7790–7820. DOI: `10.1002/2016JB013316`.

Yang, Y., D. W. Forsyth, and D. S. Weeraratne (2007). “Seismic attenuation near the East Pacific Rise and the origin of the low-velocity zone”. In: *Earth and Planetary Science Letters* 258, pp. 260–268.

Yao, H., R.D. van der Hilst, and M.V. de Hoop (2006). “Surface-wave array tomography in SE Tibet from ambient seismic noise and two-station analysis – I. Phase velocity maps”. In: *Geophys J. Int.* 166, pp. 732–744.

Yardley, B.W.D., F.J. Vine, and C.T. Baldwin (1982). “The plate tectonic setting of NW Britain and Ireland in Late Cambrian and early Ordovicain times”. In: *Journal of the Geological Society of London* 139, pp. 455–463.

Zhang, Y.-S. and T. Tanimoto (1993). “High-resolution global upper mantle structure and plate tectonics”. In: *Journal of Geophysical Research* 98 (B6), pp. 9793–9823.

Zhao, Dapeng (2004). “Global tomographic images of mantle plumes and subducting slabs: Insight into deep Earth dynamics”. In: *Physics of the Earth and Planetary Interiors* 146.1-2, pp. 3–34. ISSN: 00319201. DOI: `10.1016/j.pepi.2003.07.032`.

Appendix D

Co-authored works

The following are co-authored works as explained in the "Statement of co-authorship" on page iv. Their formatting is as in their original form, and their pages are not numbered according to the rest of this thesis. Each work (Appendices D.1 to D.3) contains its own bibliography section.

D.1 Education and public engagement using an active research project: lessons and recipes from the SEA-SEIS North Atlantic Expedition's programme for Irish schools

Geosci. Commun., 2, 143–155, 2019
https://doi.org/10.5194/gc-2-143-2019

Research article

Education and public engagement using an active research project: lessons and recipes from the SEA-SEIS North Atlantic Expedition's programme for Irish schools

Sergei Lebedev[1], Raffaele Bonadio[1], Clara Gómez-García[1], Janneke I. de Laat[1], Laura Bérdi[1], Bruna Chagas de Melo[1], Daniel Farrell[2], David Stalling[3], Céline Tirel[4], Louise Collins[1], Sadhbh McCarthy[1], Brendan O'Donoghue[5], Arne Schwenk[6], Mick Smyth[1], Christopher J. Bean[1], and the SEA-SEIS Team*

[1]Geophysics Section, Dublin Institute for Advanced Studies, Dublin, Ireland
[2]Coast Monkey, coastmonkey.ie
[3]Dundalk Institute of Technology, Dundalk, County Louth, Ireland
[4]Lycée Français d'Irlande, Dublin, Ireland
[5]St. Columba's College, Stranorlar, County Donegal, Ireland
[6]K.U.M., Umwelt- und Meerestechnik Kiel GmbH, Kiel, Germany
*For further information regarding the team, please visit the link which appears at the end of the paper.

Correspondence: Sergei Lebedev (sergei@cp.dias.ie)

Received: 28 June 2019 – Discussion started: 9 July 2019
Accepted: 16 September 2019 – Published: 11 October 2019

Abstract. An exciting research project, for example with an unusual field component, presents a unique opportunity for education and public engagement (EPE). The adventure aspect of the fieldwork and the drive and creativity of the researchers can combine to produce effective, novel EPE approaches. Engagement with schools, in particular, can have a profound impact, showing the students how science works in practice, encouraging them to study science, and broadening their career perspectives. The project SEA-SEIS (Structure, Evolution And Seismicity of the Irish offshore, https://www.sea-seis.ie, last access: 6 October 2019) kicked off in 2018 with a 3-week expedition on the research vessel (RV) *Celtic Explorer* in the North Atlantic. Secondary and primary school students were invited to participate and help scientists in the research project, which got the students enthusiastically engaged. In a nation-wide competition before the expedition, schools from across Ireland gave names to each of the seismometers. During the expedition, teachers were invited to sign up for live, ship-to-class video link-ups, and 18 of these were conducted. The follow-up survey showed that the engagement was not only exciting but encouraged the students' interest in science, technology, engineering, and mathematics (STEM) and STEM-related careers. With most of the lead presenting scientists on the ship being female, both girls and boys in the classrooms were presented with engaging role models. After the expedition, the programme continued with follow-up, geoscience-themed competitions (a song-and-rap one for secondary and a drawing one for primary schools). Many of the programme's best ideas came from teachers, who were its key co-creators. The activities were developed by a diverse team including scientists and engineers, teachers, a journalist, and a sound artist. The programme's success in engaging and inspiring school students illustrates the EPE potential of active research projects. The programme shows how research projects and the researchers working on them are a rich resource for EPE, highlights the importance of an EPE team with diverse backgrounds and expertise, and demonstrates the value of co-creation by the EPE team, teachers, and school students. It also provides a template for a multifaceted EPE programme that school teachers can use with flexibility, without extra strain on their teaching schedules. The outcomes of an EPE programme coupled with research projects can include both an increase in the students' interest in STEM and STEM careers and an increase in the researchers' interest and proficiency in EPE.

Published by Copernicus Publications on behalf of the European Geosciences Union.

1 Introduction

STEM subjects are recognized by a large majority of people in Ireland as essential for the country's prosperity (SFI, 2015). Yet, most people are not comfortable with STEM, perceiving the subjects as too specialized. Careers in STEM and, specifically, Earth science do not appear attractive to most school students, in large part due to the lack of information on and exposure to them (Neenan and Roche, 2016). Among specific sections of the public and school students, women's and girls' interest in STEM and careers in STEM is still relatively low, and students in disadvantaged areas have insufficient resources and role models to motivate their interest in STEM (SFI, 2015).

These barriers to STEM engagement are not unique to Ireland (e.g. Tytler et al., 2008), although in Ireland, in particular, the public interest in science and the pride in the national achievements in science have long been well below those for the arts (Ahlstrom, 2019). The world-class research performed in Ireland today in many areas of science is something the country can be proud of and inspired by, adding to the public interest in STEM in the long term. In a more immediate and direct sense, however, research projects themselves and the researchers who work on them represent a rich resource for education and public engagement (EPE).

Getting involved in an ongoing research project offers an appealing gateway to STEM to both school students and adults. Interactions with researchers reveal them to the public as friendly, "normal" people, enthusiastic about their jobs. These interactions are effective in alleviating the common stereotype of scientists as isolated, aloof and focussed on obscure or highly specialized experiments. The exposure to real researchers can thus increase the students' interest in STEM and in careers in STEM.

In this paper, we present, as a case study, an EPE programme developed around a major research project. Started by researchers, the programme grew to include school teachers as co-creators and expanded to the national scale. We describe the best practice developed in the course of the programme, draw lessons from its development, discuss some general inferences, and aim to identify useful templates and recipes for EPE projects that connect researchers to school students and to the general public.

2 The SEA-SEIS research project

2.1 Background

About 90 % of the Irish territory is offshore, most of it to the west of Ireland. Beneath the ocean, spectacular mountains and deep valleys show elevation variations of up to 3–4 km. There are extinct volcanoes, with remarkable biodiversity on their slopes. Ireland's largest sedimentary basins are also here, as are its greatest natural hazards: undersea slope failures have caused tsunamis in the geologically recent past (e.g. Salmanidou et al., 2017; Georgiopoulou et al., 2019).

In the project SEA-SEIS (Structure, Evolution And Seismicity of the Irish offshore), Earth scientists from the Dublin Institute for Advanced Studies (DIAS) are investigating the dynamic processes within the Earth that have shaped the seafloor and caused intraplate volcanic eruptions in the Irish offshore and the broader Northeast Atlantic (Lebedev et al., 2018, 2019a, b; Steinberger et al., 2019). In order to investigate the structure and flow of the rock within the Earth's crust and mantle, 18 seismic stations have been installed at the bottom of the North Atlantic Ocean. The ocean-bottom seismometers were deployed from the RV *Celtic Explorer* between 17 September and 5 October 2018, to be retrieved 18–20 months later. The network covers the entire Irish offshore, with a few sensors also in the UK and Iceland's waters (Fig. 1).

This major project represents the first successful attempt to instrument a large area of the Atlantic Ocean with ocean-bottom seismometers. It is particularly significant for Ireland, an island with extensive coastlines and a special place for the sea in its culture and history. In addition to its pioneering science, the project also features state-of-the-art technology: the compact, ocean-bottom seismometers can withstand the enormous pressure at the bottom of the ocean while recording its tiniest vibrations, as small as nanometres in amplitude.

2.2 The 2018 SEA-SEIS Expedition

The 2018 SEA-SEIS expedition covered over 5000 km in 18 d in the North Atlantic Ocean. Its main purpose was to install the 18 ocean-bottom seismic stations. It also offered spectacular EPE opportunities and provided a focus for the EPE programme that we have developed.

Scientists onboard included the chief scientist (Sergei Lebedev) and seismology (Raffaele Bonadio, Janneke I. de Laat, Clara Gómez-García) and geology (Laura Bérdi) PhD students. The team also included the engineer who had led the development of the ocean-bottom seismometers (Arne Schwenk) and an expert technician from DIAS (Mick Smyth). It also included a journalist and digital media expert (Daniel Farrell) and a sound artist (David Stalling). The diversity of the team was its key strength. All the members joined forces in the technical and EPE work, which came across clearly to school audiences onshore.

3 Development of the EPE programme

The programme was initiated by researchers, motivated by exploratory conversations with school teachers that indicated that it would be useful and in demand. The activities were funded primarily by small amounts from research-project budgets.

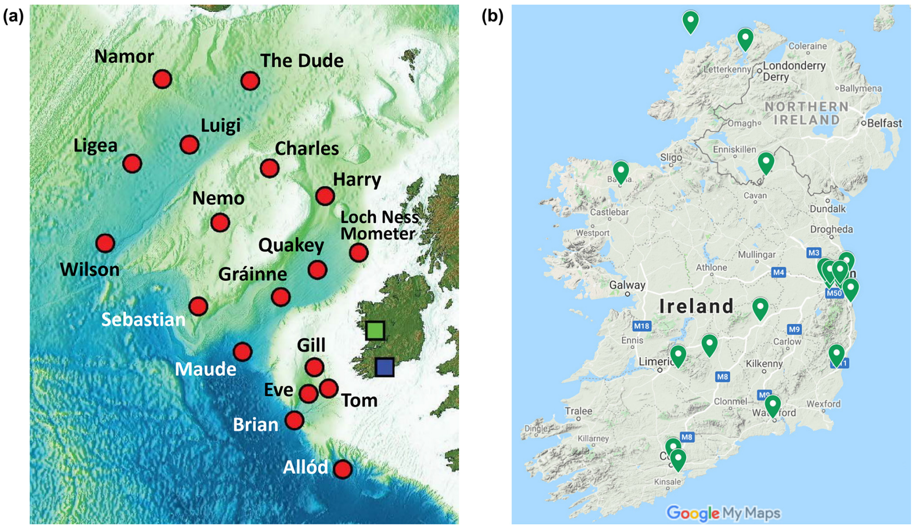

Figure 1. **(a)** The ocean-bottom seismic stations of the SEA-SEIS network (red circles), named by secondary school students in the seismometer-naming competition. **(b)** The locations of the schools across Ireland that suggested the winning names (for an interactive map, see https://sea-seis.ie/competitions/naming-competition, last access: 6 October 2019).

Starting with the realization that the North Atlantic expedition was simply too good an EPE opportunity to be missed, the programme grew and expanded through contributions from researchers and other members of the team onboard the RV *Celtic Explorer* and from teachers at secondary and primary schools. The programme benefited immediately from synergy with established EPE projects. The Marine Institute, which operates the RV *Celtic Explorer* and has its own, long-running EPE programme (Joyce, 2009; Joyce et al., 2018), offered berths on the ship to a journalist (Daniel Farrell) and a sound artist (David Stalling), who then made important contributions to the development of our programme. Some of the teachers of the Irish Seismology in Schools network (Blake et al., 2008) participated in the programme and also made contributions to its development.

We reviewed best practices of previous EPE projects connected to active research and looked for any ideas that could be applicable to ours. Teacher–scientist collaboration aiming to promote hands-on, inquiry-based science teaching is, generally, an established approach. In seismology, specifically, the Princeton Earth Physics Project (PEPP) installed seismometers in schools across the US for use in teaching and in science projects (Nolet, 1993; Steinberg et al., 2000; Phinney, 2002), and a number of seismology-in-schools programmes operate elsewhere around the world (e.g. Bullen, 1998; Virieux, 2000; Blake et al., 2008; Denton, 2008; Courboulex et al., 2012; Balfour et al., 2014; Zollo et al., 2014; Tataru et al., 2016). Collaborative teacher–scientist research projects improve, on the one hand, the scientists' awareness of classroom practices and, on the other hand, the teachers' understanding of scientific research, exposing each group to the other's culture and highlighting the advantages of integrating scientific inquiry into the curriculum (Gosselin et al., 2003). In the joint scientist–teacher–student research projects, the participants particularly enjoy being part of authentic research in which they could take initiative and feel a sense of ownership (Jarrett and Burnley, 2003). Scientist–educator partnerships can produce new teacher resources and lesson plans, incorporating cutting-edge research (Madden et al., 2007).

Recent trends in Earth-science outreach (e.g. Drake et al., 2014; Tong, 2014) include the use of video projects in the science classroom (Dengg et al., 2014; Wade and Courtney, 2014) and storytelling via diverse media (Barrett et al., 2014; Moloney and Unger, 2014). Hut et al. (2016) reviewed the theory of effective geoscience communication through audio-visual media, with a particular focus on television, and identified six major themes and challenges: scientist motivation, target audience, narratives and storytelling, jargon and information transfer, relationship between scientists and journalists, and stereotypes of scientists among the general public. Live video has already been used extensively in the practice of EPE coupled with marine research: ship-to-shore video events have been performed for a number of years by the International Ocean Discovery Program (IODP) (Kulhanek et al., 2014; IODP, 2019). We were able to use the idea successfully in our programme, with a specific focus on ship-to-classroom video link-ups and with our own event templates (Sect. 3.2).

McAuliffe et al. (2018) reported on the creation of a science book for 7–12 year olds. The book showcased the importance of STEM in today's society and aimed to give the children their first conceptions of STEM career pathways. Importantly, children were co-creators in the content development, character design, and "try at home" activities offered in the book. As a result, 93 % of parents of participating children felt that the children became more interested in science than they were before. The Irish research examples used in the book were also found to shift the perception that major scientific discoveries could only take place abroad (McAuliffe et al., 2018).

Further insight into the state of the art in the relevant EPE practice can be gained through direct communication with the practitioners. Contacting and talking to a lot of people – teachers, researchers, EPE and communications experts – was of key importance in the development of the present programme. Best practical ideas and essential partnerships emerged from some of these discussions.

Shortly before the start of the North Atlantic expedition, a press release on the project was circulated by DIAS through a PR company (Alice PR). This triggered broad coverage of the project in the national media (https://sea-seis.ie/media, last access: 6 October 2019), which then helped, to some extent, to attract schools to the programme. However, it was the direct contact with schools and announcements through national networks of teachers and principals that were the most effective.

3.1 Before the expedition: seismometer-naming competition

The seismologists among us have a natural tendency to give their seismic stations names like S01, S02, S03, etc. This is, indeed, how our offshore sites were referred to at the experiment design stage, when we determined the locations for the seismometers.

Then, just over 2 weeks before the expedition, we announced a secondary-school competition to name our seismometers. Two weeks is a short time for a teacher who may meet their science or geography class only once a week. Having more time for the competition would have been beneficial as more classes would be likely to participate. However, this was not possible as the expedition started shortly after the beginning of the academic year.

The competition was advertised through the email list of the Irish secondary school principals. To kick it off, we proposed the first name, Brian, ourselves. This was after Brian Jacob (Senior Professor of Geophysics at DIAS, 1989–2001), who led the work on the continental nature of the basins west of Ireland, which resulted in the Irish territory increasing by about a factor of 10.

A total of 20 schools – 19 across Ireland and 1 in Italy – participated in the competition. Our appeal for help in an important research project has generated genuine enthusiasm in students and got them engaged with the project. The teachers used this to have discussions on geoscience and marine science, as well as Irish and international Earth scientists and explorers. Among the winning names (https://sea-seis.ie/competitions/naming-competition, last access: 6 October 2019), Maude, for example, was named after Maude Delap, the Irish marine biologist, Tom – after Thomas Crean, the Irish seaman and Antarctic explorer, and Charles and Harry – after the American seismologists Charles Richter and Harry Hess.

Some teachers used the competition to talk with their students about the sea in Irish history and culture. Allód was named for the ancient Irish god of the sea, and Gráinne – for Gráinne Ni Mhaille, the "Pirate Queen", the well-known, 16th-century lord of the Ó Máille dynasty in the west of Ireland. Yet another approach was to let the students' imagination roam free, giving us names like Eve (for "eavesdropping on the Earth"), Gill, and Loch Ness Mometer.

Most schools proposed multiple names, and some names were proposed by more than once school. The SEA-SEIS researchers at DIAS selected and announced the winning names prior to the start of the expedition. Apart from the merit of the names themselves, an additional consideration was to have as many schools as possible among the winners. With some winning names proposed more than once, all the schools that submitted entries by the deadline were among the winners. The students in participating classes – now well engaged with the project – were particularly interested in how their seismometer would do. Most winning classes then participated in the live video links to the ship during the expedition, and the students were keen to see the videos and photos of the deployment of the seismometer that they had named.

3.2 "It was like speaking to Indiana Jones!" – ship-to-class video link-ups

Live ship-to-shore video links had been performed in international EPE programmes before ours, in particular by the International Ocean Discovery Program (IODP) using RV *JOIDES Resolution*'s scientific cruises (Kulhanek et al., 2014; IODP, 2019). Some of the teachers we knew in Ireland had participated in these video links and used them to stimulate their students' interest in STEM.

Following IODP, we started the video link-ups with an introduction from the ship that set the stage for a question and answer session with the students in the classroom. In contrast to the IODP video events, which, with rare exceptions, are led by educators (Kulhanek et al., 2014), all our video links were led by PhD students onboard. We also had to develop our own template for live video events. Because the weather during our expedition was mostly stormy – which is often the case in the North Atlantic, – the initially planned live tours of the ship, as performed on RV *JOIDES Resolution*'s scientific cruises (Kulhanek et al., 2014), would have been dangerous for the presenters and had to be abandoned. Instead, we started each session with a brief greeting by a PhD student, acting as the main host on-board, from outside on the deck. This was followed by an 8 min prerecorded video with an introduction to the project and team (https://doi.org/10.5446/43586) and short videos and photos of the seismometer deployments.

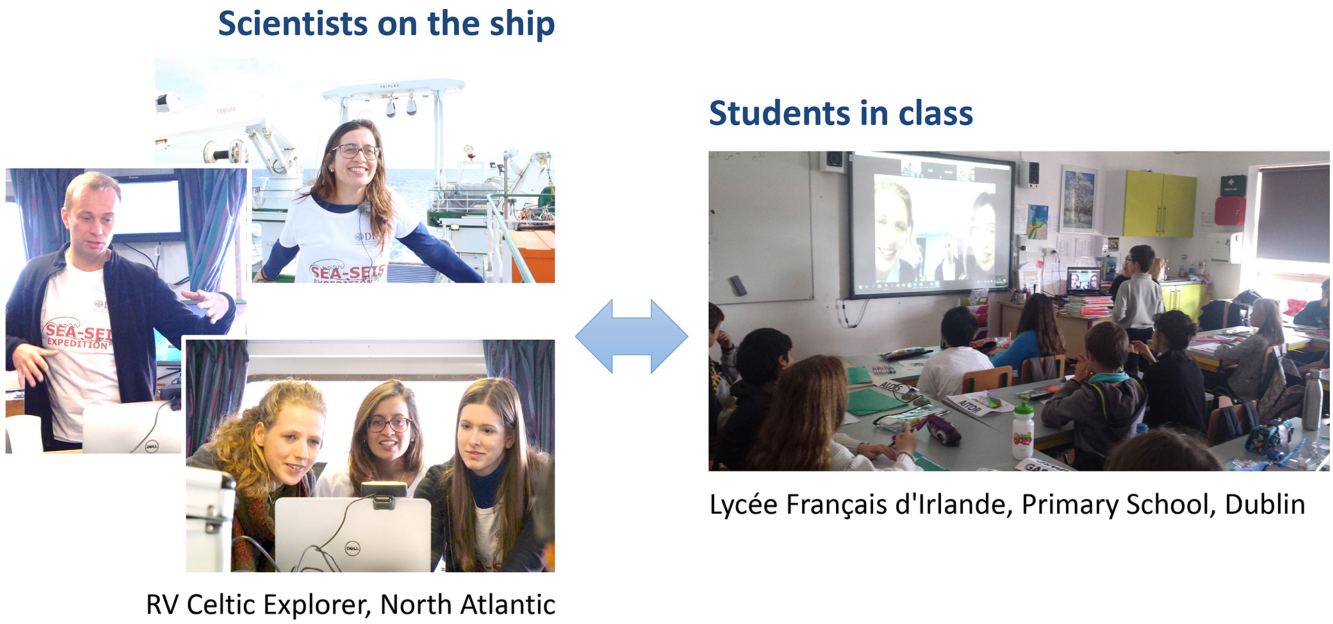

Figure 2. Live, ship-to-classroom video link-ups started with a brief introduction of the project and the team and continued with a 20–70 min Q&A session.

With the Marine Institute's assistance, we had secured, in advance and at an additional cost, a dedicated satellite broadband connection from the ship. Following RV *JOIDES Resolution*'s EPE programme's example, we used the videoconferencing software Zoom (https://www.zoom.us, last access: 6 October 2019). During the video links, all non-essential internet activity on the ship was turned off. With all of that, the connection was of surprisingly high quality. Nevertheless, every video event also included our colleagues at DIAS as the third party in the video conference – and the co-hosts at the "DIAS HQ". They would greet the school audience at the beginning of the live stream and broadcast the pre-recorded videos using their reliable broadband connection. They were also ready to step in if the connection from the ship deteriorated, which happened once, towards the end of a video link, when the ship moved out of the area of the satellite's coverage.

After the introduction to the project, the science, and the team, the students were invited to ask questions (Fig. 2). Prior to the video link, they were asked by their teachers to think of some. Most questions that were asked related to the life on the ship, to the project (its goals, hypotheses and methods), to Earth science (earthquakes, volcanoes, tsunamis and other natural hazards; plate tectonics and dynamics of the Earth interior), to the equipment (how it works and how it was developed), to what scientists do in their jobs, and to how one becomes a scientist. The Q&A sessions lasted between 20 and 70 min, depending on how much time the classes had and on our schedule.

Because of the limited number of video link-ups that could realistically be performed, invitations were sent only to the participants of the seismometer-naming competition (20, over half of them then requesting a slot) and to the members of the Irish Seismology in Schools network (Blake et al., 2008), operated by DIAS (45, a few of them requesting a slot). We were able to schedule and perform a video link with every teacher who asked for one.

In total, 18 video link-ups were carried out. The classes were in schools all around Ireland, and there was one connection to a school in Italy – reported on by a regional TV station (https://youtu.be/1vBFLKV8nG0, last access: 6 October 2019). In some schools, we talked to a large class or to two classes in the same room, sometimes with students sitting on the floor in the isles. On Tory Island, County Donegal, there were only five students in the room, but that was 100 % of the students in this secondary school – and on this island. For remote schools, the video-link format opens new possibilities and makes it much easier to arrange interactions of school students with STEM practitioners.

Most presenters on the ship and at DIAS were female. This offered opportunities to all-girl classes and girls in co-educational schools to connect to and identify with their own role models among the scientists.

Both female and male students were clearly excited to chat with scientists and engineers on a ship in the middle of the North Atlantic. According to the teachers, their students would then tell the entire school as well as their parents of this experience, which further broadened the reach of the event. "It was like speaking to Indiana Jones!" was how the students of Lycée Français d'Irlande, Dublin, summarized it.

Some teachers used the engagement with researchers to accompany special Earth science projects, conducted prior

Scoil Mhuire, Buncrana, Co. Donegal

Gaelcholáiste Charraig Uí Leighin, Co. Cork

Coláiste Phobail Cholmcille Tory Island, Co. Donegal

Kingswood Community College, Dublin

I.C. Don Milani Lamezia Terme, Italy

Figure 3. Live, ship-to-classroom video link-ups with different schools in Ireland and Italy.

to the video link (Fig. 3). Other teachers spent only one or two periods on the video link and the discussions before and after it. Given the already packed curricula, this flexibility was useful and appreciated by the teachers. The video links provided a "low-cost, high-impact" activity, inspiring the students and encouraging their interest in STEM and STEM careers but not putting excessive strain on the teachers' schedules.

3.3 Drawing competition for primary schools

The SEA-SEIS Drawing Competition for Primary Schools ran from October to December 2018. It was advertised on the SEA-SEIS website and in *InTouch*, the Irish National Teachers' Organisation's monthly magazine (InTouch, 2018).

We invited the students to draw one of our friendly, adventurous seismometers. Noting the primary school children's concern for the seismometers (Will they be scared at the bottom of the sea, all alone?), we made sure that the competition announcement mentioned that diving deep into the sea was the seismometers' favourite thing to do. The announced evaluation criteria included relevance, artistic merit, and originality.

We received nearly 70 entries in total (https://sea-seis.ie/sea-seis-art-18, last access: 6 October 2019). Most of these came from two schools in different counties in Ireland and two classes in the same school in Italy. The remainder came from a few other schools in Ireland.

Because this was a primary-school competition, we awarded a prize to every student who sent us a drawing. The prize was the 2019–2020 SEA-SEIS Calendar, featuring the art by the students (Fig. 4). Every drawing was printed in the calendar, with the ones ranked highest by the SEA-SEIS researcher jury printed on a full page, and the others a few per page.

The feedback from the participating teachers and students indicated that the competition was enjoyable and increased the students' interest in STEM (see Sect. 4). The number of schools who entered, however, was relatively small. This was, in part, because primary schools already have their own art competitions and may feel they are already busy enough with those. In order to increase the participation in the future, it will be useful to communicate to schools more explicitly how the competition can raise the students' interest in STEM and also mention that every valid entry will win a prize, which we had not done in this case.

3.4 Song and rap competition for secondary schools

The SEA-SEIS Song and Rap Competition for Secondary Schools ran from October to December 2018. It was advertised on the SEA-SEIS website and through teacher networks. We invited the students to compose and record a song or a rap on a topic related to seismology, the SEA-SEIS Expedition, Earth science, or exploration of the interior of the Earth. For information, we directed the students to the project website, to video link-ups with the ship if their class participated, and to further reading. Entries from entire classes or smaller groups of students were accepted. The evaluation criteria included relevance, scientific insight and accuracy, artistic merit, and originality.

The competition received excellent entries – creative, imaginative, artistic, and with a variety of original takes on Earth science and seismology at sea (https://sea-seis.ie/

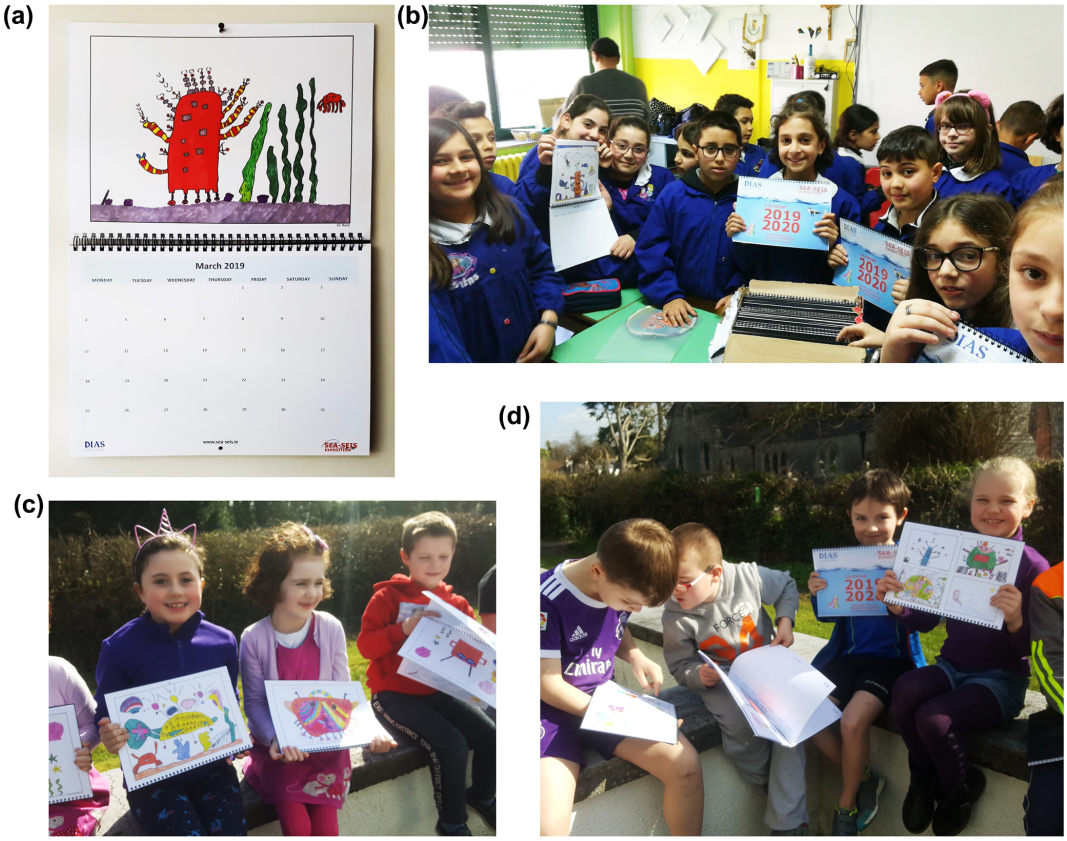

Figure 4. Participants of the Primary School Drawing Competition with their prizes, calendars featuring their art. **(a)** The 2019–2020 calendar. **(b)** Students at Istituto Comprensivo Don Lorenzo Milani, Lamezia Terme, Italy. **(c, d)** Students at Abbeyleix South National School, Abbeyleix, County Laois, Ireland.

sea-seis-rap-18, last access: 6 October 2019). The competition Grand Prize was shared by two top entries. Runners-up were distinguished by the jury of SEA-SEIS researchers with Special Mentions. The Grand Prize winning groups received the SEA-SEIS/DIAS-branded flash drives (16 GB, waterproof to 100 m depth), one for each student in the group and one for their teacher. These were appreciated by all the recipients (Fig. 5). Classes contributing entries that received Special Prizes and Special Mentions received inspirational science books and four-colour SEA-SEIS-branded pens, also successful as prizes.

One of the teacher authors of this paper (Céline Tirel) offered the production of a competition entry as a graded Technology project to one of her classes. This was a successful and effective approach, with the production of an entry comprising research on the science, creation of the piece, recording, and preparation of a report.

It was clear from the entries that many students made an effort to research the subject and learn more of the science. Others, however, seemed less interested to learn, and some succeeded in creating impressive entries in spite of that. At one end of the spectrum, one of the winning compositions referred to most SEA-SEIS seismometers by their names, also with a reference to their location and to what they were recording on the seafloor, which showed substantial research on the subject. At the other end, some of the entries showed little understanding and probably no research behind them.

Drawing a line separating “research” from “no research”, however, would be difficult. The competition was developed in order to combine art and science, to get the students to create science-themed art and to get them more interested in science. The pieces the students composed and recorded were free-form, and there were no correct answers they could insert into in their songs. For this reason, it is not possible to gauge precisely the amount of research students put into Earth-science research in the course of this activity.

By the very nature of the art–science approach, it is not always possible to measure everything. We do draw a lesson from the first edition of this competition, however: in its future editions, it will be useful to steer students more firmly towards learning and towards communicating science and technology in their pieces.

Figure 5. Prizes and some of the winners of the geoscience song-and-rap competition for secondary schools. **(a)** Inspirational science books went to classes with winning and runner-up groups. **(b)** One of the two Grand Prize winning groups (Lycée Français d'Irlande, Dublin). **(c)** SEA-SEIS-branded, 16 GB flash drives were awarded to every student in the winning groups and to their teachers.

3.5 Ethics

The study complied with the *Guidance for developing ethical research projects involving children* (Department of Children and Youth Affairs, 2012). No personal information on children was collected. No interactions of project participants with children in the participating schools took place, other than the live video link-ups between the researchers and the classrooms, which were conducted by the teachers on the classroom side. The photographs of the children were supplied by the teachers, who confirmed the consent for their use in the online publication. Data collected in the evaluation survey of teachers were undertaken in accordance with good practice. The survey was anonymous by default. Contributors to this study were under no obligation to become the paper's co-authors.

4 Evaluation

Formal evaluations were conducted after all ship-to-classroom video link-ups, using a SurveyMonkey online survey. The survey was anonymous by default, but the names of the school and the teacher could be given as an option. All teachers that we contacted right after the video link, on the same day, responded and completed the evaluation form. Of those contacted 3 d after the video link (once, the ship lost the internet connection over an entire weekend), half did not respond.

Overall, the teachers rated the educational activity at 4.7 out of 5, on average. Eighty-six percent reported that the video link encouraged the students' interest in science, with 14 % reporting "somewhat encouraged" and none reporting "did not encourage". The respondents also reported that the video links triggered the students' curiosity, showed them that science is part of real life, highlighted the importance of collaborating and broadened their career ideas. Getting to know scientists as "open, friendly people" impressed the students. For the classes who had participated in the seismometer-naming competition, the main highlight was, invariably, seeing the deployment of the seismometer they had named.

The evaluation relating to the drawing competition was informal, based on the feedback from the primary school teachers and students themselves. The bulk of the feedback came in the form of 24 thank-you cards from 7–8-year-old students from Abbeyleix South National School, County Laois, Ireland. It was clear that the children were encouraged to write the cards by their teacher and that the teacher must have mentioned a number of things that could be included in the cards. However, different children opted to include different things in their text, and the phrasing was their own, different in different cards. Nearly all the students wrote that they enjoyed learning about the seismometers and the project, with some mentioning explicitly that they explained what they had learned to their parents. All were pleased with their prizes and happy that everybody got a prize. Some wrote that they would like to work with the SEA-SEIS researchers in the future.

This evidence would not yield robust statistical inferences (only one class, influenced by their teacher) but, even though the evidence may be regarded as anecdotal, we consider it encouraging and useful. It confirms that young primary school students are curious about and receptive to the general ideas of Earth science research and that rewarding every participant with a prize is an effective approach in primary-school competitions. It also highlights the key role of an actively participating teacher and the importance of a teacher network in order for such a competition to reach a broad, national scale.

5 Discussion

In this section, we focus on the lessons and recipes provided by our EPE programme. We discuss the approaches shown to be particularly important and useful. We also point out what did not work as expected and why. In addition, we consider potential next steps towards an expanded, sustainable EPE programme coupled with Earth-science research projects.

5.1 Researchers as EPE leaders

Academic researchers are a source of essential STEM expertise. They also possess genuine enthusiasm for science. Their potential capacity for EPE resource development and EPE activities is remarkable: scientists are creative and resourceful, and they have excellent technical and computer skills. The researchers' motivation to participate in STEM activities, however, is not universally high, for a number of reasons. The incentive structures (assessment criteria) at academic institutions prioritize research, published in top journals of the field, as well as service to the institutions, including administration and teaching (Lam, 2011; Hillier et al., 2019). In informal networks of international researchers, achievements in research are also prioritized. Outreach work can be dismissed by a colleague with a quick "Ah, it's not science". Misguided as this may be, most researchers have heard this, and the opinion of the community of peers affects not only their self-esteem but also their employment and funding opportunities.

For the academics still keen to develop EPE activities, allocating time for this can be difficult, especially if this is unrelated to any of their current research projects. Also, even though most funding agencies encourage EPE, they often do not provide any funds for it in regular research grants.

Researchers thus tend to leave EPE development to outreach specialists and participate in the activities occasionally. They are often used as presenters in pre-designed EPE activities, which gives them opportunities for improving their communication skills (e.g. Illingworth et al., 2018) – often not their greatest strength to begin with. However, consistently using researchers for what many of them do not particularly enjoy or excel at does not, obviously, get the best out of them, pushing some away altogether.

EPE coupled with active research projects can channel the academic researchers' drive and creativity into the development of spectacular, novel EPE programmes. Not all research projects are equally suitable for this, and smaller projects may lack the scale and personnel. A certain proportion of research projects, however, will always present excellent opportunities for the development of effective EPE programmes, led by scientists or by scientists and educators together. Projects with an exciting field component, in particular, easily capture the imagination of school students and engage them, as illustrated by the SEA-SEIS and a number of other EPE programmes (e.g. Kulhanek et al., 2014; IODP, 2019).

5.2 Team with diverse backgrounds

Our programme benefited greatly from its integration of practitioners from different disciplines. The team that developed ideas, produced digital content, and conducted the EPE activities included Earth scientists, engineers and technicians, secondary school teachers, a journalist, and a sound artist. Our teachers (Céline Tirel and Brendan O'Donoghue) made key contributions to the development of classroom-activity ideas, from the early stages of the programme planning. Our journalist and media expert (Daniel Farrell) had participated in the programme development since before the expedition and produced a popular blog that covered the expedition, also professionally maintaining the project's digital media presence, increasingly recognized as essential in science communication (Drake et al., 2014). Together with our sound artist (David Stalling), they shot and edited onboard the project-introduction and tour-of-the-ship videos. The sound artist, whose primary work using the sounds recorded on the ship will be presented in a month-long show as part of a major international festival, made sure we were all heard during the video links, even outside in strong winds. The engineers and technicians (Arne Schwenk, Mick Smyth, Louise Collins) presented and explained with authority the technology aspect of the project. All the team members onboard the RV *Celtic Explorer* presented their perspectives on the project to the school students, conveying the importance of collaboration and the diversity of backgrounds and skills that is required by a major science project.

5.3 Students co-creating with scientists

School students were invited to help scientists and made a real contribution to the project. Their names for the ocean-bottom stations (Fig. 1) have permanently replaced the tentative S01, S02, etc. After the data are collected, these names (abbreviated when required) will remain attached indefinitely to seismograms in international data repositories. In our two art competitions, the participants produced pieces that are now themselves effective tools for education and public engagement.

We found that inviting students to become co-creators gets them engaged with enthusiasm. They are, then, motivated to learn more on the project, the scientific hypotheses behind it, and what the scientists do in the course of the project. Even though the students do not perform any of the project's key technical tasks, co-creation does help to get across the excitement and creative nature of scientific research more effectively than a pure exchange of information would. This, in turn, is likely to contribute to increasing the students' interest in STEM and STEM careers.

5.4 Multifaceted, "low-cost, high-gain" programme

We offered the teachers the flexibility of activities that could be fit into just one or two periods, used in science and technology lessons and projects, or integrated into the Earth science part of the curriculum, according to their needs at the time. The different activities were inter-related but independent (the naming competition prior to the expedition, live video link-ups during the expedition, and the song and drawing competitions after the expedition). Some classes participated in only one of the activities, others – in two or three, with the teachers choosing what was the most suitable for them. The activities were "low-cost" in the sense of the minimum required classroom time commitment. Their impact was "high gain" when compared to the modest amount of the class-time investment required. The gain is in terms of encouraging the students' interest in STEM and STEM careers, which was achieved thanks to the captivating adventure aspect of the project's fieldwork, engagement of students through co-creation with scientists, and direct, live-video communications between students and scientists.

5.5 What should be improved and perspectives

Our competitions were, in a sense, experiments. When announcing them, we could not predict the level of participation in either of them or their effectiveness in promoting STEM. The seismometer-naming competition was successful and got the students who participated in it engaged in the project. The follow-up drawing and song-and-rap competitions produced some excellent entries, but the number of participating schools was lower than expected. A proportion of entries to the song-and-rap competition showed little evidence of the students researching either Earth science or the SEA-SEIS project's scientific goals.

While successful as a proof of concept, the competitions also highlighted what was missing: an effective network of teachers. We worked closely with a few teachers and attracted around 30 more from different schools through project announcements. But many other teachers did not respond to invitations to join our EPE activities, possibly not finding them sufficiently compelling or sufficiently informative. Our aim is to help the teachers to get their students more interested in STEM. In order to do this more effectively and develop our EPE programme further, we would need to grow an extensive, national-scale teacher network, offering the teachers continuing professional development, workshops, and resources.

An expanded, sustainable EPE programme should also offer more activities. Video links can be performed not only from the ship but from the lab and from other fieldwork locations. The expanded programme could have joint activities with multiple research projects and a wider group of researchers associated with them. The programme could also broaden so as to target adult audiences as well as school students. Generally, more engagement, co-creation, discussion, and debate are needed in order to get people of all ages more interested, involved, and comfortable with STEM subjects (SFI, 2015). Using the approaches, lessons, and recipes from the present programme, this can be addressed through the work with schools supported by the development of an effective teacher network, through presenting science through arts, and through the use of a sophisticated digital platform. Such expansion of the programme would, however, require dedicated funding – being sought at the moment.

6 Conclusions

A research project with an exciting field component presents a unique opportunity for broad public engagement. Educational activities with schools, in particular, can have a profound, lasting impact, showing the students how science works, encouraging them to study science, and broadening their career perspectives. Participation in a real research project and co-creation with scientists gets the students enthusiastically engaged.

The EPE programme presented here as a case study comprised of live video link-ups between scientists on a ship in the North Atlantic and students in classrooms and three school competitions, before and after the expedition. Survey responses from the teachers confirmed that the video links encouraged the students' interest in STEM. Researchers – both experienced and early-career – could see the real impact of the outreach and got involved with enthusiasm and commitment. The outcomes of an educational programme coupled with a research project can thus include both the school students getting more interested in STEM and STEM careers and researchers getting more experienced and proficient in the education and public engagement work.

This case study offers useful lessons and recipes for EPE programmes coupled with active research projects. First of all, it highlights how the research projects and the researchers working on them are a rich resource for EPE. Researchers can be effective EPE leaders, with the EPE programmes channelling their drive and creativity into the development of effective, novel EPE activities.

Secondly, it illustrates the importance of an EPE team with diverse backgrounds and complementary expertise and skill sets. In EPE with primary and secondary schools, the most essential partners are the school teachers and principals. The development of a network of actively engaged teachers is a prerequisite of successful EPE with schools and should, if possible, be initiated at the earliest stages of the programme. Beyond that, our programme capitalized on contributions of not only scientists and teachers, but also engineers and technicians and a sound artist. An effective national media campaign around the start of the SEA-SEIS Expedition and EPE programme was orchestrated by our communication manager, working with a partner PR firm. Our digital media presence was maintained primarily by the team's digital journalist, his expertise increasing its effectiveness greatly.

Thirdly, the programme demonstrates the value of co-creation by the EPE team, teachers, and school students. Close collaboration with the teachers was essential in planning and developing the programme activities. Getting the school students to co-create with scientists in the course of the school competitions got them engaged and genuinely interested.

Finally, our project can be seen as a template for a multifaceted, "low-cost, high-gain" EPE programme. Recognizing that the school curricula are already packed, making it difficult for teachers to allocate a lot of time to extra material, we offered them the flexibility of activities that could be fit into just one or two periods or integrated into the Earth science part of the curriculum, according to their needs at the time. We offered a series of different, inter-related but independent activities (the naming competition prior to the expedition, live video events during the expedition, and the song and drawing competitions after the expedition). Some classes participated in only one of the activities, others in two or three, with the teachers choosing which was the most suitable for them. In the sense of the minimum required classroom time commitment, the activities were low-cost. The high gain, relative to the amount of class-time investment and in terms of increasing the students' interest in STEM and STEM careers, is achieved thanks to the captivating adventure aspect of the project's fieldwork, engagement of students through co-creation with scientists, and direct, live-video communications between students and scientists.

Data availability. The evaluation survey data are provided in the Supplement.

Video supplement. In our three video supplements, we present

- an 8 min introductory video created for our ship-to-classroom video link-ups (https://doi.org/10.5446/43586; Farrell and Stalling, 2018);
- a light-hearted but informative account of instrument deployments in rough weather – an example of the presentation of an aspect of the project to a broad audience (https://youtu.be/i2lmBIpcgfI, Bonadio and Lebedev, 2019a);
- an entertaining compilation of selected images and sounds from our competitions for the primary and secondary schools (https://doi.org/10.5446/43587; Bonadio and Lebedev, 2019b).

Supplement. The supplement related to this article is available online at: https://doi.org/10.5194/gc-2-143-2019-supplement.

Team list. The complete member list of the SEA-SEIS Team can be found at https://sea-seis.ie/team (last access: 9 October 2019).

Author contributions. SL prepared the manuscript with contributions from all co-authors. RB, DF, and DS produced the project EPE videos. SL, BO'D, CT, DF, SM, RB, CGG, JIdL, LB, and BCdM developed and ran school competitions. SL and DF performed programme-evaluation surveying. SL, LB, RB, JIdL, CGG, AS, DF, DS, LC, and BCdM developed, managed, and performed live video link-ups between the ship, classrooms, and DIAS. CT and BO'D contributed key ideas and co-created the competition and video-link activities.

Competing interests. The authors declare that they have no conflict of interest.

Acknowledgements. We thank the secondary and primary school teachers and principals in Ireland and Italy who participated in the SEA-SEIS competitions and video link-ups (https://www.sea-seis.ie/competitions, last access: 6 October 2019, https://www.sea-seis.ie/ship-to-classroom-live-video-link-ups, last access: 6 October 2019). Without their dedication and hard work, the activities would not have been successful. Special thanks are owed to Ruth Wallace, primary school teacher at the Abbeyleix South National School, County Laois. Constructive comments and suggestions of the referees, Anthony Lelliott and Penny Haworth, have helped us to improve the first version of the manuscript substantially. We are grateful to Eucharia Meehan (Registrar and CEO, DIAS) for continuous support and to Fergus McAuliffe (iCRAG) for a helpful EPE discussion during the planning stages of this programme. We thank Louise Manifold, curator of the AerialSparks project for Galway2020, for initiating the artist residence programme on the RV *Celtic Explorer*. The ocean-bottom seismometers for SEA-SEIS are provided by iMARL, the Insitu Marine Laboratory for Geosystems Research hosted by DIAS (https://imarl.ie, last access: 6 October 2019). The RV *Celtic Explorer* is run by the Marine Institute (https://www.marine.ie, last access: 6 October 2019). We are grateful to Captain Denis Rowan, the crew of the RV *Celtic Explorer*, and Aodhán Fitzgerald, Research Vessel Operations Manager, Marine Institute, for their expert assistance in achieving our scientific and EPE objectives. Marc O'Connor and Lukasz Pawlikowski provided superb ICT support on-board. The SEA-SEIS project is co-funded by the Science Foundation Ireland, the Geological Survey of Ireland, and the Marine Institute (grant 16/IA/4598). We acknowledge additional support from Science Foundation Ireland grants 13/CDA/2192 and 13/RC/2092, the latter cofunded under the European Regional Development Fund.

Financial support. This research has been supported by the Science Foundation Ireland, Geological Survey of Ireland, Marine Institute, European Regional Development Fund (grant nos. 16/IA/4598, 13/CDA/2192, and 13/RC/2092).

Review statement. This paper was edited by Marina Joubert and reviewed by Anthony Lelliott and Penny Haworth.

References

Ahlstrom, D.: Ireland's stellar contributions go under the radar: Recognition of formidable history in space and science always eclipsed by success in arts, 7 March 2019, The Irish Times, Dublin, Ireland, 2019.

Balfour, N. J., Salmon, M., and Sambridge, M.: The Australian seismometers in schools network: Education, outreach, research, and monitoring, Seismol. Res. Lett., 85, 1063–1068, https://doi.org/10.1785/0220140025, 2014.

Barrett, B. F., Notaras, M., and Smith, C.: Communicating scientific research through the Web and social media: experience of the United Nations University with the Our World 2.0 web magazine, in: Geoscience Research and Outreach, 91–101, Springer, Dordrecht, 2014.

Blake, T., Jones, A. G., and Campbell, G.: The DIAS Outreach Seismology in Schools (Seismeolaíocht sa Scoil) Pilot Programme, EOS T. Am. Geophys. Un., 89, Fall Meet. Suppl., Abstract ED53A-0576, San Francisco, California, USA, 2008.

Bonadio, R. and Lebedev, S.: SEA-SEIS in the Storm, available at: https://youtu.be/i2lmBIpcgfI, last access: 6 October 2019a.

Bonadio, R. and Lebedev, S.: SEA-SEIS Art 2018, TIB, https://doi.org/10.5446/43587, 2019b.

Bullen, S.: Seismology in schools, Astron. Geophys., 39, 4–25, 1998.

Courboulex, F., Berenguer, J. L., Tocheport, A., Bouin, M. P., Calais, E., Esnault, Y., Larroque, C., Nolet, G., and Virieux, J.: Sismos à l'Ecole: A worldwide network of real-time seismometers in schools, Seismol. Res. Lett., 83, 870–873, 2012.

Dengg, J., Soria-Dengg, S., and Tiemann, S.: Marine Geosciences from a Different Perspective: "Edutainment" Video Clips by Pupils and Scientists, in: Geoscience Research and Outreach, 103–119, Springer, Dordrecht, 2014.

Denton, P.: Seismology in schools: 10 years on, Astron. Geophys., 49, 6–13, https://doi.org/10.1111/j.1468-4004.2008.49613.x, 2008.

Department of Children and Youth Affairs (DCYA): Guidance for developing ethical research projects involving children, Dublin, DCYA, 2012.

Drake, J. L., Kontar, Y. Y., and Rife, G. S. (Eds.): New trends in earth-science outreach and engagement: the nature of communication, Vol. 38, ISBN 978-3-319-01820-1, Springer Science & Business Media, Cham, Switzerland, 2014.

Farrell, D. and Stalling, D.: 2018 SEA SEIS Expedition – Meet the Team, TIB, https://doi.org/10.5446/43586, 2018.

Georgiopoulou, A., Krastel, S., Finch, N., Zehn, K., McCarron, S., Huvenne, V. A. I., Haughton, P. D. W., and Shannon, P. M.: On the timing and nature of the multiple phases of slope instability on eastern Rockall Bank, Northeast Atlantic, Geochem. Geophy. Geosy., 20, 594–613, https://doi.org/10.1029/2018GC007674, 2019.

Gosselin, D. C., Levy, R. H., and Bonnstetter, R. J.: Using earth science research projects to develop collaboration between scientists at a research university and K-12 educators: Insights for future efforts, Journal of Geoscience Education, 51, 114–120, https://doi.org/10.5408/1089-9995-51.1.114, 2003.

Hillier, J. K., Saville, G. R., Smith, M. J., Scott, A. J., Raven, E. K., Gascoigne, J., Slater, L. J., Quinn, N., Tsanakas, A., Souch, C., Leckebusch, G. C., Macdonald, N., Milner, A. M., Loxton, J., Wilebore, R., Collins, A., MacKechnie, C., Tweddle, J., Moller, S., Dove, M., Langford, H., and Craig, J.: Demystifying academics to enhance university–business collaborations in environmental science, Geosci. Commun., 2, 1–23, https://doi.org/10.5194/gc-2-1-2019, 2019.

Hut, R., Land-Zandstra, A. M., Smeets, I., and Stoof, C. R.: Geoscience on television: a review of science communication literature in the context of geosciences, Hydrol. Earth Syst. Sci., 20, 2507–2518, https://doi.org/10.5194/hess-20-2507-2016, 2016.

Illingworth, S., Stewart, I., Tennant, J., and von Elverfeldt, K.: Editorial: Geoscience Communication – Building bridges, not walls, Geosci. Commun., 1, 1–7, https://doi.org/10.5194/gc-1-1-2018, 2018.

InTouch (Irish National Teachers' Organisation's Monthly): Sea monitors: Learning more about Ireland's marine territory – Drawing competition for primary schools, Issue No. 182, ISSN 1393-4813 (Print), ISSN 2009-6887 (Online), 2018.

IODP (International Ocean Discovery Program): JOIDES Resolution Science Operator, available at: https://joidesresolution.org/live-video-events-with-the-joides-resolution, last access: 25 June 2019.

Jarrett, O. S. and Burnley, P. C.: Engagement in authentic geoscience research: Evaluation of research experiences of undergraduates and secondary teachers, J. Geosci. Educ., 51, 85–90, https://doi.org/10.5408/1089-9995-51.1.85, 2003.

Joyce, J.: Reaching the Next Generation of Marine Scientists, Geophys. Res. Abstr., EGU2009-2205-3, EGU General Assembly 2009, Vienna, Austria, 2009.

Joyce, J., Dromgool-Regan, C., and Burke, N.: Creating Marine Outreach Programmes that Work – The Marine Institute Explorers Education Programme™, in: Exemplary practices in marine science education: A resource for practitioners and researchers, edited by: Fauville, G., Payne, D. L., Marrero, M. E., Lantz-Andersson, A., and Crouch, F., 171–189, Springer, Cham, Switzerland, 2018.

Kulhanek, D. K., Cooper, S. K., Dadd, K. A., Colwell, F. S., Mote, A. S., and Christiansen, E. A.: Live Ship-to-shore Video Events from the JOIDES Resolution during International Ocean Discovery Program Expeditions, Abstract ED11C-3427 presented at 2014 Fall Meeting, 15–19 December 2014, AGU, San Francisco, Calif., 2014.

Lam, A.: What motivates academic scientists to engage in research commercialization: "Gold", "ribbon" or "puzzle"?, Polar Res., 40, 1354–1368, https://doi.org/10.1016/j.respol.2011.09.002, 2011.

Lebedev, S., Schaeffer, A. J., Fullea, J., and Pease, V.: Seismic tomography of the Arctic region: Inferences for the thermal structure and evolution of the lithosphere, in: Circum-Arctic Lithosphere Evolution, edited by: Pease, V. and Coakley, B., Geological Society, London, Special Publications, 460, 419–440, https://doi.org/10.1144/SP460.10, 2018.

Lebedev, S., Bean, C., Judge, M. Bonadio, R., Bérdi, L., de Laat, J., Gómez Garcia, C., Chagas de Melo, B., Collins, L., McCarthy, S., Farrell, D., Stalling, D., Schwenk, A., and the SEA-SEIS Team: Project SEA-SEIS: Structure, Evolution And Seismicity of the Irish offshore, Irish Geol. Res. Meet., 1–3 March 2019, Dublin, 2019a.

Lebedev, S., Bonadio, R., Bérdi, L., de Laat, J., Gómez Garcia, C., Chagas de Melo, B., Collins, L., McCarthy, S., Farrell, D., Stalling, D., Schwenk, A., Bean, C., and the SEA-SEIS Team: National-scale engagement of school students using an active research project: the SEA-SEIS North Atlantic Expedition's outreach programme, Geophys. Res. Abstr., EGU2019-11445-4, EGU General Assembly 2019, Vienna, Austria, 2019b.

Madden, A. S., Knefel, A. M. C., Grady, J. R., Glasson, G. E., Hochella Jr., M. H., Eriksson, S. C., Bank, T. L., Cecil, K., Green, A. M., Hurst, A. N., and Norris, M.: Nano2earth: Incorporating cutting-edge research into secondary education through scientist-educator partnerships, Journal of Geoscience Education, 55, 402–412, https://doi.org/10.5408/1089-9995-55.5.402, 2007.

McAuliffe, F., Boland, M. A., and Boyd, A.: Development of geoscience education books with schoolchildren from low STEM engagement areas, Abstract ED51I-0738, 10–14 December 2018, 2018 AGU Fall Meeting, Washington, D.C., 2018.

Moloney, K. and Unger, M.: Transmedia storytelling in science communication: one subject, multiple media, unlimited stories, in: New Trends in Earth-Science Outreach and Engagement, 109–120, Springer, Cham., 2014.

Neenan, E. E. and Roche, J.: Geoscience Education in an Irish Context: A Need for Research, Journal of Geoscience and Environment Protection, 4, 1–8, https://doi.org/10.4236/gep.2016.46001, 2016.

Nolet, G.: A Volksseismometer? IRIS newsletter, Spring 1993, 10–11, available at: http://www.iris.edu/hq/publications/newsletters/iris (last access: 6 October 2018), 1993.

Phinney, R. A.: Retrospective on the PEPP Experience, EOS T. Am. Geophys. Un., 83, Fall Meet. Suppl., Abstract ED71C-13, 6–10 December 2002, San Francisco, California, USA, 2002.

Salmanidou, D. M., Guillas, S., Georgiopoulou, A., and Dias, F.: Statistical emulation of landslide-induced tsunamis at the Rockall Bank, NE Atlantic. P. R. Soc. A, 473, 20170026, https://doi.org/10.1098/rspa.2017.0026, 2017.

SFI (Science Foundation Ireland): Science in Ireland Barometer: An analysis of the Irish public's perceptions and awareness of STEM in society, Dublin, available at: http://www.sfi.ie/research-news/publications/SFI-Science-in-Ireland-Barometer(2).pdf, last access: 25 June 2015.

Steinberg, D. J., Phinney, R. A., and Nolet, A. M.: The Princeton Earth Physics Project presents: Seismometers-Telescopes for the Earth's Interior, 196th AAS Meeting, id.24.04, Bulletin of the American Astronomical Society, Vol. 32, p. 707, Rochester, NY, USA, 2000.

Steinberger, B., Bredow, E., Lebedev, S., Schaeffer, A., and Torsvik, T. H.: Widespread volcanism in the Greenland-North Atlantic region explained by the Iceland plume, Nat. Geosci., 12, 61–68, https://doi.org/10.1038/s41561-018-0251-0, 2019.

Tataru, D., Zaharia, B., Grecu, B., Tibu, S., Brisan, N., and Georgescu, E. S.: Seismology in Romanian Schools: education, outreach, monitoring and research, Rom. Rep. Phys., 68, 1589–1602, 2016.

Tong, V. C. (Ed.): Geoscience Research and Outreach: Schools and Public Engagement, Vol. 21, Springer Science & Business Media, Dordrecht, the Netherlands, 2014.

Tytler, R., Osborne, J. F., Williams, G., Tytler, K., Clark, J. C., Tomei, A., and Forgasz, H.: Opening up pathways: Engagement in STEM across the Primary-Secondary school transition. A review of the literature concerning supports and barriers to Science, Technology, Engineering and Mathematics engagement at Primary-Secondary transition, Commissioned by the Australian Department of Education, Employment and Workplace Relations, Melbourne, Deakin University, 2008.

Virieux, J.: Educational seismological project: EDUSEIS, Seismol. Res. Lett., 71, 530–535, 2000.

Wade, P. D. and Courtney, A. R.: Using video projects in the science classroom, in: New Trends in Earth-Science Outreach and Engagement, 177–192, Springer, Cham., 2014.

Zollo, A., Bobbio, A., Berenguer, J. L., Courboulex, F., Denton, P., Festa, G., Sauron, A., Solarino, S., Haslinger, F., and Giardini, D.: The European experience of educational seismology, in: Geoscience Research and Outreach, 145–170, Springer, Dordrecht, 2014.

D.2 Evidence for high temperature in the upper mantle beneath Cape Verde archipelago from Rayleigh-wave phase-velocity measurements

Tectonophysics 770 (2019) 228225

Contents lists available at ScienceDirect

Tectonophysics

journal homepage: www.elsevier.com/locate/tecto

Evidence for high temperature in the upper mantle beneath Cape Verde archipelago from Rayleigh-wave phase-velocity measurements

Joana Carvalho[a,*], Raffaele Bonadio[b], Graça Silveira[a,c], Sergei Lebedev[b], João Mata[a], Pierre Arroucau[d], Thomas Meier[e], Nicolas L. Celli[b]

[a] Instituto Dom Luiz (IDL), Faculdade de Ciências, Universidade de Lisboa, Campo Grande, 1749-016, Lisboa, Portugal
[b] School of Cosmic Physics, Geophysics section, Dublin Institute for Advanced Studies, Dublin, Ireland
[c] Instituto Superior de Engenharia de Lisboa, Rua Conselheiro Emídio Navarro, 1, 1959-007, Lisboa, Portugal
[d] EDF/DI/TEGG, Seismic Hazard Group, 905 Avenue du Camp de Menthe, 13097, Aix-en-Provence, France
[e] Institute of Geosciences, Christian-Albrechts University Kiel, Otto-Hahn-Platz 1, 24118, Kiel, Germany

ARTICLE INFO

Keywords:
Cape Verde hotspot
Oceanic lithosphere rejuvenation
Intraplate volcanism
Asthenosphere low-velocity anomaly
Teleseismic Rayleigh-wave phase-velocity

ABSTRACT

Cape Verde is an intraplate archipelago located in the Atlantic Ocean about 560 km west of Senegal, on an ~ 130 Ma old oceanic lithosphere. The upper-mantle structure beneath the islands was poorly known, until recently, in large part due to the lack of broadband seismic stations. In this study we used data from two temporary deployments across the archipelago, measuring the phase velocities of Rayleigh-waves fundamental-modes in a broad period range (8–250 s), by cross-correlating teleseismic earthquake data between pairs of stations. We derived a robust average, phase-velocity curve for the Cape Verde region, and inverted it for a shear-wave velocity profile. Our results show significantly low velocities of ~ 4.2 km/s in the asthenosphere, indicating the presence of anomalously high temperatures and, eventually, partial melting. The temperature anomaly is probably responsible for the thermal rejuvenation of the lithosphere to an effective age as young as about 30 Ma, which we infer from the comparison of seismic velocities beneath Cape Verde archipelago and those representative of different ages in the Central Atlantic. The anomalously high temperature in the asthenosphere, together with previously published evidence on low seismic velocities in the lower mantle and relatively He-unradiogenic isotopic ratios, suggests a hot plume, rooted deep in the lower mantle, as the origin of the Cape Verde hotspot.

1. Introduction

Most of the mass transfer between the Earth's mantle and crust occurs at plate boundaries. A conspicuous exception, albeit with much smaller volumes, is the intraplate basaltic magmatism, often associated with significant swells, as in the case of the Hawaii and Cape Verde archipelagos (e.g. Phipps Morgan et al., 1995; Crough, 1982; Laske et al., 2011). This intraplate magmatism has been attributed to hotspots in the upper asthenosphere, as first proposed by Wilson (1963), and then ascribed in their origin to hot mantle plumes (Morgan, 1971). Alternative models for such magmatism include the existence in the asthenosphere of wet spots, as hypothesized for the specific case of the Azores (e.g. Bonatti, 1990; Asimow et al., 2004), or the passive response of the asthenosphere to lithospheric breakup (e.g. Anderson, 2000; Lustrino and Anderson, 2015).

The Cape Verde intraplate archipelago is located on the Nubian Plate in the eastern Central Atlantic, approximately 560 km away from the African coast (Fig. 1a), where the age of the oceanic crust ranges between 115 and 140 Ma. The last eruption occurred in 2014–2015 at Fogo volcano, the latest in a period of ca 26 Ma of sub-aerial or shallow water volcanism, responsible for the emergence of the islands (e.g. Mata et al., 2017 and references therein). The archipelago is composed of nine inhabited islands and some islets, situated on top of a large topographic anomaly known as the Cape Verde Rise (~ 1200 km in diameter; up to ~ 2000 m high), considered the largest oceanic intraplate bathymetric anomaly (e.g. Parsons and Sclater, 1977; Monnereau and Cazenave, 1990).

Cape Verde has been included in most hotspot catalogues (e.g. Courtillot et al., 2003; Boschi et al., 2007; King and Adam, 2014). Large-scale tomographic studies have shown low-velocity anomalies in the lower mantle consistent with the Cape Verde magmatism being the result of a mantle plume anchored in the deep mantle (e.g. Montelli

---

[*] Corresponding author at: Instituto Dom Luiz, Lisbon, Campo Grande, 1749-016, Lisboa, Portugal.
E-mail address: jfcarvalho@fc.ul.pt (J. Carvalho).

https://doi.org/10.1016/j.tecto.2019.228225
Received 10 May 2019; Received in revised form 1 October 2019; Accepted 8 October 2019

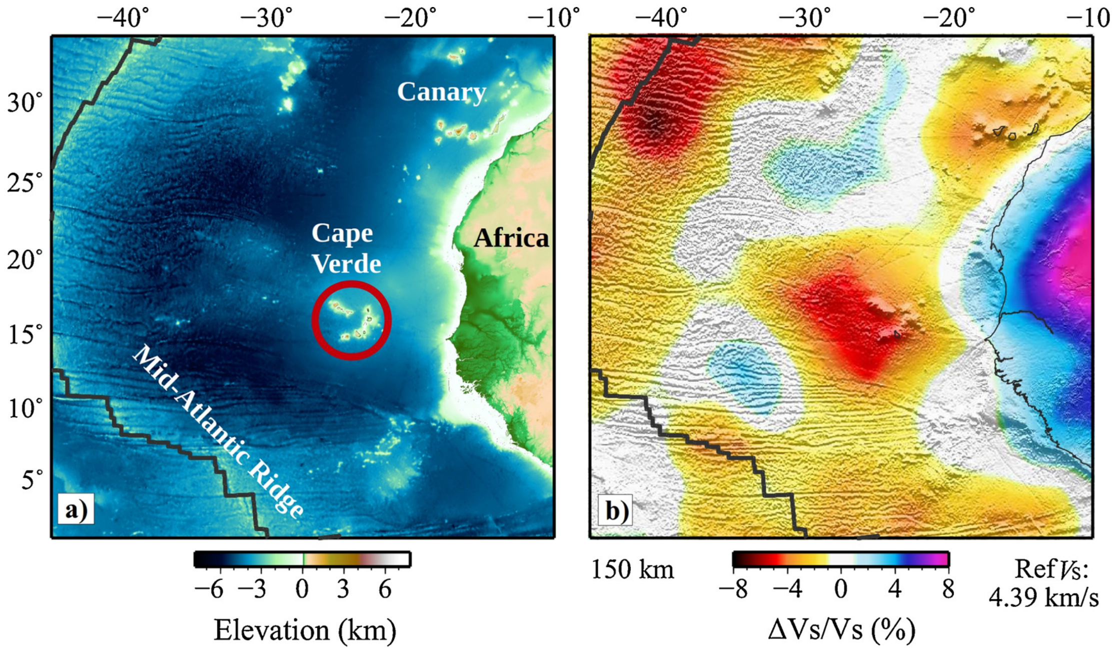

Fig. 1. (a) Topographic map of the Central Atlantic region. A red circle marks the location of Cape Verde, 560 km west of Africa. (b) Shear wave speed anomalies at 150 km depth beneath the region, according to the waveform tomography of Celli et al. (2019). A strong low velocity (Vs) anomaly can be observed beneath the Cape Verde region (For interpretation of the references to colour in this figure legend, the reader is referred to the web version of this article.).

et al., 2006; Forte et al., 2010; Liu and Zhao, 2014; French and Romanowicz, 2015). However, the lack of resolution of such studies at local and regional scales, in particular at upper-mantle depths, has left the existence of a plume beneath Cape Verde still in doubt. The origin of magmatism in Cape Verde is debated and models invoking mantle plumes (e.g. Montelli et al., 2006; Liu and Zhao, 2014) and, alternatively, edge-driven convection (e.g. King and Ritsema, 2000; King, 2007) have been proposed. Regional shear-wave velocity (Vs) models obtained from global observations of surface and shear waves (Fig. 1b) display low asthenospheric velocities beneath the Cape Verde region (e.g. Schaeffer and Lebedev, 2015; Celli et al., 2019) suggesting an anomalously hot asthenosphere compatible with both the above-mentioned models. However, the amplitude and depth extent of the anomaly remains uncertain. In an alternative interpretation, Patriat and Labails (2006) argued that the continuous morphological basement ridge between the archipelagos of Canary and Cape Verde and the simultaneous geological events, at both, may indicate a causal link between lithospheric deformation events and the origin of magmatism.

Before the XXI Century, the seismic-station coverage in Cape Verde was poor, with only one permanent station belonging to the Global Seismographic Network (GSN) installed at the island of Santiago (SACV). A network of seven broadband stations was then deployed from 2002 to 2004 (Lodge and Hellfrich, 2006). More recently, in 2007, another temporary network of 38 stations was deployed for ten months. The 2002–2004 data from the seven stations network has already been used in receiver functions studies (Lodge and Hellfrich, 2006; Hellfrich et al., 2010) and P and S wave tomography (Liu and Zhao, 2014). Vinnik et al. (2012) presented the results obtained through the joint analysis of PS and SP receiver functions using both networks. However, there is still no agreement on the inferences from these studies.

In order to better constrain the Earth's lithosphere and sublithospheric mantle beneath Cape Verde, we measured Rayleigh-wave phase velocities using an elaborate implementation of the two-station method that can produce measurements in very broad period ranges (Meier et al., 2004). This method overcomes some limitations ascribed to traditional passive methods (e.g.: source-receiver geometry and/or sparse and irregular seismicity distribution) and allows imaging the local lithospheric structure underneath Cape Verde. We then inverted the average regional phase velocities for the Vs distribution with depth using a non-linear gradient-search algorithm. The Vs profile constrained by our broadband dispersion data provides valuable new insights on the structure of the lithosphere and asthenosphere beneath Cape Verde.

2. Seismic data and phase-velocity measurements

2.1. Seismic network and pre-processing

We processed data records from seven temporary broadband Guralp 3 Ts (120 s) stations deployed from 2002 to 2004 (Lodge and Hellfrich, 2006) and 38 stations equipped with Earth Data PR6-24 data loggers and Guralp CMG-3ESP (60 s) seismometers (Vinnik et al., 2012; Carvalho et al., 2019), recording continuously from December 2007 to September 2008 (Fig. 2).

The challenges presented by our data included: 1) the high level of ambient noise, which limited the number of successful measurements; 2) remoteness of Cape Verde from the seismically active areas (Vales et al., 2014); and 3) the unevenness of the station-to-station path coverage, due to the distribution of the islands and the absence of ocean bottom seismometers (Fig. 2). In order to perform accurate phase-velocity measurements and obtain a robust average phase-velocity curve for Cape Verde, while meeting these challenges, we applied processing steps developed explicitly for our dataset. For each station pair, we chose teleseismic earthquakes with less than ten-degree angles between station-station and the event-station great circle paths. Subject to this criterion, all the events from the global CMT catalogue (Ekström et al., 2012) with moment magnitudes higher than 4.2 were considered.

2.2. Phase-velocity measurements

Phase velocities were measured through a recent implementation of the two-station method (Meier et al., 2004; Soomro et al., 2015). For each station pair, the teleseismic earthquake recordings were cross-correlated, and the dispersion curves of fundamental-mode Rayleigh waves were calculated from the phase of the cross-correlation functions weighted in the time-frequency plane. To overcome the effect of other

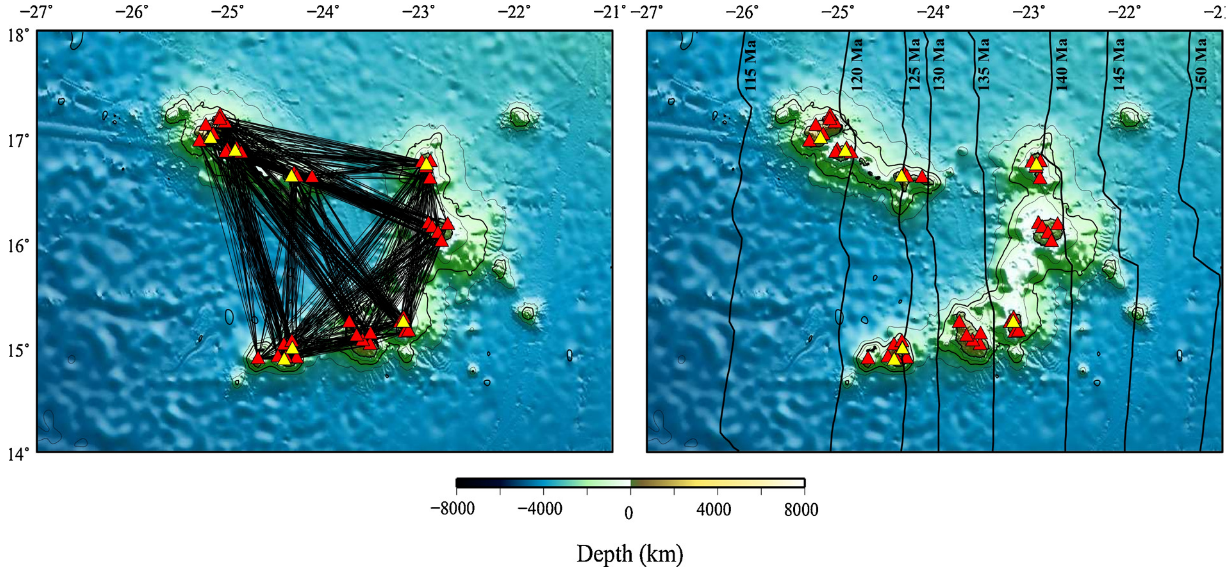

Fig. 2. Left: Seismic network (red triangles - 9A network (2007–2008); yellow triangles - YW network (2002–2004)) and station-to-station path coverage (black lines). Right: Seismic network and seafloor age isochrons (Müller et al., 2008) (For interpretation of the references to colour in this figure legend, the reader is referred to the web version of this article.).

signals, such as higher-modes and scattered fundamental-mode arrivals, the cross-correlation function was filtered with a frequency-dependent Gaussian band-pass filter and windowed in the time domain, enhancing the signal-to-noise ratio (Meier et al., 2004).

The selection of the dispersion curves was performed manually, in an interactive procedure based on some criteria including the smoothness and length of the dispersion curve and its deviation from a reference one (Soomro et al., 2015). The number of measurements for each frequency is also important whereby a minimum of two measurements was established. However, for some station pairs, even this number was not achieved, given the relatively short operation time of most of the stations (9A network). We thus computed more robust, "inter-island" dispersion curves, by gathering all the station-station paths between the same two islands and computing the average of all the phase-velocity measurements at each frequency. For the purpose of this study, each island is now represented by a single virtual station, located at a geographical midpoint. Fig. 3 represents the final ray distribution as well as each virtual station.

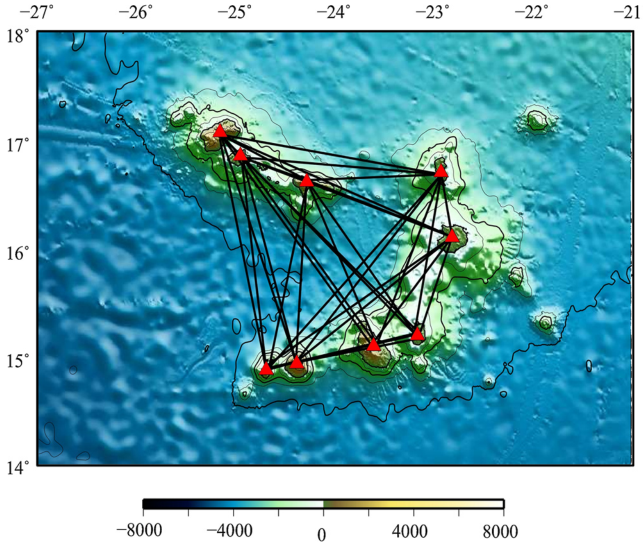

Fig. 3. Virtual seismic stations (red triangles) and final ray path distribution (black lines) (For interpretation of the references to colour in this figure legend, the reader is referred to the web version of this article.).

To remove the 2π ambiguity of the arctangent function and to eliminate outliers, a reference dispersion curve was required. We tested AK135 as a reference curve (Kennett et al., 1995) but a more accurate and regional model was needed. The automated phase-velocity measurement routine of Soomro et al. (2015) allowed us to obtain a preliminary selection of all possible phase-velocity curves in the entire period range, applying loose selection criteria and discarding only the curves from seismograms dominated by noise. The selected measurements were stacked together in the broad period range, resulting in a density distribution plot (Fig. 4a). From the maximum values of the distribution at each period, a dispersion curve was then extracted and used as reference curve in the following definitive, interactive selection of measurements (Bonadio et al., 2018).

We measured the inter-station phase velocities in a broad period range (8–250 s). Long-period measurements were obtained only with data from true-broadband sensors (YW network). To constrain the lithosphere and upper-mantle structure beneath the Cape Verde area, we performed a strict selection of the most accurate measurements from all the station pairs and computed the average dispersion curve for entire Cape Verde region. Only a small number of measurements were successfully measured with cross-correlation at periods longer than 120 s. We thus complemented them with phase velocities measured using waveform inversion (e.g. Lebedev et al., 2006) and merged the measurements of both types to obtain our average curve. The curves from the cross-correlation and waveform-inversion measurements are in very good agreement for the intermediate range of periods, indicating that merging them is a robust procedure (Lebedev et al., 2006) (Fig. 4b). Fig. 5 shows the final average dispersion curve (red line), plotted together with the individual dispersion curves (dark grey).

The average dispersion measurements from "inter-island" pairs were also inverted to phase-velocity maps at different periods. We used the LSQR algorithm (Paige and Saunders, 1982) with lateral smoothing and slight norm damping, as described by Lebedev and Van Der Hilst (2008). We performed several inversion tests using different parametrization and regularization coefficients, in order to identify the optimal achievable resolution for the maps. We also applied an outlier removal procedure to the data, removing the 15% of the data with largest misfits (Lebedev and Van Der Hilst, 2008; Endrun et al., 2011), likely presenting the largest measurement errors. The phase-velocity maps (Supplementary material Fig. A1) show weak regional-scale

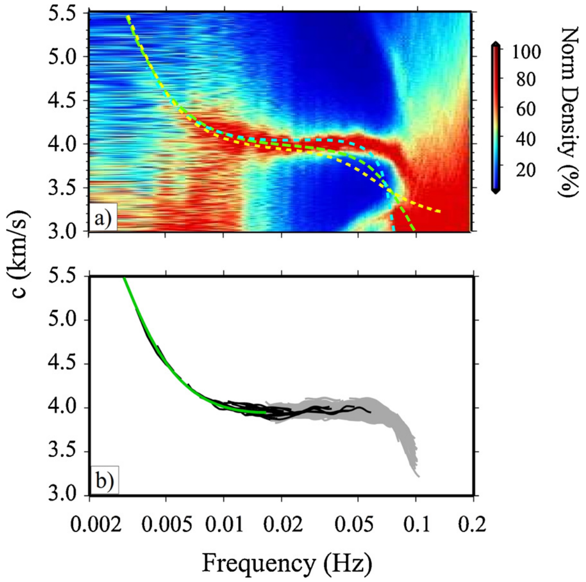

Fig. 4. a) Density distribution plot for the stack of automated preliminary measurements, normalized to the maximum at each period. The regional reference curve is substantially different from the global reference curves AK135 (yellow dashed line) (Kennett et al., 1995) and PREM (green dashed line) (Dziewonski and Anderson, 1981), and also from the PA5 model for the Pacific (blue dashed line) (Gaherty et al., 1996). b) Dispersion curves obtained from all the station pairs, evincing the good match between short-period (grey) and long-period (black) measurements. The green curve represents the average curve calculated through the waveform inversion, complementing the cross-correlation measurements (For interpretation of the references to colour in this figure legend, the reader is referred to the web version of this article.).

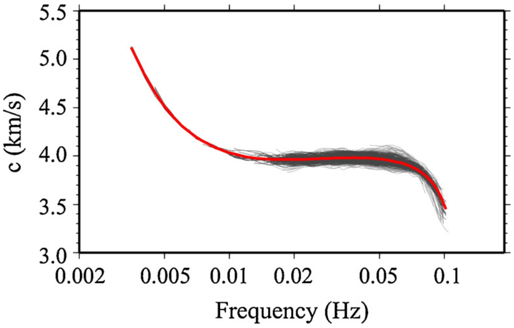

Fig. 5. Average phase-velocity curve (red line) obtained from the smoother dispersion curves (dark grey), used for the 1D inversion for Vs profile in depth. A loose selection is represented in pale grey (For interpretation of the references to colour in this figure legend, the reader is referred to the web version of this article.).

heterogeneities across the area. This shows that an inversion of a region-average, phase-velocity curve should produce a meaningful, region-average Vs profile characterizing the upper mantle structure beneath Cape Verde.

We compared our results with the Atlantic Rayleigh-wave phase velocities averaged for different lithospheric ages (James et al., 2014). The comparison, displayed in Fig. 6, reveals that the Cape Verde phase-velocities at periods longer than 40 s (frequencies lower than ~ 0.025 Hz, sampling the lithosphere and asthenosphere) are lower than the Atlantic average for a lithosphere older than 20 Ma. This suggests that the lithosphere was effectively reset to a younger age and the asthenosphere beneath the Cape Verde region is hotter than average.

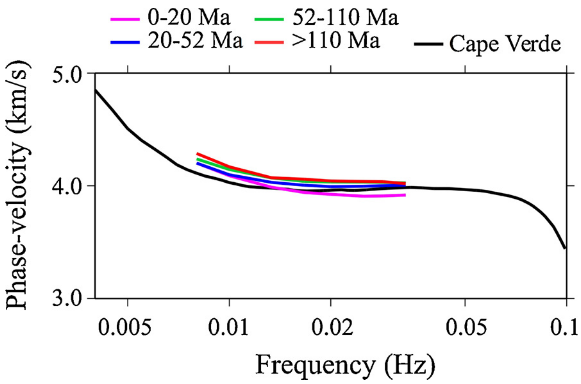

Fig. 6. Comparison of Cape Verde-region average dispersion curve (black line) with the Atlantic Rayleigh-wave phase velocities averaged for different lithospheric ages (James et al., 2014) (For interpretation of the references to colour in this figure legend, the reader is referred to the web version of this article.).

3. Average shear-wave velocity structure

We inverted the average, fundamental-mode, Rayleigh-wave dispersion curve to obtain a 1D Vsv (vertically polarized shear wave speed) profile using a non-linear, Levenberg-Marquardt (damped least-squares), gradient-search algorithm (e.g. Meier et al., 2004; Agius and Lebedev, 2014) . Our initial model is similar to that used by Bonadio et al. (2018): a four-layered model for the crust, taken from CRUST 2.0 (Bassin et al., 2000), followed in the mantle by a modified version of AK135 (Kennett et al., 1995). The chosen reference model is characterized by constant shear-wave velocities (4.45 km/s) from the Moho down to 220 km depth and with linearly increasing shear-wave velocities below that depth. The shear Q profile is from AK135. The inversion is parameterized, from the surface to the uppermost lower mantle, using boxcar basis functions for the crustal layers and triangle basis functions for the mantle. The Moho discontinuity depth is also an inversion parameter, allowed to vary during the inversion computation, in order to avoid constraining too much the upper mantle, and obtaining unreliable velocities, as consequence. We present the inversion result in Fig. 7a. The observed and synthetic phase-velocities, as well as the relative data-synthetic misfit, are presented in Fig. 7b and c, respectively.

Considering that we used only the fundamental mode Rayleigh waves, it is important to understand how well our data can resolve the low-velocity anomaly at the asthenospheric depths. Fig. A2 of the supplementary material presents the sensitivity kernels calculated for different periods, using our initial model. Our model should be well constrained down to at least 300 km depth.

The most striking feature of our inversion result is a low-velocity zone, from ~ 60 to ~ 210 km depth, with a minimum velocity of about 4.2 km/s. At 280–350 km, S-wave velocity is indistinguishable from that in the reference model.

4. Discussion

4.1. Vs evidence of a rejuvenated lithosphere

An average S-wave velocity profile, for the region of the Cape Verde archipelago is shown on Fig. 7a, depicting a Vs decrease from ~ 4.6 km/s to about 4.2 km/s. The asthenosphere extends down to about 210 km.

The seafloor depth is normally determined by the isostatic equilibrium of the oceanic plate. It depends on the plate's density and thickness, which usually increase with the plate's age, the oceanic lithosphere getting colder and thicker with time. The lithosphere-asthenosphere boundary (LAB) can be defined by an isotherm, which deepens as the plate ages and moves away from the mid-ocean ridge. The

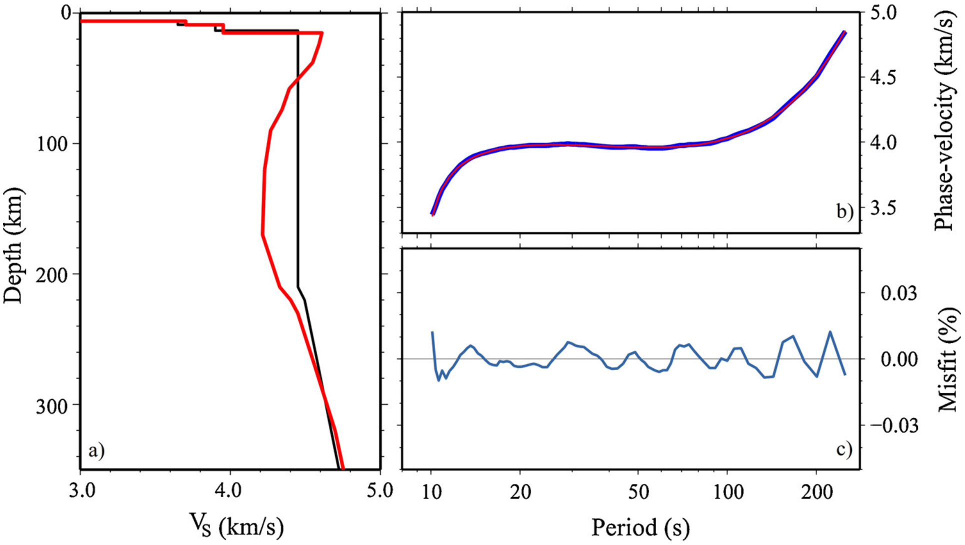

Fig. 7. Results of the inversion. (a) Inversion result (red line) and the modified AK135 (black line) as a reference model (Kennett et al., 1995). (b) Measured dispersion curve (blue line) and the synthetic phase-velocities (red line). (c) The relative data-synthetic misfit (For interpretation of the references to colour in this figure legend, the reader is referred to the web version of this article.).

thickening becomes approximately asymptotic for ages above approximately 70 Ma according to most of lithospheric cooling models (see Stein and Stein, 1992; Mckenzie et al., 2005; Hamza and Vieira, 2012). In the presence of anomalously high temperatures in the asthenosphere beneath the plate (e.g., due to asthenospheric flow, small-scale convection, or hotspots; Artemieva, 2011, and references therein), the plate will be re-heated and acquire a geotherm normally characteristic of a younger lithospheric age, the process referred to as thermal rejuvenation (Menard and McNutt, 1982).

We compared our profile, derived from the phase-velocity inversion, with average Vs profiles of different lithospheric ages for the Central Atlantic Ocean from waveform tomography (Celli et al., 2019) and from the global model SL2013sv of Schaeffer and Lebedev (2015) (Fig. 8). Both methods present similar results with slightly lower velocities using the SL2013sv model, especially for the 30 Ma age profile. The Cape Verde profile is clearly different from what would be expected for a region with the age of the ocean crust ranging from 115 to 140 Ma, showing anomalously low velocities. This is confirmed by a different independent study (James et al., 2014) revealing Rayleigh-wave phase velocities slower than the Atlantic averages (see Fig. 6). This feature, observed both at the lithospheric and asthenospheric depths, suggests anomalously hot mantle beneath the Cape Verde archipelago, consistent with the anomalous heat flow characterizing the Cape Verde Rise, which at its centre presents a thermal anomaly of 16 ± 4 mW/m^2 above the expected value of 45.5 ± 3.4 mW/m^2 stipulated for the crustal age of the Cape Verde region (Courtney and White, 1986). These authors considered such anomaly as indicative of lithospheric reset to a thermal age of ∼ 59 Ma. However, the Cape Verde shear velocity is even lower than that estimated for a 59 Ma old lithosphere, being instead indicative of a lithospheric thermal age of about 30 Ma.

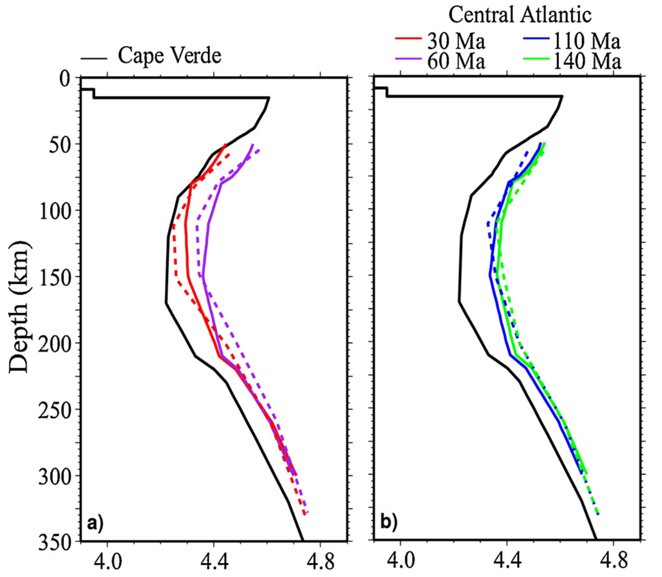

Fig. 8. Comparison of Cape Verde average profile (black line) with different lithospheric ages profiles for the Central Atlantic Ocean from (Celli et al., 2019). (a) 30 Ma (red) and 60 Ma (purple) age profiles (b) 110 Ma (blue) and 140 Ma (green) age profiles. Dashed lines correspond to the same lithospheric ages calculated from the SL2013sv model (Schaeffer and Lebedev, 2015) (For interpretation of the references to colour in this figure legend, the reader is referred to the web version of this article.).

While the Cape Verde Vs profile for the lithosphere matches the one of 30 Ma for the Central Atlantic, it must be emphasized that at asthenospheric depths the velocity beneath Cape Verde is still lower than that determined for the normal Atlantic asthenosphere in regions of 30 Ma old crust. This indicates that the cause for the rejuvenated character of the Cape Verde lithosphere is an anomalously hot asthenosphere, i.e., the existence of a hotspot (Wilson, 1963). This view is supported when using a geophysical-petrological approach. Bonadio et al. (2018) used petrological modeling and, alternatively, published Vs-T relationships (Goes et al., 2012) to estimate the lithospheric geotherm, and the mantle potential temperature beneath the Tristan da Cunha hotspot, based on their phase-velocity data and Vs models. Using the same approach, we estimate Tp of 1400–1420 °C for Cape Verde, higher than in the average ambient mantle (1337 ± 35 °C (Katsura et al., 2010)), indicating excess temperatures beneath Cape Verde. Shear Q at asthenospheric depths in the multi-parameter petrological models for Tristan da Cunha (Bonadio et al., 2018) is lower than according to AK135, and this is accounted for in their Tp estimate. Because the Vs structure we observe is very similar to that beneath Tristan (Fig. 9a), we could use the results of the petrological modeling of Bonadio et al (2018), making sure our Tp estimate is not biased by overestimated Q values. The same conclusion was obtained by Putirka (2008), using olivine-melt equilibrium. He estimated, for Cape Verde, a mantle potential temperature of 1511 °C, well above the estimation, using the same methodology, for the ambient upper mantle sampled by the MORB (1396 °C).

4.2. The role of the rejuvenation of lithosphere on the origin of Cape Verde Rise

The Cape Verde islands rise atop the largest intraplate swell, with a

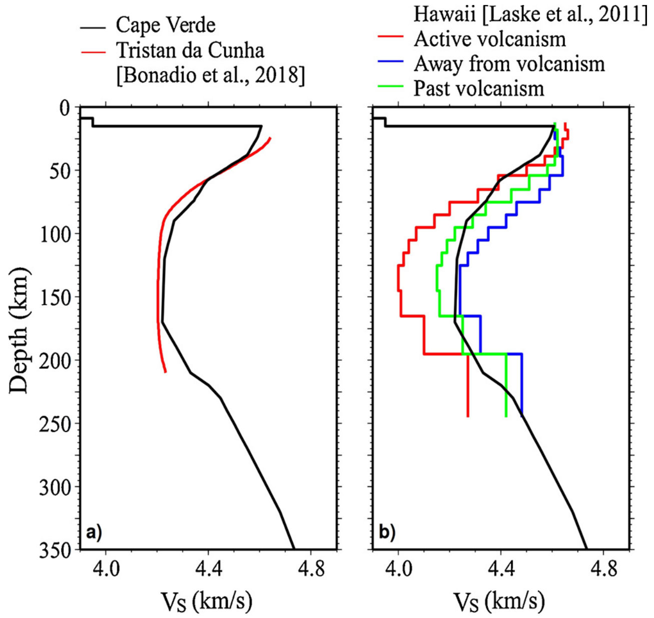

Fig. 9. (a) Vs profiles for Tristan da Cunha (red line) (Bonadio et al., 2018) and Cape Verde (black line). (b) Cape Verde (black line) and Vs profiles for three different regions in Hawaii (see Fig. 11 of Laske et al., 2011) (For interpretation of the references to colour in this figure legend, the reader is referred to the web version of this article.).

depth anomaly of about 2000 m. The origin of ocean floor swells has been debated and several types of models can be considered (e.g. Menard and McNutt, 1982; Sleep, 1990; Ali et al., 2003): 1) thermal rejuvenation of the lithosphere by the occurrence of sublithospheric hot mantle material; 2) dynamic support by the upwelling sublithospheric material; 3) underplating with less dense residual material after melt extraction.

Lodge and Helfrich (2006) considered the existence of a depleted/refractory root beneath Cape Verde to be the main cause of the bathymetric anomaly. This residue of melting generation processes would be Mg-enriched/Fe-depleted and, owing its relatively low density, would constitute a positively buoyant body underplating the lithosphere and causing the observed uplift (see also Phipps Morgan et al., 1995). For Cape Verde, this model was discarded by Pim et al. (2008) based on gravimetric data and by Wilson et al. (2010) using seismic and gravimetric arguments.

According to the thermal rejuvenation model, the oceanic lithosphere is heated and thinned when it passes over a hotspot with the consequent isostatic readjustment and uplift. The evidence shown above for the existence of a temperature anomaly beneath Cape Verde is consistent with the thermal rejuvenation, which is also supported by high heat flow on top of the Cape Verde Rise (Courtney and White, 1986). Using a value 20 mW/m^2 for the heat flux anomaly, Sleep (1990) considered the occurrence of a reset to a thermal age of ~ 59 Ma, to which should correspond a bathymetric anomaly of only 1200 m instead of the about 2000 m observed, leaving space to complementary cause(s) for the origin of swell.

Some authors attributed at least a large part of the swell to the dynamic role of ascending sublithospheric material (Courtney and White, 1986; Sleep, 1990; Wilson et al., 2010, 2013). However, our results, pointing to a thermal age of 30 Ma, allows considering a more important role of thermal rejuvenation on the origin of the Cape Verde Rise that inferred from the measured heat flow and bathymetric anomaly. The significant role of thermal rejuvenation of the lithosphere on the swell origin is in line with the recent results of Lodhia et al. (2018), based on the calculated sub-lithospheric temperature excess. Nevertheless, it does not completely rule out the complementary role of other mechanisms, such as dynamic support by upwelling mantle material, a combination proposed, for example, by Wilson et al. (2013) using a multidisciplinary approach.

4.3. On the origin of Cape Verde hotspot

Lithospheric, age-dependent profiles for the Central Atlantic show that S-wave velocities for different plate ages tend to converge at a depth of ~200 km (Fig. 8). The Vs profile of the Cape Verde region is distinctly different: down to 300 km, it shows Vs values lower than typical for the Central Atlantic. This behaviour is consistent with a deep (> 300 km) origin for the hotspot, which would be compatible with a mantle plume or, alternatively, with the existence of mantle upwelling caused by edge-driven or other regional small-scale convection pattern. This small-scale convection would have been developed in the upper mantle at the transition between cratonic and thinner oceanic lithosphere and would explain some magmatic provinces like Cape Verde (King, 2007). Our study does not allow the distinction between these two hypotheses, but this subject may be discussed based on other geophysical arguments and, also, from a geochemical point of view.

If Cape Verde is originated from a mantle plume anchored in the lower mantle, the mantle transition zone (MTZ) beneath it should be anomalously hot. As a consequence, it would be expected a perturbation on the thickness of the MTZ, i.e., between the discontinuities at ~ 410 km and ~ 660 km. These discontinuities are due to pressure-induced phase transitions from α-olivine to β-spinel (wadsleyite), at ~ 410 km and from γ-spinel (ringwoodite) to perovskite and magnesiowustite (~ 660 km). Those phase transitions are characterized by positive and negative Clayperon slopes, respectively (e.g. Lebedev et al., 2003). Consequently, the thickness of the MTZ responds to temperature variation by thickening when cooled (e.g. by a subducting slab), or by thinning in the presence of an ascending hot mantle plume.

Several seismic studies performed at different spatial scales and using different approaches, have assessed the thickness of the MTZ beneath Cape Verde, with surprisingly different results (c.f. Deuss, 2007; Gu et al., 2009; Hellfrich et al., 2010; Vinnik et al., 2012; Saki et al., 2015). Deuss (2007) and Gu et al. (2009) both used SS precursors, Deuss (2007) reporting no MTZ thinning and Gu et al. (2009) significant MTZ thinning, as much as beneath Hawaii. Saki et al. (2015) used precursor arrivals to PP and SS seismic phases and also inferred an anomalously thin MTZ, in agreement with the result obtained by Gu et al. (2009). Hellfrich et al. (2010) measured the arrival time of the Ps waves converted at 410 and 660 km discontinuities and inferred a standard, global-average MTZ thickness. However, their data would not be inconsistent with anomalously thin MTZ if the anomaly extended over less than 250 km laterally. Vinnik et al. (2012), reported a pronounced thinning of the MTZ, using both PS and SP receiver functions. The evidence on the temperature in the MTZ beneath Cape Verde from converted and reflected body waves thus remains overall inconclusive.

Noble gas isotopic geochemistry is considered an important tool to assess the nature of contributions of distinct mantle reservoirs to magma sources (e.g. Moreira, 2013; Jackson et al., 2014). Noble gas studies on the Cape Verde rocks have evinced the occurrence of He isotope signatures clearly more unradiogenic than the canonical value of 8 ± 1 Ra of the N-MORB or the mean MORB value of 8.8 ± 2.1 (Graham, 2002). Indeed, for Cape Verde ^{3}He/^{4}He ratios up to 15.7 (Doucelance et al., 2003) and 15.5 (Mata et al., 2010) Ra has been described for silicate rocks and carbonatites, respectively. Such values suggest that relatively unradiogenic signatures preserved in the lower mantle could have contributed to the Cape Verde origin. The possibility of the preservation in the deepest mantle of such unfractionated domains for periods as long as 4.5 Ga was made possible by the inefficacy of chemical diffusion and mixing in the highly-viscous lower mantle (Jackson et al., 2010).

Moreover, for Cape Verde ^{206}Pb/^{204}Pb ratios up to 20.251 (Mourão et al., 2012) and 20.238 (Hoernle et al., 2002) has been measured for silicate and carbonatite rocks, respectively. These values are evidence, albeit indirect, for an origin related to a deep rooted plume. Indeed, a recent study showed that hotspots with a strong contribution of the HIMU (high time-integrated U/Pb mantle component), as is the case of Cape Verde, are more likely to be associated with deeply anchored mantle plumes (Jackson et al., 2018).

In conclusion, several kinds of geochemical arguments are strongly suggestive of an origin of the Cape Verde hotspot related with a mantle plume rooted in the lowest levels of the mantle, in agreement with global scale tomographic studies (e.g. Montelli et al., 2006; Forte et al., 2010; French and Romanowicz, 2015).

4.4. Comparison with other hotspots

In addition to the comparison with both fundamental-mode Rayleigh-wave phase velocities (Fig. 6) and 1D shear-wave velocity profiles for different lithospheric ages of the Atlantic Ocean (Fig. 8), we also compared our profile with those beneath other hotspots. In Fig. 9 we compare the Cape Verde Vs profile with the results for two other intraplate hotspots, Tristan da Cunha (Bonadio et al., 2018) and Hawaii (Laske et al., 2011).

Fig. 9 reveals that the Cape Verde and Tristan da Cunha regions are characterized by similar Vs profiles, nevertheless with higher velocities than that beneath the active volcanoes of Hawaii (Laske et al., 2011). This is consistent with Hawaii being characterized by significantly higher mantle potential temperatures (Tp = 1687 °C) than Cape Verde (Tp = 1511 °C) and Tristan da Cunha (Tp = 1573 °C) as determined by Putirka (2008). The slightly higher Vs characterizing Cape Verde, as compared with Tristan da Cunha (see Fig. 9), is in agreement with its lower mantle potential temperature as calculated by Putirka (2008) or when using the Bonadio et al. (2018) approach (Tristan da Cunha Tp = 1410–1430 °C; Cape Verde T = 1400–1420 °C).

We also made a comparison with hotspots located on, or close to, the Mid Atlantic Ridge - Iceland, Azores and Ascension (Gaherty and Dunn, 2007), for which local Vsv models are available (Fig. 10). When the Cape Verde profile is compared with the profiles obtained for these hotspots, it is noticeable that Vs at depths down to 150 km is higher beneath Cape Verde than beneath Iceland, Azores and Ascension (with exception of the 15–20 Ma profile which presents velocities similar to Cape Verde), suggesting a thicker lithosphere beneath Cape Verde when compared with the "near-ridge" archipelagos. This explains the very low degrees of partial melting inferred from the highly SiO_2-unsaturated composition of the Cape Verde rocks. Such low extent of melting severely limited the ability for compositional homogenization of the source heterogeneities, which is reflected, for example, in the heterogeneous character of the Cape Verde lavas erupted in the last 60 years from volcanic vents located less than 2 km away (Mata et al., 2017).

5. Conclusions

In a local-scale study of the Cape Verde region, we measured fundamental-mode Rayleigh-wave dispersion curves in a broad period range, yielding an accurate and definitive local Vs profile than available previously. Our data reveals a low-velocity zone reaching a minimum Vs of ~ 4.2 km/s at 170 km depth, suggestive of a temperature anomaly. This temperature anomaly is likely to have been the cause for a significant thermal rejuvenation of the oceanic lithosphere beneath Cape Verde to an apparent age of approximately 30 Ma, which we infer from comparisons of the Cape Verde Vs profile and normal Central Atlantic lithosphere for different ages. This rejuvenated age is much lower than the previously proposed value of 59 Ma (Sleep, 1990) reducing the need to invoke a significant role of dynamic support of the Cape Verde swell. The minimum value of Vs at the Cape Verde asthenosphere is higher than the one reported for under the active volcanoes of Hawaii but similar to that for Tristan da Cunha, consistent with higher potential temperatures for Hawaii compared to Cape Verde and Tristan da Cunha. Our results, interpreted together with the published evidence on the relatively He-unradiogenic signatures and low-seismic-velocity anomalies in the lower mantle, strongly suggest an origin of the Cape Verde hotspot related to a deeply anchored mantle plume.

Data availability

Data from the YW network were obtained from Incorporated Research Institutions for Seismology (IRIS) Data Management Center at http://ds.iris.edu/mda, code YW. Data from the 9A network can be downloaded from the GFZ Seismological Data Archive at geofon.gfz-potsdam.de/waveform/archive.

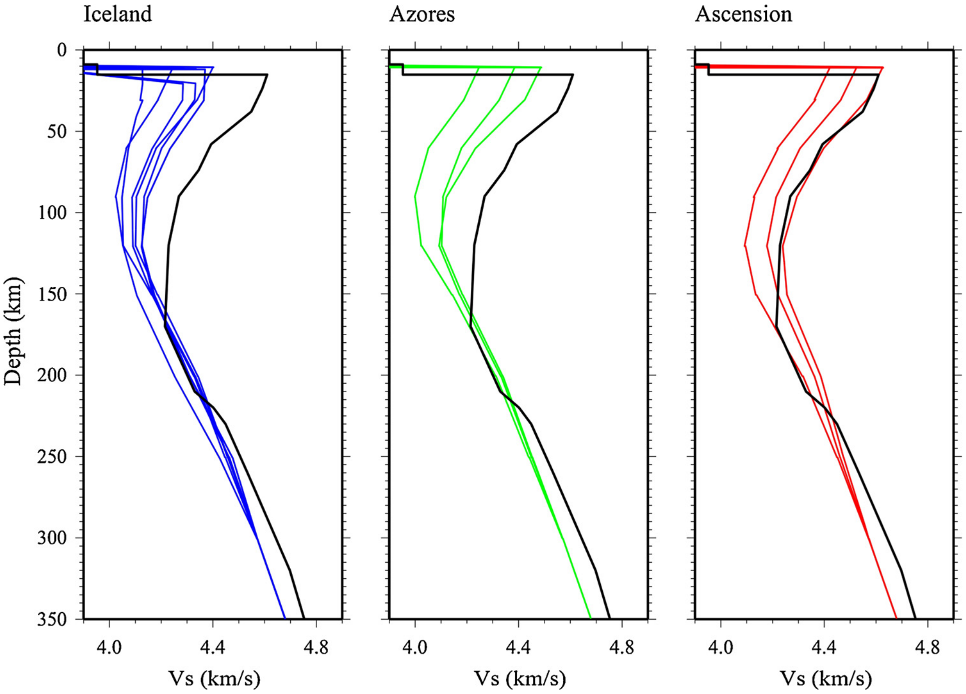

Fig. 10. Vs profiles for Iceland (blue lines), Azores (green lines) and Ascension (red lines) hotspots (Gaherty and Dunn, 2007). Cape Verde Vs profile is represented by a black line. The several lines of the same color for each hotspot represent different oceanic lithosphere ages (For interpretation of the references to colour in this figure legend, the reader is referred to the web version of this article.).

Declaration of Competing Interest

There are no competing interests.

Acknowledgments

We thank projects CVPLUME (Ref. PTDC/CTE-GIN/64330/2006) and Cape Verde Mantle Structure (YW network) for providing the broadband seismic data we used in this research. Thanks are also due to Gabi Laske and Esther K. James for sharing their Rayleigh-wave phase velocity results, which helped to interpret our phase velocity measurements. We thank James B. Gaherty for providing the 1D S-wave velocity profiles for Azores, Ascension and Iceland, for comparison. All figures were made using GMT - Generic Mapping Tools (Wessel et al., 2013). This study was supported by FIRE project (Ref. PTDC/GEO-GEO/1123/2014). Publication supported by FCT - project UID/GEO/50019/2019 - Instituto Dom Luiz. FCT PhD Grant Ref. PD/BD/114480/2016 supported Joana Carvalho. Raffaele Bonadio, Sergei Lebedev and Nicolas L. Celli are supported by the Science Foundation Ireland (SFI) grant13/CDA/2192, with additional support from grant 16/IA/4598, co-funded by SFI, the Geological Survey of Ireland, and the Marine Institute and from the SFI grant 13/RC/2092, co-funded under the European Regional Development Fund. We acknowledge discussions and mobility supported by COST Action ES1401-TIDES. The authors also acknowledge the two anonymous reviewers and the editor Ling Chen for their help on improving the article.

Appendix A. Supplementary data

Supplementary material related to this article can be found, in the online version, at doi:https://doi.org/10.1016/j.tecto.2019.228225.

References

Agius, M.R., Lebedev, S., 2014. Shear-velocity structure, radial anisotropy and dynamics of the Tibetan crust. Geophys. J. Int. 199 (3), 1395–1415. https://doi.org/10.1093/gji/ggu326.

Ali, M., Watts, A., Hill, I., 2003. A seismic reflection profile study of lithospheric flexure in the vicinity of the cape verde islands. J. Geophys. Res. Solid Earth 108 (B5). https://doi.org/10.1029/2002JB002155.

Anderson, D.L., 2000. The thermal state of the upper mantle; no role for mantle plumes. Geophys. Res. Lett. 27 (22), 3623–3626.

Artemieva, I., 2011. Lithosphere: an Interdisciplinary Approach. Cambridge University Press.

Asimow, P.D., Dixon, J., Langmuir, C., 2004. A hydrous melting and fractionation model for mid-ocean ridge basalts: application to the mid-atlantic ridge near the Azores. Geochem. Geophys. Geosystems 5 (1).

Bassin, C., Laske, G., Masters, G., 2000. The current limits of resolution for surface wave tomography in North America. Eos Trans. Am. Geophys. Union 81 (48) (Fall Meet. Suppl., Abstract S12A-03).

Bonadio, R., Geissler, W.H., Lebedev, S., Fullea, J., Ravenna, M., Celli, N.L., Jokat, W., Jegen, M., Sens-Schönfelder, C., Baba, K., 2018. Hot upper mantle beneath the tristan da cunha hotspot, from probabilistic Rayleigh-wave inversion and petrological modeling. Geochem. Geophys. Geosystems 107–111. https://doi.org/10.1002/2017GC007347.

Bonatti, E., 1990. Not so hot "hot spots" in the oceanic mantle. Science.

Boschi, L., Becker, T., Steinberger, B., 2007. Mantle plumes: dynamic models and seismic images. Geochem. Geophys. Geosystems 8 (10). https://doi.org/10.1029/2007GC001733.

Carvalho, J., Silveira, G., Schimmel, M., Stutzmann, E., 2019. Characterization of microseismic noise in Cape Verde. Bull. Seismol. Soc. Am. 109 (3), 1099–1109. https://doi.org/10.1785/0120180291.

Celli, N.L., Lebedev, S., Schaeffer, A.J., Ravenna, M., Gaina, C., 2019. The upper mantle beneath the South Atlantic Ocean and South America from waveform tomography with massive datasets. Geophysics Journal International In review.

Courtillot, V., Davaille, A., Besse, J., Stock, J., 2003. Three distinct types of hotspots in the earths mantle. Earth Planet. Sci. Lett. 205 (3–4), 295–308.

Courtney, R.C., White, R.S., 1986. Anomalous heat flow and geoid across the cape verde rise: evidence for dynamic support from a thermal plume in the mantle. Geophys. J. Int. 87 (3), 815–867.

Crough, S.T., 1982. Geoid height anomalies over the cape verde rise. Mar. Geophys. Res. 5 (3), 263–271.

Deuss, A., 2007. Seismic observations of transition-zone discontinuities beneath hotspot locations. Special Papers-Geological Society of America 430, 121. https://doi.org/10.1130/2007.2430(07).

Doucelance, R., Escrig, S., Moreira, M., Gariépy, C., Kurz, M.D., 2003. Pb-sr-he isotope and trace element geochemistry of the cape verde archipelago. Geochim. Cosmochim. Acta 67 (19), 3717–3733.

Dziewonski, A.M., Anderson, D.L., 1981. Preliminary reference earth model. Phys. Earth Planet. Inter. 25 (4), 297–356.

Ekström, G., Nettles, M., Dziewoński, A., 2012. The global cmt project 2004–2010: Centroid moment tensors for 13,017 earthquakes. Phys. Earth Planet. Inter. 200, 1–9. https://doi.org/10.1016/j.pepi.2012.04.002.

Endrun, B., Lebedev, S., Meier, T., Tirel, C., Friederich, W., 2011. Complex layered deformation within the aegean crust and mantle revealed by seismic anisotropy. Nat. Geosci. 4 (3), 203. https://doi.org/10.1038/ngeo1065.

Forte, A.M., Quéré, S., Moucha, R., Simmons, N.A., Grand, S.P., Mitrovica, J.X., Rowley, D.B., 2010. Joint seismic–geodynamic-mineral physical modeling of African geodynamics: a reconciliation of deep-mantle convection with surface geophysical constraints. Earth Planet. Sci. Lett. 295 (3–4), 329–341. https://doi.org/10.1016/j.epsl.2010.03.017.

French, S.W., Romanowicz, B., 2015. Broad plumes rooted at the base of the Earth's mantle beneath major hotspots. Nature 525 (7567), 95. https://doi.org/10.1093/gji/ggu334.

Gaherty, J.B., Jordan, T.H., Gee, L.S., 1996. Seismic structure of the upper mantle in a central Pacific corridor. J. Geophys. Res. Solid Earth 101 (B10), 22291–22309.

Gaherty, J.B., Dunn, R.A., 2007. Evaluating hot spot–ridge interaction in the Atlantic from regional-scale seismic observations. Geochem. Geophys. Geosystems 8 (5). https://doi.org/10.1029/2006GC001533.

Goes, S., Armitage, J., Harmon, N., Smith, H., Huismans, R., 2012. Low seismic velocities below mid-ocean ridges: attenuation versus melt retention. J. Geophys. Res. Solid Earth 117 (B12). https://doi.org/10.1029/2012JB009637.

Graham, D., 2002. Noble gases in morb and oib: observational constraints for the characterization of mantle source reservoirs. Rev Mineral Geochem 47, 247–318. https://doi.org/10.2138/rmg.2002.47.8.

Gu, Y.J., An, Y., Sacchi, M., Schultz, R., Ritsema, J., 2009. Mantle reflectivity structure beneath oceanic hotspots. Geophys. J. Int. 178 (3), 1456–1472. https://doi.org/10.1111/j.1365-246X.2009.04242.x.

Hamza, V., Vieira, F., 2012. Global distribution of the lithosphere-asthenosphere boundary: a new look. Solid Earth 3 (2), 199–212. https://doi.org/10.5194/se-3-199-2012.

Hellfrich, G., Faria, B., Fonseca, J.F.B.D., Lodge, A., Kaneshima, S., Month, 2010. Transition zone structure under a stationary hot spot: cape verde. Earth Planet. Sci. Lett. 289 (Number), 156–161. https://doi.org/10.1016/j.epsl.2009.11.001.

Hoernle, K., Tilton, G., Le Bas, M.J., Duggen, S., Garbe-Schönberg, D., 2002. Geochemistry of oceanic carbonatites compared with continental carbonatites: mantle recycling of oceanic crustal carbonate. Contrib. Mineral. Petrol. 142 (5), 520–542. https://doi.org/10.1007/s004100100308.

Jackson, M., Becker, T., Konter, J., 2018. Evidence for a deep mantle source for em and himu domains from integrated geochemical and geophysical constraints. Earth Planet. Sci. Lett. 484, 154–167. https://doi.org/10.1016/j.epsl.2017.11.052.

Jackson, M., Hart, S., Konter, J., Kurz, M., Blusztajn, J., Farley, K., 2014. Helium and lead isotopes reveal the geochemical geometry of the samoan plume. Nature 514 (7522), 355. https://doi.org/10.1038/nature13794.

Jackson, M.G., Carlson, R.W., Kurz, M.D., Kempton, P.D., Francis, D., Blusztajn, J., 2010. Evidence for the survival of the oldest terrestrial mantle reservoir. Nature 466 (7308), 853. https://doi.org/10.1038/nature09287.

James, E.K., Dalton, C.A., Gaherty, J.B., 2014. Rayleigh wave phase velocities in the atlantic upper mantle. Geochem. Geophys. Geosystems 15 (11), 4305–4324. https://doi.org/10.1002/2014GC005518.

Katsura, T., Yoneda, A., Yamazaki, D., Yoshino, T., Ito, E., 2010. Adiabatic temperature profile in the mantle. Phys. Earth Planet. Inter. 183 (1–2), 212–218. https://doi.org/10.1016/j.pepi.2010.07.001.

Kennett, B., Engdahl, E., Buland, R., 1995. Constraints on seismic velocities in the earth from traveltimes. Geophys. J. Int. 122 (1), 108–124.

King, S.D., 2007. Hotspots and edge-driven convection. Geology 35 (3), 223–226. https://doi.org/10.1130/G23291A1.1.

King, S.D., Adam, C., 2014. Hotspot swells revisited. Phys. Earth Planet. Inter. 235, 66–83. https://doi.org/10.1016/j.pepi.2014.07.006.

King, S.D., Ritsema, J., 2000. African hot spot volcanism: small-scale convection in the upper mantle beneath cratons. Science 290 (5494), 1137–1140. https://doi.org/10.1126/science.290.5494.1137.

Laske, G., Markee, A., Orcutt, J.A., Wolfe, C.J., Collins, J.A., Solomon, S.C., Detrick, R.S., Bercovici, D., Hauri, E.H., 2011. Asymmetric Shallow Mantle Structure beneath the Hawaiian Swell - Evidence from Rayleigh Waves Recorded by the PLUME network., 187, 1725-1742, 2011. Geophys. J. Int.

Lebedev, S., Chevrot, S., Van der Hilst, R.D., 2003. Correlation between the shear-speed structure and thickness of the mantle transition zone. Phys. Earth Planet. Inter.

Lebedev, S., Meier, T., van der Hilst, R.D., 2006. Asthenospheric flow and origin of volcanism in the baikal rift area. Earth Planet. Sci. Lett. 249 (3–4), 415–424. https://doi.org/10.1016/j.epsl.2006.07.007.

Lebedev, S., Van Der Hilst, R.D., 2008. Global upper-mantle tomography with the automated multimode inversion of surface and s-wave forms. Geophys. J. Int. 173 (2), 505–518. https://doi.org/10.1111/j.1365-246X.2008.03721.x.

Liu, X., Zhao, D., 2014. Seismic evidence for a mantle plume beneath the cape verde hotspot. Int. Geol. Rev. 56 (10), 1213–1225. https://doi.org/10.1080/00206814.2014.930720.

Lodge, A., Hellfrich, G., 2006. Depleted swell root beneath the Cape Verde islands. Geology 34 (6), 449–452. https://doi.org/10.1130/G22030.1.

Lodhia, B.H., Roberts, G.G., Fraser, A.J., Fishwick, S., Goes, S., Jarvis, J., 2018. Continental margin subsidence from shallow mantle convection: example from west

Africa. Earth Planet. Sci. Lett. 481, 350–361. https://doi.org/10.1016/j.epsl.2017.10.024.

Lustrino, M., Anderson, D.L., 2015. The mantle isotopic printer: basic mantle plume geochemistry for seismologists and geodynamicists. Geol. Soc. Am. Spec. Pap. 514, 257–279. https://doi.org/10.1130/2015.2514(16).

Mata, J., Martins, S., Mattielli, N., Madeira, J., Faria, B., Ramalho, R., Silva, P., Moreira, M., Caldeira, R., Moreira, M., et al., 2017. The 2014-15 eruption and the short-term geochemical evolution of the Fogo volcano (Cape Verde): evidence for small-scale mantle heterogeneity. Lithos 288–289, 91–107. https://doi.org/10.1016/j.lithos.2017.07.001.

Mata, J., Moreira, M., Doucelance, R., Ader, M., Silva, L.C., 2010. Noble gas and carbon isotopic signatures of Cape Verde oceanic carbonatites: implications for carbon provenance. Earth Planet. Sci. Lett. 291 (1), 70–83. https://doi.org/10.1016/j.epsl.2009.12.052.

McKenzie, D., Jackson, J., Priestley, K., 2005. Thermal structure of oceanic and continental lithosphere. Earth Planet. Sci. Lett. 233 (3–4), 337–349. https://doi.org/10.1016/j.epsl.2005.02.005.

Meier, T., Dietrich, K., Stöckhert, B., Harjes, H.-P., 2004. One-dimensional models of shear wave velocity for the eastern Mediterranean obtained from the inversion of Rayleigh-wave phase velocities and tectonic implications. Geophys. J. Int. 156 (1), 45–58. https://doi.org/10.1111/j.1365-246X.2004.02121.x.

Menard, H., McNutt, M., 1982. Evidence for and consequences of thermal rejuvenation. J. Geophys. Res. Solid Earth 87 (B10), 8570–8580. https://doi.org/10.1029/JB087iB10p08570.

Monnereau, M., Cazenave, A., 1990. Depth and geoid anomalies over oceanic hotspot swells: a global survey. J. Geophys. Res. Solid Earth 95 (B10), 15429–15438. https://doi.org/10.1029/JB095iB10p15429.

Montelli, R., Nolet, G., Dahlen, F., Masters, G., 2006. A catalogue of deep mantle plumes: new results from finite-frequency tomography. Geochem. Geophys. Geosystems 7 (11). https://doi.org/10.1029/2006GC001248.

Moreira, M., 2013. Noble gas constraints on the origin and evolution of earths volatiles. Geochem. Perspect. 2 (2), 229–230.

Morgan, W.J., 1971. Convection plumes in the lower mantle. Nature 230 (5288), 42.

Mourão, C., Mata, J., Doucelance, R., Madeira, J., Millet, M.-A., Moreira, M., 2012. Geochemical temporal evolution of brava island magmatism: constraints on the variability of cape verde mantle sources and on carbonatite–silicate magma link. Chem. Geol. 334, 44–61. https://doi.org/10.1016/j.chemgeo.2012.09.031.

Müller, R.D., Sdrolias, M., Gaina, C., Roest, W.R., 2008. Age, spreading rates and spreading symmetry of the world's ocean crust, Geochemistry. Geochem. Geophys. Geosyst. 9, Q04006. https://doi.org/10.1029/2007GC001743.

Paige, C.C., Saunders, M.A., 1982. Lsqr: an algorithm for sparse linear equations and sparse least squares. Acm Trans. Math. Softw. 8 (1), 43–71.

Parsons, B., Sclater, J.G., 1977. An analysis of the variation of ocean floor bathymetry and heat flow with age. J. Geophys. Res. 82 (5), 803–827.

Patriat, M., Labails, C., 2006. Linking the canary and Cape Verde hot-spots, north-west Africa. Mar. Geophys. Res. 27 (3), 201–215. https://doi.org/10.1007/s11001-006-9000-7.

Phipps Morgan, J., Morgan, W.J., Price, E., 1995. Hotspot melting generates both hotspot volcanism and a hotspot swell? J. Geophys. Res. Solid Earth 100 (B5), 8045–8062.

Pim, J., Peirce, C., Watts, A., Grevemeyer, I., Krabbenhöft, A., 2008. Crustal structure and origin of the cape verde rise. Earth Planet. Sci. Lett. 272 (1–2), 422–428. https://doi.org/10.1016/j.epsl.2008.05.012.

Putirka, K., 2008. Excess temperatures at ocean islands: implications for mantle layering and convection. Geology 36 (4), 283–286. https://doi.org/10.1130/G24615A.1.

Saki, M., Thomas, C., Nippress, S.E., Lessing, S., 2015. Topography of upper mantle seismic discontinuities beneath the north Atlantic: the Azores, canary and Cape Verde plumes. Earth Planet. Sci. Lett. 409, 193–202. https://doi.org/10.1016/j.epsl.2014.10.052.

Schaeffer, A., Lebedev, S., 2015. Global heterogeneity of the lithosphere and underlying mantle: a seismological appraisal based on multimode surface-wave dispersion analysis, shear-velocity tomography, and tectonic regionalization. The Earth's Heterogeneous Mantle. Springer, pp. 3–46. https://doi.org/10.1007/978-3-319-15627-9_1.

Sleep, N.H., 1990. Hotspots and mantle plumes: some phenomenology. J. Geophys. Res. Solid Earth 95 (B5), 6715–6736.

Soomro, R., Weidle, C., Cristiano, L., Lebedev, S., Meier, T., Group, P.W., 2015. Phase velocities of Rayleigh and Love waves in central and northern Europe from automated, broad-band, inter-station measurements. Geophys. J. Int. 204 (1), 517–534. https://doi.org/10.1093/gji/ggv462.

Stein, C.A., Stein, S., 1992. A model for the global variation in oceanic depth and heat flow with lithospheric age. Nature 359 (6391), 123.

Vales, D., Dias, N.A., Rio, I., Matias, L., Silveira, G., Madeira, J., Weber, M., Carrilho, F., Haberland, C., 2014. Intraplate seismicity across the Cape Verde swell: a contribution from a temporary seismic network. Tectonophysics 636, 325–337. https://doi.org/10.1016/j.tecto.2014.09.014.

Vinnik, L., Silveira, G., Kiselev, S., Farra, V., Weber, M., Stutzmann, E., Month, 2012. Cape verde hotspot from the upper crust to the top of the lower mantle. Earth Planet. Sci. Lett. 319–320 (Number), 259–268. https://doi.org/10.1016/j.epsl.2011.12.017.

Wilson, D., Peirce, C., Watts, A., Grevemeyer, I., Krabbenhöft, A., 2010. Uplift at lithospheric swells I: seismic and gravity constraints on the crust and uppermost mantle structure of the cape verde mid-plate swell. Geophys. J. Int. 182 (2), 531–550. https://doi.org/10.1111/j.1365-246X.2010.04641.x.

Wilson, D., Peirce, C., Watts, A., Grevemeyer, I., 2013. Uplift at lithospheric swells II: is the Cape Verde mid-plate swell supported by a lithosphere of varying mechanical strength? Geophys. J. Int. 193 (2), 798–819. https://doi.org/10.1093/gji/ggt034.

Wilson, J.T., 1963. A possible origin of the Hawaiian islands. Can. J. Phys. 41 (6), 863–870.

D.3 SISMIKO: emergency network deployment and data sharing for the 2016 central Italy seismic sequence

ANNALS OF GEOPHYSICS, 59, FAST TRACK 5, 2016; DOI: 10.4401/AG-7212

SISMIKO: emergency network deployment and data sharing for the 2016 central Italy seismic sequence

MILENA MORETTI*, SILVIA PONDRELLI*, LUCIA MARGHERITI*, LUIGI ABRUZZESE*, MARIO ANSELMI*, PIERRE ARROUCAU°, PAOLA BACCHESCHI*, BRIAN BAPTIE°°, RAFFAELE BONADIO°, ANDREA BONO*, AUGUSTO BUCCI*, MAURO BUTTINELLI*, MARCO CAPELLO*, VINCENZO CARDINALE*, ANGELO CASTAGNOZZI*, MARCO CATTANEO*, GIANPAOLO CECERE*, CLAUDIO CHIARABBA*, LAURO CHIARALUCE*, GIOVANNI BATTISTA CIMINI, ROCCO COGLIANO*, GIANFRANCO COLASANTI*, MARCO COLASANTI*, FABIO CRISCUOLI*, EZIO D'ALEMA*, ANTONINO D'ALESSANDRO*, CIRIACO D'AMBROSIO*, PETER DANECEK*, MARIAGRAZIA DE CARO*, PASQUALE DE GORI*, ALBERTO DELLADIO*, GAETANO DE LUCA*, GIOVANNI DE LUCA*, MARTINA DEMARTIN*, MARIA DI NEZZA*, RAFFAELE DI STEFANO*, LUIGI FALCO*, MASSIMO FARES*, MASSIMO FRAPICCINI*, ALBERTO FREPOLI*, DANILO GALLUZZO*, EDOARDO GIANDOMENICO*, LUCIAN GIOVANI*, CARLO GIUNCHI*, ALADINO GOVONI*, DAVID HAWTHORN°, CHIARA LADINA*, VALENTINO LAUCIANI*, ANTHONY LINDSAY°°°, SIMONE MANCINI*, ALFONSO GIOVANNI MANDIELLO*, SIMONE MARZORATI*, MARCO MASSA*, ANTONINO MEMMOLO*, FRANCO MIGLIARI*, FELICE MINICHIELLO*, GIANCARLO MONACHESI*, CATERINA MONTUORI*, RAFFAELE MOSCHILLO*, SHANE MURPHY*, NICOLA MAURO PAGLIUCA*, MARINA PASTORI*, DAVIDE PICCININI*, ULDERICO PICCOLINI*, STEFANO PINTORE*, GIULIO POGGIALI°, SANDRO RAO*, GILBERTO SACCOROTTI*, MARGARITA SEGOU°°, ANDREA SERRATORE*, MARCELLO SILVESTRI*, STEFANO SILVESTRI*, MASSIMILIANO VALLOCCHIA*, LUISA VALOROSO*, LUCIANO ZUCCARELLO*, ALBERTO MICHELINI* AND SALVATORE MAZZA*

*Istituto Nazionale di Geofisica e Vulcanologia, Italy
°Dublin Institute for Advanced Studies, Ireland
°°British Geological Survey, United Kingdom
°°° University of Ulster, United Kingdom

milena.moretti@ingv.it

Abstract

At 01:36 UTC (03:36 local time) on August 24th 2016, an earthquake Mw 6.0 struck an extensive sector of the central Apennines (coordinates: latitude 42.70° N, longitude 13.23° E, 8.0 km depth). The earthquake caused about 300 casualties and severe damage to the historical buildings and economic activity in an area located near the borders of the Umbria, Lazio, Abruzzo and Marche regions. The Istituto Nazionale di Geofisica e Vulcanologia (INGV) located in few minutes the hypocenter near Accumoli, a small town in the province of Rieti. In the hours after the quake, dozens of events were recorded by the National Seismic Network (Rete Sismica Nazionale, RSN) of the INGV, many of which had a ML > 3.0. The density and coverage of the RSN in the epicentral area meant the epicenter and magnitude of the main event and subsequent shocks that followed it in the early hours of the seismic sequence were well constrained. However, in order to better constrain the localizations of the aftershock hypocenters, especially the depths, a denser seismic monitoring network was needed.

Just after the mainshock, SISMIKO, the coordinating body of the emergency seismic network at INGV, was activated in order to install a temporary seismic network integrated with the existing permanent network in the epicentral area. From August the 24th to the 30th, SISMIKO deployed eighteen seismic stations, generally six components (equipped with both velocimeter and accelerometer), with thirteen of the seismic station transmitting in real-time to the INGV seismic monitoring room in Rome. The design and geometry *of the temporary network was decided in collaboration with other groups who were deploying seismic stations in the region, namely EMERSITO (a group studying site-effects), and the emergency Italian strong motion network (RAN) managed by the National Civil Protection Department (DPC). Further 25 BB temporary seismic stations were deployed by colleagues of the British Geological Survey (BGS) and the School of Geosciences, University of Edinburgh in collaboration with INGV.*

All data acquired from SISMIKO stations, are quickly available at the European Integrated Data Archive (EIDA). The data acquired by the SISMIKO stations were included in the preliminary analysis that was performed by the Bollettino Sismico Italiano (BSI), the Centro Nazionale Terremoti (CNT) staff working in Ancona, and the INGV-MI, described below.

I. INTRODUCTION

SISMIKO is an operational group in the Istituto Nazionale di Geofisica e Vulcanologia (INGV) which coordinates all the seismic emergency networks of INGV (Fig. 1). The staff involved in this group come from the different sections within the INGV which deal with seismic monitoring on a daily basis [Moretti et al. 2016]. The aim of SISMIKO is to deploy additional seismic stations in a region following a significant earthquake. Increasing the density of a seismic monitoring network, during a seismic sequence following a significant earthquake has the effect of improving the detection capabilities of the network and the precision of the earthquake locations. This in turn allows for the definition the geometry of the activated fault structures and to constrain the spatial distribution of the seismicity, moreover it provides high quality data for hazard and seismotectonic studies and investigations into the physics of earthquakes.

SISMIKO deals with important decisions, procedures and actions that the INGV undertakes during a seismic emergency, in cooperation with other emergency groups like EMERSITO, who study site effects [Cultrera et al. 2016]; QUEST, which is involved in damage relief (QUick Earthquake Survey Team [QUEST working group 2016]); EMERGEO, which focuses on mapping geological surface effects [EMERGEO Working Group 2016]; and IES [Nostro at al. 2011] who provide an information service for the general public (Information in emergency earthquake).

Following the formalization of these INGV emergency groups, a training test of the protocols for the different individual emergency groups was organized on 26th November 2015 [Pondrelli et al. 2016]. The lessons learnt during this training test helped the coordination of the different INGV groups to handle the central Italy emergency.

Figure 1: *INGV offices that are involved in the SISMIKO group with equipment and/or personnel that is available for emergency response.*

II. TIMING OF THE DEPLOYMENT

The Mw 6.0 Amatrice event occurred on August 24th, 2016 it was recorded by INGV National Seismic Network (Rete Sismica Nazionale, RSN, http://doi.org/10.13127/SD/X0FXNH7QFY), and the epicenter was located near the village of Accumoli at a depth of 8 km (http://cnt.rm.ingv.it/7073641). As per protocol in the INGV for emergency events, the national SISMIKO coordinators received an SMS with preliminary information about the earthquake a few minutes after the origin time of the event. The alert was then forwarded to local representatives of SISMIKO group and the coordination for the deployment of an emergency seismic network commenced.

After checking the performance of the permanent stations of the RSN in the epicentral area and taking into account the trend of the initial aftershocks, the SISMIKO group prepared, in less than three hours from the mainshock, the theoretical distribution of the deployment to guide the teams on the field.

On the first day of activation of the SISMIKO group personnel in the INGV offices closest to the epicentral area were used: Ancona (1 team), Grottaminarda (2 teams), L'Aquila (1 team) and Rome (1 team), in total fourteen people were in the field and ten stations were deployed. The team from Ancona, reached the epicentral area at around 7:15 UTC, and installed three temporary stations each one equipped with one velocimetric sensor and one accelerometer in the northern and eastern side of the initial aftershock sequence. The first installation was completed at around 08:40 UTC (i.e. station T1243). This station, as well as station T1241 (which start recording at around 11:15 UTC) and station T1242 (14:40 UTC), were in UMTS realtime transmission. INGV personnel based in Grottaminarda organized two teams to go in the field for maintenance of the permanent seismic stations that were part of the RSN and for the installation of temporary stations. This group installed three temporary stations located near Amatrice, one equipped with an accelerometer, one with a short period seismometer and the other with Broad Band (BB). The first temporary station installed, T1201 was completed around 15:30 UTC, after this T1202 and T1204 were positioned; all stations are in UMTS real-time transmission. INGV Rome contributed to the deployment with four stations in local acquisition, each equipped with a short period seismometer and an accelerometer. These stations were installed on western side of the seismic sequence. The first installation by the Rome group was station T1211 at about 7:30 UTC and was located on the road which leads from Rome to the epicentral area; T1212, T1213 and T1214 were deployed in the following hours.

During the day of August 24th the Grottaminarda, L'Aquila and Ancona staff performed maintenance on stations AQT1, NRCA, SMA1 and LNSS (Fig. 2), in the RSN, which had experienced electrical power and data transmission problems due to collapses and damages in the epicentral area, in the initial hours after the main earthquake.

In the next two days, six teams from Ancona (1), Grottaminarda (2), L'Aquila (1) and Rome (2), continued the field work. Five additional stations were installed, of which two were in realtime, moreover the teams visited the stations that were operating in local acquisition mode where they downloaded the data.

Looking at the evolution of the seismicity in the evening of August 26 it was decided a further improvement to the network in the southern sector was required. On Sunday 28 a team of INGV Pisa installed two Broad Band stations (BB) (T1246 and T1247).

On August 30 station T1299 was the final station installed in the temporary network by the INGV Roma RSN staff. The station, equipped with a short period velocimeter and an accelerometer, transmitted data in real-time via satellite connection, it was deployed in the village Casale Bucci, close Amatrice, in the southern sector of the sequence.

Similar to the Emilia emergency in 2012 [Moretti et al. 2012; 2013], there has been a continuous interaction with EMERSITO (Fig. 2, fuchsia hexagons) and with the mobile network group of the Italian Strong Motion Network (RAN-DPC, http://ran.protezionecivile.it/; Fig. 2, orange hexagons) for the sharing of information in order to integrate the different temporary networks without redundant overlapping. In addition, at the start of September colleagues of the British Geological Survey (BGS) and the School of Geosciences at the University of Edinburgh arrived in the epicentral area. The INGV was in contact with these two groups since the start of the seismic emergency when they had expressed interest in deploying a Broad Band network (BB) to supplement the INGV-SISMIKO network in region. Thus, as in the 1997-98 seismic sequence in Umbria [Amato et al. 1998] and in 2009 in Abruzzo [Margheriti et al. 2011], and in Emilia 2012 [Moretti et al. 2012] we welcomed this international collaboration between European research institutes. This collaboration resulted in two weeks of fieldwork starting at the beginning of September, has led to the installation of an additional 25 BB seismic stations (Fig. 2, blue hexagons). The installation of these stations, which remained in acquisition for a period of about 6 months and whose data will be available on the web site of the Incorporated Research Institutions for Seismology (IRIS; http://ds.iris.edu/ds/nodes/dmc/). These extra stations have enabled us to halve the inter-distance between seismic stations from approximately 15-18km to 6-8km (see Fig. 2).

In Fig. 3, shows the timing of installation and maintenance of temporary network SISMIKO during the first emergency month. In the tables in Annex A, the list of installed stations and the type of instrumentation used.

At the end of October 2016, on the 30th the strongest earthquake of the sequence Mw=6.5, stoke again the same area, this event was preceded by two earthquakes of magnitude greater than 5.0 on October the 26th, the total length of the fault system interested by the seismicity is now about 55 km. After these events, SISMIKO has installed 4 new temporary stations in the area north of the sequence (Fig. 2, orange triangles).

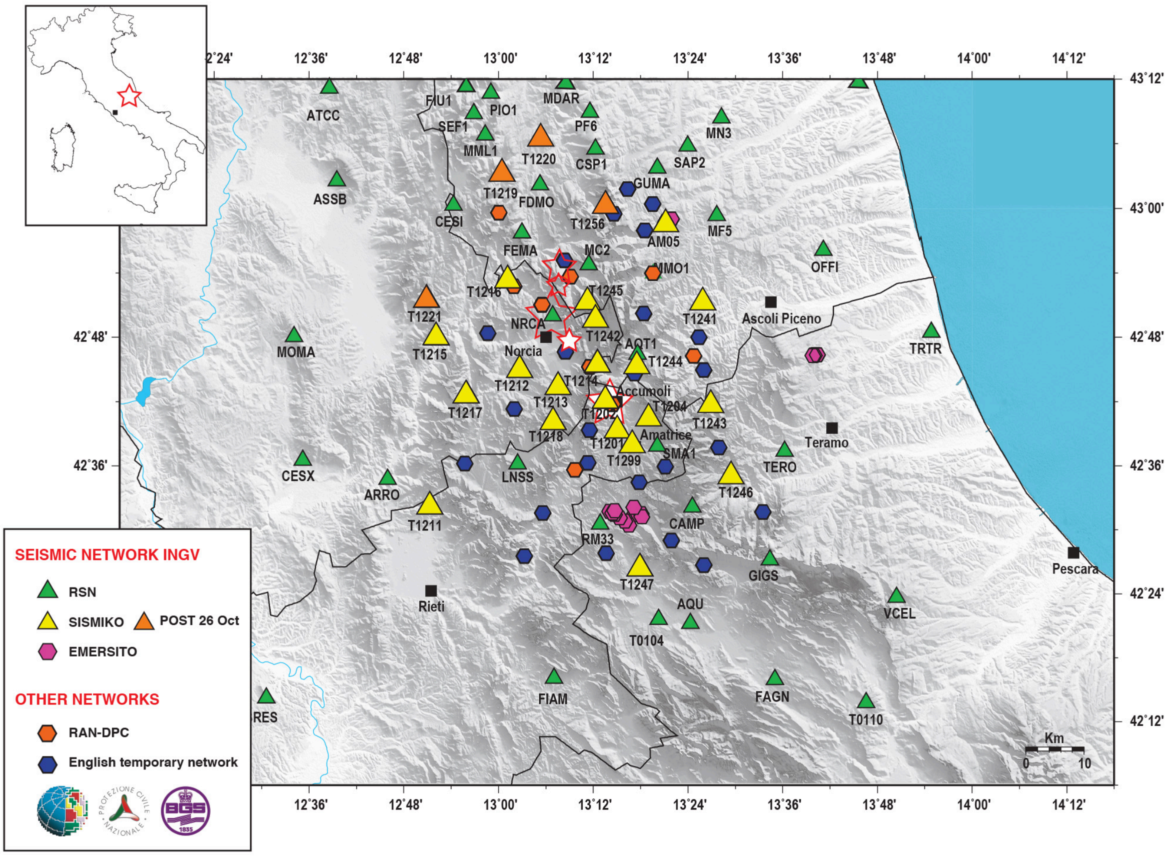

Figure 2: *Map of the seismic stations deployed after August 24th: INGV permanent stations (green triangles) and SISMIKO temporary stations (yellow triangles), EMERSITO stations (fuchsia hexagons), RAN-DPC stations (orange hexagons) and the BB network (blue hexagons). The orange triangles are seismic stations deployed after the events October 26th. The stars show the strongest earthquakes of the sequence up to the submission of the paper: the full stars shows those at end of August, the stars empty at end of October.*

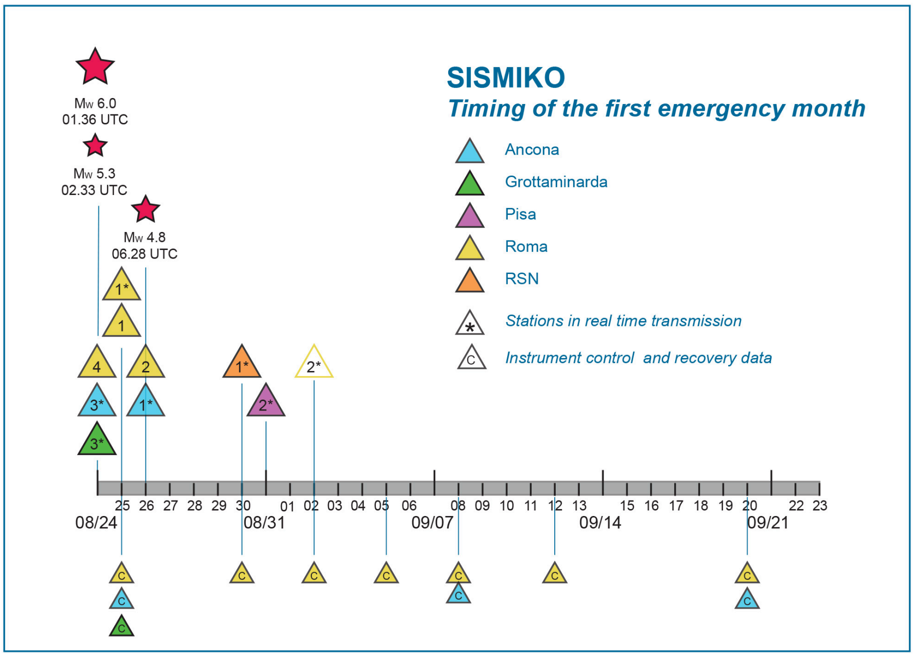

Figure 3: *Timing of installation and maintenance of temporary network SISMIKO during the first emergency month. Red stars show the strongest earthquakes of the sequence. The numbers inside the triangles, in different colours, depending on the INGV office which carried out the activities, indicating the stations installed throughout the day. With an asterisk are the ones highlighted in real-time transmission and, in the case of stations T1216 and T1217, initially in local acquisition, and then subsequently have been equipped with UMTS router (September 2). The triangles in the lower part of the timeline indicating when it was controlled instrumentation and were collected of data.*

III. PRELIMINARY ANALYSIS OF THE DATA ACQUIRED BY SISMIKO STATIONS

The mainshock was followed by sustained seismic activity; in the first month after the main event there have been about 12,000 events, including 16 ML ≥ 4.0 (Fig. 4). All data collected by the stations installed by SISMIKO, are available at the European Integrated Data Archive (EIDA; http://eida.rm.ingv.it/ [Mazza et al. 2012]). The inclusion in the EIDA of waveforms was done immediately at the deployment of the stations, while the integration of data in the surveillance system at the INGV headquarters in Rome was gradual; in fact, during an emergency the surveillance room has the duty of alerting DPC and the technical operations needed to allow stations in the automatic location system should be done with extreme caution. Starting from September 9, 2016, in weekly steps, data from the SISMKO stations recording in local acquisition were collected; converted and published in the international Standard for Exchange of Earthquake data (SEED) format and archived in in EIDA [Mazza et al. 2012]. The availability of real-time data from the temporary stations allowed for the analysis of the seismic sequence in almost real-time with quality and accuracy.

On the morning of August 24, the first stations that broadcast real-time data from the epicentral area were T1242, T1243 and T1244. There data was first transmitted to the servers in the Ancona office, and in short time were incorporated into the automatic analyzes of the ongoing seismic activity. In particular, station T1243 was used for the first time in the automatic location of an event at 08:45:30 UTC; stations T1241 and T1242 at 11:20:36 UTC and 14:42:59 UTC respectively. At the same time station

T1243 was also integrated in the seismic monitoring system in the Rome office and used for the first time in the event of ML 3.1 of 15:39:32 UTC [http://cnt.rm.ingv.it/event/7116751]. At the same time as station T1243 was included in the central seismic monitoring system an additional two permanent stations of the Marche Regional network, managed by INGV headquarters in Ancona was incorporated into the network. The two stations, MC2 and MMO1 (Fig. 2) before the emergency were not acquired by INGV-Rome but after the mainshock were included for the good coverage that guaranteed in the area North and Northeast of the sequence.

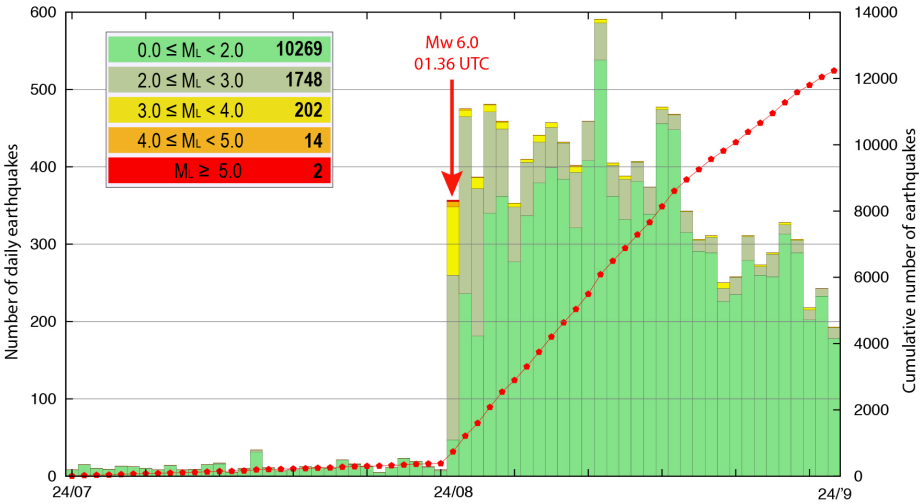

Area:42.70°N - 13.23°E - radius 50km | Periodo of time : 24/07-24/09/2016

Data Source: ISIDe

***Figure 4**: Evolution of seismic activity in the area of the seismic sequence in the first month of seismic activity and the month immediately preceding. The selection of events was made in a circular area of 50km centered in the mainshock (42.70° N - 13:23° E). The figure shows the locations produced by seismologists on duty at the INGV seismic monitoring center in Rome.*

There are several advantages associated with the integration of temporary stations in the analysis of data that were observed in the initial hours of the emergency. The thirteen temporary stations that transmitted in real-time were gradually added in the seismic monitoring system making it possible to lower the detection threshold of the network and improve the quality of the hypocenter determinations especially as regards to the depth of the hypocenters. To evaluate the contribution of the SISMIKO temporary network to locate local seismicity in the Amatrice area, we have applied the Seismic Network Evaluation through Simulation (SNES) method [D'Alessandro et al. 2011] to two different network that are the RSN and the RSN+SISMIKO. The SNES method allows determining, as a function of magnitude, hypocentral depth and confidence level, the spatial distribution of the number of active stations in the location procedure and their relative azimuthal gap and the confidence levels of hypocentral parameters (see Annex B).

Data relayed in real-time together with data from temporary stations in local acquisition (i.e. stations T1211-12-13-14-18 and 16-17), represented a major contribution in the localization of earthquakes for the Italian Seismic Bulletin (BSI) [Nardi et al. 2015]; BSI is reviewing the sequence with two main goals: a) improve as mentioned the location of aftershocks detected by the automatic system and b) insert into catalogue events not localized by the seismologist on shifts in the surveillance room. More details can be found in the "Preliminary report on the activities carried out by the Italian Seismic Bulletin Group [Bollettino Sismico Italiano – Gruppo di lavoro Amatrice (2016); Marchetti et al. 2016].

The proximity of the area affected by the seismic earthquake sequence in relation to the area monitored by INGV Ancona office allowed us to use automatic procedures, to make automatic quality control analysis [Marzorati et al. 2012] on the real-time data.

Moreover, the continuous band-pass filtered signals are analyzed by the STA/LTA trigger algorithm to detect triggers at each station, an event is declared when a trigger is detect at a number of key stations. In particular, event declaration is controlled by the weights assigned to each individual component of the seismic stations on the basis of their average noise level to enhance the influence of the best stations. This procedure allows the maintenance of low STA/LTA ratios (and thus high sensitivity) without increasing too much the probability of false events declaration due to triggering occurring by chance. The core of the automatic system is the RSNI-Picker [Spallarossa et al. 2014; Scafidi et al. 2016]. This picker uses the "Akaike information criterion" (AIC; Akaike, 1974), which strongly limits the occurrence of false pickings. Moreover, a user-calibrated procedure assigns to each picking a weight that attempts to mimic a human operator. This procedure has automatically located 4174 events between the 24th and 31st August, and 7245 events between the 1st and 20th September.

Moreover, from August 24th, 2016 (01:36:32 UTC) to 30th September 2016 (last update) the accelerometric database of the INGV (http://ismd.mi.ingv.it/; [ISMD Working Group 2016]), analyzed and published in near real-time over 21,300 waveforms belonging to about 121 earthquakes with a magnitude range between 3.0 and 6.0. In particular, about 1600 accelerometer recordings are relative only to stations installed in the epicentral area by SISMIKO. All the real-time accelerometer data from the SISMIKO stations (see Table 2 in Annex A) are available after 1 or 2 hours since the origin time of each earthquake, in SAC and ASCII formats. For each earthquake, there is 5 minutes of signal from the origin time determined by the monitoring room in Rome and published on the CNT website (cnt.rm.ingv.it). Details on the automatic data and analysis method are described in Massa et al. [2014].

ACKNOWLEDGEMENTS

We do thank the many people who contributed to the success of the seismic rapid-response in the earthquake area in Amatrice. We are grateful to Elisa Zambonelli and other DPC colleagues for coordinating with us during the deployment. The study benefited from funding provided by the Italian Presidenza del Consiglio dei Ministri, Dipartimento della Protezione Civile (DPC); scientific papers funded by DPC do not represent its official opinion and policies.

REFERENCES

Amato, A. et al. (1998). The Colfiorito, Umbria–Marche earthquake sequence in central Italy (Sept.–Nov., 1997): a first look to mainshocks and after- shocks, *Geophys. Res. Lett.* 25, 2861–2864.

BOLLETTINO SISMICO ITALIANO – Gruppo di lavoro Amatrice (2016). Rapporto preliminare sulle attività svolte dal gruppo bollettino sismico italiano a seguito del terremoto di Amatrice Mw 6.0 (24 agosto 2016, italia centrale). Doi: 10.5281/zenodo.157545.

D'Alessandro, A., Papanastassiou, D., Baskoutas, I. (2011). Hellenic Unified Seismological Network: an evaluation of its performance through SNES method, *Geophysical Journal Int.*, 185, 3, 1417-1430. Doi: 10.1111/j.1365-246X.2011.05018.x.

EMERGEO Working Group (2016). Coseismic effects of the 2016 Amatrice seismic sequence: first geological results, *Ann. Geophyiscs*, this issue. DOI: 10.4401/ag-7195.

Cultrera G., D'Alema E., Amoroso S., Angioni B., Bordoni P. , Cantore L. , Cara F., Caserta A., Cogliano R., D'Amico M., Di Giulio G., Di Naccio D., Famiani D., Felicetta C., Fodarella A., Lovati S., Luzi L., Mascandola C., Massa M., Mercuri A., Milana G., Pacor F., Pischiutta M., Pucillo S., Puglia R., Riccio G., Tarabusi G., Vassallo M. (2016). Site effect studies following the 2016 Mw 6.0 Amatrice Earthquake (Italy): the Emersito Task Force activities, *Ann. Geophyiscs*, this issue**.**

ISMD Working Group (2016). INGV Strong Motion database: Dati accelerometrici INGV in tempo quasi reale.

https://sites.google.com/a/ingv.it/dati-emergenza/attivita-scientifiche/ground-motion. Doi: 10.5281/zenodo.154703.

Marchetti, A. et al. (2016). The Italian Seismic Bulletin: strategies, revised pickings and locations of the Amatrice seismic sequence, Ann. Geophyiscs, this issue. DOI: 10.4401/ag-7169.

Margheriti, L. et al. (2011). Rapid response seismic networks in Europe: lessons learnt from the L'Aquila earthquake emergency, *Ann. Geophys.*, 54 (4). Doi: 10.4401/ag-4953.

Marzorati, S., Carannante, S., Cattaneo, M., D'Alema, E., Frapiccini, M., Ladina, C., Monachesi G., and Spallarossa. D. (2012). Automated control procedures and first results from the temporary seismic monitoring of the 2012 Emilia sequence. *Ann. Geophys.*, 55 (4); doi:10. 4401/ag-6116.

Massa, M., Lovati, S., Franceschina, G., D'Alema, E., Marzorati, S., Mazza, S., Cattaneo, M., Selvaggi, G., Amato, A., Michelini, A. and Augliera. P. (2014). ISMD, a web portal for the realtime processing and dissemination of INGV strong-motion data, *Seism. Res. Letters*, 85, 4, 727-734.

Mazza, S., Basili, A., Bono, A., V., Lauciani, Mandiello, A.G., Marcocci, C., Mele, F.M., Pintore, S. M. Quintiliani, L., Scognamiglio and G. Selvaggi (2012). AIDA – Seismic data acquisition, processing, storage and distribution at the National Earthquake Center, INGV, *Ann. Geophys.*, 55 (4). Doi:10.4401/ag-6145.

Moretti, M. et al. (2012). Rapid-response to the earthquake emergency of May 2012 in the Po Plain, Northern Italy, *Ann. Geophys.*, 55 (4), 583 – 590. Doi: 10.4401/ag-6152.

Moretti, M., et al. (2013). Terremoto in Emilia: le attività del Pronto Intervento Sismico durante il primo mese di emergenza. Modalità e tempistica, *Quaderni di Geofisica*, 110.

Moretti, M., Margheriti, L., Govoni, A. (2016). Rapid response to earthquake emergencies in Italy: temporary seismic network coordinated deployments in the last five years, in: D'Amico S. (Ed): Earthquakes and their impacts on Society, Springer.

Nardi, A. et al. (2015). Bollettino Sismico Italiano: novità, 34° GNGTS, Trieste, novembre 2015.

Nostro, C., Camassi, R., Crescimbene, M., La Longa, F., Ercolani E. et al. (2011). Emergenza e informazione, estratto da "Sintesi dei lavori del Workshop. EDURISK 2002 – 2011 | 10 anni di progetti di educazione al rischio", *Miscellanea INGV*, 13.

Pintore, S., Bernardi, F., Bono, A., Danecek, P., Faenza, L., Fares, M., Lauciani, V., Lucente, F.P., Marcocci, C., Pietrangeli, D., Quintiliani, M., Mazza, S., Michelini A. (2016). INGV data lifecycle management system performances during Mw 6.0 2016 Amatrice Earthquake Sequence, *Ann. Geophyiscs*, this issue.

Pondrelli, S. et al. (2016). Pianificazione e gestione di un'emergenza sismica: esercitazione INGV del 26 novembre 2015 effettuata nell'ambito della Linea di Attività T5 "Sorveglianza sismica e operatività post terremoto", *Quaderni di Geofisica*, 137.

Scafidi, D., Spallarossa, D., Turino, C., Ferretti, G. and Viganò, A. (2016). Automatic P-and S-Wave Local Earthquake Tomography: Testing Performance of the Automatic Phase-Picker Engine RSNI-Picker, *Bull. Seism. Society of America*, 106 (2), 526-536. Doi:10.1785/0120150084.

Spallarossa, D., G., Ferretti, D., Scafidi, C., Turino and M., Pasta (2014). Performance of the RSNI-Picker, *Seismol. Res. Lett*. 85, 1243–1254.

QUEST working group (2016). The 24 August 2016 Amatrice earthquake: macroseismic survey in the damage area and EMS intensity assessment, *Ann. Geophyiscs*, this issue. DOI: 10.4401/ag-7203.